Estimating natural and anthropogenic responses of the water cycle in the Earth system using comprehensive coupled climate models

Inauguraldissertation

der Philosophisch–naturwissenschaftlichen Fakultät
der Universität Bern

vorgelegt von

Flavio Lehner

aus Basel (BS)

Leiter der Arbeit:

Prof. Dr. Thomas F. Stocker
PD. Dr. Christoph C. Raible

Abteilung für Klima– und Umweltphysik
Physikalisches Institut der Universität Bern

Estimating natural and anthropogenic responses of the water cycle in the Earth system using comprehensive coupled climate models

Inauguraldissertation

der Philosophisch–naturwissenschaftlichen Fakultät
der Universität Bern

vorgelegt von

Flavio Lehner

aus Basel (BS)

Leiter der Arbeit:

Prof. Dr. Thomas F. Stocker
PD. Dr. Christoph C. Raible

Abteilung für Klima– und Umweltphysik
Physikalisches Institut der Universität Bern

Von der Philosophisch–naturwissenschaftlichen Fakultät angenommen.

Der Dekan
Bern, 19. Juni 2013   Prof. Dr. Silvio Decurtins

Contents

Thesis summary

Strong and growing quantitative evidence is at hand that the Earth's climate has undergone distinct changes in the past. During the last millennium the influence of external and internal processes rendered both warmer and colder periods, the most pronounced of which are referred to as the Medieval Climate Anomaly and the Little Ice Age, respectively. To disentangle the different influences and to determine the importance of individual forcing factors during such periods is a key task of climate research. In view of the current anthropogenically induced climate change, a robust understanding of the climate system's sensitivity to different forcings represents a crucial prerequisite for reliable projections of future climate change. However, achieving this understanding is not always straightforward as the climate system's internal variability is often large and different forcings act at the same time, making the detection and attribution of climate change a delicate endeavor. Further, most information of past climate variations comes from stationary proxy archives that can only draw an incomplete picture of the dynamics associated with those climate variations.

At this point climate models become an indispensable tool, offering unique possibilities to tackle these issues. Unlike in the real world, natural and anthropogenic forcing can be kept constant or applied separately in models and thereby permit the study of their isolated influence on climate. Additionally, ensembles of simulations that apply identical forcing but are started from different initial conditions are used to separate a forcing signal from internal variability. Ultimately, these approaches are applied across different models to reduce the risk that a single model lacks a crucial process. When thoroughly validated against observations and reconstructions, these models can be used to project future climate change, based on an expected evolution of the natural and anthropogenic forcing.

This thesis embraces all of these model approaches to address past and future changes in the hydrological cycle. The model studies in this thesis are to a large part motivated by the temporal and spatial limitations of observations and reconstructions and aim at closing the gap between the signal from such data sources and the dynamical understanding of it. Given the potential for advancing our knowledge of past climate change, collaborations between the observational and modeling community are still too few. Often, reconstructions are founded solely on the author's interpretation and are weakly supported by process understanding and model results, thereby increasing the chance for misinterpretation. Growing availability of state-of-the-art model output offers an excellent opportunity to test and back up the interpretation of reconstructions.

The hydrological cycle receives increasing attention in climate research as its future fate is of great importance for society and for the climate system itself. Freshwater stored in reservoirs of the polar regions is an important component of the global hydrological cycle, and a redistribution of this freshwater can have climatic impacts beyond the polar region. Therefore, the sensitivity of these reservoirs to climate change has been of interest for quite a while, yet, the scarceness of observations and reconstructions in the polar regions complicates the analysis of it. Using model simulations from 1500-2100 AD, we are able to put past changes in the polar freshwater cycle into context of ongoing and projected future climate change in these regions. The different reservoirs sea ice, ocean, and atmosphere exhibit different response

behavior to preindustrial changes in external forcing such as low solar activity or volcanic eruptions. While being significant in some cases, these variations are dwarfed compared to future changes, when both polar regions are projected to become a strong source of freshwater for lower latitudes with implications for ocean circulation.

A second study investigates the issue of stationarity in a millennial proxy reconstruction of the North Atlantic Oscillation (NAO). This reconstruction has received a considerable level of attention as it suggests that the NAO has remained in a positive state for several centuries during the Medieval Climate Anomaly, potentially exhibiting a strong control on European climate during that time. Using pseudo-proxies from model simulations the explanatory power of the precipitation proxies used in this reconstruction is estimated. In the particular case, the proxy locations were found to be insufficient to robustly describe the NAO over the last millennium. Recommendations are made as to the improvement of the reconstruction concept.

Following from the criticism of this NAO reconstruction, alternative explanations for the North Atlantic-European climate variations during the last millennium are explored in an ensemble of model simulations from the Medieval Climate Anomaly to the Little Ice Age. A feedback mechanism between sea ice, ocean, and atmosphere is discovered in the region of the subpolar North Atlantic and Nordic Seas that can account for much of the climate variations during the transition from the Medieval Climate Anomaly to the Little Ice Age without relying on significant excursions of the NAO. This feedback mechanism is thoroughly tested with sensitivity experiments in which sea ice growth is artificially enhanced in certain locations of the Arctic Ocean and the northern North Atlantic. This represents a new approach to study the impact of sea ice on climate in the coupled system. Potential future applications of this approach are discussed in the outlook.

In the appendix of this thesis, preliminary results of a last millennium simulation with a comprehensive coupled Earth system model are presented. This simulation offers new opportunities to address a variety of research questions and will allow us to improve our understanding of past and future climate change.

Chapter 1

Introduction

Driven by the paramount need to project the climate system's response to ongoing and future changes in Earth's atmospheric composition, understanding the causes and mechanisms behind past and present variations in Earth's climate is a key task of today's climate research. Reconstructions of natural and anthropogenic forcing parameters and climate variables allow to draw a picture of past climate variations. Models, driven by the reconstructed forcing, attempt to reproduce these climate variations and provide the opportunity to study the dynamics underlying the variations.

In this thesis the impact of natural and anthropogenic external forcing on the climate system is investigated in simulations with global climate models. This chapter provides a brief introduction to the climate system and processes governing its variability on timescales of months to centuries. As the hydrological cycle represents the overarching theme of this thesis, it is introduced in more detail. Thereby, a focus is set on regions and processes important for this thesis. Further, a section on climate modeling provides a description of the model of choice for this thesis as well as the simulations conducted. The outline of the thesis is given at the end of this chapter.

1.1 The climate system

Climate is defined as average weather in terms of its mean and variability over a certain time period and a certain area (IPCC, 2007). However, climate is also often referred to as the state of the climate system as a whole, whereby the hydrosphere, the cryosphere, the land surface, and the biosphere are considered along with the atmosphere. These climate components are constantly exchanging energy, mass, and momentum on different time scales (Fig. 1.1). The primary energy source for this system is the incoming shortwave radiation from the Sun. The amount of energy not directly reflected back to space is absorbed or redistributed across the globe and eventually leaves the system via thermal radiation. Thus, when neglecting the geothermal heat flux, Earth's energy balance is closed. However, the climate system can never be considered in equilibrium. This paradox arises from the facts that, (i) the Earth's orbital configuration varies on multi-millennial time scales, (ii) the incoming energy from the Sun is not constant over time, and (iii) the different mechanisms that redistribute or temporally store energy on Earth are neither stable nor do they act synchronously. For these reasons, the climate has undergone substantial changes in the past. Strong variations in Earth's temperature and the accompanied degree of global glaciation during the Quaternary (glacial-interglacial cycles) represent well-documented – but not necessarily well-understood – manifestations of the interplay between the above-mentioned parameters. On shorter time scales, such as during the Holocene, changes in system-internal processes gain importance relative to the slow-changing parameters of Earth's orbital configuration. This thesis focuses on variations in the climate system during the late Holocene and the twenty-first century.
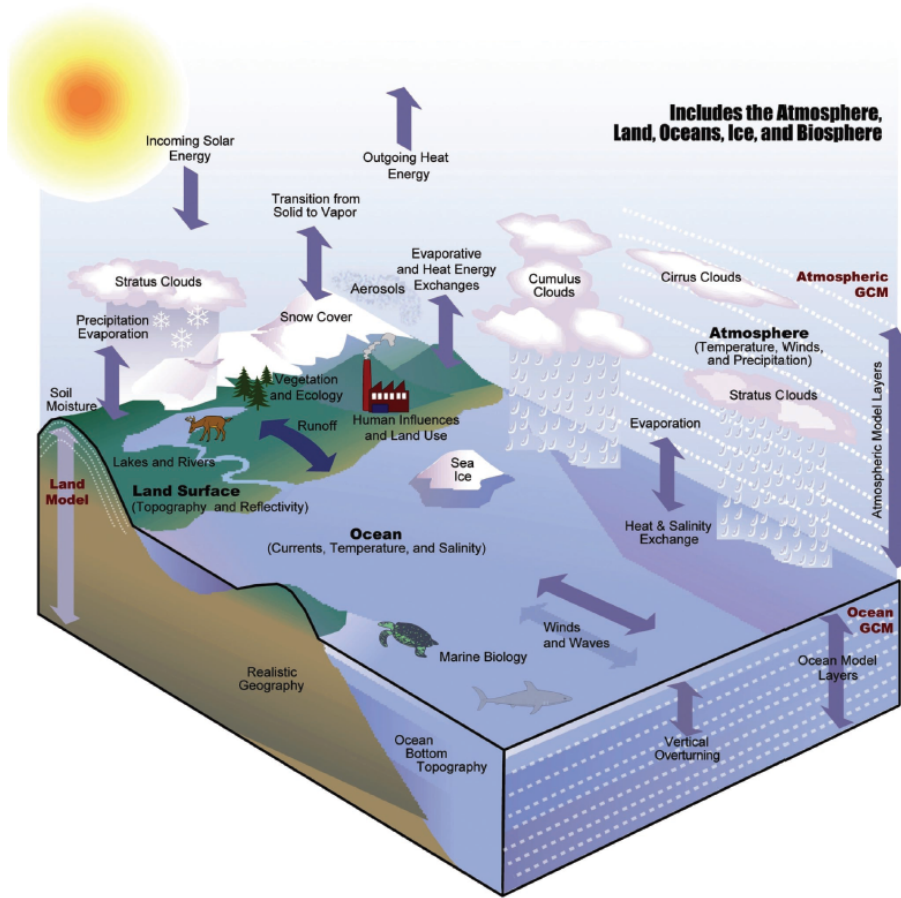
Figure 1.1: Components of the climate system and the interactions among them, including the human component (modified from Karl and Trenberth, 2003).

1.1.1   Climate components

The atmosphere is the fastest changing component of the climate system with reaction times ranging from virtually instantaneous (e.g., condensation of water vapor) to a few years (e.g., inter-hemispheric exchange). Considering a dry atmosphere, it consists of nitrogen (N_2, 78.09% volume mixing ratio), oxygen (O_2, 20.95%), argon (Ar, 0.93%), several trace gases and aerosols (small solid and liquid particles). In the real atmosphere water vapor (H_2O, varying volume mixing ratio <1-4%) forms an additional constituent. As some of these constituents (e.g., water vapor and the trace gases CO_2, CH_4, N_2O, and O_3) can emit and absorb radiation, they play a key role in Earth's energy balance: part of the thermal radiation emitted by land and ocean is absorbed by these atmospheric constituents and is radiated back to the Earth's surface resulting in an additional increase of surface air temperature. This process is coined greenhouse effect, and the involved constituents are called greenhouse gases (GHGs). The natural greenhouse effect, i.e., considering the preindustrial atmospheric composition, amounts to a global temperature difference of about $33\,°C$, implying that without GHGs the Earth's mean temperature would be about $-19\,°C$. Based on their concentration and radiative properties, the individual GHGs contribute differently to this natural greenhouse effect, with water vapor and CO_2 being the most important ones (causing warming of $\sim21\,°C$ and $\sim7\,°C$, respectively; e.g., Mitchell, 1989; Schmidt et al., 2010).

The Earth receives a total solar irradiance of about $1{,}361\ \mathrm{W\,m^{-2}}$ (e.g., Kopp and Lean, 2011), however, due to the Earth's spherical shape the mean daily incoming solar radiation

is with 340 $\mathrm{W\,m^{-2}}$ only a quarter of this (Fig. 1.2). Depending on cloud cover, aerosol concentration and atmospheric humidity, about 22% of the incoming solar radiation is directly reflected back to space. Together with the direct reflection at the Earth's surface, this so-called planetary albedo reflects back about 30% of the total incoming solar radiation. The thermal upward emission of 397 $\mathrm{W\,m^{-2}}$ is to a large extent absorbed by the GHGs in the atmosphere (the atmospheric window between 8 and 14 μm allows for about 40 $\mathrm{W\,m^{-2}}$ to pass through the atmosphere directly). The atmosphere emits the absorbed radiation in all directions amounting to a downward emission of 342 $\mathrm{W\,m^{-2}}$. Given these fluxes, about 106 $\mathrm{W\,m^{-2}}$ are available at the surface to drive evaporation (85 $\mathrm{W\,m^{-2}}$) and heat the air (20 $\mathrm{W\,m^{-2}}$). Note that Fig. 1.2 features a residual radiative flux indicating the current imbalance of the energy fluxes at the top of the atmosphere. This residual is predominantly going into the ocean (Trenberth et al., 2009; Wild et al., 2012).

The fact that the solar irradiance is larger at the equator than at the poles results in a distinct meridional temperature gradient. Due to the second law of thermodynamics this gradient drives a constant poleward energy transport in the atmosphere and ocean. In both climate components the most efficient means of energy tranpsort is via circulation, such as overturning cells (e.g., the Hadley cell in the atmosphere or the Atlantic Meridional Over-turning Circulation) but also smaller-scale phenomena (e.g., atmospheric cyclones or oceanic eddies).
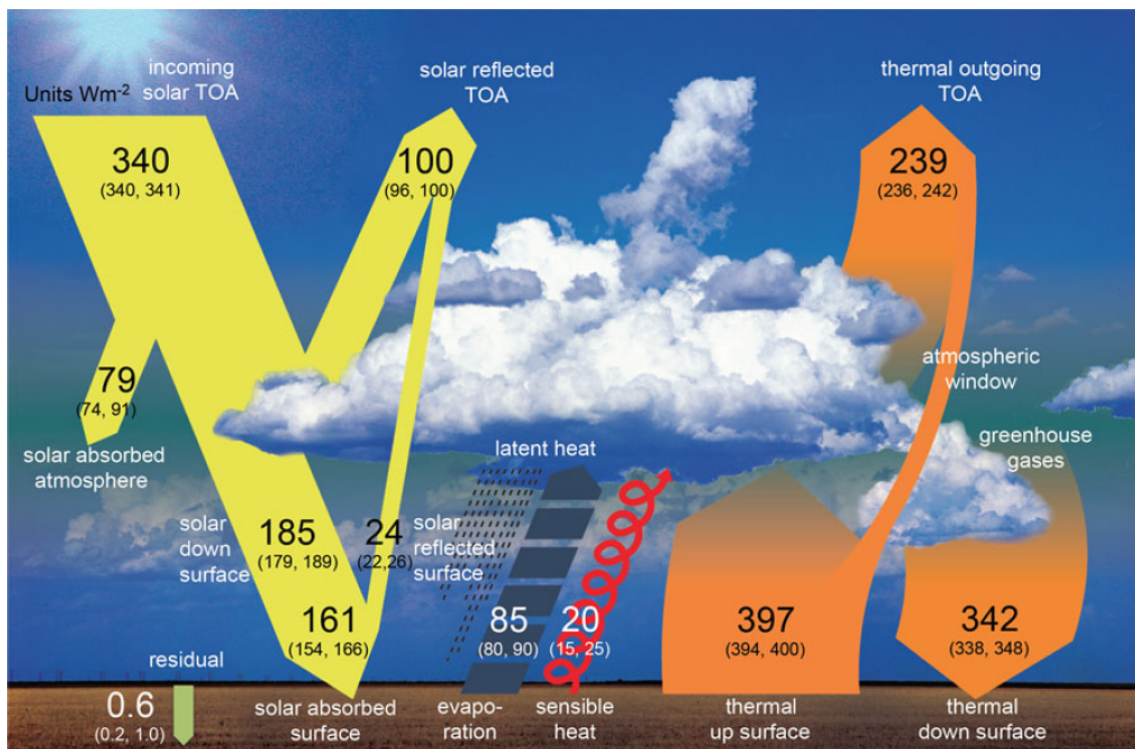
Figure 1.2: The global mean energy balance of the Earth for present-day (units of $\mathrm{W\,m^{-2}}$). The uncertainty range is given in brackets. TOA refers to top of the atmosphere. Fig. from Wild et al. (2012)

The ocean stores a large amount of energy that is redistributed across the globe via wind- and density-driven circulations. Due to its large inertia, the ocean has a profound regulating function for global temperature. Compared to the atmosphere, the ocean has larger over-turning times of up to several thousand years and transports – except for the inner tropics – substantially less energy polewards than the atmosphere (Trenberth and Caron, 2001; Fasullo and Trenberth, 2008). Nevertheless, in certain areas of the globe the oceanic heat transport

exerts a strong control on regional climate. In the Atlantic, for example, the net meridional heat transport is northward everywhere, leading to higher surface temperatures and different ecosystems in the North Atlantic than at similar latitudes in other regions (Kuhlbrodt et al., 2009, and references therein). When transferring its heat to the atmosphere the North Atlantic cools and therefore becomes denser. Surface freshening from precipitation and melting sea ice from the Arctic tend to counteract this density trend. Nevertheless, the surface waters eventually start to sink in the Labrador and Nordic Seas and form deep water that flows southward in deeper layers. This process is called the Atlantic Meridional Overturning Circulation (AMOC) and has its analogue in the Southern Ocean, where denser waters subside in the Weddell and Ross Sea. These deep water formation sites are essentially drivers of the global thermohaline circulation, a density-driven circulation system connecting all ocean basins (for an overview on the thermohaline circulation and the AMOC, see Kuhlbrodt et al., 2007).

The Atlantic meridional heat transport is also of interest in the context of glacial-interglacial climate change, as it links the two hemispheres in a seesaw mechanism (Stocker, 1998). Chapter 4 will touch on the role of the heat transport into the North Atlantic and Arctic region during the last millennium. Representing the largest reservoir of water, the ocean is further a key player in the hydrological cycle, as will be illustrated in section 1.3 and in chapter 2. During glacial times as well as during the industrial age the ocean has also taken up large amounts of carbon, characterizing it as a crucial reservoir of the global carbon cycle (Sarmiento and Gruber, 2006, see appendix A).

The cryosphere includes land ice (glaciers, ice caps, ice sheets) and sea ice and impacts the Earth's climate on a range of temporal and spatial scales. The slow-reacting masses of land ice are integrators of climate change with response times of centuries to millennia and contribute strongly to changes in global sea level. Together with the faster-reacting sea ice they further influence deep water formation and therewith ocean circulation (IPCC, 2007). Finally, the albedo of land and sea ice directly impacts the above surface climate on a regional to hemispheric scale through alteration of surface heat fluxes (see chapter 4).

1.1.2   The hydrological cycle

The hydrological cycle is of crucial importance for the climate system as it is involved in the global distribution of energy and moisture, but also nutrients. While temperature has been observed widely during the industrial era by simple thermometer measurements, monitoring the hydrological cycle has proven more difficult. Gridded land precipitation data exists only back into the nineteenth century and with large spatial gaps (Dai et al., 2004; Mitchell and Jones, 2005). The same is true for evaporation, river runoff and many oceanic parameters such as sea surface temperature, salinity, or precipitation over the ocean (Woodruff et al., 2011). It was not before the start of the satellite era in the 1970s that spatial coverage improved significantly for many of these quantities. One of the first detailed estimates of the hydrological cycle is the book by Baumgartner and Reichel (1975). An updated and more comprehensive estimate was compiled in Gleick (1993). Finally, Trenberth et al. (2007) used these and newer data in an estimate of the mean hydrological cycle for the period 1979-2000, including reservoirs and exchange fluxes (see Fig. 1.3).

Due to the variety of techniques with which individual components of the hydrological cycle have been measured and estimated in the past, it is difficult to combine these numbers into a closed budget (Trenberth et al., 2007). Also, the limited temporal length of the data prohibits a placement of reliable error bars. After the ocean (96.9% of total) the largest reservoirs of water are global ice masses (1.9%) and groundwater (1.1%). The remaining water is stored in rivers and lakes, soil moisture, permafrost, and the atmosphere. Note that some of these components currently exhibit a trend and cannot be regarded as constant (e.g, shrinking ice

volumes and diminishing groundwater aquifers; Pritchard et al., 2009; Gleeson et al., 2012).
The ocean, being the primary source of water for the hydrological cycle, evaporates about
$413 \cdot 10^3$ km^3 yr^{-1}, 90% of which is precipitated back onto the ocean surface. The remaining
40 km^3 yr^{-1} are transported over land where they join with the water evaporated from the
land surface (73 km^3 yr^{-1}) to form continental precipitation of about 113 km^3 yr^{-1}. The main
source of land precipitation is therefore the land surface itself. This finding signifies that areas
where (seasonal) precipitation is limited by the availability of surface moisture rather than
by atmospheric moisture convergence face the potential for a positive drought feedback (e.g.,
southern Europe; Lorenz et al., 2010).
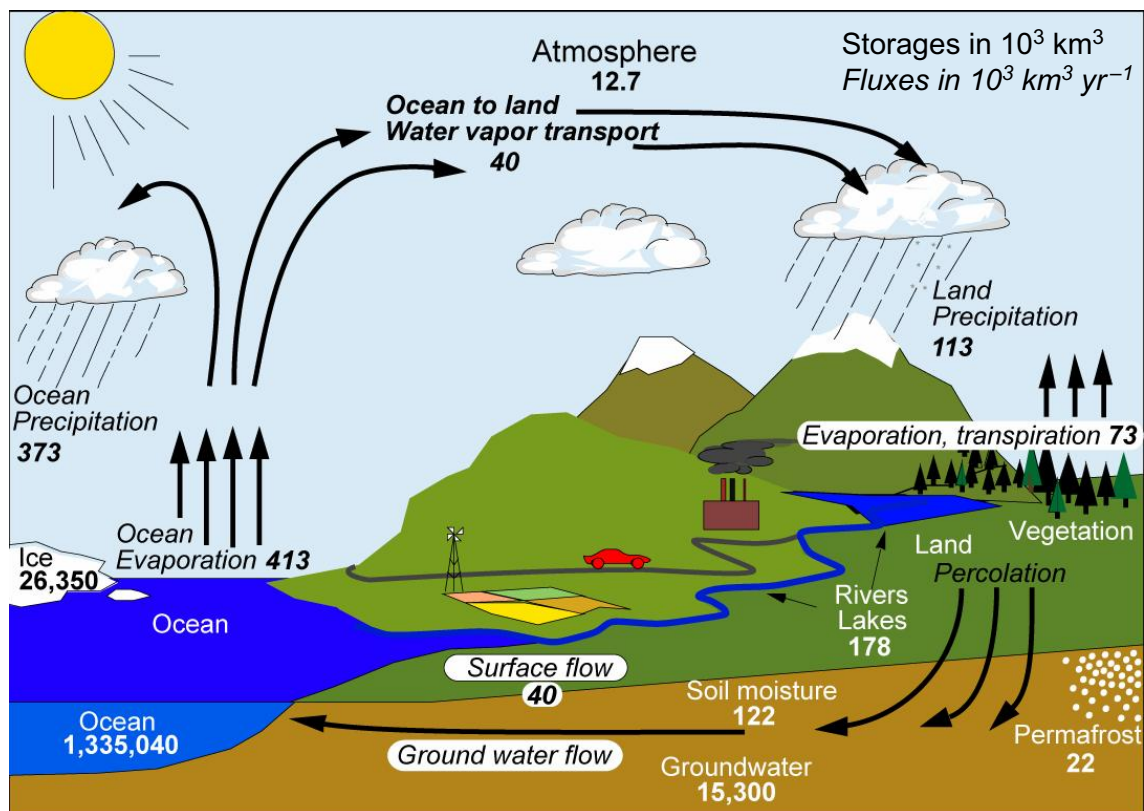
Figure 1.3: The hydrological cycle (modified from Trenberth et al., 2007).

The global picture

Using evaporation (E)−precipitation (P) from the reanalysis ERA-40 (hindcast simulations of
a forecasting model with data assimilation; Uppala et al., 2005) one can readily illustrate the
present-day large-scale dynamics of the atmospheric branch of the hydrological cycle (Fig. 1.4):
in the subtropics over the oceans strong evaporation occurs due to high temperatures and the
constantly blowing trade winds (E > P). In the intertropical convergence zone on the other
hand, atmospheric moisture convergence and convection lead to heavy precipitation and con-
sequently E < P. The Atlantic is a net evaporative basin with positive values dominating.
Once evaporated from the subtropical Atlantic, moisture is transported across Central Amer-
ica to the Pacific. The return flow from the Pacific to the Atlantic at mid-latitudes, however,
is hindered by the Rocky Mountains, making the Atlantic saltier than the Pacific (Durack
and Wijffels, 2010). The Arabian Sea and the Indian subcontinent clearly show the Monsoon

pattern with positive $E - P$ values over the ocean (moistening of the air) and negative values in the larger region of Bangladesh (rain-out). In the mid-latitudes of both hemispheres negative values dominate along the westerly path of extra-tropical cyclones, which are primarily responsible for precipitation at these latitudes. Over land one would generally expect negative $E - P$ as there occurs a permanent runoff to the ocean, although in dry regions such as Australia $E - P$ can become positive. However, uncertainties remain with these values as the moisture budget in ERA-40 is not closed (Trenberth et al., 2007).
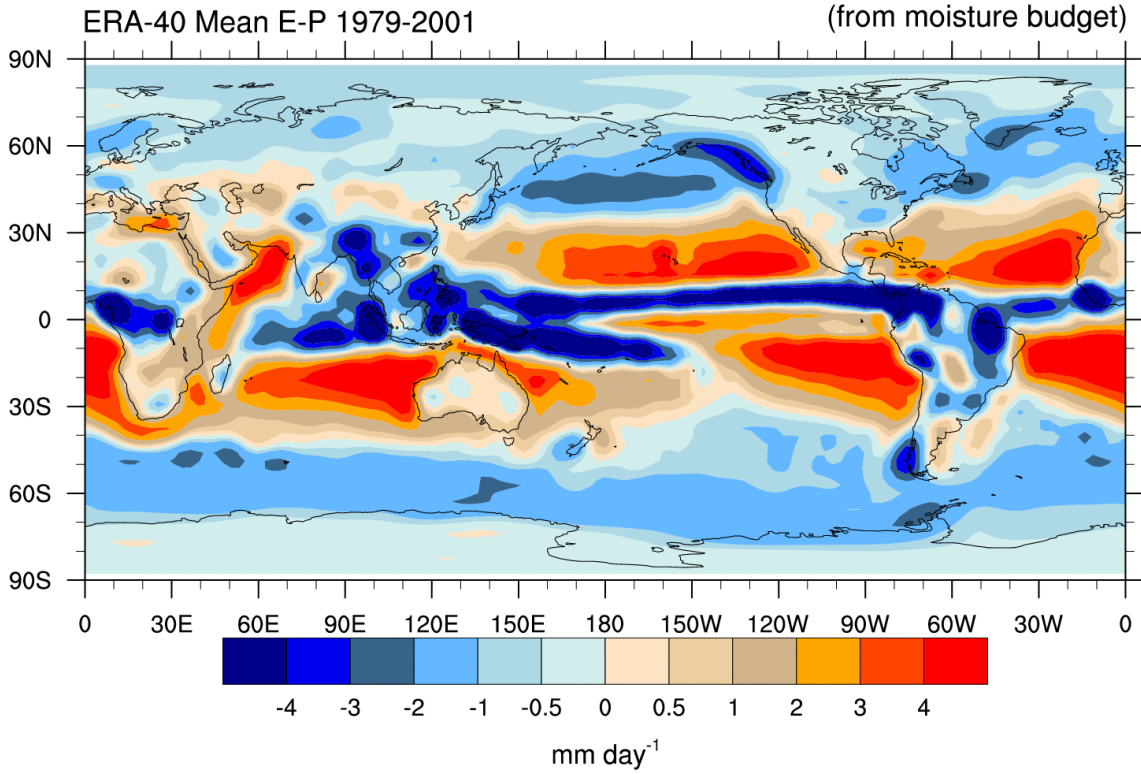

Figure 1.4: The 1979-2001 annual mean evaporation$-$precipitation $(E - P)$ computed from monthly means of the vertically integrated atmospheric moisture budget using the 6-hourly ERA-40 reanalyis. Fig. from Trenberth et al. (2007).

On a more regional scale certain characteristic circulation patterns determine much of the precipitation and evaporation signal throughout the year. In the North Atlantic-European region, the North Atlantic Oscillation (NAO) is the leading mode of atmospheric winter circulation (see also chapter 3, which features a study of the NAO in models and reconstructions). Generally described by the meridional gradient in sea level pressure over the North Atlantic, the NAO is considered to be a measure of the strength and direction of the westerly winds (Wanner et al., 2001). These in turn dictate the moisture distribution over Europe as their mean flow transports relatively wet and warm air into the continent. Depending on the domain and time period selected, the twentieth century NAO accounts for about 35-45% of the winter variability in sea level pressure (SLP) or 500 hPa geopotential height (e.g., Marshall et al., 2001, and references therein). During an NAO positive phase (strong meridional SLP gradient), a rain band across the northern North Atlantic with increased precipitation in Northern Europe goes along with drier conditions in the Mediterranean region; and vice versa during the negative phase (weak meridional SLP gradient). During summer, the classical NAO pattern is less dominant and continental blockings and localized convection are more important for the hydrological signature over Europe. However, in recent years the term 'summer NAO' has emerged as a description of the dominant July-August SLP pattern over

the North Atlantic-European region (e.g., Portis et al., 2001; Bladé et al., 2012). This pattern features centers of action shifted from the Azores to the British Isles and from Iceland to Greenland and an explained variance of about 28-34% (Bladé et al., 2012). Given the spatial displacement relative to the classical SLP pattern of winter, the temperature and precipitation patterns associated with this leading summer mode are also quite different from the ones associated with the winter NAO (Fig. 1.5).
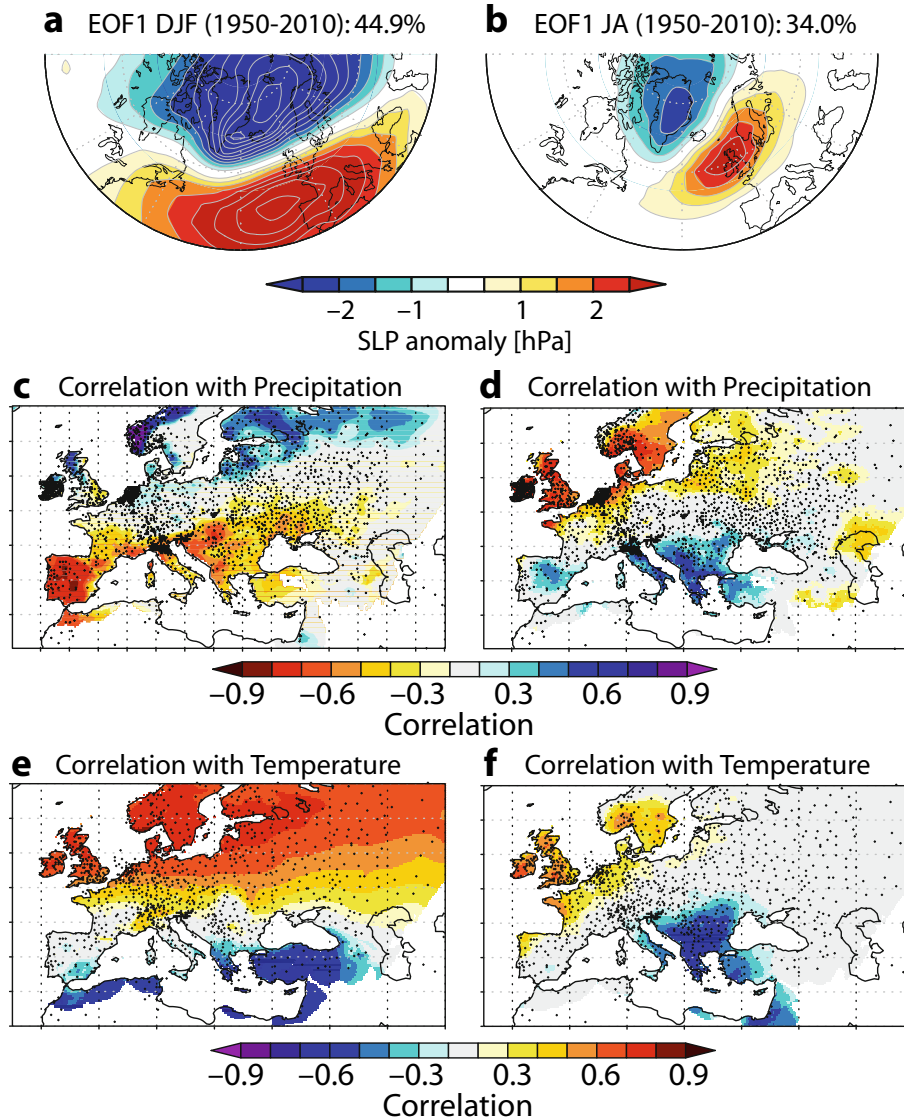
Figure 1.5: Patterns of leading winter and summer mode of sea level pressure (SLP) in the North Atlantic-European domain. (a) First Empirical Orthogonal Function (EOF1) of December-February (DJF) mean SLP, regressed onto SLP anomalies, and the explained variance. This is one of the definitions of the winter NAO. (b) EOF1 of July-August (JA) mean SLP. (c-d) Correlation of winter and summer leading mode, respectively, with precipitation. (e-f) Correlation of winter and summer leading mode, respectively, with temperature. SLP is based on the extended dataset of Trenberth and Paolino (1980), precipitation and temperature on E-OBS version 3.0 (Haylock et al., 2008). Figures compiled and modified from Bladé et al. (2012).

Emphasis is put here on the fact that robust knowledge of the NAO's spatial and temporal variability is limited to the twentieth and twenty-first century when the spatial coverage of observations and reanalyses enables us to study the underlying dynamics of the NAO. Despite these limitations, many attempts to reconstruct the NAO further back in time using proxy data have been made in recent years (for an overview see Pinto and Raible, 2012). The fact

that these reconstructions disagree considerably among each other is a manifestation of the
potential instabilities of atmospheric circulation patterns and teleconnections over time, and
with them the regional precipitation signal (Raible et al., 2006; Lehner et al., 2012a).

The $E - P$ signature seen in Fig. 1.4 can also be used to estimate the oceanic branch of the
hydrological cycle, i.e., the transport of mass and freshwater between basins. When integrating
evaporation$-$precipitation$-$runoff meridionally over each basin, the residual represents an
estimate of the oceanic freshwater transport into or out of the corresponding basin. Together
with an increasing availability of observational data of oceanic mass transports, a number of
estimates for the oceanic mass and freshwater transport have been published (e.g., Wijffels
et al., 1992; Ganachaud and Wunsch, 2000; Talley, 2008; Large and Yeager, 2009). Fig. 1.6
displays comprehensive mass and freshwater transport estimates.
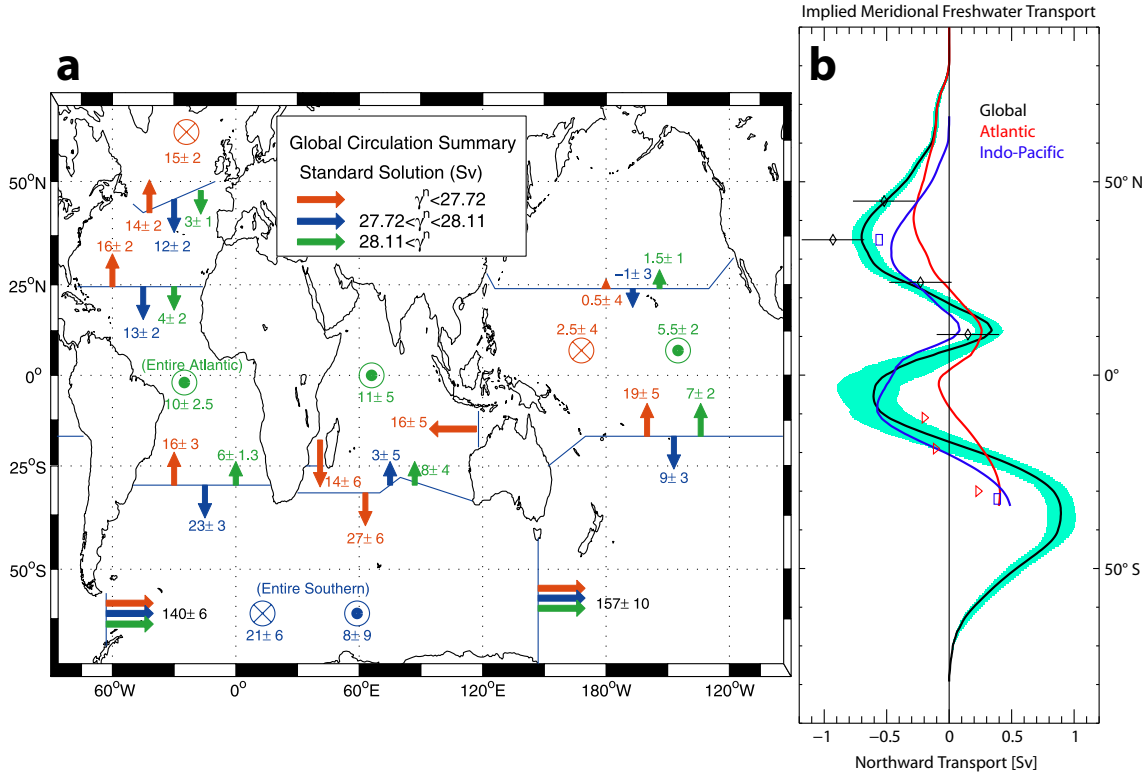
Figure 1.6: Global oceanic water transport. (a) Zonally integrated layer mass transports. The estimated
water transports are indicated for the different density classes bounded by neutral surfaces (λ^n, in $kg\,m^{-3}$)
and across selected hydrographic sections. Mass transport is derived from observed temperature, salinity and
tracer transects using an inverse model. Generally, upper waters (red arrows) are lighter than intermediate
and bottom waters (blue and green arrows). The color of the upwelling or downwelling arrows indicates the
layer from which the water is coming. Fig. from Ganachaud and Wunsch (2000). (b) Northward meridional
freshwater transports implied from surface fluxes for the global ocean, the Atlantic and the Indo-Pacific.
Symbols are direct estimates across entire basins. Modified from Large and Yeager (2009).

In the Atlantic, the structure of the Meridional Overturning Circulation (AMOC) is well
visible with a northward mass transport in the upper layer (red; Fig. 1.6a), downwelling
in the subpolar North Atlantic, and a compensating return flow at depth (blue; Fig. 1.6a).
In the Southern Ocean downwelling mainly occurs at the deep water formation site in the
Weddell Sea, while the upwelling distribution is less certain (Ganachaud, 2003; Marshall and
Speer, 2012). With its low latitude northern boundary the Indian Ocean basin has a special
bathymetry compared to the other ocean basins, leading to temperature-dominated convection
and thus upwelling. It is fed by the warm Indonesian Throughflow, much of which is balanced
by a strong transport through the Mozambique Channel (between the African mainland and

Madagascar). At the southern tip of Africa this latter current transforms into the so-called Agulhas leakage, a water transport around South Africa that represents the main source of warm and salty waters for the Atlantic (Biastoch et al., 2008). Through its influence on the density distribution of the Atlantic the Agulhas leakage is thought to play an important role in pacing the AMOC on decadal scale as well as during glacial periods (Franzese et al., 2006). The Pacific imports water at around $15\,°\,$S, which is nearly balanced by the export through the Indonesian Throughflow. Unlike in the North Atlantic, no deep water is formed in the North Pacific. Additionally, the North Pacific exchanges only a small amount of water mass with the Central Pacific. Thus, the deep North Pacific water masses are the oldest in the world oceans (DeVries and Primeau, 2011). Finally, the Antarctic Circumpolar Current connects all three ocean basins in a massive volume transport, illustrated in Fig. 1.6a by an estimated flow through the Drake Passage of 140 Sv.

The freshwater transports are often closely coupled to the mass transports. Due to the northward transport of warm and salty water in the Atlantic by the upper branch of the AMOC seen in Fig. 1.6a, the corresponding freshwater transport (that can be interpreted as negative salt transport) in the Atlantic is mainly southward, although uncertainties on the direction exist in the South Atlantic (Fig. 1.6b). The same holds true for the Indo-Pacific that transports freshwater southward on much of the Northern Hemisphere and down to $20\,°\,$S. Consequently, a strong northward freshwater transport in the Southern Ocean closes the global budget.

Arctic

While not evident in the zonal means of Fig. 1.6b, the freshwater cycle in the Arctic region is of particular interest for the climate science community. Large quantities of freshwater are stored in the form of the Greenland ice sheet, the perennial Arctic sea ice cover, and the – compared to the North Atlantic – relatively fresh Arctic Ocean. As this freshwater, once released into the North Atlantic, has the potential to alter sea level and the oceanic circulation, the sensitivity of these freshwater reservoirs to past and future climate change is investigated intensively. The modeling study in chapter 4 found an increase in Arctic sea ice export at the inception of the Little Ice Age ($\sim$1450 AD) to have the potential to alter the Atlantic Meridional Overturning Circulation (Lehner et al., in press). Another study in chapter 2 projects the Arctic Ocean to substantially increase its freshwater export in the future and that this increase is well outside the simulated natural variability of the past 500 years (Lehner et al., 2012b).

However, the scarceness of observational data is particularly pronounced in polar regions making it difficult to establish reliable estimates even for the present-day Arctic freshwater cycle. The main sources of freshwater for the Arctic region are the meridional import through the atmosphere ($\sim$60% of total import) and the inflow of low-salinity waters through the Bering Strait ($\sim$30%; Serreze et al., 2006). A large fraction of the atmospheric import is precipitated over the land domain of the Arctic (for details on the domain see Serreze et al., 2006), which – due to the northward river-rooting in Canada and Siberia – leads to substantial runoff to the Arctic Ocean. River runoff, together with direct precipitation over the ocean and brine rejection from sea ice formation, translates into a strong freshwater forcing for the upper Arctic Ocean. As a consequence, a stable halocline exists that prevents warm Atlantic waters residing below about 100 m from rising to the surface. The freshwater is primarily exported from the Arctic in liquid form through the Canadian Arctic Archipelago and the Fram Strait ($\sim$69% of total export). Another considerable portion leaves the Arctic in the form of drifting sea ice through the Fram Strait ($\sim$28%), representing an important freshwater forcing to the Nordic Seas and the subpolar North Atlantic.

Ongoing changes

Considering theoretical arguments and numerical models, an intensification of the hydrological cycle is expected in a warming climate (e.g. Allen and Ingram, 2002; Stocker and Raible, 2005; Held and Soden, 2006; O'Gorman et al., 2012). Among the more robust responses is an increase in horizontal moisture transport and the associated enhancement of the pattern of evaporation minus precipitation, leading to the general rule of 'wet gets wetter and dry gets drier' (Held and Soden, 2006; O'Gorman et al., 2012). As global temperature has increased by about $0.7\,^{\circ}\mathrm{C}$ over the last 100 years (IPCC, 2007, and updates of the various temperature data sets), the detection of a corresponding response in the hydrological cycle has become a crucial verification exercise. Allen and Ingram (2002) illustrated, on the example of precipitation, that such a global intensification, however, does not scale with the Clausius-Clapeyron relation between a change in specific humidity Δq_s and temperature ΔT ($\frac{\Delta q_s}{\Delta T} \sim 6.5\%\,\mathrm{K}^{-1}$). Instead, global precipitation is thought to change only by about $2\text{-}3\%\,\mathrm{K}^{-1}$ because of the latent heat from precipitation not being radiated away by the troposphere fast enough. This makes it harder – together with the large natural variability of precipitation – to detect significant changes in the short observational record. Nevertheless, on a regional basis significant trends have been detected for the twentieth century that are coherent with the theoretical framework laid out in the literature (Huntington, 2006).

The Arctic region, for example, has been warming at more than twice the speed of the global average during the twentieth century (IPCC, 2007; Kaufman et al., 2009) and a number of changes in its freshwater cycle have been detected already (White et al., 2007). Along with a global increase in runoff (Syed et al., 2010), the rivers routing to the Arctic Ocean show increased discharge over recent decades (Peterson et al., 2002). Together with melting sea ice cover and increased atmospheric moisture import one would expect a freshening of the Arctic Ocean. However, changes in the atmospheric circulation lead to a simultaneous increase in oceanic freshwater export to the North Atlantic, making it difficult to detect a significant freshening trend in the Arctic Ocean (White et al., 2007; McPhee et al., 2009).

1.1.3   Perturbations

Following thermodynamic laws the Earth has to radiate away as much energy as it receives from the Sun, implying that the three radiative fluxes at the top of the atmosphere (incoming and reflected solar radiation, outgoing thermal radiation) balance each other. As mentioned previously, there are several possibilities how these radiative fluxes can become unbalanced and change the mean climate (as is the case in Fig. 1.2). Such a radiative imbalance is referred to as radiative forcing (in $\mathrm{W\,m}^{-2}$) and takes negative or positive values when cooling or warming the Earth, respectively (IPCC, 2007). Processes that govern the radiative forcing are either of natural or anthropogenic origin and are summarized under the term 'external forcing'. Additionally, the energy storage and distribution on Earth itself can change through climate system-internal processes and feedbacks, also leading to perturbations of the mean climate.

External forcing

On time scales of decades to centuries, the natural external forcing is mainly caused by variations in the Sun's activity and volcanic eruptions. When considering time scales of millennia, changes in Earth's orbital parameters eccentricity, obliquity, and precession become increasingly important in determining the net solar energy available on Earth. On even longer time scales, weathering, continental drift, uplift, or lowering due to plate tectonics can cause profound climate change. As this thesis focuses on the last millennium, the time scales of millennia and beyond are not addressed in detail.

Measurements and reconstructions of the Sun's activity show a relatively regular oscillation with a period of about eleven years and a varying amplitude of about 0.5-2.0 $\mathrm{W\,m^{-2}}$ (Froehlich, 2006; Muscheler et al., 2007). However, larger variations, occurring on decadal to centennial time scales, tend to be more important for climate. Pronounced highs and lows in solar activity during the last millennium, such as the increased activity during the Middle Ages or decreased activity during the Maunder Minimum, are usually linked to warmer or colder climate, respectively (e.g., Crowley, 2000; Mann et al., 2009).

Volcanic eruptions, when explosive enough, influence the climate via emission of sulfate aerosols into the lower stratosphere, where the aerosols scatter and absorb solar and thermal radiation inducing stratospheric warming and tropospheric cooling (Robock, 2000, and references therein). Explosive tropical eruptions are the most influential ones for global climate as in this case aerosols can be distributed across both hemispheres. The radiative perturbation disappears within a few years as aerosols settle out from the stratosphere, while in the upper ocean the cooling signal remains detectable for several decades (e.g., Stenchikov et al., 2009). Further, the cumulative climate impact of serial volcanic eruptions has been proposed to contribute to prolonged cold periods such as the Little Ice Age (Zhong et al., 2011; Miller et al., 2012).

The accelerated consumption of natural resources by humans during the last roughly 250 years has several impacts on global climate in terms of radiative forcing:

- The anthropogenic burning of fossil fuels, intensification of agriculture, and the release of halocarbons change the chemical composition of Earth's atmosphere and along with that its radiative properties. Increasing concentration of GHGs cause a positive radiative forcing of about 2.6 $\mathrm{W\,m^{-2}}$, dominating the global radiative imbalance observed since about 1750. CO_2 increases at the highest rate since 22,000 years (Joos and Spahni, 2008) and exceeds any concentration measured during the last 800,000 years (Luethi et al., 2008) and is the main contributor. Interestingly, while not considered a major forcing agent in 2007 (IPCC, 2007), new estimates of the radiative forcing from black carbon suggest it to be the second most important contribution to anthropogenic radiative forcing since 1750 (on the order of 1.1 $\mathrm{W\,m^{-2}}$; Bond et al., 2013).

- The anthropogenic emission of aerosols has a complex, not yet well understood impact on Earth's climate through direct and indirect effects on atmosphere's interaction with radiation, cloud formation, precipitation, or snow albedo (for reviews see, e.g., Haywood and Boucher, 2000; Tao et al., 2012). Despite the medium-low level of scientific understanding of their climatic impact, the net radiative forcing of aerosols is estimated to be negative. However, the uncertainty range for the magnitude of negative forcing is large. Since the Intergovernmental Panel on Climate Change's (IPCC) 4th assessment in 2007, progress in observing and modeling of aerosol-climate interactions has slightly improved the scientific understanding (e.g., Loeb and Su, 2010; Lohmann et al., 2010; Myhre et al., 2013). It nevertheless remains the largest source of uncertainty in the estimate of anthropogenic radiative forcing.

- The anthropogenic change of Earth's reflective properties through changes in land-use (e.g., urbanization, deforestation) is estimated to provide another small negative radiative forcing.

Internal processes

The climate system varies even in the absence of varying external forcing, indicating that climate system-internal processes are in part responsible for climate variations. This behavior of the climate system is termed internal variability and can be illustrated by, e.g., coupled

model simulations with fixed external forcing, i.e., constant TSI and GHGs, and no volcanic eruptions (e.g., Goosse et al., 2002; Hofer et al., 2011): climate variables (e.g., ocean circulation) are found to vary or oscillate due to either internal processes in one component or interaction between different components of the system. Particularly in the case of interactions between components, non-linearities can occur that limit our possibilities to forecast climate on interannual to decadal time scales.

A prominent example is the El Niño-Southern Oscillation, a climate mode that involves a complex coupling of ocean and atmosphere in the tropical Pacific and impacts climate globally through teleconnections. At present-day it exerts a quasi-periodic oscillation of 2-7 years (AchutaRao and Sperber, 2006), yet there is only little forecast skill beyond the seasonal time scale for the occurrence of its anomalous states El Niño and La Niña (e.g., Jin et al., 2008; Zhu et al., 2013).

Feedback mechanisms

The response of a climate system process to external forcing or internal variability can trigger a response in a second process that in turn influences the initial one. This so-called feedback can intensify (positive feedback) or weaken (negative feedback) the original process (IPCC, 2007). A number of feedbacks have been discovered within the climate system, which are crucial for our understanding of climate's natural variability as well as its response to external forcing.

An important feedback in the context of current and future anthropogenic warming is the water vapor feedback: a warmer atmosphere will hold more water vapor that acts as a GHG and further amplifies the warming. This positive feedback is estimated to roughly double the warming from external forcing alone, e.g., due to increased GHG concentrations (Held and Soden, 2000). Water vapor is therefore not considered an external forcing but a feedback. In turn, increased moisture in the tropical troposphere triggers a negative feedback: the upper troposphere warms more than the surface and the lapse rate decreases, which results in increased upward emission of thermal radiation and therefore a cooling of the Earth (Bony et al., 2006; Sherwood et al., 2010). This negative feedback only dampens the aforementioned positive feedback, but does not outweigh it. Overall, the water vapor feedback is a net positive feedback that enhances warming from external forcing by about 50%.

Feedback mechanisms are also discussed in the context of climate variations during the last millennium, as often the regional scale temperature variations found in reconstructions cannot be explained solely by changes in external forcing (Wanner et al., 2008). Chapter 4 of this thesis investigates the transition from the Medieval Climate Anomaly (MCA, ∼950-1250) to the cold period of the Little Ice Age (LIA, ∼1400-1700) and introduces a feedback mechanism that acts to amplify and prolong the cold phase of the LIA: with negative external forcing from decreasing TSI and serial volcanic eruptions, Arctic sea ice expands and is increasingly exported to the subpolar North Atlantic, where it melts and reduces convection. The Atlantic overturning circulation is weakened to the extent that less heat is transported northward, which reinforces the initial Arctic sea ice growth (positive feedback). In the Barents Sea the expanded sea ice cover has a direct thermal effect on the ambient air temperature and the atmospheric circulation. Thereby, the externally-induced cooling over Northern Europe is amplified by an internal feedback mechanism.

Detection and attribution of forced perturbations

In order to detect a perturbation of the climate system and to then attribute this perturbation to a specific forcing, two criteria have to be fulfilled: (i) the perturbation must stand out against natural internal variability, i.e., the hypothesis that an observed pattern occurred solely due to internal variability must be rejected at a certain confidence level. (ii) A specific

external forcing must be able to explain the observed pattern, i.e., the hypothesis that this forcing can explain the observed pattern must withstand rejection at a certain confidence level. Both criteria are difficult to fulfill in climate science as the natural internal variability of the climate system is large and/or not yet fully known due to limited observational records.

At that point, climate models become an indispensable tool, offering two possibilities to fulfill the before-mentioned criteria of detection and attribution:

- By running a climate model with fixed external forcing for a long time (i.e., a control simulation), an approximation to the full range of the internal variability of the climate system is created. Then a set of transient simulations – a so-called ensemble – with temporally varying external forcing (e.g., increasing GHG concentrations) is performed, using different initial conditions from the control simulation. Each ensemble member represents a physically consistent realization of the real world's climate evolution. However, given the different initial conditions of each ensemble member, the sampling of internal variability is more comprehensive than in the sole observational record and enables to estimate the amplitude of the actual internal variability. Synchronous changes in all ensemble members indicate the influence of external forcing. The expanded sample size of an ensemble allows statistical tests to detect such changes with higher confidence. This ensemble approach is used in all the studies presented in this thesis.

- Alternatively, the prescribed external forcing is changed between different simulations and the model is run only with a single or a subset of the known external forcing. This allows studying the isolated influence of different forcings on climate. To determine the importance of natural versus anthropogenic external forcing in driving the global warming since the beginning of the industrial era, this approach has been combined with the ensemble approach to arrive at particularly robust conclusions (e.g., IPCC, 2007; Meehl et al., 2012). When using a state-of-the-art coupled model the combination of the two approaches is costly due to the many high-resolution simulations needed. Despite increasing computational power, this combinatory approach is rarely applied in the context of multi-century paleoclimatic simulations.

Both approaches – and model-based sciences in general – are limited by our understanding of the underlying physics and the models' ability to correctly represent these physics.

1.2 Past and future climate change

1.2.1 Last millennium

The last approximately 1,000 years saw a relatively stable climate (e.g., as compared to glacial-interglacial cycles) and are therefore a good test bed for studies of natural climate variability. The abundance of proxy data (climate data inferred from natural archives such as tree rings or speleothems) permits a rough reconstruction of the overall climate evolution over the last millennium. However, spatial or temporal details of the climate evolution as well as underlying dynamics are usually not resolved sufficiently by the proxy data. This provides an opportunity for climate models to complement the proxy data. In order to make meaningful use of models in paleoclimatic research, the external forcing needs to be known and a possibility for model validation must exist. Unfortunately, both criteria are not easily fulfilled. On the one hand, a consensus on the external forcing over the last millennium does not yet exist. On the other hand, until now only a few climate parameters, such as temperature, have been reconstructed and can be used for model validation. Here, the origin of these issues is discussed along with an overview on the last millennium's climate evolution and a brief discussion of model applications in paleoclimatic research.

Forcing uncertainties

TSI has been varying throughout the last millennium and is thought to have played a key role in multi-decadal departures from the mean climate trend of the Holocene. Slightly higher TSI values have prolonged from about 850-1250 AD, followed by weaker TSI until the beginning of the nineteenth century (Fig. 1.7b). The variations in TSI over the last millennium have been reconstructed by use of satellite data (since 1978; e.g., Fröhlich, 2009), observations of sunspot numbers (since the seventeenth century; Lean et al., 1995, e.g.,), and cosmogenic isotopes from tree rings (^{14}C) or ice cores (^{10}Be; several thousand years, but only low-frequency variations, i.e., without resolving the 11-year solar cycle; Steinhilber et al., 2009). Most of these reconstructions show similar temporal variations, but differ considerably in amplitude due to different assumptions made in the reconstruction concepts. A common measure of this amplitude is the mean TSI difference between the Maunder Minimum (a phase of particularly weak solar activity around 1700 AD) and present-day. In recent years, a range of new reconstructions seemed to converge towards an amplitude of about 0.1% (Muscheler et al., 2007; Vieira and Solanki, 2010; Steinhilber et al., 2009; Delaygue and Bard, 2011). However, Shapiro et al. (2011) recently proposed a much higher amplitude again. To account for these uncertainties, the protocol of the third phase of the Paleoclimate Model Intercomparison Project (PMIP3) includes all of these reconstructions as well as a synthetic 11-year solar cycle back to 850 AD (see Schmidt et al. (2012) and appendix A for further details). Another source of uncertainty is found in variations of the spectral solar irradiance (SSI). Measured with satellites only since about a decade, the past variability of SSI and its influence on climate are still debated and not yet widely used in simulations of the last millennium (Schmidt et al., 2011).

Volcanic eruptions constitute the second major external forcing during the last millennium and are proposed to have been involved in triggering or amplifying the onset of the Little Ice Age during the thirteenth century (e.g., Miller et al., 2012). Prior to that only smaller eruptions are recorded and volcanoes are thought to have had a minor influence on climate. For the reconstruction of past volcanic eruptions there are even more degrees of freedom than for TSI, as the spatial distribution and radiative properties of the volcanic aerosols have to be known in addition to the timing and magnitude of an event. Using satellite data (since the 1980s; Stenchikov et al., 1998, and references therein), ground-based observations (since about 1850; Sato et al., 1993; Ammann et al., 2003), or ice cores (last millennium; e.g., Crowley, 2000), several reconstructions of volcanic eruptions (reconstructed as changes in optical depth or aerosol mass) have been created that differ in their timing or their magnitude. Especially on time scales where only information from ice cores exists, the differences can be substantial due to diverse assumptions in the reconstruction concepts (Fig. 1.7a and Schmidt et al., 2011).

As mentioned in section 1.1.3, the main anthropogenic influence on climate started around 1750 AD with the emission of GHGs and changes in land cover. Prior to that anthropogenic changes in land cover may had regional effects on climate via the albedo (IPCC, 2007), however, these are subject to some uncertainty as agricultural activity has not been documented in detail before about 1700 AD (Pongratz et al., 2008). Continuous measurements of GHGs exist only since the mid-twentieth century (e.g., CO_2 since 1958 Keeling, 1960; Keeling et al., 1976), which is why the reconstruction of GHGs bases primarily on ice cores. The finding that the GHGs are well-mixed allows us to infer robust estimates of global concentrations from ice core measurements in Antarctica and Greenland for the last millennium and beyond (e.g., Luethi et al., 2008; Schilt et al., 2010). During the last about 150 years anthropogenic aerosols became an important forcing agent, the exact strength of which is still associated with large uncertainties due to their spatially heterogeneous distribution and the low level of scientific understanding of their radiative properties.

Reconstruction of past climate evolution

The large majority of reconstructions available are concerned with temperature. The abundance of temperature-sensitive proxies, such as tree rings, ice cores, boreholes, sediments, corals, and documentary evidence, has been utilized to reconstruct temperature on global, hemispheric, or even regional scale for the last millennium (e.g., Mann et al., 2008; Neukom et al., 2011; PAGES 2k network, 2013). The uncertainties of those reconstructions generally increases further back in time as the number of proxies and their temporal resolution decrease (Fig. 6.11 in IPCC, 2007). Additional uncertainties arise from measurement errors or differing calibration techniques for the individual proxies (Jones et al., 2009). Fig. 1.7d displays the overlap of many individual reconstructions of the Northern Hemisphere temperature back to 900 AD, where the growing spread further back in time illustrates these uncertainties. Beginning in the eighteenth century, instrumental temperature measurements start to reduce the uncertainties. The last millennium generally is composed of a warm first half, followed by a colder period lasting until the onset of a rapid warming during the nineteenth and twentieth century.

The number of proxies has grown steadily, and in recent years this allowed one to reconstruct temperature also spatially (e.g., Luterbacher et al., 2004; Mann et al., 2009). These spatial reconstructions, while agreeing with the broad hemispheric signal, show that the timing and geographic signature of temperature variations can be quite heterogeneous. A prominent example is the Medieval Climate Anomaly (MCA; ~950-1250 AD), during which temperatures exceeded those of today in some location while remaining below globally (Mann et al., 2009). Similarly, the inception of the subsequent Little Ice Age (LIA; ~1400-1700 AD) was not synchronous globally nor was the amplitude of the cooling the same everywhere (for a review see, e.g., Diaz et al., 2011). These examples indicate that not only uniform external forcing, but also internal processes and feedbacks are needed to fully explain spatial heterogeneities in temperature evolution (Wanner et al., 2008). Chapter 4 of this thesis specifically addresses the question of external forcing versus internal processes/feedbacks at the example of the amplified cooling of Northern Europe at the onset of the LIA.

Attempts to reconstruct climate variables other than temperature are often limited to certain regions or time periods or provide no or only coarse spatial resolution; for example European precipitation (e.g., Pauling et al., 2006; Büntgen et al., 2011), European sea level pressure (e.g., Luterbacher et al., 2002b; Kuettel et al., 2010), Arctic sea ice extent (Kinnard et al., 2011), North Atlantic sea surface temperature (SST; Sicre et al., 2008), or the occurrence of droughts in Africa, Asia, or North America (e.g., Cook et al., 2010a,b). These reconstructions nevertheless help to draw a picture of past hydro-climate and, e.g., describe the MCA as warm and wet in central to northern Europe.

Selected proxies have also been applied in reconstructions of past variability in atmospheric circulation patterns, such as the NAO (e.g., Glueck and Stockton, 2001; Luterbacher et al., 2002a; Cook et al., 2002; Trouet et al., 2009), or even oceanic modes, such as the Atlantic Multidecadal Oscillation (AMO; e.g., Gray et al., 2004; von Gunten et al., 2012). In case of the NAO, proxies that are known to be influenced by the NAO are used to retrace the signature of the NAO in the North Atlantic region and condense it into a temporal index. Obviously, due to the chaotic nature and the many non-linearities in the atmospheric circulation, a temperature or precipitation proxy can only be indirectly linked to a specific circulation pattern. Additionally, the proxy itself is only an indirect measure for temperature or precipitation, relying on an empirical transfer function between the proxy signal, e.g., tree ring width, and the climate signal, e.g., precipitation. These caveats assign a great deal of uncertainty to such reconstructions, and a thorough validation of an applied reconstruction concept is inevitable. Recently, an NAO-reconstruction proposed the warm and wet northern Europe during the MCA to mainly originate from a persistent positive NAO-phase, that
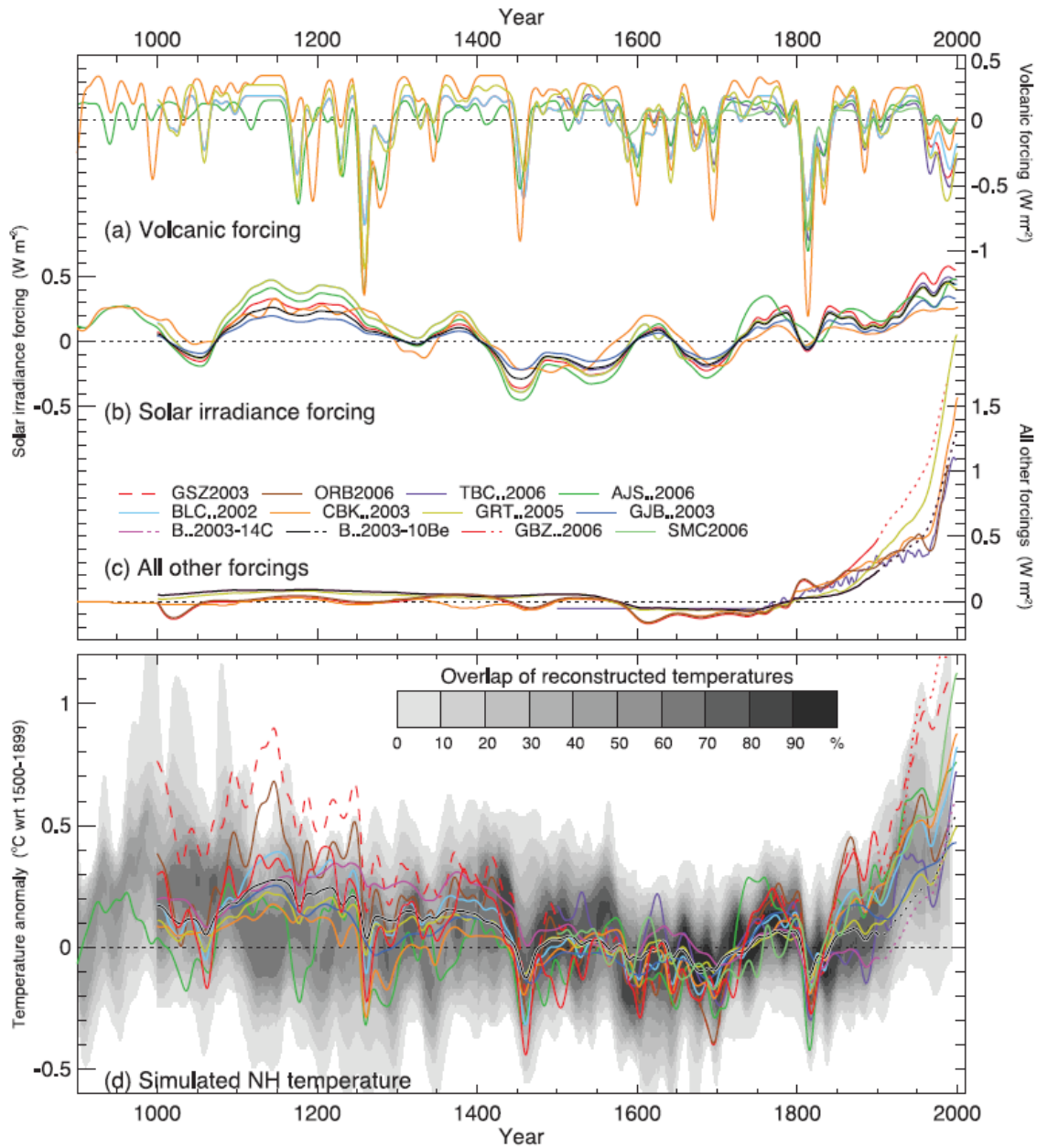
Figure 1.7: (a-c) Radiative forcing used in model simulations and (d) simulated and reconstructed Northern Hemisphere temperature over the last millennium. All time series are expressed as anomalies from their 1500-1899 AD means and are smoothed with a Gaussian-weighted filter to remove fluctuations on time scales less than 30 years. Fig. from IPCC (2007).

shifted into a more negative phase during the LIA (Trouet et al., 2009). However, relying on only two precipitation-sensitive proxies, the underlying reconstruction concept is error-prone and has therefore been criticized in a recent paper (Lehner et al., 2012a, chapter 3).

Model applications

Fig. 1.7d also shows results from last millennium simulations with different climate models. Despite them applying different forcing datasets and implementing the physics in different ways, the models show a reasonable agreement with the reconstructions of the major features of last millennium's temperature evolution. While discrepancies exist regarding the amplitude, higher-frequency variations, or the exact regional pattern of temperature, models still are

useful analogues of the reconstructions and can be used in multiple ways. Models provide a consistent physical framework and, once validated against observations or reconstructions, can be used to study the dynamics underlying the patterns seen in reconstructions or to expand our understanding into areas and time periods where reconstructions are scarce. Here, a few examples of model applications in paleoclimatic research are given, including the studies of this thesis.

As mentioned in section 1.1.2, observations on the Arctic freshwater cycle reach back only a couple of decades and there are relatively few reconstructions of climate parameters in the Arctic in general. In a model study in chapter 2 we attempt to close this gap with transient model simulations of the Arctic and Antarctic freshwater cycle from 1500 AD to the present (and beyond). Thereby, ongoing changes in the Arctic today can be placed in context of past variability in a consistent manner (Lehner et al., 2012b).

In another model study, Graham et al. (2011) introduced artificial warming in the Indian and Eastern Pacific Ocean in a climate model to mimic the reconstructed SST pattern during the MCA in these basins. They found many of the reconstructed climate signals across the globe to be reproduced by this perturbed model and concluded that an enhanced Indo-Pacific SST gradient is able to dynamically explain certain climate signals reconstructed for the MCA. Similarly, artificial sea ice growth in a climate model is used in chapter 4 to understand the influence of sea ice on the North Atlantic-Arctic region during the inception of the LIA. Interestingly, results from these simulations provide an explanation for the European MCA-LIA temperature change that does not rely on significant changes in the NAO as proposed by Trouet et al. (2009) (Lehner et al., in press).

Models can further be used in so-called 'pseudo-proxy' approaches (e.g., Briffa and Jones, 1993; Bradley, 1996; Zorita and González-Rouco, 2002; Mann et al., 2005). There, output from model simulations at the location of a specific real-world proxy is essentially considered a mimic of the real-world proxy. This mimic or pseudo-proxy can then be studied in the model world, where no temporal or spatial data gaps exist. Commonly, this approach is used to determine whether a certain proxy location is suitable to be used in a reconstruction of a climate parameter. Zorita et al. (2003), for example, used model output to give a theoretical estimate of the number of proxies needed to reliably reconstruct the global temperature and its variance. In the study in chapter 3, a similar approach is used to test the NAO reconstruction concept of Trouet et al. (2009). By taking model-simulated precipitation at the location of the two proxies used in Trouet et al. (2009), these proxies are mimicked multiple times. Unlike in the real world, the NAO index can be calculated from simulated SLP and is therefore known. The ability of the pseudo-proxies to describe this simulated NAO index can now be tested, e.g., by means of correlation analysis, and inferences can be made on the suitability of the real-world proxies (Lehner et al., 2012a). In a similar method, the proxy surrogate reconstruction (PSR; Graham et al., 2007) approach, model states are selected when they match certain point-scale proxy signals, providing a plausible climate field for a specific combination of proxies (e.g., Franke et al., 2011). Of course, such analyses depend on the model's ability to actually reproduce the variability and trends of the real-world climate. To account for that, output from several different models is used.

Finally, models are applied in combination with assimilation of observational and proxy data to reproduce last millennium's climate evolution as realistically as possible while still founding on the physical understanding as implemented in climate models. Such endeavors are computationally expensive as they usually require large ensemble simulations, which is why models of intermediate complexity or atmosphere-only models rather than state-of-the-art coupled model are commonly used in data assimilation (e.g., Goosse et al., 2010; Bhend et al., 2012).

1.2.2   Future

Similar to reconstructions of past climate, projections of future climate are inevitably uncer-
tain due to our incomplete understanding of the system. In the case of future projections,
however, the outcome does not depend solely on physics and our understanding of them, but
also on the future human development. Therefore, the term 'projection' is used rather than
'prediction' or 'forecast': future climate is *projected* based on certain assumptions regarding
demographic, social, economic, technological and environmental development. In so-called
scenarios a variety of narrative storylines of future human development are created that re-
sult in different GHG emission pathways, which are then used in climate models to project
the climate response to those pathways. An overview on recent scenarios is given here along
with a brief discussion of concepts and challenges in modeling the future climate and the
hydrological cycle in particular.

Scenarios

For the last IPCC report in 2007 four distinct scenario families were developed that project
emissions of GHGs (often illustrated by CO_2) to peak within the twenty-first century (A1 and
B1 scenarios) or continue to increase throughout the twenty-first century at a high and low rate
(A2 and B2; Special Report on Emissions Scenarios (SRES), IPCC, 2000). The A2 scenario,
which is used in model simulations in chapter 2, represents the so-called 'business-as-usual'
scenario with emissions continuing to rise at roughly the present-day rate during the twenty-
first century, based on a heterogeneous world with more fragmented and slower technological
change than in other scenario families. This scenario projects a doubling of today's CO_2
concentration until the 2090s. Recent estimates of global annual CO_2 emissions since 2000
are on track with the A2 scenario (Le Quere et al., 2009; Friedlingstein et al., 2010; Peters
et al., 2012, and updates from the International Energy Agency (IEA, 2013)).
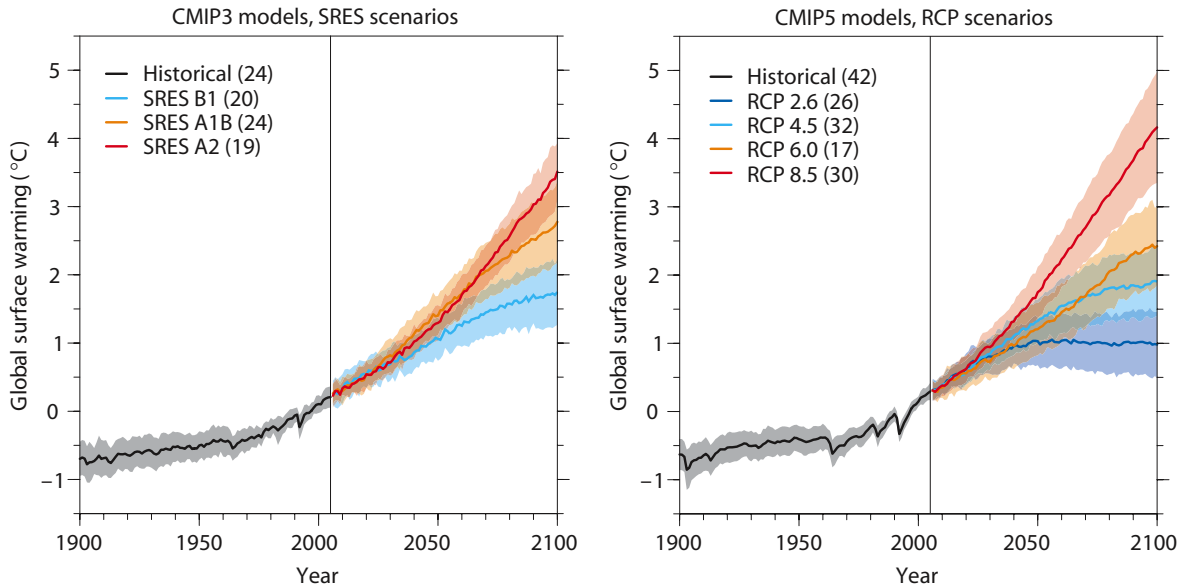
Figure 1.8: Global temperature change (mean and one standard deviation as shading) relative to 1986-2005
for (left) the SRES scenarios run within the third World Climate Research Programme's (WCRP's) Coupled
Model Intercomparison Project (CMIP3; Meehl et al., 2007) and (right) the RCP scenarios run within CMIP5.
The number of models used is given in brackets. Fig. from Knutti and Sedláček (2012).

For simulations with the most recent generation of climate models to be used in studies
contributing to the upcoming IPCC Fifth Assessment Report, new scenarios have been devel-

oped (Moss et al., 2010; van Vuuren et al., 2012). These scenarios are based on projections of a prescribed radiative forcing relative to preindustrial for the year 2100. Using integrated assessment models (coupled energy-economy-land use-climate models), representative concentration pathways (RCP) were selected that result in radiative forcing at year 2100 of about 2.6 $\mathrm{W\,m^{-2}}$, 4.5 $\mathrm{W\,m^{-2}}$, 6.0 $\mathrm{W\,m^{-2}}$, or 8.5 $\mathrm{W\,m^{-2}}$ (termed RCP 2.6 and so forth). Reduced-complexity carbon cycle climate models then calculate corresponding GHG concentrations, thereby taking climate-feedbacks between temperature and the carbon cycle into account (e.g., Meinshausen et al., 2011). Resulting GHG concentrations, which cover a larger range than in the SRES scenarios, are then used to force comprehensive high-resolution coupled models (Fig. 1.8). Models with prognostic carbon cycle components are forced directly by GHG emissions (e.g., Jungclaus et al., 2010).

Uncertainties

The larger spread in GHG concentrations in the new RCP scenarios and the larger number of models leads to a widening of the spread in projected global mean temperature anomaly as compared to the last IPCC report (Fig. 1.8). This, however, does not mean that model projections have become more uncertain. As models now incorporate more processes, confidence has grown that the crucial components of the climate system are actually considered (Knutti and Sedláček, 2012). Also, Hawkins and Sutton (2009) illustrated that projection uncertainty for decadal global temperature is dominated by model uncertainty and climate-system internal variability only during the first decades of the twenty-first century but then quickly gives way to scenario uncertainty, i.e., an uncertainty that is difficult to constrain further by the scientific community (Fig. 1.9c). Interestingly, the sum of these uncertainties results in the mid twenty-first century being the time of smallest total uncertainty, as trends start to stand out against internal variability while the different scenarios have not diverged that much yet (Fig. 1.9a).

The picture changes on the regional scale, e.g., temperature on the British Isles, where internal variability and model uncertainty (e.g., due to limited spatial resolution) are far greater sources of uncertainty. They dominate the cumulative uncertainty throughout the whole twenty-first century and lead to a higher total uncertainty (Fig. 1.9b and d). This has been confirmed by similar examples from North America, where the spread between the warmest and coldest or wettest and driest member in an ensemble of projections serves as indicator for the influence of internal variability in future projections of regional climate (Deser et al., 2012).

Hydrological cycle

The hydrological cycle is expected to intensify in a warming world (see section 1.1.2). The overall intensity of the hydrological cycle is controlled by the available energy rather than the available moisture. As touched upon in section 1.1.2, the ability of the troposphere to radiate away latent heat comprises the key handle on the hydrological cycle. This can be depicted in a simple model of the tropospheric energy budget for the case of a warming world (due to doubling of CO_2) using theoretical or observational estimates for the different quantities (Mitchell et al., 1987; Allen and Ingram, 2002, and references therein):

$$L\Delta P = \Delta R_C + \Delta R_T = \Delta R_C + k\Delta T, \qquad (1.1)$$

where $L\Delta P$ is the latent heating due to changes in precipitation ($\sim 1\ \mathrm{W\,m^{-2}}$ per 1% precipitation change; note that ΔP here stands for $\frac{\Delta P}{P}$), ΔR_C is the change in radiation independent from changes in temperature ΔT (i.e., decreased net outgoing thermal radiation due to doubling of CO_2; -2 to $-3\ \mathrm{W\,m^{-2}}$), and $\Delta R_T = k\Delta T$ is the change in tropospheric radiation dependent on ΔT and a radiative property of the troposphere k ($\sim 3\ \mathrm{W\,m^{-2}\,K^{-1}}$). First,
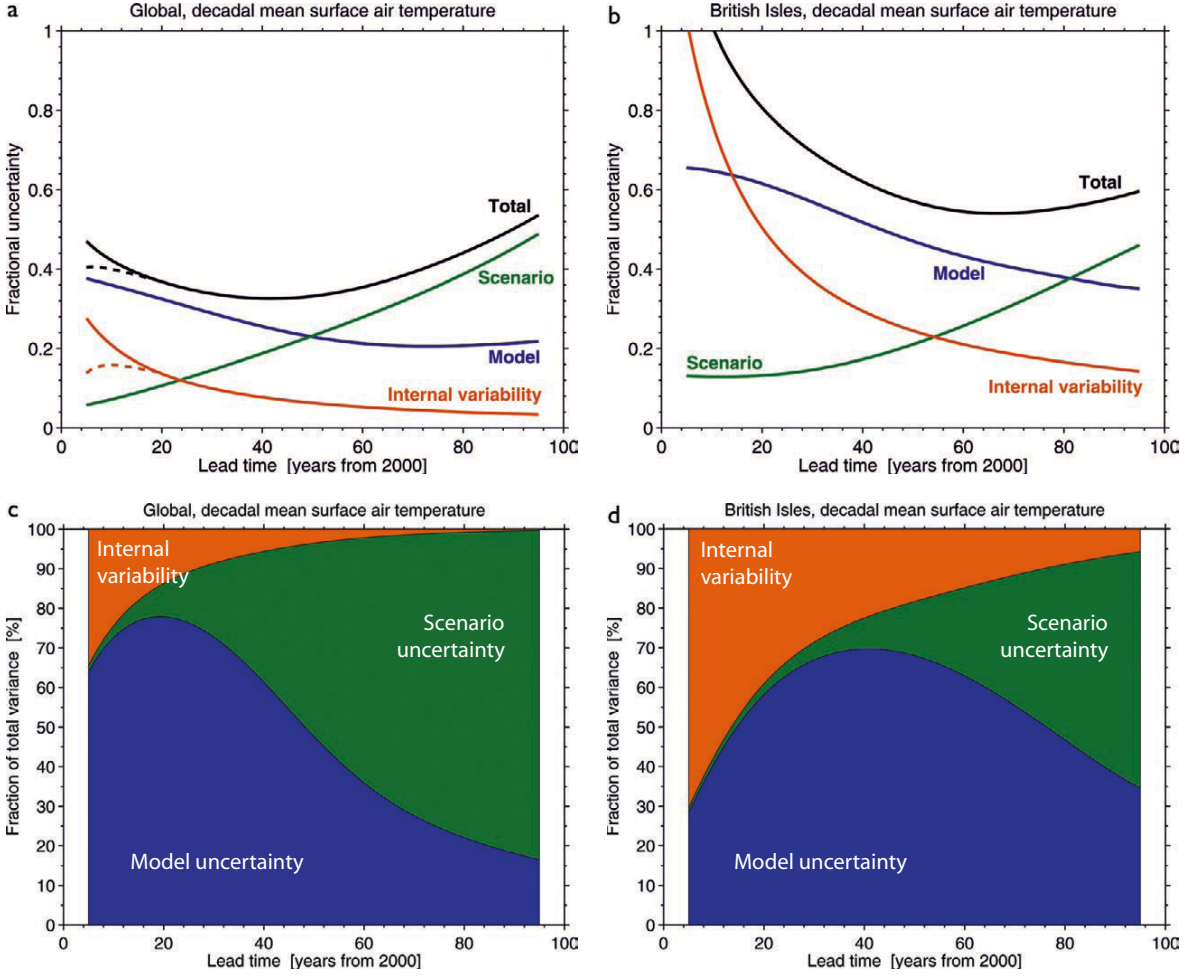
Figure 1.9: (a-b) The relative importance of sources of uncertainty in decadal mean surface temperature projections (relative to 1971-2000) as fractional uncertainty, calculated as the 90% confidence level divided by the mean prediction. (c-d) Fraction of total variance in decadal mean surface air temperature predictions explained by the three components of total uncertainty. Modified from Hawkins and Sutton (2009).

it becomes obvious that the effect of CO_2 alone (ΔR_C) would decelerate the hydrological cycle as it would yield a negative $L\Delta P$. Therefore, the slope of $\frac{\Delta P}{\Delta T}$ in Fig. 1.10 does not go through zero but through ΔR_C. Second, and more importantly, it can be seen that the radiative property of the troposphere, k, determines the slope of the relation $\frac{\Delta P}{\Delta T}$ (values for k around 8 $\mathrm{W\,m^{-2}\,K^{-1}}$ would yield a Clausius-Clapeyron-like relation).

$\frac{\Delta P}{\Delta T}$ in model simulations for equilibrium climate sensitivity (ECS) or transient climate response (TCR) come to lie on a slope of about $3\,\%\,\mathrm{K^{-1}}$ (Fig. 1.10). The blue circles in Fig. 1.10 show actual $\frac{\Delta P}{\Delta T}$ from TCR simulations from the new fifth Coupled Model Intercomparison Project (CMIP5; Taylor et al., 2012), while for the green and orange circles CMIP5-based TCR and ECS values, respectively, by Andrews et al. (2012) were simply fed into Eq. 1.1. This confirms that the theoretical principle behind Eq. 1.1 is a good approximation to the results from complex models. This finding is largely independent of the model generation, as the slope of this circle distribution is very similar to the slope by Allen and Ingram (2002), who used $\frac{\Delta P}{\Delta T}$ from older GCMs of the second Coupled Model Intercomparison Project (CMIP2; Covey et al., 2000).

On the other hand, the intensification of extreme precipitation events is expected to follow Clausius-Clapeyron, as in that case the amount of precipitation is determined by the amount of moisture in the air (e.g. Allan and Soden, 2008; Lau et al., 2013). Therefore, extreme
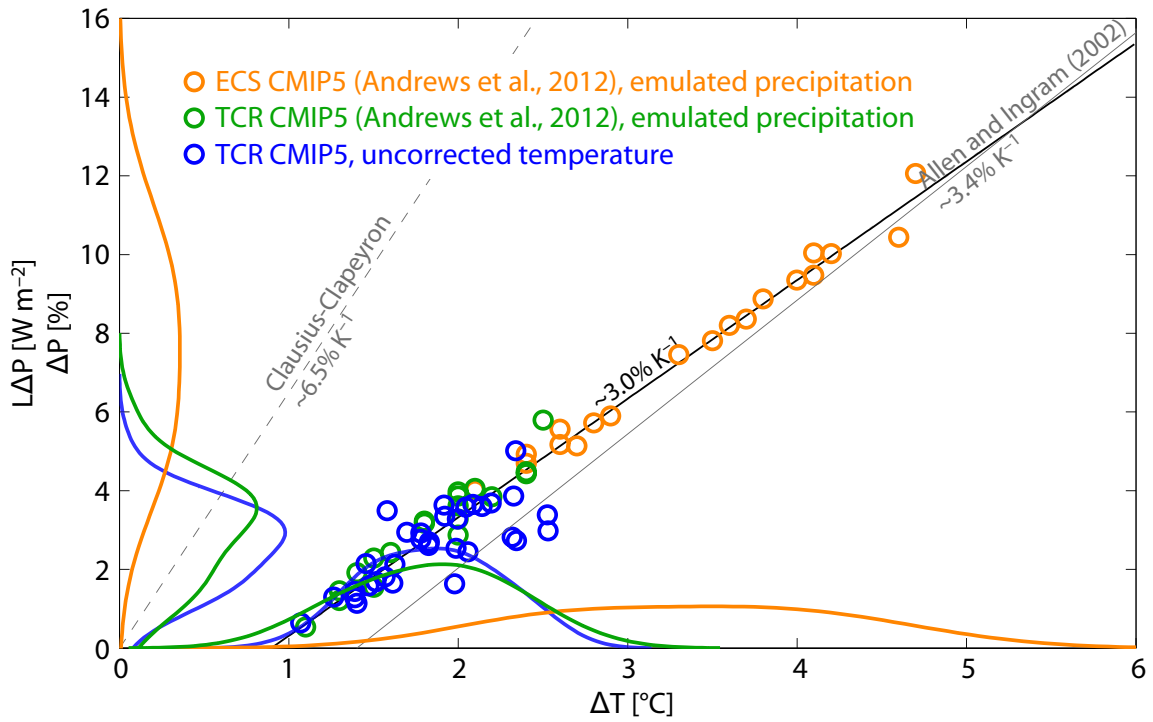
Figure 1.10: Revisiting Allen and Ingram (2002). The solid gray line is the relation $\frac{\Delta P}{\Delta T}$, derived by Allen and Ingram (2002) from CMIP2 (second Coupled Model Intercomparison Project) equilibrium climate sensitivity (ECS) and transient climate response (TCR) experiments. The dashed gray line indicates the slope if $\frac{\Delta P}{\Delta T}$ were to follow Clausius-Clapeyron. Orange circles are estimates of $\frac{\Delta P}{\Delta T}$ using ΔT from CMIP5 ECS by Andrews et al. (2012) and Eq. 1.1 to estimate ΔP (emulated precipitation). Thereby, k is $3 \, \mathrm{W \, m^{-2} \, K^{-1}}$ and ΔR_C is mimicked as a random normal distribution with $\mu = -2.5 \, \mathrm{W \, m^{-2}}$ and $\sigma = 0.3 \, \mathrm{W \, m^{-2}}$. Green circles are estimates of $\frac{\Delta P}{\Delta T}$ using ΔT from CMIP5 TCR by Andrews et al. (2012) and again Eq. 1.1 to estimate ΔP (emulated precipitation). Blue circles are estimates of $\frac{\Delta P}{\Delta T}$ using ΔT and actual ΔP from the CMIP5 1pctCO2 experiments ($+1\% \, \mathrm{CO_2 \, yr^{-1}}$) at the year of CO_2 doubling (20 year average centered on year 70), i.e., the TCR (IPCC, 2007). In the latter case no correction of ΔT for disequilibrium, such as accounting for the ocean heat uptake, has been conducted. Kernel-estimated probability density functions for the samples of ΔP and ΔT are given on the y-axis and x-axis, respectively. The linear trend of all circles is given by the solid black line.

precipitation events are expected to intensify faster than the mean precipitation and changes due to global warming will therefore be easier to detect (Min et al., 2011; IPCC, 2012).

Nevertheless, and despite our robust understanding of the energetics of the hydrological cycle, projections of future changes in precipitation are still more uncertain than the ones for temperature. Also, the confidence in regional precipitation projections has not changed markedly since the last IPCC's assessment (Knutti and Sedláček, 2012).

1.3 Modeling the climate

As illustrated at a number of examples in the previous sections, climate models are an indispensable tool for climate change research and are applied on a variety of time scales. In the context of past and present climate change, models offer the possibility to investigate and understand the dynamics underlying observations and reconstructions (chapter 2), to validate concepts of proxy reconstruction (chapter 3), or to test hypotheses of a mechanism (chapter 4). To project future climate change, models are in fact the only tool available, as illustrated in Fig. 1.10.

Today, a large number of models exists, differing by their spatial resolution, their set of components, or their computational requirements. Therefore, the first step of a modeling

study is to choose a suitable model. The following provides a brief overview on different climate models available, introduces the model of choice for this thesis – the Community Climate System Model –, and outlines the general experimental setup.

1.3.1   Model hierarchy

Climate models are usually classified according to the set of components that they include and the complexity of those components (usually the atmosphere or ocean are the decisive components; Stocker, 2011). Simpler models comprise of boxes for the different components atmosphere, ocean, and land that exchange tracers based on conservation laws and parametrizations and are usually applied to explore theoretical considerations and to establish principle understanding. In this case, the atmosphere can be represented by, e.g., a one-layer energy (and moisture) balance model (EBM). Similarly, the ocean is a so-called 'slab ocean', a box model that allows for heat exchange with the atmosphere, but only parameterizes the heat distribution across the ocean and therefore cannot account for dynamic changes in currents.

Evolving from that, ocean models based on zonally averaged equations to conserve momentum, mass, heat, and salt allow for a dynamical representation of meridional transports of these quantities. Combined with a zonally averaged atmospheric EBM this already enables the investigation of the role of the ocean in different climate states (e.g., Stocker et al., 1992). In some models, the atmosphere EBM is substituted by a statistical dynamical (e.g., Sokolov and Stone, 1998), a two-dimensional dynamical (e.g., Petoukhov et al., 2000), or a quasi-geostrophic atmospheric component (e.g., Opsteegh et al., 1998). Analogously, the ocean can be simulated by a coarse-resolution three-dimensional dynamical GCM (OGCM; e.g., Ritz et al., 2011). These models are summarized under the term 'climate models of reduced complexity' and, when additionally coupled to biogeochemical components or (dynamical) ice sheet models, are called 'earth system models of intermediate complexity' (EMIC). Due to their computational efficiency EMICs can be used for either paleoclimatic research (e.g., Ritz et al., 2013), which requires long simulations, or multi-ensemble projections (e.g., Steinacher et al., 2010).

The most complex class of climate models relies on a high-resolution three-dimensional numerical solution of the Navier-Stokes equations to describe atmospheric or oceanic dynamics and, when coupled, forms an atmosphere-ocean GCM (AOGCM). Often these models also include a thermodynamic or dynamic-thermodynamic sea ice model and a land model that dynamically exchanges energy and moisture with the atmosphere, computes runoff, or changes albedo due to snow cover. These fully-coupled models are sometimes referred to as coupled GCM (CGCM) and the model used in this thesis, the Community Climate System Model, falls into this class. Due to their high-resolution and the many processes implemented, these models are computationally expensive and are used to simulate shorter time scales up to several centuries. Among the longest simulations conducted with CGCMs are the deglaciation simulation by Liu et al. (2009) and the Holocene simulations by Varma et al. (2012), albeit in the latter case orbital forcing was changed faster than in reality to shorten the integration time. Depending on the research question, a complex atmospheric GCMs (AGCM) is still coupled to prescribed sea surface temperatures or a 'slab ocean' (e.g., Hofer et al., 2012; Frierson and Hwang, 2012) or, vice versa, a high-resolution OGCM is forced with prescribed atmospheric conditions (e.g., Timmermann et al., 2009). The model classes discussed here are all global climate models. There exists a variety of regional climate models as well, which are not addressed here.

With the development of an increasing number of independent models, the urge for a structured model intercomparison arose. Today, a number of intercomparison projects provide a helpful overview on across-model performance and potential consensus with regard to scientific questions, e.g., AMIP (Atmospheric Modeling Intercomparison Project), OMIP (Ocean

MIP), C^{4}MIP (Coupled Climate-Carbon Cycle MIP), CMIP (Coupled MIP), or PMIP (Paleo MIP).

1.3.2   Community Climate System Model

The Community Climate System Model version 3 (CCSM3) is the third generation in a family of coupled climate models by the National Center for Atmospheric Research in Boulder, Colorado, USA. The fact that its code, released in 2004, is freely available to the scientific community makes it one of the most-used climate models to date.

A comprehensive description of CCSM3 is given by Collins et al. (2006b) and summarized here. The model consists of the four components atmosphere, ocean, sea ice, and land, all linked through a coupler that exchanges flux and state information. Initially developed by different modeling centers, the individual components can be discretized on a variety of spatial grids. The coupled version, however, provides only three scientifically tested resolutions, applying the same set of components at different resolutions:

- The low-resolution version (T31x3) includes the Community Atmosphere Model (CAM) version 3.1 (Collins et al., 2006a). Truncated at T31, the atmosphere has a nominal horizontal resolution of approximately $3.75\,° \times 3.75\,°$. The horizontal grid resolves 26 hybrid sigma-pressure levels, i.e., they gradually transform from terrain-following levels at the bottom to purely pressure-based levels at the top of the atmosphere from about 83 hPa to 2.9 hPa.

  The land component is the Community Land Model (CLM) version 3, applying the same horizontal resolution as CAM (Oleson et al., 2004). Each land grid cell is further divided into a specific land unit (glacier, wetland, vegetated, lake, or urban), which determines soil characteristics and multiple plant functional types of a grid cell. The soil resolves ten layers, while on the surface up to five levels of snow height are distinguished. River runoff is calculated by a separate river transport model, operating on a high-resolution grid of $0.5\,° \times 0.5\,°$.

  The ocean component is the Parallel Ocean Program (POP) version 1.4.3 (Smith and Gent, 2004) with an irregular displaced-pole grid for the Northern Hemisphere that smoothly transforms into a standard Mercator grid at the equator ($3.6\,°$ in longitude and $0.6\,°$ to $2.8\,°$ in latitude). Refinements around Greenland and in the Tropics allow for an open passage through the Canadian Arctic Archipelago and a better representation of equatorial upwelling, respectively. POP has a maximum depth of 5,000 m, stretched over 25 levels with a layer thickness expanding from 8 m at the top to 500 m towards the bottom. An implicit free-surface formulation in the solution of the barotropic equation allows the surface layer thickness to vary – the ocean volume, however, is kept constant as freshwater fluxes are implemented as virtual salt fluxes.

  The Community Sea Ice Model (CSIM) version 5 is the dynamic-thermodynamic sea ice component of CCSM3 and is discretized on the same horizontal grid as POP (Briegleb et al., 2004). Ice dynamics are based on the elastic-viscous-plastic rheology. A parameterized subgrid-scale ice thickness distribution allows for a diversified computation of vertical heat conduction through the ice. An explicit salt exchange with the ocean based on a non-zero reference salinity guarantees salt conservation in the coupled ocean-sea ice system.

  The Coupler version 6 (Kauffmann et al., 2004) receives flux and state information from the different components every hour (atmosphere, land, sea ice) or once per day (ocean) and passes them on, conserving state variables.

  A description of the present-day climate of the low-resolution CCSM3 is provided by Yeager et al. (2006). This resolution version is used in chapters 2 and 3.

- The intermediate-resolution (T42x1) version's atmosphere and land component are truncated at T42, which yields a horizontal resolution of approximately $2.8\,° \times 2.8\,°$ while the vertical resolution is the same as in the low-resolution version. The marked difference is in the ocean and sea ice component, where a nominal grid spacing of about $1\,°$ results in an order of magnitude more grid cells than in T31x3. Again, the displaced North pole leads to a refinement around Greenland with grid cells as small as $20{\times}30$ km. The ocean component deploys 40 levels at depth, reaching 5,500 km.

  Otto-Bliesner et al. (2006) used the intermediate-resolution version for control simulations of the Last Glacial Maximum and the mid-Holocene. This resolution version is used in chapters 3 and 4.

- The high-resolution version (T85x1) applies a T85 truncation for atmosphere and land with a horizontal resolution of approximately $1.41\,° \times 1.41\,°$. The ocean and sea ice components work at the same resolution as in the intermediate-resolution version.

  A review of the high-resolution version's performance is given in Collins et al. (2006b). Due to limitations regarding the computational resources, the high-resolution version was not used in this thesis.
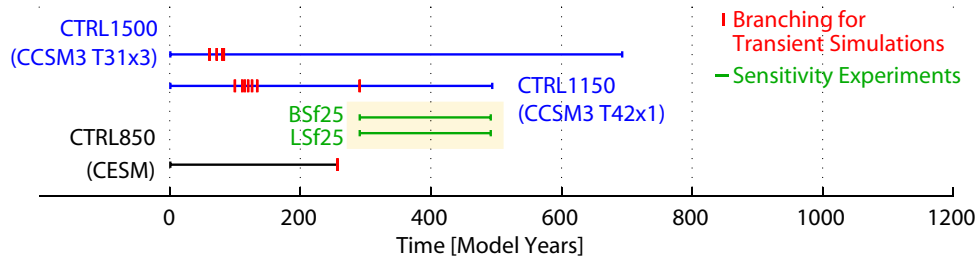
1.3.3   Simulations used in this thesis

Several simulations with different resolution versions of CCSM3 as well as complementary simulations from other modeling groups are used in this thesis. The simulations can be grouped into (i) control simulations with perpetual external forcing, (ii) transient simulations with realistic, time-varying external forcing, and (iii) sensitivity experiments with an idealized external forcing. The simulations conducted with CCSM3 specifically for this thesis were performed on a CRAY XT5 and XE6 at the Swiss National Supercomputing Centre (CSCS) in Manno (now Lugano), Switzerland.

An overview on the simulations is given in Fig. 1.11. Chapter 2 features simulations with the low-resolution CCSM3 (T31x3) conducted by Masakazu Yoshimori and Dominik Hofer on an IBM SP4, a CRAY XT3, and a CRAY XT5 (the simulations were checked for scientific consistency when the machine at CSCS was changed; Yoshimori et al., 2010; Hofer et al., 2011). An ensemble of four transient simulations from 1500-2098 AD (TR1a-TR4a) was branched from different initial states of a 1500 AD control simulation (CTRL1500), which itself was branched from an extension of the multi-century NCAR 1990 AD control simulation by Yeager et al. (2006). CTRL1500 has weaker external forcing than the 1990 AD control simulation (e.g., 282.3 ppm versus 355.0 ppm CO_2; 1,364.3 $W\,m^{-2}$ versus 1,367.0 $W\,m^{-2}$, respectively), which resulted in the CTRL1500 drifting towards a new, colder equilibrium after branching from the 1990 AD control simulation. While the atmosphere adjusts within a couple of years, the ocean does not equilibrate due to the long time scale of deep ocean adjustment (Yeager et al., 2006). Therefore, at the time of branching for the transient simulations, CTRL1500 still exhibits a trend that is accounted for by detrending each variable in the transient simulations by a quadratic least-squares fit derived from CTRL1500 (for details see Hofer, 2010). The results in chapter 2 were additionally compared to a three-member ensemble of high-resolution CCSM3 (T85x1) simulations from 1870-2100 AD by Meehl et al. (2006).

For the study in chapter 3 an ensemble of transient simulations from 1150-1500 AD was performed with the intermediate-resolution CCSM3 (T42x1). Therefore, a control simulation with 1150 AD external forcing was run (CTRL1150), based on restart files from a reasonably equilibrated 400 year-long 1870 AD control simulation by the NCAR (Otto-Bliesner et al., 2006). The changes in external forcing from 1870 AD to 1150 AD are relatively small (Table 1.1), which is why no strong trends are observed after branching for the CTRL1150.

Control Simulations
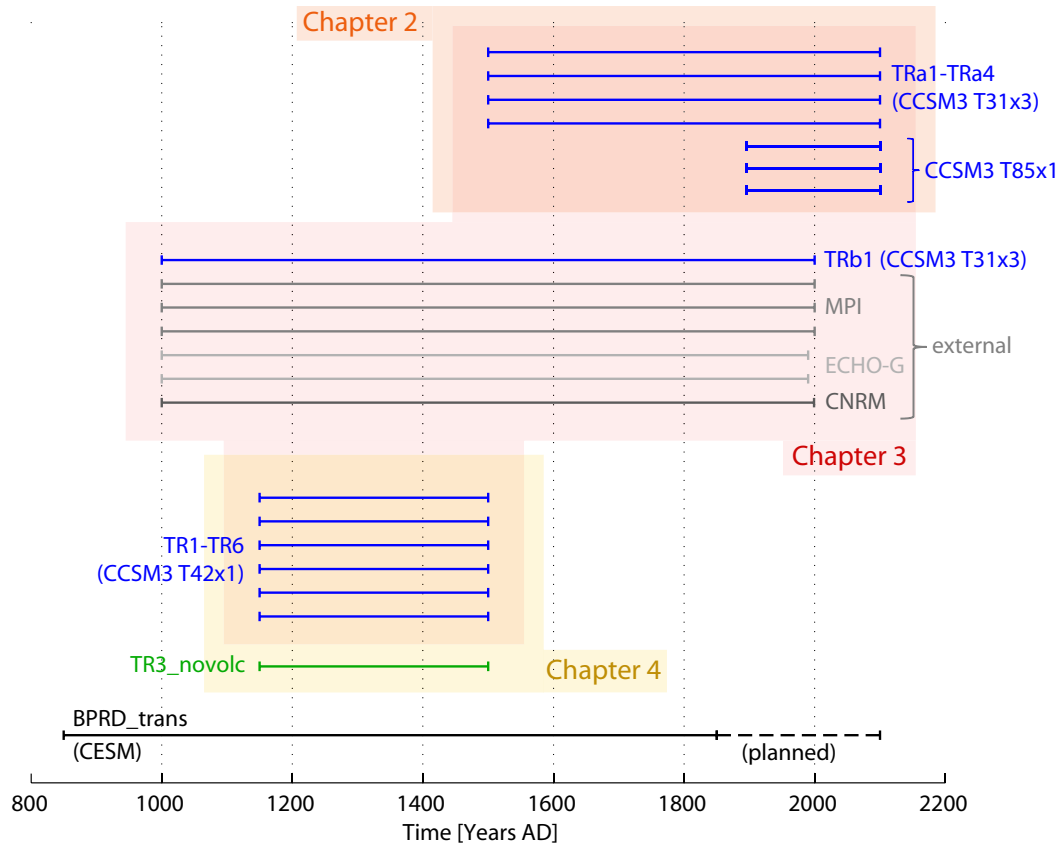

Transient Simulations

Figure 1.11: Overview of simulations used and conducted for this thesis. Upper panel shows the control simulations (time in model years), including the time of branching for the ensemble members of the transient simulations. For CCSM3, the model resolution is given in brackets. Two sensitivity experiments (BSf25, LSf25) were branched from CTRL1150 (see chapter 4). The lower panel shows the ensembles of transient simulations. Six simulations from other modeling groups ('external', see text for details) are also shown, as well as the sensitivity experiment TR3_novolc, a transient simulation with solar but no volcanic forcing. The shading indicates in which chapter the simulations are used. The last millennium simulation with the Community Earth Sysem Model (CESM) is described in appendix A.

The individual members of the transient ensemble were branched at different times between 100-150 years from CTRL1150. The start dates were chosen to cover a broad range of AMOC states with the goal to sample the North Atlantic internal variability (Fig. 1.12). At the time of branching for the transient simulations, CTRL1150 was not yet completed, making it difficult to optimally place these start dates. When CTRL1150 finished, it was revealed that the chosen AMOC states are on average slightly above the long-term AMOC mean of CTRL1150.

After testing on our own simulations, the analysis in chapter 3 was extended to an ensemble

Table 1.1: Forcings changes in the CTRL1500 simulation from their specifications in the 1870 AD control simulation from NCAR. Greenhouse gases are expressed as volume mixing ratios.

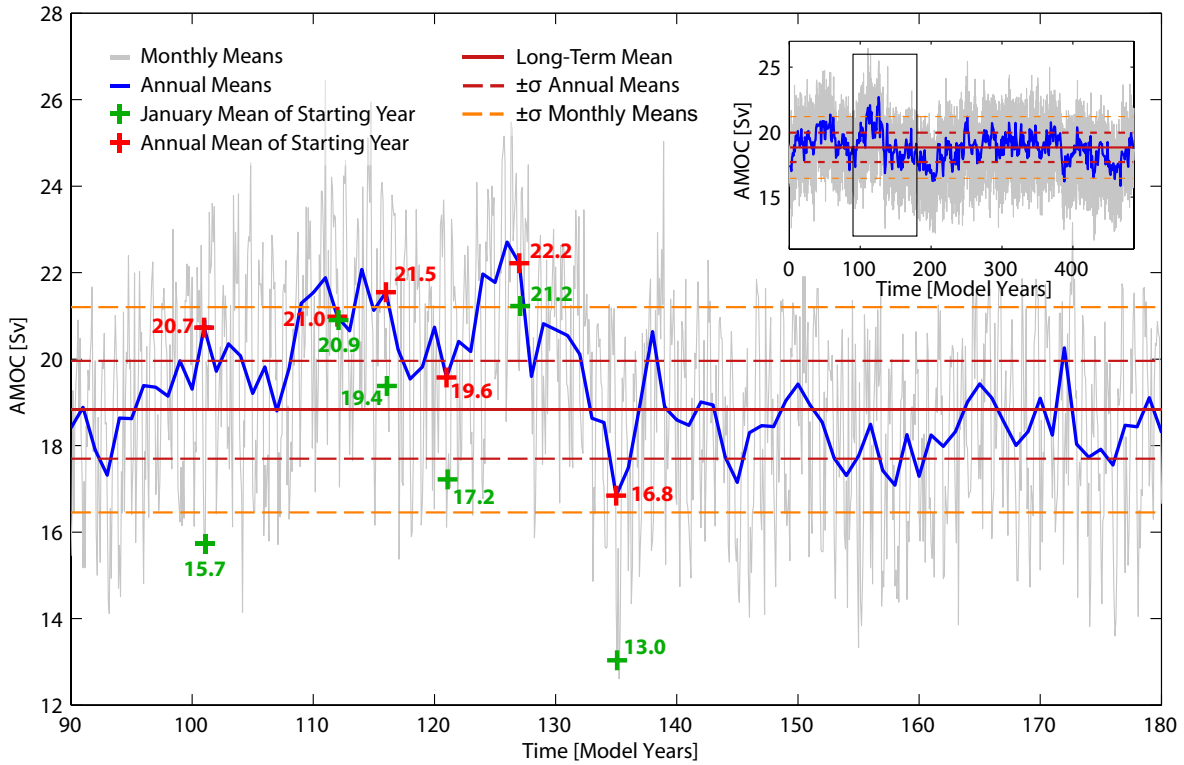| Forcing	1870 AD control simulation Otto-Bliesner et al. (2006)	CTRL1150 this thesis
CO_2	280.0 ppm	283.9 ppm
CH_4	760.0 ppb	704.9 ppb
N_2O	270.0 ppb	265.0 ppb
CFC11	0	0
CFC12	0	0
TSI	1,365.0 $\mathrm{W\,m^{-2}}$	1,366.4 $\mathrm{W\,m^{-2}}$
Orbital configuration	1950 AD	1150 AD

Figure 1.12: Initial conditions for the transient ensemble with CCSM3 T42x1. Time series of the Atlantic Meridional Overturning Circulation (AMOC) as the maximum of the meridional overturning circulation in the Atlantic north of $28\,^\circ$N in CTRL1150. The inset shows the entire simulation with the zoom-in indicated. The AMOC values for the start dates of the individual transient simulations are marked with crosses and given in Sv next to the crosses (January mean and annual mean of start year).

of last millennium simulations with other models: a three-member ensemble with the Max Planck Institute for Meteorology Earth System Model (MPI-ESM, here MPI; Jungclaus et al., 2010), two simulations with the ECHO-g (ECHAM4 and HOPE-g; González-Rouco et al., 2006), and a simulation with the Centre National de Recherches Météorologiques Climate Model (CNRM-CM3.3; Swingedouw et al., 2011). The simulations were kindly provided by the authors.

For the study in chapter 4 complementary sensitivity experiments were conducted. One member of the ensemble of transient simulations from 1150-1500 AD was rerun with the same setup except that volcanic eruptions were omitted to isolate the effect of solar versus volcanic

forcing (TR3_novolc). Additionally, two 200-year simulations were branched from CTRL1150 at the same time, in which the external forcing of CTRL1150 prevailed, but frazil ice growth was artificially enhanced by a factor of 25 in the Barents Sea (BSf25) and the Labrador Sea (LSf25) for the first 100 years. As the latter sensitivity experiments are a novelty in coupled modeling, they are described in more detail in chapter 4.

1.3.4 Transient forcings and their implementation

In its standard configuration CCSM3 is forced exclusively in the atmosphere. The technical description of CAM (Collins et al., 2004) provides a detailed depiction of the implementation of forcing, a short summary of which is provided here along with the forcing datasets used.

The solar irradiance depends on the orbital year and the TSI and in CAM is calculated according to Berger (1978). The orbital year, which determines Earth's orbital parameters eccentricity, obliquity, and precession, is held fixed in the simulations with the low-resolution version (chapters 2 and 3) and is implemented manually as time-varying in this thesis' intermediate-resolution version (chapters 3 and 4). The TSI is prescribed as time-varying annual means, based on a scaling of the net radiative forcing from Crowley (2000) to a solar irradiance reconstruction by Lean et al. (1995) (Fig. 1.13b; details in Yoshimori et al., 2010). The model's formulation for the actual solar irradiance at the top of the atmosphere further includes the solar zenith angle and diurnal cycle. The spectral distribution resolves 19 fixed bands from 0.2 to 5 μm and does not allow for temporal changes in spectral distribution.

The volcanic forcing is prescribed as zonal and monthly means of volcanic aerosol mass. These were obtained by converting the TSI changes due to volcanoes of Crowley (2000) to aerosol mass using linear regression coefficients obtained from the six strongest volcanic eruptions post-1890 (Ammann et al., 2003). The model assumes the aerosols to consist of 75% sulfuric acid and 25% water and their sizes to be log-normal distributed with an effective radius = 0.426 μm and σ = 1.25 μm. These assumptions determine the optical properties of the aerosols for the different spectral bands, which results in a column-integrated optical depth for incoming solar radiation (Fig. 1.13c). Due to limited knowledge of the exact timing of past volcanic eruptions, the forcing starts at the beginning of a specific year and is kept constant throughout the year. Besides volcanic aerosols, other aerosols such as sulfate, sea salt, black and organic carbon, or soil dust can be included. No anthropogenic sulfate emissions are included in the transient simulations, which leads to an overestimated increase in surface air temperatures during the twentieth century (Hofer et al., 2011).

The GHGs CO_2, CH_4, N_2O, and chlorofluorocarbons (CFC11 and CFC12) are prescribed as annual means based on splined reconstructions (Etheridge et al., 1996; Blunier et al., 1995; Flückiger et al., 1999, respectively) joined with measurements from 1970 to 2005 (Keeling and Whorf, 2005; Dlugokencky et al., 2003; Thompson et al., 2004, Fig. 1.13d-h). For the rest of the twenty-first century, the concentrations follow the A2 scenario from the IPCC Special Report on Emissions Scenarios (IPCC, 2000). While the GHGs are considered well-mixed in the troposphere, a latitudinal dependence is applied in the stratosphere to mimic the spatial distribution due to stratospheric circulation. Ozone (O_3) is prescribed as three-dimensional present-day climatology. The radiative calculation treats the transmission of incoming solar radiation according to absorptivity and emissivity of the atmospheric composition in several different spectral bands.

The CCSM3 does not allow simulating transient land cover changes, as a change in the land cover data requires a recompilation of the model code. In the simulations for this thesis, a fixed present-day land cover mask was implemented.
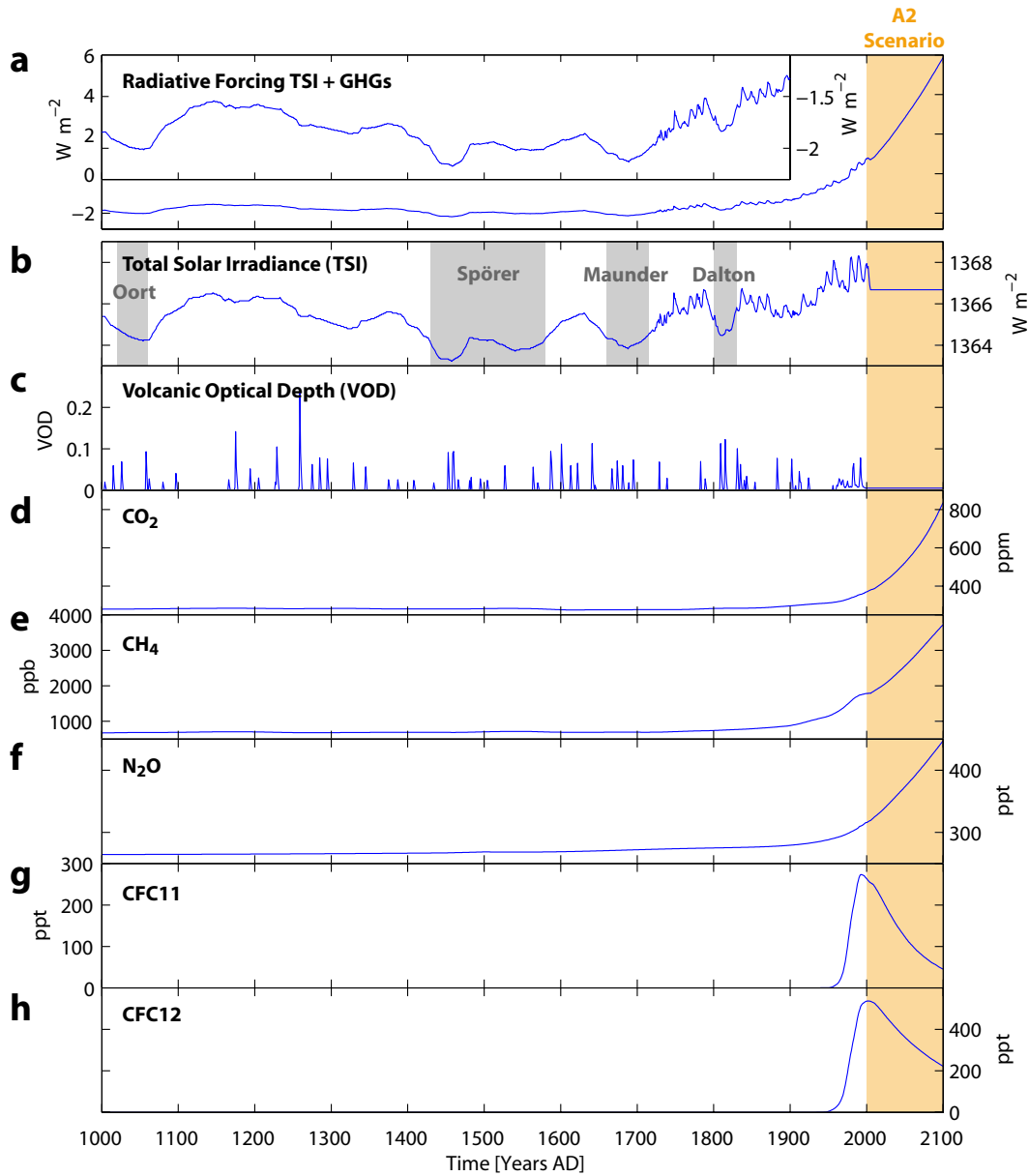
Figure 1.13: Natural and anthropogenic forcing used in the transient simulations with CCSM3 (T31x3 and T42x1). (a) Radiative forcing from total solar irradiance (TSI) and greenhouse gases (GHGs) relative to 1961-1990 AD is calculated according to IPCC (2001). The inset in (a) shows the period 1000-1900 AD. (b) Total solar irradiance with minima of solar activity indicated by gray shading. (c) Volcanic forcing as optical depth changes due to volcanic aerosols. (d-h) Concentration of GHGs. The continuation of these forcing functions into the twenty-first century is prescribed by the A2 scenario (orange shading; see text for details).

1.4   Outline

This thesis is part of the third phase of the project MONALISA (Modelling and Reconstruction of the North Atlantic Climate System Variability), a project initiated within the National Centre for Competence in Research (NCCR) Climate (2001-2012). Within the project the following leading research question was derived for this thesis:

> *"What is the response of the hydrological cycle to changes in external forcing functions in the North Atlantic during key periods of the past 1000 years and which feedback mechanisms are operating between the atmosphere and the ocean?"*

The overall aim of this thesis is therefore to investigate the hydro-climatic variability of the climate system during the last millennium.

The thesis is structured as follows:

- Chapter 2 addresses the polar freshwater cycle in transient simulations over the time period 1500-2100 AD. The sensitivity of the freshwater reservoirs and exchange fluxes to variations in external forcing is investigated. Thereby, future changes in polar regions – which have been studied intensively already with other and higher resolved models – are for the first time put in the context of centennial-scale preindustrial natural variability. The study was published in Climate Dynamics (Lehner et al., 2012b).

- Chapter 3 investigates the decadal-to-centennial-scale variability of the North Atlantic Oscillation (NAO) in model simulations over the last millennium. Thereby, the question is addressed whether a significant NAO shift dominated the transition from the warm Medieval Climate Anomaly to the cold Little Ice Age – a claim made by a recent proxy-based NAO reconstruction. The concept underlying this reconstruction is further tested in a classical pseudo-proxy approach using different models and reanalyses. As the concept is found to lack robustness, suggestions are made regarding achieving a possible stabilization of the approach. The study was published in Quaternary Science Reviews (Lehner et al., 2012a).

- Chapter 4 deals with the role of Arctic sea ice in the transition from the Medieval Climate Anomaly to the Little Ice Age. In an ensemble of simulations with CCSM3 sea ice advances in the Barents Sea are found to exhibit a strong control on Northern European temperature. Using a new style of sensitivity experiments with artificial sea ice growth a complex sea ice-ocean-atmosphere feedback mechanism is revealed that is able to explain a large part of the temperature pattern expected from proxy reconstruction. The study will be published in Journal of Climate (Lehner et al., in press).

- Chapter 5 provides a short discussion of this thesis' results, their shortcomings and an outlook of potential follow-up studies.

- In appendix A a currently running last millennium simulation with the Community Earth System Model is introduced and preliminary results are presented.

Bibliography

AchutaRao, K. and K. Sperber, 2006: ENSO simulation in coupled ocean-atmosphere models: are the current models better? *Clim. Dyn.* (27), 1–15, doi:10.1007/s00382-006-0119-7.

Allan, R. P. and B. J. Soden, 2008: Atmospheric warming and the amplification of precipitation extremes. *Science* (321), 1481–1484, doi:10.1126/science.1160787.

Allen, M. R. and W. J. Ingram, 2002: Constraints on future changes in climate and the hydrological cycle. *Nature* (419), 224–232.

Ammann, C., G. Meehl, W. Washington, and C. Zender, 2003: A monthly and latitudinally varying volcanic forcing dataset in simulations of 20th century climate. *Geophys. Res. Let.* (30), doi:10.1029/2003GL016875.

Andrews, T., J. M. Gregory, M. J. Webb, and K. E. Taylor, 2012: Forcing, feedbacks and climate sensitivity in CMIP5 coupled atmosphere-ocean climate models. *Geophys. Res. Let.* (39), doi:10.1029/2012GL051607.

Baumgartner, A. and E. Reichel, 1975: *The World Water Balance*, Elsevier, New York, 179 pp.

Berger, A. L., 1978: Long-term variations of caloric insolation resulting from the earth's orbital elements. *J. Atm. Sci.* (35), 2362–2367, doi:10.1016/0033-5894(78)90064-9.

Bhend, J., J. Franke, D. Folini, M. Wild, and S. Broennimann, 2012: An ensemble-based approach to climate reconstructions. *Clim. Past* (8), 963–976, doi:10.5194/cp-8-963-2012.

Biastoch, A., C. W. Boening, and J. R. E. Lutjeharms, 2008: Agulhas leakage dynamics affects decadal variability in Atlantic overturning circulation. *Nature* (456), 489–492, doi:10.1038/nature07426.

Bladé, I., B. Liebmann, D. Fortuny, and G. J. van Oldenborgh, 2012: Observed and simulated impacts of the summer NAO in Europe: implications for projected drying in the Mediterranean region. *Clim. Dyn.* (39), 709–727, doi:10.1007/s00382-011-1195-x.

Blunier, T., J. Chappellaz, J. Schwander, B. Stauffer, and D. Raynaud, 1995: Variations in atmospheric methane concentration during the Holocene epoch. *Nature* (374), 46–49, doi:10.1038/374046a0.

Bond, T. C., et al., 2013: Bounding the role of black carbon in the climate system: A scientific assessment. *J. Geophys. Res.*, doi:10.1002/jgrd.50171, in press.

Bony, S., et al., 2006: How well do we understand and evaluate climate change feedback processes? *J. Clim.* (19), 3445–3482, doi:10.1175/JCLI3819.1.

Bradley, R. S., 1996: Are there optimum sites for global paleotemperature reconstruction? *Climate Variations and Forcing Mechanisms of the Last 2000 Years*, P. D. Jones, R. S. Bradley, and J. Jouzel, Eds., Springer-Verlag, NATO ASI Series, 603–624.

Briegleb, B. P., C. M. Bitz, E. C. Hunke, W. H. Lipscomb, M. M. Holland, J. L. Schramm, and R. E. Moritz, 2004: Tech. Rep. Scientific description of the sea ice component in the Community Climate System Model, Version 3, National Center for Atmospheric Research, Boulder, CO.80307-3000. 66 pp.

Briffa, K. and P. Jones, 1993: Global surface air temperature variations during the twentieth century: Part 2 , implications for large-scale high-frequency palaeoclimatic studies. *The Holocene* (3), 77–88, doi: 10.1177/095968369300300109.

Büntgen, U., et al., 2011: 2500 Years of European Climate Variability and Human Susceptibility. *Science* (331), 578–582, doi:10.1126/science.1197175.

Collins, W., et al., 2006a: The formulation and atmospheric simulation of the Community Atmosphere Model version 3 (CAM3). *J. Clim.* (19), 2144–2161, doi:10.1175/JCLI3760.1.

Collins, W. D., et al., 2004: Tech. Rep. Description of the NCAR Community Atmosphere Model (CAM3), National Center for Atmospheric Research (NCAR). 226 pp.

Collins, W. D., et al., 2006b: The Community Climate System Model version 3 (CCSM3). *J. Clim.* (19), 2122–2143, doi:10.1175/JCLI3761.1.

Cook, E. R., K. J. Anchukaitis, B. M. Buckley, R. D. D'Arrigo, G. C. Jacoby, and W. E. Wright, 2010a: Asian Monsoon Failure and Megadrought During the Last Millennium. *Science* (328), 486–489, doi: 10.1126/science.1185188.

Cook, E. R., R. D. D'Arrigo, and M. E. Mann, 2002: A well-verified, multiproxy reconstruction of the winter North Atlantic Oscillation index since A.D. 1400. *J. Clim.* (15), 1754–1764, doi:10.1175/1520-0442(2002)015<1754:AWVMRO>2.0.CO;2.

Cook, E. R., R. Seager, R. R. Heim, Jr., R. S. Vose, C. Herweijer, and C. Woodhouse, 2010b: Megadroughts in North America: placing IPCC projections of hydroclimatic change in a long-term palaeoclimate context. *J. Quat. Sci.* (25), 48–61, doi:10.1002/jqs.1303.

Covey, C., K. M. AchutaRao, S. J. Lambert, and K. E. Taylor, 2000: Tech. Rep. Intercomparison of Present and Future Climates Simulated by Coupled Ocean-Atmosphere GCMs, Program for Climate Model Diagnosis and Intercomparison, Lawrence Livermore National Laboratory, Livermore, California.

Crowley, T. J., 2000: Causes of climate change over the past 1000 years. *Science* (289), 270–277.

Dai, A., K. Trenberth, and T. Qian, 2004: A global dataset of Palmer Drought Severity Index for 1870-2002: Relationship with soil moisture and effects of surface warming. *J. Hydrometeorology* (5), 1117–1130, doi:10.1175/JHM-386.1.

Delaygue, G. and E. Bard, 2011: An Antarctic view of Beryllium-10 and solar activity for the past millennium. *Clim. Dyn.* (36), 2201–2218, doi:10.1007/s00382-010-0795-1.

Deser, C., R. Knutti, S. Solomon, and A. S. Phillips, 2012: Communication of the role of natural variability in future North American climate. *Nature Climate Change* (2), 775–779, doi:10.1038/NCLIMATE1562.

DeVries, T. and F. Primeau, 2011: Dynamically and Observationally Constrained Estimates of Water-Mass Distributions and Ages in the Global Ocean. *J. Phys. Oceanogr.* (41), 2381–2401, doi:10.1175/JPO-D-10-05011.1.

Diaz, H. F., R. Trigo, M. K. Hughes, M. E. Mann, E. Xoplaki, and D. Barriopedro, 2011: Spatial and temporal characteristics of climate in medieval times revisited. *Bull. Am. Meteorol. Soc.* (92), 1487–1500, doi:10.1175/2011BAMS-D-10-05003.1.

Dlugokencky, E., S. Houweling, L. Bruhwiler, K. Masarie, P. Lang, J. Miller, and P. Tans, 2003: Atmospheric methane levels off: Temporary pause or a new steady-state? *Geophys. Res. Let.* (30), doi: 10.1029/2003GL018126.

Durack, P. J. and S. E. Wijffels, 2010: Fifty-Year Trends in Global Ocean Salinities and Their Relationship to Broad-Scale Warming. *J. Clim.* (23), 4342–4362, doi:10.1175/2010JCLI3377.1.

Etheridge, D. M., L. P. Steele, R. L. Langenfelds, R. J. Francey, J.-M. Barnola, and V. I. Morgan, 1996: Natural and anthropogenic changes in atmospheric CO_2 over the last 1000 years from air in Antarctic ice and firn. *J. Geophys. Res.* (101), 4115–4128.

Fasullo, J. T. and K. E. Trenberth, 2008: The annual cycle of the energy budget. Part II: Meridional structures and poleward transports. *J. Clim.* (21), 2313–2325, doi:10.1175/2007JCLI1936.1.

Flückiger, J., A. Dallenbach, T. Blunier, B. Stauffer, T. Stocker, D. Raynaud, and J. Barnola, 1999: Variations in atmospheric N2O concentration during abrupt climatic changes. *Science* (285), 227–230, doi: 10.1126/science.285.5425.227.

Franke, J., J. Fidel Gonzalez-Rouco, D. Frank, and N. E. Graham, 2011: 200 years of European temperature variability: insights from and tests of the proxy surrogate reconstruction analog method. *Clim. Dyn.* (37), 133–150, doi:10.1007/s00382-010-0802-6.

Franzese, A. M., S. R. Hemming, S. L. Goldstein, and R. F. Anderson, 2006: Reduced Agulhas Leakage during the Last Glacial Maximum inferred from an integrated provenance and flux study. *Earth Planet. Sci. Lett.* (250), 72–88, doi:10.1016/j.epsl.2006.07.002.

Friedlingstein, P., et al., 2010: Update on CO2 emissions. *Nature Geoscience* (3), 811–812, doi: 10.1038/ngeo1022.

Frierson, D. M. W. and Y.-T. Hwang, 2012: Extratropical Influence on ITCZ Shifts in Slab Ocean Simulations of Global Warming. *J. Clim.* (25), 720–733, doi:10.1175/JCLI-D-11-00116.1.

Froehlich, C., 2006: Solar irradiance variability since 1978 - Revision of the PMOD composite during solar cycle 21. *Space Sci. Rev.*. (125), 53–65, doi:10.1007/s11214-006-9046-5.

Fröhlich, C., 2009: Evidence of a long-term trend in total solar irradiance. *Astronomy & Astrophysics* (501), L27–U508, doi:10.1051/0004-6361/200912318.

Ganachaud, A., 2003: Large-scale mass transports, water mass formation, and diffusivities estimated from World Ocean Circulation Experiment (WOCE) hydrographic data. *J. Geophys. Res.* (108), doi:10.1029/2002JC001565.

Ganachaud, A. and C. Wunsch, 2000: Improved estimates of global ocean circulation, heat transport and mixing from hydrographic data. *Nature* (408), 453–457, doi:10.1038/35044048.

Gleeson, T., Y. Wada, M. F. P. Bierkens, and L. P. H. van Beek, 2012: Water balance of global aquifers revealed by groundwater footprint. *Nature* (488), 197–200, doi:10.1038/nature11295.

Gleick, P. H., 1993: *Water in Crisis: A Guide to the World's Freshwater Resources*, Oxford University Press, New York, 504 pp.

Glueck, M. F. and C. W. Stockton, 2001: Reconstruction of the North Atlantic Oscillation, 1429-1983. *International J. Climatology* (21), 1453–1465, doi:10.1002/joc.684.

González-Rouco, J., H. Beltrami, E. Zorita, and H. von Storch, 2006: Simulation and inversion of borehole temperature profiles in surrogate climates: Spatial distribution and surface coupling. *Geophys. Res. Let.* (33), doi:10.1029/2005GL024693.

Goosse, H., E. Crespin, A. de Montety, M. E. Mann, H. Renssen, and A. Timmermann, 2010: Reconstructing surface temperature changes over the past 600 years using climate model simulations with data assimilation. *J. Geophys. Res.* (115), doi:10.1029/2009JD012737.

Goosse, H., H. Renssen, F. Selten, R. Haarsma, and J. Opsteegh, 2002: Potential causes of abrupt climate events: A numerical study with a three-dimensional climate model. *Geophys. Res. Let.* (29), doi:10.1029/2002GL014993.

Graham, N. E., C. M. Ammann, D. Fleitmann, K. M. Cobb, and J. Luterbacher, 2011: Support for global climate reorganization during the "Medieval Climate Anomaly". *Clim. Dyn.* (37), 1217–1245, doi:10.1007/s00382-010-0914-z.

Graham, N. E., et al., 2007: Tropical Pacific – mid-latitude teleconnections in medieval times. *Clim. Change* (83), 241–285.

Gray, S., L. Graumlich, J. Betancourt, and G. Pederson, 2004: A tree-ring based reconstruction of the Atlantic Multidecadal Oscillation since 1567 AD. *Geophys. Res. Let.* (31), doi:10.1029/2004GL019932.

Hawkins, E. and R. Sutton, 2009: The potential to narrow uncertainty in regional climate predictions. *Bull. Am. Meteorol. Soc.* (90), 1095–1107, doi:10.1175/2009BAMS2607.1.

Haylock, M. R., N. Hofstra, A. M. G. K. Tank, E. J. Klok, P. D. Jones, and M. New, 2008: A European daily high-resolution gridded data set of surface temperature and precipitation for 1950-2006. *J. Geophys. Res.* (113), doi:10.1029/2008JD010201.

Haywood, J. and O. Boucher, 2000: Estimates of the direct and indirect radiative forcing due to tropospheric aerosols: A review. *Rev. Geophys.* (38), 513–543, doi:10.1029/1999RG000078.

Held, I. and B. Soden, 2000: Water vapor feedback and global warming. *Annu. Rev. Energy Environ* (25), 441–475, doi:10.1146/annurev.energy.25.1.441.

Held, I. M. and B. J. Soden, 2006: Robust responses of the hydrological cycle to global warming. *J. Clim.* (19), 5686–5699, doi:10.1175/JCLI3990.1.

Hofer, D., 2010: Simulations of the last millennium using a comprehensive climate model: The impact of the external forcing on the climate. Ph.D. thesis, University of Bern.

Hofer, D., C. C. Raible, N. Merz, A. Dehnert, and J. Kuhlemann, 2012: Simulated winter circulation types in the North Atlantic and European region for preindustrial and glacial conditions. *Geophys. Res. Let.* (39), doi:10.1029/2012GL052296.

Hofer, D., C. C. Raible, and T. F. Stocker, 2011: Variations of the Atlantic meridional overturning circulation in control and transient simulations of the last millennium. *Clim. Past* (7), 133–150, doi:10.5194/cp-7-133-2011.

Huntington, T., 2006: Evidence for intensification of the global water cycle: Review and synthesis. *J. Hydrology* (319), 83–95, doi:10.1016/j.jhydrol.2005.07.003.

IEA, 2013: Tech. Rep. CO_2 emissions from fuel combustion, International Energy Agency, 133 pp.

IPCC, 2000: *Special Report on Emissions Scenarios (SRES)*, Cambridge University Press, Cambridge, United Kingdom and New York, NY, USA, 599 pp.

IPCC, 2001: *Climate Change 2001: The Scientific Basis. Contribution of Working Group I to the Third Assessment Report of the Intergovernmental Panel on Climate Change*, Cambridge University Press, Cambridge, United Kingdom and New York, NY, USA, 881 pp.

IPCC, 2007: *Climate Change 2007: The Physical Science Basis. Contribution of Working Group I to the Fourth Assessment Report of the Intergovernmental Panel on Climate Change*, Cambridge University Press, Cambridge, United Kingdom and New York, NY, USA, 996 pp.

IPCC, 2012: *Managing the Risks of Extreme Events and Disasters to Advance Climate Change Adaptation. A Special Report of Working Groups I and II of the Intergovernmental Panel on Climate Change*, Cambridge University Press, Cambridge, UK, and New York, NY, USA, 582 pp.

Jin, E. K., et al., 2008: Current status of ENSO prediction skill in coupled ocean-atmosphere models. *Clim. Dyn.* (31), 647–664, doi:10.1007/s00382-008-0397-3.

Jones, P. D., et al., 2009: High-resolution palaeoclimatology of the last millennium: a review of current status and future prospects. *The Holocene* (19), 3–49, doi:10.1177/0959683608098952.

Joos, F. and R. Spahni, 2008: Rates of change in natural and anthropogenic radiative forcing over the past 20,000 years. *Proc. Natl. Acad. Sci.* (105), 1425–1430, doi:10.1073/pnas.0707386105.

Jungclaus, J. H., et al., 2010: Climate and carbon-cycle variability over the last millennium. *Clim. Past* (6), 723–737, doi:10.5194/cp-6-723-2010.

Karl, T. and K. Trenberth, 2003: Modern global climate change. *Science* (302), 1719–1723, doi: 10.1126/science.1090228.

Kauffmann, B. G., R. Jacob, T. Craig, and W. G. Large, 2004: Tech. Rep. The CCSM Coupler Version 6.0. User's Guide, Source Code Reference and Scientific Description, National Center for Atmospheric Research, Boulder, CO.80307-3000.

Kaufman, D. S., et al., 2009: Recent warming reverses long-term Arctic cooling. *Science* (325), 1236–1239, doi:10.1126/science.1173983.

Keeling, C., 1960: The concentration and isotopic abundances of carbon dioxide in the atmosphere. *Tellus* (12), 200–203.

Keeling, C., R. Bacastow, A. Bainbridge, C. Ekdahl, P. Guenther, L. Waterman, and J. Chin, 1976: Atmospheric carbon-dioxide variations at Mauna-Loa observatory, Hawaii. *Tellus* (28), 538–551.

Keeling, C. D. and T. P. Whorf, 2005: Atmospheric CO2 records from sites in the SIO air sampling network. *Trends: A Compendium of Data on Global Change*, Carbon Dioxide Information Analysis Center, Oak Ridge National Laboratory, U.S. Department of Energy, Oak Ridge.

Kinnard, C., C. M. Zdanowicz, D. A. Fisher, E. Isaksson, A. de Vernal, and L. G. Thompson, 2011: Reconstructed changes in Arctic sea ice over the past 1,450 years. *Nature* (479), 509–U231, doi: 10.1038/nature10581.

Knutti, R. and J. Sedláček, 2012: Robustness and uncertainties in the new CMIP5 climate model projections. *Nature Climate Change*, doi:10.1038/NCLIMATE1716, published online.

Kopp, G. and J. L. Lean, 2011: A new, lower value of total solar irradiance: Evidence and climate significance. *Geophys. Res. Let.* (38), doi:10.1029/2010GL045777.

Kuettel, M., et al., 2010: The importance of ship log data: reconstructing North Atlantic, European and Mediterranean sea level pressure fields back to 1750. *Clim. Dyn.* (34), 1115–1128, doi:10.1007/s00382-009-0577-9.

Kuhlbrodt, T., A. Griesel, M. Montoya, A. Levermann, M. Hofmann, and S. Rahmstorf, 2007: On the driving processes of the Atlantic meridional overturning circulation. *Rev. Geophys.* (45), doi: 10.1029/2004RG000166.

Kuhlbrodt, T., et al., 2009: An Integrated Assessment of changes in the thermohaline circulation. *Clim. Change* (96), 489–537, doi:10.1007/s10584-009-9561-y.

Large, W. G. and S. G. Yeager, 2009: The global climatology of an interannually varying air-sea flux data set. *Clim. Dyn.* (33), 341–364, doi:10.1007/s00382-008-0441-3.

Lau, W. K.-M., H.-T. Wu, and K.-M. Kim, 2013: A Canonical Response of Precipitation Characteristics to Global Warming from CMIP5 Models. *Geophys. Res. Let.*, doi:10.1002/grl.50420, accepted.

Le Quere, C., et al., 2009: Trends in the sources and sinks of carbon dioxide. *Nature Geoscience* (2), 831–836, doi:10.1038/ngeo689.

Lean, J., J. Beer, and R. Bradley, 1995: Reconstruction of solar irradiance since 1610 - implications for climate-change. *Geophys. Res. Let.* (22), 3195–3198, doi:10.1029/95GL03093.

Lehner, F., A. Born, C. C. Raible, and T. F. Stocker, in press: Amplified inception of European Little Ice Age by sea ice-ocean-atmosphere feedbacks. *J. Clim.*

Lehner, F., C. C. Raible, and T. F. Stocker, 2012a: Testing the robustness of a precipitation proxy-based North Atlantic Oscillation reconstruction. *Quat. Sci. Rev.* (45), 85–94, doi:10.1016/j.quascirev.2012.04.025.

Lehner, F., C. C. Raible, T. F. Stocker, and D. Hofer, 2012b: The freshwater balance of polar regions in transient simulations from 1500 to 2100 AD using a comprehensive coupled climate model. *Clim. Dyn.* (39), 347–363, doi:10.1007/s00382-011-1199-6.

Liu, Z., et al., 2009: Transient simulation of last deglaciation with a new mechanism for Bolling-Allerod warming. *Science* (325), 310–314, doi:10.1126/science.1171041.

Loeb, N. G. and W. Su, 2010: Direct Aerosol Radiative Forcing Uncertainty Based on a Radiative Perturbation Analysis. *J. Clim.* (23), 5288–5293, doi:10.1175/2010JCLI3543.1.

Lohmann, U., et al., 2010: Total aerosol effect: radiative forcing or radiative flux perturbation? *Atmos. Chem. Phys.* (10), 3235–3246.

Lorenz, R., E. B. Jaeger, and S. I. Seneviratne, 2010: Persistence of heat waves and its link to soil moisture memory. *Geophys. Res. Let.* (37), doi:10.1029/2010GL042764.

Luethi, D., et al., 2008: High-resolution carbon dioxide concentration record 650,000-800,000 years before present. *Nature* (453), 379–382, doi:10.1038/nature06949.

Luterbacher, J., D. Dietrich, E. Xoplaki, M. Grosjean, and H. Wanner, 2004: European seasonal and annual temperature variability, trends, and extremes since 1500. *Science* (303), 1499–1503, doi: 10.1126/science.1093877.

Luterbacher, J., et al., 2002a: Extending North Atlantic Oscillation reconstructions back to 1500. *Atmospheric Science Letters* (2), 114–124, doi:10.1006/asle.2002.0047.

Luterbacher, J., et al., 2002b: Reconstruction of sea level pressure fields over the eastern north atlantic and europe back to 1500. *Clim. Dyn.* (18), 545–561, doi:10.1007/s00382-001-0196-6.

Mann, E. M., et al., 2009: Global signatures and dynamical origins of the Little Ice Age and Medieval Climate Anomaly. *Science* (326), 1256–1260, doi:10.1126/science.1177303.

Mann, M., S. Rutherford, E. Wahl, and C. Ammann, 2005: Testing the fidelity of methods used in proxy-based reconstructions of past climate. *J. Clim.* (18), 4097–4107, doi:10.1175/JCLI3564.1.

Mann, M. E., Z. Zhang, M. K. Hughes, R. S. Bradley, S. K. Miller, S. Rutherford, and F. Ni, 2008: Proxy-based reconstructions of hemispheric and global surface temperature variations over the past two millennia. *Proc. Natl. Acad. Sci.* (105), 13 252–13 257, doi:10.1073/pnas.0805721105.

Marshall, J. and K. Speer, 2012: Closure of the meridional overturning circulation through Southern Ocean upwelling. *Nature Geoscience* (5), 171–180, doi:10.1038/NGEO1391.

Marshall, J., et al., 2001: North Atlantic climate variability: Phenomena, impacts and mechanisms. *International J. Climatology* (21), 1863–1898, doi:10.1002/joc.693.

McPhee, M. G., A. Proshutinsky, J. H. Morison, M. Steele, and M. B. Alkire, 2009: Rapid change in freshwater content of the Arctic Ocean. *Geophys. Res. Let.* (36), doi:10.1029/2009GL037525.

Meehl, G., et al., 2006: Climate change projections for the twenty-first century and climate change commitment in the CCSM3. *J. Clim.* (19), 2597–2616, doi:10.1175/JCLI3746.1.

Meehl, G. A., C. Covey, T. Delworth, M. Latif, B. McAvaney, J. F. B. Mitchell, R. J. Stouffer, and K. E. Taylor, 2007: The WCRP CMIP3 multimodel dataset - A new era in climate change research. *Bull. Am. Meteorol. Soc.* (88), 1383–1394, doi:10.1175/BAMS-88-9-1383.

Meehl, G. A., et al., 2012: Climate system response to external forcings and climate change projections in CCSM4. *J. Clim.* (25), 3661–3683, doi:10.1175/JCLI-D-11-00240.1.

Meinshausen, M., et al., 2011: The RCP greenhouse gas concentrations and their extensions from 1765 to 2300. *Clim. Change* (109), 213–241, doi:10.1007/s10584-011-0156-z.

Miller, G. H., et al., 2012: Abrupt onset of the Little Ice Age triggered by volcanism and sustained by sea-ice/ocean feedbacks. *Geophys. Res. Let.* (39), doi:10.1029/2011GL050168.

Min, S.-K., X. Zhang, F. W. Zwiers, and G. C. Hegerl, 2011: Human contribution to more-intense precipitation extremes. *Nature* (470), 378–381, doi:10.1038/nature09763.

Mitchell, J. F. B., 1989: The Greenhouse-effect and Climate Change. *Rev. Geophys.* (27), 115–139, doi: 10.1029/RG027i001p00115.

Mitchell, J. F. B., C. A. Wilson, and W. M. Cunnington, 1987: On CO_2 climate sensitivity and model dependence of results. *Quarterly J. Royal Meteor. Soc.* (113), 293–322, doi:10.1256/smsqj.47516.

Mitchell, T. D. and P. D. Jones, 2005: An improved method of constructing a database of monthly climate observations and associated high-resolution grids. *International J. Climatology* (25), 693–712, doi: 10.1002/joc.1181.

Moss, R. H., et al., 2010: The next generation of scenarios for climate change research and assessment. *Nature* (463), 747–756, doi:10.1038/nature08823.

Muscheler, R., F. Joos, J. Beer, S. A. Mueller, M. Vonmoos, and I. Snowball, 2007: Solar activity during the last 1000 yr inferred from radionuclide records. *Quat. Sci. Rev.* (26), 82–97, doi:10.1016/j.quascirev.2006.07.012.

Myhre, G., et al., 2013: Radiative forcing of the direct aerosol effect from AeroCom Phase II simulations. *Atmos. Chem. Phys.* (13), 1853–1877, doi:10.5194/acp-13-1853-2013.

Neukom, R., et al., 2011: Multiproxy summer and winter surface air temperature field reconstructions for southern South America covering the past centuries. *Clim. Dyn.* (37), 35–51, doi:10.1007/s00382-010-0793-3.

O'Gorman, P. A., R. P. Allan, M. P. Byrne, and M. Previdi, 2012: Energetic Constraints on Precipitation Under Climate Change. *Surv. Geophys.* (33), 585–608, doi:10.1007/s10712-011-9159-6.

Oleson, K. W., et al., 2004: Tech. Rep. Technical description of the Community Land Model (CLM). Technical Report NCAR/TN-461+STR, National Center for Atmospheric Research, Boulder, CO.80307-3000, 174 pp.

Opsteegh, J., R. Haarsma, F. Selten, and A. Kattenberg, 1998: ECBILT: a dynamic alternative to mixed boundary conditions in ocean models. *Tellus, Ser. A* (50), 348–367, doi:10.1034/j.1600-0870.1998.t01-1-00007.x.

Otto-Bliesner, B., R. Tomas, E. Brady, C. Ammann, Z. Kothavala, and G. Clauzet, 2006: Climate sensitivity of moderate- and low-resolution versions of CCSM3 to preindustrial forcings. *J. Clim.* (19), 2567–2583, doi:10.1175/JCLI3754.1.

PAGES 2k network, 2013: Continental-scale temperature variability during the past two millennia. *Nature Geoscience* (6), 339–346.

Pauling, A., J. Luterbacher, C. Casty, and H. Wanner, 2006: Five hundred years of gridded high-resolution precipitation reconstructions over Europe and the connection to large-scale circulation. *Clim. Dyn.* (26), 387–405, doi:10.1007/s00382-005-0090-8.

Peters, G. P., G. Marland, C. Le Quere, T. Boden, J. G. Canadell, and M. R. Raupach, 2012: Rapid growth in CO2 emissions after the 2008-2009 global financial crisis. *Nature Climate Change* (2), 2–4.

Peterson, B. J., R. M. Holmes, J. W. McClelland, C. J. Vörösmarty, R. B. Lammers, A. I. Shiklomanov, I. A. Shiklomanov, and S. Rahmstorf, 2002: Increasing river discharge to the Arctic Ocean. *Science* (298), 2171–2173.

Petoukhov, V., A. Ganopolski, V. Brovkin, M. Claussen, A. Eliseev, C. Kubatzki, and S. Rahmstorf, 2000: CLIMBER-2: a climate system model of intermediate complexity. Part I: model description and performance for present climate. *Clim. Dyn.* (16), 1–17, doi:10.1007/PL00007919.

Pinto, J. G. and C. C. Raible, 2012: Past and recent changes in the North Atlantic Oscillation. *Wiley Interdisciplinary Reviews: Climate Change* (3), 79–90, doi:10.1002/wcc.150.

Pongratz, J., C. Reick, T. Raddatz, and M. Claussen, 2008: A reconstruction of global agricultural areas and land cover for the last millennium. *Global Biogeochem. Cyc.* (22), doi:10.1029/2007GB003153.

Portis, D., J. Walsh, M. El Hamly, and P. Lamb, 2001: Seasonality of the North Atlantic oscillation. *J. Clim.* (14), 2069–2078, doi:10.1175/1520-0442(2001)014<2069:SOTNAO>2.0.CO;2.

Pritchard, H. D., R. J. Arthern, D. G. Vaughan, and L. A. Edwards, 2009: Extensive dynamic thinning on the margins of the Greenland and Antarctic ice sheets. *Nature* (461), 971–975, doi:10.1038/nature08471.

Raible, C. C., et al., 2006: Climate variability-observations, reconstructions, and model simulations for the Atlantic-European and Alpine region from 1500-2100 AD. *Clim. Change* (79), 9–29, doi:10.1007/s10584-006-9061-2.

Ritz, S. P., T. F. Stocker, J. O. Grimalt, L. Menviel, and A. Timmermann, 2013: Estimated strength of the Atlantic overturning circulation during the last deglaciation. *Nature Geoscience*, doi:10.1038/NGEO1723, published online.

Ritz, S. P., T. F. Stocker, and F. Joos, 2011: A coupled dynamical ocean-energy balance atmosphere model for paleoclimate studies. *J. Clim.* (24), 349–375, doi:10.1175/2010JCLI3351.1.

Robock, A., 2000: Volcanic eruptions and climate. *Rev. Geophys.* (38), 191–219, doi:10.1029/1998RG000054.

Sarmiento, J. L. and N. Gruber, 2006: *Ocean Biogeochemical Dynamics*, Princeton University Press.

Sato, M., J. Hansen, M. McCormick, and J. Pollack, 1993: Stratospheric optical depth, 1850-1990. *J. Geophys. Res.* (98), 22 987–22 994, doi:10.1029/93JD02553.

Schilt, A., et al., 2010: Atmospheric nitrous oxide during the last 140,000 years. *Earth Planet. Sci. Lett.* (300), 33–43, doi:10.1016/j.epsl.2010.09.027.

Schmidt, G. A., R. A. Ruedy, R. L. Miller, and A. A. Lacis, 2010: Attribution of the present-day total greenhouse effect. *J. Geophys. Res.* (115), doi:10.1029/2010JD014287.

Schmidt, G. A., et al., 2011: Climate forcing reconstructions for use in PMIP simulations of the last millennium (v1.0). *Geoscientific Model Development* (4), 33–45, doi:10.5194/gmd-4-33-2011.

Schmidt, G. A., et al., 2012: Climate forcing reconstructions for use in PMIP simulations of the Last Millennium (v1.1). *Geoscientific Model Development* (5), 185–191, doi:10.5194/gmd-5-185-2012.

Serreze, M. C., et al., 2006: The large-scale freshwater cycle of the Arctic. *J. Geophys. Res.* (111), doi:10.1029/2005JC003424.

Shapiro, A. I., W. Schmutz, E. Rozanov, M. Schoell, M. Haberreiter, A. V. Shapiro, and S. Nyeki, 2011: A new approach to the long-term reconstruction of the solar irradiance leads to large historical solar forcing. *Astronomy & Astrophysics* (529), doi:10.1051/0004-6361/201016173.

Sherwood, S. C., R. Roca, T. M. Weckwerth, and N. G. Andronova, 2010: Tropospheric water vapor, convection, and climate. *Rev. Geophys.* (48), doi:10.1029/2009RG000301.

Sicre, M.-A., et al., 2008: Decadal variability of sea surface temperatures off North Iceland over the last 2000 years. *Earth Planet. Sci. Lett.* (268), 137–142, doi:10.1016/j.epsl.2008.01.011.

Smith, R. and P. Gent, 2004: *Reference Manual for the Parallel Ocean Program (POP). Ocean component of the Community Climate System Model (CCSM2.0 and 3.0).*, Los Alamos National Laboratory, Los Alamos, New Mexico, LAUR-02-2484., 75 pp.

Sokolov, A. and P. Stone, 1998: A flexible climate model for use in integrated assessments. *Clim. Dyn.* (14), 291–303, doi:10.1007/s003820050224.

Steinacher, M., et al., 2010: Projected 21st century decrease in marine productivity: a multi-model analysis. *Biogeosciences* (7), 979–1005.

Steinhilber, F., J. Beer, and C. Froehlich, 2009: Total solar irradiance during the Holocene. *Geophys. Res. Let.* (36), doi:10.1029/2009GL040142.

Stenchikov, G., T. L. Delworth, V. Ramaswamy, R. J. Stouffer, A. Wittenberg, and F. Zeng, 2009: Volcanic signals in oceans. *J. Geophys. Res.* (114), doi:10.1029/2008JD011673.

Stenchikov, G., I. Kirchner, A. Robock, H. Graf, J. Antuna, R. Grainger, A. Lambert, and L. Thomason, 1998: Radiative forcing from the 1991 Mount Pinatubo volcanic eruption. *J. Geophys. Res.* (103), 13 837–13 857, doi:10.1029/98JD00693.

Stocker, T. and C. Raible, 2005: Climate change - Water cycle shifts gear. *Nature* (434), 830–833, doi:10.1038/434830a.

Stocker, T. F., 1998: The seesaw effect. *Science* (282), 61–62.

Stocker, T. F., 2011: in Advances in Geophysical and Environmental Mechanics and Mathematics, Springer Verlag, 179 pp.

Stocker, T. F., D. G. Wright, and L. A. Mysak, 1992: A zonally averaged, coupled ocean-atmosphere model for paleoclimate studies. *J. Clim.* (5), 773–797.

Swingedouw, D., L. Terray, C. Cassou, A. Voldoire, and J. Salas-Mélia, D. Servonnat, 2011: Natural forcing of climate during the last millennium: fingerprint of solar variability. *Clim. Dyn.* (36), 1349–1364, doi:10.1007/s00382-010-0803-5.

Syed, T. H., J. S. Famiglietti, D. P. Chambers, J. K. Willis, and K. Hilburn, 2010: Satellite-based global-ocean mass balance estimates of interannual variability and emerging trends in continental freshwater discharge. *Proc. Natl. Acad. Sci.* (107), 17 916–17 921, doi:10.1073/pnas.1003292107.

Talley, L. D., 2008: Freshwater transport estimates and the global overturning circulation: Shallow, deep and throughflow components. *Prog. Oceanogr.* (78), 257–303, doi:10.1016/j.pocean.2008.05.001.

Tao, W.-K., J.-P. Chen, Z. Li, C. Wang, and C. Zhang, 2012: Impact of aerosols on cenvective clouds and precipitation. *Rev. Geophys.* (50), doi:10.1029/2011RG000369.

Taylor, K. E., R. J. Stouffer, and G. A. Meehl, 2012: An overview of CMIP5 and the experiment design. *Bull. Am. Meteorol. Soc.* (93), 485–498, doi:10.1175/BAMS-D-11-00094.1.

Thompson, A. M., et al., 2004: Halocarbons and other atmospheric trace species. *Climate Monitoring and Diagnostics Laboratory, Summary Report No. 27*, NOAA CMDL, Boulder, CO, 115–135.

Timmermann, R., S. Danilov, J. Schroeter, C. Boening, D. Sidorenko, and K. Rollenhagen, 2009: Ocean circulation and sea ice distribution in a finite element global sea ice-ocean model. *Ocean Modelling* (27), 114–129, doi:10.1016/j.ocemod.2008.10.009.

Trenberth, K. and J. Caron, 2001: Estimates of meridional atmosphere and ocean heat transports. *J. Clim.* (14), 3433–3443, doi:10.1175/1520-0442(2001)014<3433:EOMAAO>2.0.CO;2.

Trenberth, K. and D. Paolino, 1980: The Northern Hemisphere sea-level pressure data set - trends, errors and discintinuities. *Mon. Weather Rev.* (108), 855–872, doi:10.1175/1520-0493(1980)108<0855:TNHSLP>2.0.CO;2.

Trenberth, K. E., J. T. Fasullo, and J. Kiehl, 2009: Earth's global energy budget. *Bull. Am. Meteorol. Soc.* (90), 311–323, doi:10.1175/2008BAMS2634.1.

Trenberth, K. E., L. Smith, T. Qian, A. Dai, and J. Fasullo, 2007: Estimates of the global water budget and its annual cycle using observational and model data. *J. Hydrometeorology* (8), 758–769, doi:10.1175/JHM600.1.

Trouet, V., J. Esper, N. E. Graham, A. Baker, J. D. Scourse, and D. C. Frank, 2009: Persistent positive North Atlantic Oscillation mode dominated the Medieval Climate Anomaly. *Science* (324), 78–80, doi:10.1126/science.1166349.

Uppala, S., et al., 2005: The ERA-40 re-analysis. *Quarterly J. Royal Meteor. Soc.* (131), 2961–3012, doi: 10.1256/qj.04.176.

van Vuuren, D. P., et al., 2012: A proposal for a new scenario framework to support research and assessment in different climate research communities. *Global Environmental Change* (22), 21–35, doi: 10.1016/j.gloenvcha.2011.08.002.

Varma, V., et al., 2012: Holocene evolution of the Southern Hemisphere westerly winds in transient simulations with global climate models. *Clim. Past* (8), 391–402, doi:10.5194/cp-8-391-2012.

Vieira, L. E. A. and S. K. Solanki, 2010: Evolution of the solar magnetic flux on time scales of years to millenia. *Astronomy & Astrophysics* (509), doi:10.1051/0004-6361/200913276.

von Gunten, L., W. J. D'Andrea, R. S. Bradley, and Y. Huang, 2012: Proxy-to-proxy calibration: Increasing the temporal resolution of quantitative climate reconstructions. *Scientific Reports* (2), doi: 10.1038/srep00609.

Wanner, H., S. Brönnimann, C. Casty, D. Gyalistras, J. Luterbacher, C. Schmutz, S. D. B., and E. Xoplaki, 2001: North Atlantic Oscillation - concepts and studies. *Surveys in Geophysics* (22), 321–382.

Wanner, H., et al., 2008: Mid- to Late Holocene climate change: An overview. *Quat. Sci. Rev.* (27), 1791–1828, doi:10.1016/j.quascirev.2008.06.013.

White, D., et al., 2007: The Arctic freshwater system: Changes and impacts. *J. Geophys. Res.* (112), G04S54.

Wijffels, S. E., R. W. Schmitt, H. L. Bryden, and A. Stigebrandt, 1992: Transport of Freshwater by the Oceans. *J. Phys. Oceanogr.* (22), 155–162, doi:10.1175/1520-0485(1992)022<0155:TOFBTO>2.0.CO;2.

Wild, M., D. Folini, C. Schär, N. Loeb, E. Dutton, and G. König-Langlo, 2012: The global energy balance from a surface perspective. *Clim. Dyn.*, doi:10.1007/s00382-012-1569-8.

Woodruff, S. D., et al., 2011: ICOADS Release 2.5: extensions and enhancements to the surface marine meteorological archive. *International J. Climatology* (31), 951–967, doi:10.1002/joc.2103.

Yeager, S. G., C. A. Shields, W. G. Large, and J. J. Hack, 2006: The low-resolution CCSM3. *J. Clim.* (19), 2545–2566.

Yoshimori, M., C. C. Raible, T. F. Stocker, and M. Renold, 2010: Simulated decadal oscillations of the Atlantic meridional overturning circulation in a cold climate state. *Clim. Dyn.* (34), 101–121, doi:10.1007/s00382-009-0540-9.

Zhong, Y., G. H. Miller, B. L. Otto-Bliesner, M. M. Holland, D. A. Bailey, D. P. Schneider, and A. Geirsdottir, 2011: Centennial-scale climate change from decadally-paced explosive volcanism: A coupled sea ice-ocean mechanism. *Clim. Dyn.* (37), 2373–2387, doi:10.1007/s00382-010-0967-z.

Zhu, J., G.-Q. Zhou, R.-H. Zhang, and Z. Sun, 2013: Improving ENSO prediction in a hybrid coupled model with an embedded entrainment temperature parameterisation. *International J. Climatology* (33), 343–355, doi:10.1002/joc.3426.

Zorita, E. and F. González-Rouco, 2002: Are temperature-sensitive proxies adequate for North Atlantic Oscillation reconstructions? *Geophys. Res. Let.* (29), doi:10.1029/2002GL015404.

Zorita, E., F. Gonzalez-Rouco, and S. Legutke, 2003: Testing the Mann et al. (1998) approach to paleoclimate reconstructions in the context of a 1000-yr control simulation with the ECHO-G coupled climate model. *J. Clim.* (16), 1378–1390, doi:10.1175/1520-0442(2003)16<1378:TTMEAA>2.0.CO;2.

Chapter 2

The freshwater balance of polar regions in transient simulations from 1500 to 2100 AD using a comprehensive coupled climate model

Flavio Lehner, Christoph C. Raible, Dominik Hofer, and Thomas F. Stocker

The freshwater balance of polar regions in transient simulations from 1500 to 2100 AD using a comprehensive coupled climate model

**Flavio Lehner · Christoph C. Raible ·
Dominik Hofer · Thomas F. Stocker**

Abstract   The ocean and sea ice in both polar regions are important reservoirs of freshwater within the climate system. While the response of these reservoirs to future climate change has been studied intensively, the sensitivity of the polar freshwater balance to natural forcing variations during preindustrial times has received less attention. Using an ensemble of transient simulations from 1500 to 2100 AD we put present-day and future states of the polar freshwater balance in the context of low frequency variability of the past five centuries. This is done by focusing on different multi-decadal periods of characteristic external forcing. In the Arctic, freshwater is shifted from the ocean to sea ice during the Maunder Minimum while the total amount of freshwater within the Arctic domain remains unchanged. In contrast, the subsequent Dalton Minimum does not leave an imprint on the slow-reacting reservoirs of the ocean and sea ice, but triggers a drop in the import of freshwater through the atmosphere. During the twentieth and twenty-first century the build-up of freshwater in the Arctic Ocean leads to a strengthening of the liquid export. The Arctic freshwater balance is shifted towards being a large source of freshwater to the North Atlantic ocean. The Antarctic freshwater cycle, on the other hand, appears to be insensitive to preindustrial variations in external forcing. In line with the rising temperature during the industrial era the freshwater budget becomes increasingly unbalanced and strengthens the high latitude's Southern Ocean as a source of liquid freshwater to lower latitude oceans.

1 Introduction

The hydrological cycle is of crucial importance for the climate system in terms of energy, moisture, and nutrient distribution (Allen and Ingram 2002). Socio-economic impacts of climate and climate change are often closely linked to the corresponding regional characteristics of the hydrological cycle (floods, droughts; IPCC 2007). Along with a broad consensus on the recent and projected future anthropogenic global warming, an intensification of the hydrological cycle is expected based on the Clausius-Clapeyron relation which suggests specific humidity to increase exponentially with temperature (approximately 7% K^{-1}; IPCC 2007). In fact, widespread evidence for such an intensification is already available from twentieth century observations, as summarized, e.g., in Huntington (2005), White et al. (2007), and Syed et al. (2010).

Additionally, numerous model studies are able to reproduce the intensification of the hydrological cycle in the second half of the twentieth century and project it to continue in the twenty-first century (Wu et al. 2005; Held and Soden 2006; IPCC 2007; Williams et al. 2007; Khon et al. 2010; Seager et al. 2010). Wu et al. (2005) found the freshwater forcing to the ocean surface to change in a non-uniform way across latitudes. While high latitudes tend to receive more freshwater, the sub-tropics will receive less. However, as the rate of change of the freshwater forcing in the northern high latitudes is larger than in the southern high latitudes the question about a possible global redistribution of major water masses in the hydrological cycle and specifically in the ocean arises (Stocker and Raible 2005; Peterson et al. 2006).

F. Lehner (✉) · C. C. Raible · D. Hofer · T. F. Stocker
Climate and Environmental Physics, Physics Institute,
and Oeschger Centre for Climate Change Research,
University of Bern, Sidlerstrasse 5, 3012 Bern, Switzerland
e-mail: lehner@climate.unibe.ch

One example of major water masses are the large quantities of freshwater stored in liquid and solid form in both polar regions. This freshwater, once released, can alter the hydrography and circulation in ocean basins (Peterson et al. 2002). The cycling of freshwater within polar regions, as well as the exchange with sub-polar latitudes, is driven by an interplay of oceanic and atmospheric quantities and processes, of which many are known to respond to interannual to decadal variations in temperature, e.g., atmospheric moisture content, atmospheric circulation, sea ice extent, volume, and transport. Such variations in temperature can be caused by anthropogenic greenhouse gases (GHGs) or natural forcing, such as volcanic eruptions or changes of the solar irradiance.

The purpose of this study is to put results from climate model simulations of present-day and future polar climate in the context of multi-decadal variability of the past five centuries. We focus on the freshwater cycling within the polar regions as well as the meridional exchange with lower latitudes. The study complements earlier work which address the hydrological cycle in polar regions with a focus on the industrial era and on the Arctic Ocean alone (Holland et al. 2006b; Koenigk et al. 2007; Arzel et al. 2008).

To investigate the freshwater cycle in the polar regions at different climate states, and to estimate its sensitivity to natural and anthropogenic forcing, we analyze simulations with a coupled General Circulation Model (GCM), applying transient external forcing from 1500 to 2100 AD.

This paper is structured as follows: a description of the model and experimental setup as well as a short validation of the simulations are presented in Sect. 2 In Sects. 3 and 4 we examine the simulated freshwater budgets of both polar regions, subdivided in (1) present-day state, (2) changes in the preindustrial era, and (3) future projections. A summary and conclusions follow in Sect. 5.

2 Model and methods

2.1 Model

The model used for the simulations is the Community Climate System Model version 3.0.1 (CCSM3), which was developed by the National Center for Atmospheric Research (NCAR) (Collins et al. 2006). The model includes four components, namely the atmosphere, ocean, sea ice, and land surface, all linked through a coupler which exchanges fluxes (without flux corrections) and state information. We selected the low-resolution version: 3.75° by 3.75° in the atmosphere (26 vertical levels) and on land and a sea ice and ocean resolution of about 3.6° in longitude and 0.6° to 2.8° in latitude with finer resolution in the tropics and around Greenland, allowing for an open

passage through the Canadian Arctic Archipelago. The ocean has 25 levels and a rigid lid. The land model does not include a dynamic ice sheet model but is able to lose and grow snow and ice up to $1,000$ kg m^{-2}. Additional mass above this threshold is inserted into runoff. We discuss the implications of a missing ice sheet model for our study in Sect. 5.

More detailed descriptions of the model components are available at the NCAR CCSM webpage (http://www.cesm. ucar.edu/models/ccsm3.0). The version used here and its simulation of present-day climate is comprehensively described in Yeager et al. (2006).

2.2 Experimental setup

For this and other studies (Yoshimori et al. 2010; Hofer et al. 2011) a series of model simulations was conducted. In this paper we use the following two setups: a 1500 AD equilibrium simulation with perpetual 1500 AD conditions (hereafter CTRL1500) and an ensemble of four transient simulations from 1500 to 2100 AD (TRa1 to TRa4, as in Hofer et al. 2011).

The transient simulations were branched from different years of the multi-century control simulation CTRL1500. The CTRL1500 simulation itself was initialized from a control simulation with perpetual 1990 AD conditions, an extension of the simulation presented by Yeager et al. (2006). As the CTRL1500 simulation has not fully reached an equilibrium state it exhibits a slight drift. Therefore, all transient simulations branched from the CTRL1500 inherit this drift as well and need to be corrected for it by detrending them with a quadratic fit estimated from CTRL1500 for every quantity, grid point, and month. For most quantities the trends are in the order of $0.01-0.02\%$ year^{-1}. The time-varying forcing consists of GHG concentrations, solar forcing, and volcanic aerosols and is summarized in Fig. 1. For details on the detrending technique and on the forcing datasets the reader is referred to Hofer et al. (2011).

Our analysis focuses on six 31-year periods with different forcing levels: the quasi-equilibrium period just after branching from CTRL1500 which corresponds approximately to the beginning of the Little Ice Age (Mann et al. 2009), when the solar forcing generally is lower than today (averaged over 1500–1530 AD, hereafter Initial Conditions); the period of the pronounced solar forcing minimum of the Maunder Minimum (1685-1715 AD); the Dalton Minimum (1800-1830 AD), when a solar forcing minimum coincides with two large eruptions of tropical volcanoes; a period when GHGs start to increase (1840-1870 AD, Pre-industrial); a period of present-day climate (1960-1990 AD, Present-Day) and finally, a period at the end of the twenty-first century when the average radiative forcing is projected to be approximately 5 W m^{-2} larger than 1990
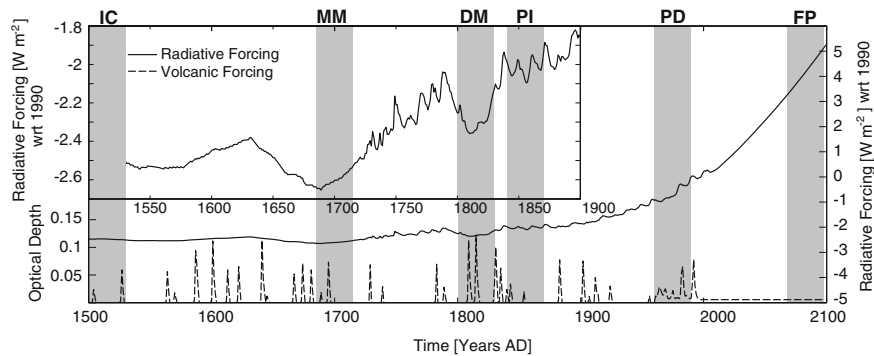
Fig. 1 Natural and anthropogenic forcing used in the simulations: the combined radiative forcing from GHGs and solar irradiance in W m^{-2}, calculated as in IPCC (2001) with reference to (wrt) 1990 (*solid line*), assuming a global average albedo of 0.3, and the volcanic forcing as optical depth (*dashed*). The inset highlights the changes in forcing by stretching the *vertical scale*, however, the *curve* is the same as in the main plot. Further details on the forcing dataset can be found in Hofer et al. (2011). The time periods as used throughout the study are indicated by the *vertical bars* and labeled at the *top*: Initial Conditions (IC, 1500–1530 AD), Maunder Minimum (MM, 1685–1715 AD), Dalton Minimum (DM, 1800–1830 AD), Preindustrial (PI, 1840–1870 AD), Present-Day (PD, 1960–1990 AD), and Future Projections (FP, 2068–2098 AD)

AD (2068-2098 AD, Future Projections). For the twenty-first century we apply the IPCC SRES A2 scenario (IPCC SRES 2000).

2.3 Methods

Freshwater budgets and transports are computed from the monthly means of the four ensemble members, however, in figures and tables we show annual means. The spatial domains are 60−90°N (as in ACIA (2005)) and 60−90°S. This selection enables us to compare equivalent areas at both polar regions and to include all major processes influencing the polar freshwater balance. To compute the freshwater balance we need to consider the atmospheric import of water, i.e., meridional water transport VQ (including eddy-induced transport), precipitation P, and evaporation E over land ($_{lnd}$), ocean ($_{ocn}$), and sea ice ($_{ice}$). Water imported into the domain over land by rivers that cross the 60°N boundary from the south as well as the discharge into the oceans (called R) is calculated by the river transport model. This is a 2-dimensional model on an independent 0.5° by 0.5° grid. The land model also allows for a limited storage of water and ice in grid cells defined as wetland and glaciers, thus changes in soil moisture, glacier mass, and permafrost are crudely represented in the model. The sea ice and ocean budget terms include the storage and transport of freshwater. The ocean liquid freshwater (FW) storage is computed as

$$FW(S) = \int \int\limits_{z_{max}}^{z_1} \frac{S_0 - S}{S_0} \, dz \, dA, \qquad (1)$$

with S being the in-situ salinity and S_0 a reference salinity. z covers all model levels while A represents the ocean

domain's area. The ocean freshwater transport across a transect is

$$FWT(u,S) = \int\limits_{l_1}^{l_2} \int\limits_{z_{max}}^{z_1} u \, \frac{(S_0 - S)}{S_0} \, dz \, dl, \qquad (2)$$

where u is the horizontal velocity perpendicular to the transect and l_1 and l_2 are the start and end point of the transect, defining its length.

In Eqs. (1) and (2) S_0 is estimated from the CTRL1500 so that the complete freshwater budget for the Arctic domain is closed in its initial state under perpetual 1500 AD conditions. This means that total net import of freshwater into the Arctic domain is nearly zero at year 1500 AD. This leads to a S_0 of 34.88 g kg^{-1} for the Arctic domain. In the Antarctic domain, however, using monthly instead of instantaneous values to calculate the FW transport introduces significant errors as the meridional velocity field shows strong variations on sub-monthly time scales. To overcome this problem we use a different approach to estimate the FW transport for the Antarctic domain, i.e., the residual from changes in FW storage (with $S_0 = 34.88$ g kg^{-1}) and all ocean surface freshwater fluxes:

$$FWT(t) = FW(t+1) - FW(t) - \frac{P_{ocn}(t) + P_{ocn}(t+1)}{2}$$
$$- \frac{E_{ocn}(t) + E_{ocn}(t+1)}{2} + \frac{R(t) + R(t+1)}{2}$$
$$+ \frac{M(t) + M(t+1)}{2} \qquad (3)$$

where M is the melt flux from sea ice and t indexing the monthly time-stepping. A comprehensive description of the significance of the reference salinity can be found in Serreze et al. (2006), and with respect to rigid lid ocean

model components in Pardaens et al. (2003). For the sea ice storage and transport, where the error from using monthly means is negligible, the salinity is set to 4 g kg^{-1} in the model. Finally, freshwater exchange rates between sea ice and ocean are calculated, whereby precipitation that directly runs off the sea ice into the ocean is included in the flux from the sea ice to the ocean.

2.4 Validation

The CCSM3 has been thoroughly tested for various resolutions (Hack et al. 2005; Yeager et al. 2006; Kiehl et al. 2006; Bryan et al. 2006; Holland et al. 2006a, b). Generally, the low-resolution version differs more strongly from observations than the middle or high-resolution version. This is largely due to the fact that the middle and high-resolution versions both run with the higher resolved 1° ocean/sea ice component. This has implications for properties such as salinity, heat flux, sea ice extent and volume as will be discussed here.

The simulated annual mean surface air temperature (SAT) evolution on the Northern Hemisphere (NH) over the past five centuries is in good agreement with reconstructions, except for an overestimation of the twentieth century warming due to the absence of sulfate aerosols in the simulations (Hofer et al. 2011). The twenty-first century is dominated by the rapid increase in GHGs (as prescribed by the IPCC SRES A2 scenario), which results in an ensemble mean NH warming of 2.9°C, calculated as the difference between the averages over the periods 1990-2000 AD and 2088-2098. The equilibrium climate sensitivity of the low-resolution version is 2.32°C (Kiehl et al. 2006) and is therefore at the lower end of the range of likely climate sensitivities (2−4.5°C, IPCC (2007)). The Arctic domain's SAT anomaly (60−90°N) follows the SAT of the NH including a cooling during the Maunder Minimum and Dalton Minimum (Fig. 2). However, due to the effect of polar amplification (Holland and Bitz 2003; Masson-Delmotte et al. 2006; Bekryaev et al. 2010) the amplitudes are generally about 100% larger than in the hemispheric average. In the Antarctic domain (60−90°S) on the other hand, no robust signal of the Little Ice Age is detectable (Fig. 2). During the twentieth century, simulations show a smaller trend of Antarctic's domain temperature and variability compared with reanalysis data. Due to the absence of time-variable ozone in the simulations the temperature over Antarctica also does not show the observed late-twentieth century dipole temperature anomaly pattern (as in Thompson and Solomon 2002, not shown). The simulated twenty-first century warming remains below the warming simulated in the Arctic domain due to the comparably weaker sea ice-albedo feedback (Masson-Delmotte et al. 2006; Walsh 2009) and larger
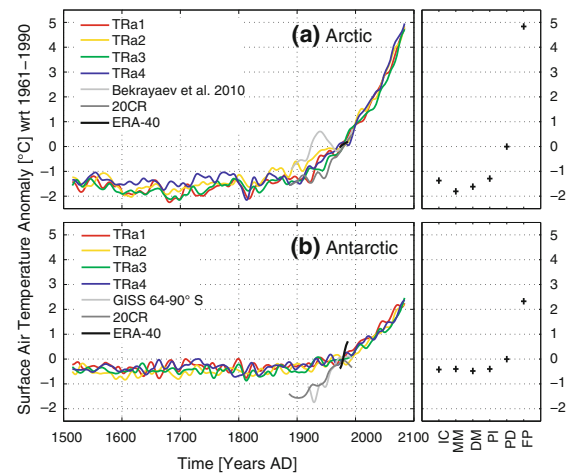

Fig. 2 a Arctic and **b** Antarctic domain's surface air temperature anomaly with reference to (wrt) 1961–1990 AD. The small panels on the *right* show mean anomalies for the different time periods Initial Conditions (IC, 1500–1530 AD), Maunder Minimum (MM, 1685–1715 AD), Dalton Minimum (DM, 1800–1830 AD), Preindustrial (PI, 1840–1870 AD), Present-Day (PD, 1960–1990 AD), and Future Projections (FP, 2068–2098 AD). The time series are smoothed by a 30-year Gaussian-weighted filter. Bekryaev et al. (2010) updated the GISS dataset (Hansen et al. 2010) in the Arctic region. 20CR is Compo et al. (2010). ERA-40 data is available from ECMWF in 2.5° × 2.5° resolution

ocean heat uptake. The simulated Arctic domain's ensemble mean during 1980–2000 AD is too cold with a bias of 3.5–7.3 K, depending on the reanalysis, while the Antarctic domain is too cold by 1.5–4.1 K. Note that this is within a 10% range of the documented general cold bias of the model (Yeager et al. 2006).

The simulated polar oceans are generally too fresh compared to the salinity field of the Polar Science Center Hydrographic Climatology (PHC, Steele et al. 2001; Fig. 3). In the Arctic Ocean the model is able to reproduce the fresh shelf conditions arising from the shallow water and the river runoff into those, although the detailed spatial pattern is not captured very well. Further, the Beaufort Gyre is larger and stores more freshwater than is estimated from observations (Fig. 4b, compare with Fig. 3 in Serreze et al. 2006). In the Barents Sea, Greenland-Iceland-Norwegian (GIN) Seas, Labrador Sea, Baffin Bay and off the south-eastern coast of Greenland, the model tends to be too fresh. The salinity biases in the Barents Sea are mainly caused by an underestimation of the meridional transport of warm and salty Atlantic waters into the Barents Sea and the Arctic Ocean (Yeager et al. 2006). Along with this the sea ice extends further to the south (especially in the Barents Sea, Fig. 3), which results in a spatial anomalous melt flux. Additionally, the simulated sea ice covers larger areas, suppressing evaporation from the ocean surface and therefore further freshening the ocean.

Fig. 3 Sea surface salinity in the **a**, **b** Arctic and **c**, **d** Antarctic domain, from the **b**, **d** Polar Science Center Hydrographic Climatology (PHC, Steele et al. 2001) and **a**, **c** model output averaged from 1990 to 1999 AD (*left*). Note the different *color scales* for the Arctic and Antarctic plots. The minimum value of 3.5 g kg^{-1} in the Arctic color scale occurs in the Baltic Sea observations. Contours are 15 and 90% sea ice concentration of March (Arctic) and September (Antarctic) from HadISST1 (Rayner et al. 2003) and the 1990–1999 AD model average. The model land mask is given in *white*
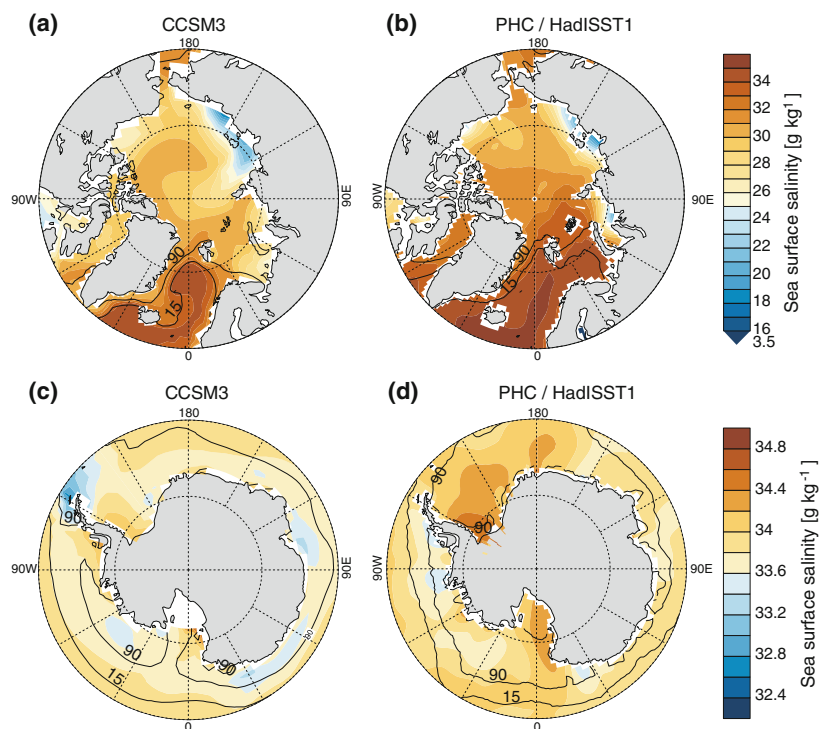
In the Antarctic region the model generally tends to be too fresh as well (Fig. 3). Still, it is able to simulate the more saline areas of the Weddell Sea and Ross Sea but it underestimates the amplitude and spatial extent. Furthermore, the model produces a patch of relatively fresh water at the northern end of the Antarctic Peninsula which is not observed in reality. The pattern of the sea ice concentration around Antarctica generally agrees with observations, while the total sea ice extent and area are overestimated by about 23 and 22%, respectively, during 1990–1999 AD (not shown). Regionally, the sea ice is overestimated in the Atlantic sector and underestimated in the Ross Sea sector.

In recent years efforts in data collection resulted in new estimates of the large-scale Arctic freshwater cycle (Serreze et al. 2006) which is compared to the ensemble mean of this study (Table 1). The numbers from a multi-model study by Holland et al. (2007) are listed for additional comparison. The simulated freshwater budget of the Arctic Ocean is in reasonably good agreement with observations regarding the oceanic and terrestrial freshwater fluxes (*FW* transport, sea ice transport, *R*) while the atmospheric fluxes *P* and *E* are underestimated by about 30 and 50%, respectively. However, a recent study reveals large uncertainties regarding absolute values still inherent in observations of $P-E$ in the Arctic (Rawlins et al. 2010). The ocean imbalance of our simulations (194 ± 331 km^3 year^{-1}) is indistinguishable from zero relative to the standard deviation and in this respect

qualitatively agrees with observations, where the imbalance is indistinguishable from zero relative to measurement errors (Serreze et al. 2006). The freshwater reservoir of the ocean is substantially overestimated due to an Arctic Ocean that is too fresh throughout the column with a larger bias in the top 400 m (Fig. 4a). This stands in contrast to the negative freshwater reservoir obtained from the high-resolution CCSM3 of the model set analyzed by Holland et al. (2007). The storage in sea ice is too large as well, a consequence of the too cold Arctic in the low-resolution version. However, the spread among models regarding these two reservoirs is known to be large (Holland et al. 2007). Confidence in the simulated Arctic hydrological cycle arises from the relatively small bias in the transport terms and in the overall balanced budget in the present-day state. For reasons of data lack we refrain from a validation of the Antarctic domain's freshwater budget.

3 Freshwater balance of the Arctic domain

3.1 Present-day climate

The simulated freshwater cycle of the Arctic domain is illustrated in Fig. 5, where the ensemble means for the time periods Initial Conditions, Maunder Minimum, Present-Day and Future Projections are presented. The standard
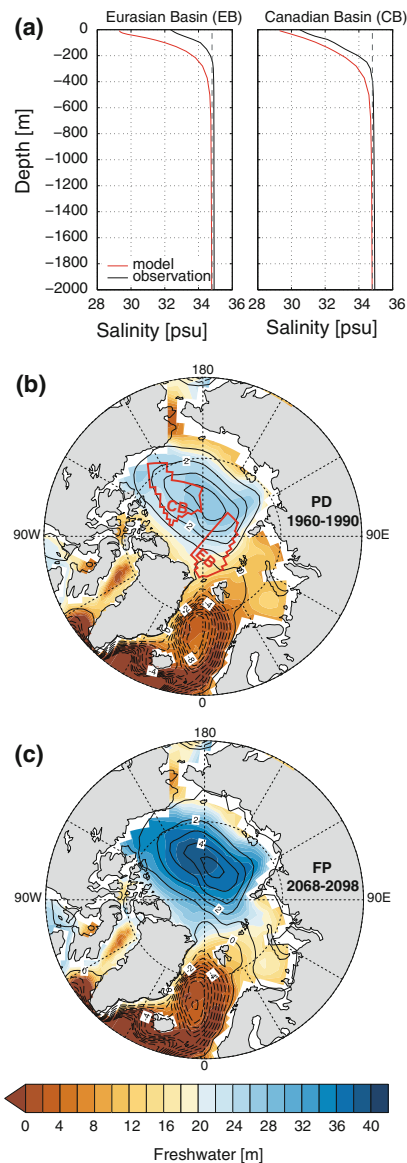
Fig. 4 Salinity profiles, freshwater storage, and barotropic stream function in the Arctic domain. **a** Salinity profiles from the Eurasian (EB) and the Canadian Basin (CB), where the ocean is deeper than 2,000 m from the model (1990–1999 AD ensemble mean) and observations (PHC, Steele et al. 2001). The vertical dashed line marks the reference salinity of 34.8 g kg^{-1} used by Serreze et al. (2006), Holland et al. (2007), and here in **b** and **c**, as well as in Table 1. The basins are indicated in **b** with EB ad CB. **b**, **c** *FW* storage and barotropic stream function for **b** Present-Day (PD, 1960–1990 AD) and **c** Future Projections (FP, 2068–2098 AD). The model land mask is given in *white*

deviation (±) for a specific budget term and time period is estimated from the 124 annual means of the four ensemble members (4 × 31 years). The difference in mean from

Initial Conditions, the Maunder Minimum and Future Projections to Present-Day is tested for significance for each ensemble member, using a Mann-Whitney rank sum test at the 5% level. A pie chart illustrates the number of ensemble members that show a significant difference between Present-Day and the other time periods (Figs. 5 and 6). This serves as a simple metric for the robustness of a given signal. The same procedure is then used to illustrate changes during the preindustrial era (Table 2). Additionally, time series and running 50-year linear trends of selected budget quantities are presented.

The simulated present-day freshwater cycle of the Arctic domain correctly reflects observations in a qualitative manner. *VQ* accounts for approximately 91% of the domains's net freshwater import. In agreement with Sorteberg and Walsh (2008) the majority of this import takes place over the Bering Sea and the Eastern North Atlantic/European sector (Fig. 7). The equivalent of less than 3% of this imported freshwater is temporarily stored in the atmosphere as water vapor *Q*. While land and ocean each cover about 50% of the total domain area, the atmospheric freshwater is preferentially delivered to the land surface where approximately 55% of total *P* and 65% of total *P–E* end up. For the ocean the largest net source by far is *R* (82%), as *P–E*, as well as the freshwater exchange between sea ice and ocean, are each nearly in balance on basis of the annual means. Note that, when focusing on the Arctic Ocean only, this distribution is somewhat different: $P_{ocn}-E_{ocn}$ is positive and the sea ice balance negative (not shown, but in agreement with Serreze et al. (2006)).

We mentioned the overestimated freshwater storage in the ocean and sea ice. The domain's freshwater budget is balanced in part by export of sea ice and ocean freshwater. Thereby, the Labrador and Irminger Sea, and to a smaller extent the western Bering Sea, are the major areas of export for both sea ice and ocean freshwater (Fig. 7). The eastern part of the Bering Sea including the Bering Strait imports about as much ocean freshwater as is exported through the Irminger Sea, thereby providing the second largest source of freshwater to the Arctic domain. Finally, rivers crossing 60°N (e.g., Ob, Yenisey, Lena, see Fig. 7) close the land budget.

3.2 Preindustrial changes

The present-day freshwater budget differs significantly from those during the two preindustrial time periods (Initial Conditions and Maunder Minimum) when NH as well as Arctic temperatures were lower than during Present-Day (see Fig. 2). *VQ* and *Q* are significantly smaller during Initial Conditions and the Maunder Minimum, resulting in a decrease of P_{lnd}, P_{ocn} and P_{ice}, i.e., total *P* over the domain. As a consequence of the reduction in P_{lnd}, *R* is

Table 1 Ensemble mean freshwater budget of the Arctic Ocean

Study	Serreze et al. (2006)	Holland et al. (2007)	This study
Averaging period	∼1980–2000 AD	1980–1999 AD	1980–2000 AD
Precipitation	3,300 ± 680	2,411 ± 360	2,265 ± 109
Evaporation	−1,300 ± 710	−868 ± 275	−687 ± 32
Runoff	3,200 ± 110	3,162 ± 776	3,482 ± 187
Ocean transp. liquid	−3,450 ± 693		−2,899 ± 569
– without CAA	*−250 ± 615*	*−1,388 ± 2,332*	*−395 ± 579*
Ocean transp. solid	−2,460 ± 340		−1,967 ± 421
– without CAA	*−2,300 ± 340*	*−1,841 ± 626*	*−1,967 ± 421*
Imbalance ocean	−710 ± 1,255		194 ± 331
Storage ocean	24,200	47,756	177,930 ± 1,652
Sea ice storage	10,000	13,851	29,347 ± 2,557

Fluxes in km^3 year^{-1}, stores in km^3, as calculated in Holland et al. (2007) and with the same reference salinity of 34.8 g kg^{-1}. Fluxes leaving the Arctic Ocean are negative. ± Corresponds to the measurement error and to the measurement error propagation in case of the ocean imbalance for Serreze et al. (2006); to the inter-model standard deviation for Holland et al. (2007); and to the standard deviation of the four ensemble members for this study. Holland et al. (2007) provide no numbers for the transport through the Canadian Arctic Archipelago (CAA) because most models investigated did not have an open passage through the CAA

Fig. 5 Freshwater budget of 60−90°N. Values are ensemble mean 31-year averages according to the *color shading* in the upper *left corner*: Initial Conditions (IC), Maunder Minimum (MM), Present-Day (PD), and Future Projections (FP). Further details in the text
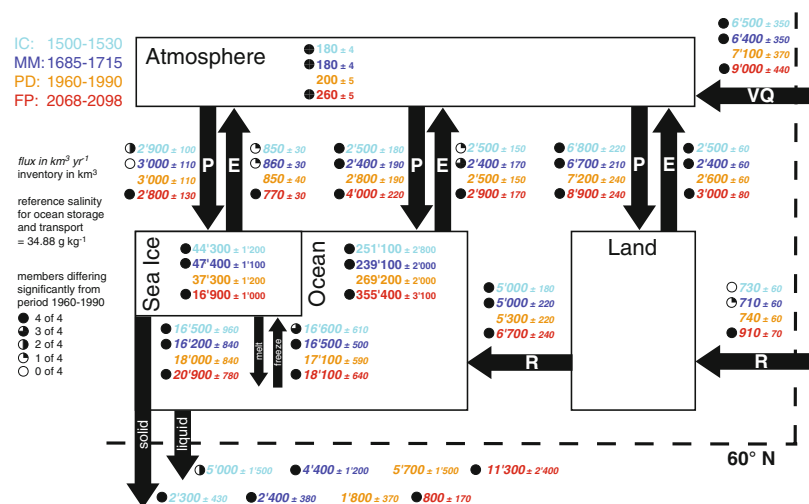
reduced as well. Changes in *E* during Initial Conditions and the Maunder Minimum are robust only over land where E_{lnd} is significantly decreased. The sea ice volume is significantly larger in Initial Conditions and the Maunder Minimum than during Present-Day, resembling the colder conditions of the preindustrial era.

The sea ice volume maximum is reached during the Maunder Minimum when the annual sea ice growth exceeds the melt rate by approximately 300 km^3 year^{-1}. Not surprisingly, the sea ice export reaches a maximum as well during that time. The ocean liquid freshwater export (*FW* transport), on the other hand, is significantly reduced during Initial Conditions and the Maunder Minimum. However, the ocean as a whole is saltier, i.e., stores less freshwater than

during Present-Day. This is largely because during the Maunder Minimum sea ice grows, resulting in a negative freshwater flux to the ocean surface. In other words, brine rejection from the sea ice growth makes the ocean saltier and overcompensates for the reduced *FW* transport. In fact, the sum of all fluxes to and from the ocean (through the surface and ocean-internal) during the Maunder Minimum is less than half of that during Present-Day (300 vs. 800 km^3 year^{-1}). Due to large internal variability, however, this difference is significant only in two ensemble members.

The detection of significant and robust changes within the preindustrial era (Initial Conditions-Preindustrial, 1500–1870 AD) proves to be difficult as the interannual variability of several budget terms is high; although in
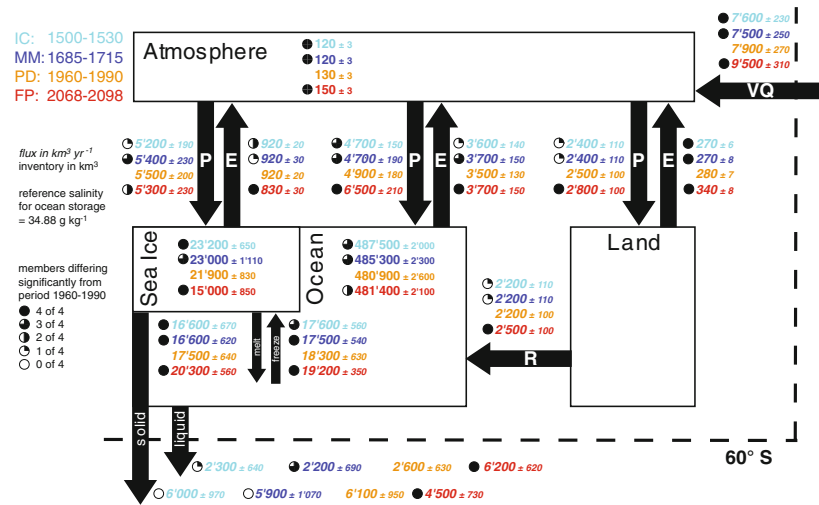
Fig. 6 As Fig. 5, but for 60−90°S

Table 2 Domain freshwater storage and transport terms at the boundary

Domain	Budget term	MM−IC	DM−IC	DM−MM	PI−IC	PI−MM	PI−DM
60-90° N	*FW* storage (ocean storage)	● *	●	◖	◔	◖	◗
	Sea ice storage	◗	◑	◔	●	◔	◐
	Q (atmosphere storage)	◔	◔	◔	●	●	◗
	FW transport (ocean export)	◔	○	◔	○	◔	○
	Sea ice export	◑	○	○	○	◐	○
	VQ (atmosphere import)	○	○	○	●	●	●
60-90° S	*FW* storage	●	◔	○	◔	◐	◐
	Sea ice storage	◐	○	○	◕	◕	◕
	Q	○	○	◔	○	◔	◐
	FW transport	○	○	○	○	○	○
	Sea ice export	○	○	○	○	○	○
	VQ	◔	◐	○	○	◔	◔

* members with significant difference, e.g.:

● 4 of 4   ◗ 3 of 4   ◐ 2 of 4   ◔ 1 of 4   ○ 0 of 4

◕ 2 members increase, 1 member decrease, 1 insignificant

Number of ensemble members, which show a significant change between certain preindustrial time periods, is given as pie chart. *Black* denotes an positive difference in mean between two time periods, *gray* a negative difference. This gives a hint whether the sign of a trend is consistent among ensemble members and how robust that trend is. *Time periods*: Initial Conditions (IC, 1500–1530 AD), Mauder Minimum (MM, 1685–1715 AD), Dalton Minimum (DM, 1800–1830 AD), and Preindustrial (PI, 1840–1870 AD)

observations of the Arctic freshwater cycle interannual variability is even larger than in GCMs (Rawlins et al. 2010). Prior to Preindustrial the freshwater balance of the Arctic domain as a whole is stable with the only notable change being internal redistribution of freshwater masses. Table 2 compares selected quantities of the polar freshwater budgets for different preindustrial time periods: *FW* storage, sea ice storage, and *Q* are storage terms inside the domain, while *FW* transport, sea ice export and *VQ* are transport terms at the domain's boundary. With the comparison of Initial Conditions, the Maunder Minimum, and the Dalton Minimum we try to determine whether these three periods of similarly weak external forcing differ significantly among each other.

In general, changes between Initial Conditions and the Maunder Minimum are more robust in the storage terms than in the transport terms. This can be seen by the significant reduction of *FW* storage in all and of *Q* in three of the ensemble members, respectively. In concert with that, the sea ice storage significantly increases in three members. This is consistent with the absolute numbers in Fig. 5 where sea ice grows at the expense of *FW*, while all

Fig. 7 Ensemble mean freshwater transport as *liquid* (*FW* transport), water vapor (*VQ*), and *solid* (sea ice) across 60°N (**a**) and 60°S (**b**), summed up over 45° longitudinal transects; *positive values* indicate a northward transport. The *bars* in the chart correspond to the time periods Initial Conditions (IC, 1500–1530 AD), Maunder Minimum (MM, 1685–1715 AD), Present-Day (PD, 1960–1990 AD), and Future Projections (FP, 2068–2098 AD). Due to the computation of *FW* transport from residuals on the SH it is not possible to show this term for each sector. The *bottom panels* in **a** and **b** show the ensemble mean freshwater flux ($P − E + R$ + sea ice melt flux) anomaly of FP minus PD, as well as river runoff during PD. The model land mask is given in *white*
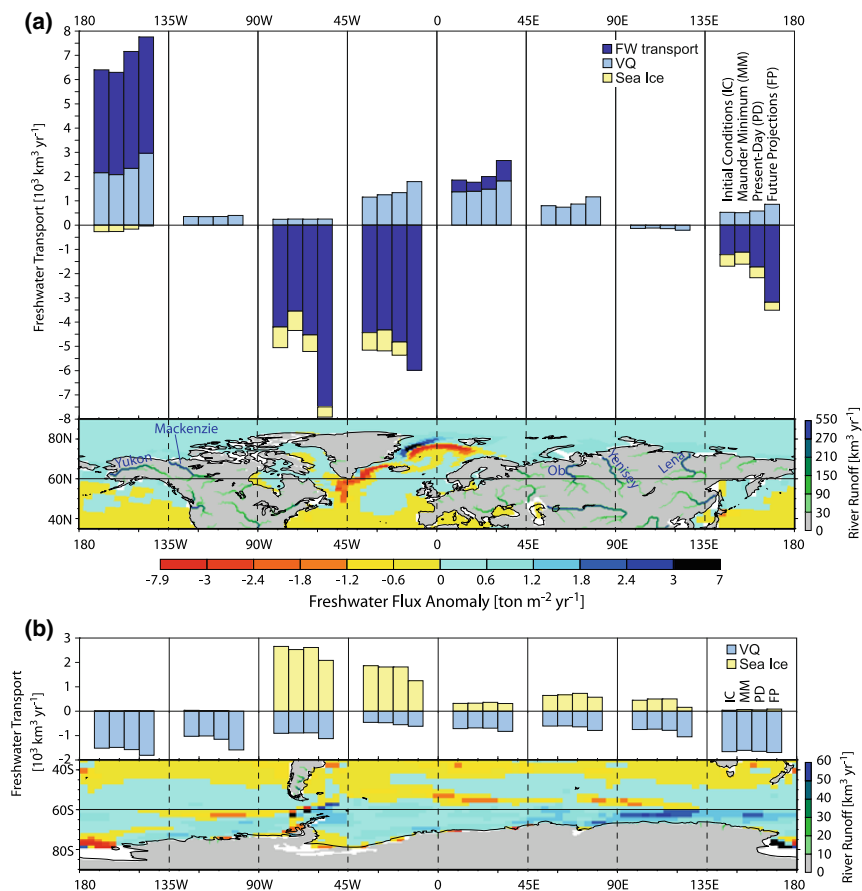
transport terms at the domain's boundary change only insignificantly. Comparing Initial Conditions to the Dalton Minimum, the decrease in *FW* storage is the only significant and robust change. Comparing the Maunder Minimum to the Dalton Minimum, the reduction of the sea ice storage is the only robust change. All other changes are either not significant or, if they are, do not show a consistent sign of change among the ensemble members. This allows for a first conclusion that the difference between the three periods Initial Conditions, Maunder Minimum and Dalton Minimum is characterized by minor redistributions of freshwater between the reservoirs of the ocean and sea ice. At the same time, the total amount of freshwater in the domain does not change notably.

To relate these domain-internal redistributions of the freshwater to changes in the external forcing, we show the transient behavior of the different budget terms (Fig. 8). The exact timing of change in the Arctic *FW* storage is not linearly connected to the external forcing. This manifests itself in the coexistence of positive and negative trends in

the *FW* storage ensemble members and the following substantial spread among the members during the seventeenth and eighteenth century (Fig. 8a). Note that the members originally started from only slightly different initial conditions and have experienced identical external forcing since. Thus to a large extent the decadal changes in *FW* storage in the preindustrial era are driven by internal variability. In fact, for the ensemble members TRa2 and TRa3 the timing of the transition of *FW* storage from its initial conditions to a lower value coincides with similar transitions found in time series of Atlantic maximum overturning circulation (AMOC) from the same simulations (Hofer et al. (2011); using their method to determine the transition phase). In these cases, a weaker AMOC is largely responsible for a decrease in salinity in the GIN Seas and the Atlantic part of the Arctic domain. The salinity decrease in these areas in turn is crucial to explain the decrease of the Arctic domains's total *FW* storage during that time. However, this indirect attribution of ramp-like *FW* storage changes to variations in the AMOC

is not robust throughout the ensemble—but a further investigation is beyond the scope of this study. The running trend of the sea ice storage, opposed to one of FW storage, follows the variations in external forcing more closely (Fig. 8b).

The atmospheric terms Q, VQ, total $P-E$, and R (which is largely controlled by $P_{lnd}-E_{lnd}$) do not show a significant response in the Maunder Minimum, but gradually increase along with the radiative forcing from the Maunder Minimum onwards (Fig. 8c, e, f). During the Dalton Minimum, however, these terms experience an abrupt dip. This dip sets them back to values similar as during Initial Conditions and the Maunder Minimum, even though the radiative forcing from solar and GHGs was approximately 5 and 10% weaker during Initial Conditions and the Maunder Minimum than during the Dalton Minimum, respectively. This raises the question of the necessity of the volcanic forcing to explain the atmospheric state of the Arctic freshwater balance during the Dalton Minimum. On a shorter time scale, the atmospheric response to volcanoes has been investigated using a composite of the years following the 21 largest eruptions from 1500 to 2000 AD (not shown). There, no significant large-scale response on high latitude total $P-E$ and VQ could be detected. However, $P-E$ and VQ are reduced just at 60°N in the first 2 years after an eruption. This contributes to the simulated reduction in the fields of $P-E$ and VQ during the Dalton Minimum, nevertheless, the solar forcing is the main driver. Note that while the direct radiative effects from volcanic aerosols are correctly represented in the CCSM3, it has its deficits in simulating the dynamical effects of volcanic eruptions. This is namely the absence of the NH mid- to high-latitude winter-warming pattern that would result from a positive phase of the North Atlantic Oscillation (Stenchikov et al. 2006). Interestingly, Schneider et al. (2009) found a winter-warming in idealized experiments with the medium resolution version of CCSM3 while the high (Stenchikov et al. 2006) and low-resolution version do not reproduce this pattern.

As the solar minimum of the Dalton Minimum ceases and GHGs start to increase the combined radiative forcing exceeds the preceding range since 1500 AD and so does the Arctic domain's SAT (Fig. 2). As a consequence the atmospheric terms VQ, Q, and total $P-E$ recover to pre-Dalton Minimum values and then continue to increase in line with the strengthening radiative forcing. At the same time trends in FW storage become positive and are better constrained, i.e., the ensemble members' spread becomes smaller. This indicates a robust response to the change in forcing. Trends in sea ice storage, however, remain around zero until the end of the nineteenth century when they finally become negative in all ensemble members. This means that the increase in FW storage just after the Dalton

Minimum cannot be attributed to a redistribution of the freshwater from sea ice to the ocean. It rather seems that the synchronous increases of total $P-E$ and R after their forcing-induced minimum during the Dalton Minimum are responsible for the freshening ocean. This increase of total $P-E$ and R is consistent with the significant and robust increase of VQ and Q from the Dalton Minimum to Pre-industrial (Table 2).

This leads to the conclusion that the mean state of the Arctic freshwater balance during Initial Conditions, the Maunder Minimum, and the Dalton Minimum is fairly stable, the exception being small but significant differences in the freshwater reservoirs which seem to reflect the multi-decadal to centennial variations in the external forcing. During the sustained cold conditions of the Maunder Minimum a saltier ocean, more sea ice and less water vapor (compared to the onset of the Little Ice Age at 1500 AD) were the marked anomalies in the freshwater balance. During the Dalton Minimum a short-lived response of the atmospheric component of the freshwater cycle occurred. However, the small signal-to-noise ratio indicates the important role of the internal variability of the freshwater cycle.

3.3 Future projections

The changes in the freshwater budget projected for the Future Projections are substantial and very robust, as for every investigated budget term all four ensemble members show a significant difference in mean compared to our reference Present-Day. VQ is roughly 27% larger than during Present-Day, caused by the thermally induced increase of the moisture holding capacity. At the same time the volume transport remains largely unchanged, which is reflected also in the cyclone activity in the domain: Both the number and mean intensity of the cyclones stay constant in winter and even decrease slightly in spring, summer, and autumn for the Future Projections (not shown). This confirms that the strengthened atmospheric water import is due to the amount of water transported by cyclones rather than by an increase of their frequency or intensity. Cyclones are detected as minima in the 12-hourly 1,000 hPa geopotential height field and need to exceed a gradient of 20 gpm 1,000 km^{-1} across a surrounding area of 1,000 km × 1,000 km (a detailed description of the cyclone detection and tracking method is given in Raible et al. 2007, 2010). The additional precipitable water in the domain is the reason for an increase of total P. As annual mean sea ice extent is reduced by 12% compared to Present-Day (not shown) the open ocean area grows and receives much more P directly from the atmosphere (+43%). Runoff from lower latitudes and $P_{lnd}-E_{lnd}$ increase as well, leading to a substantial increase in R to the
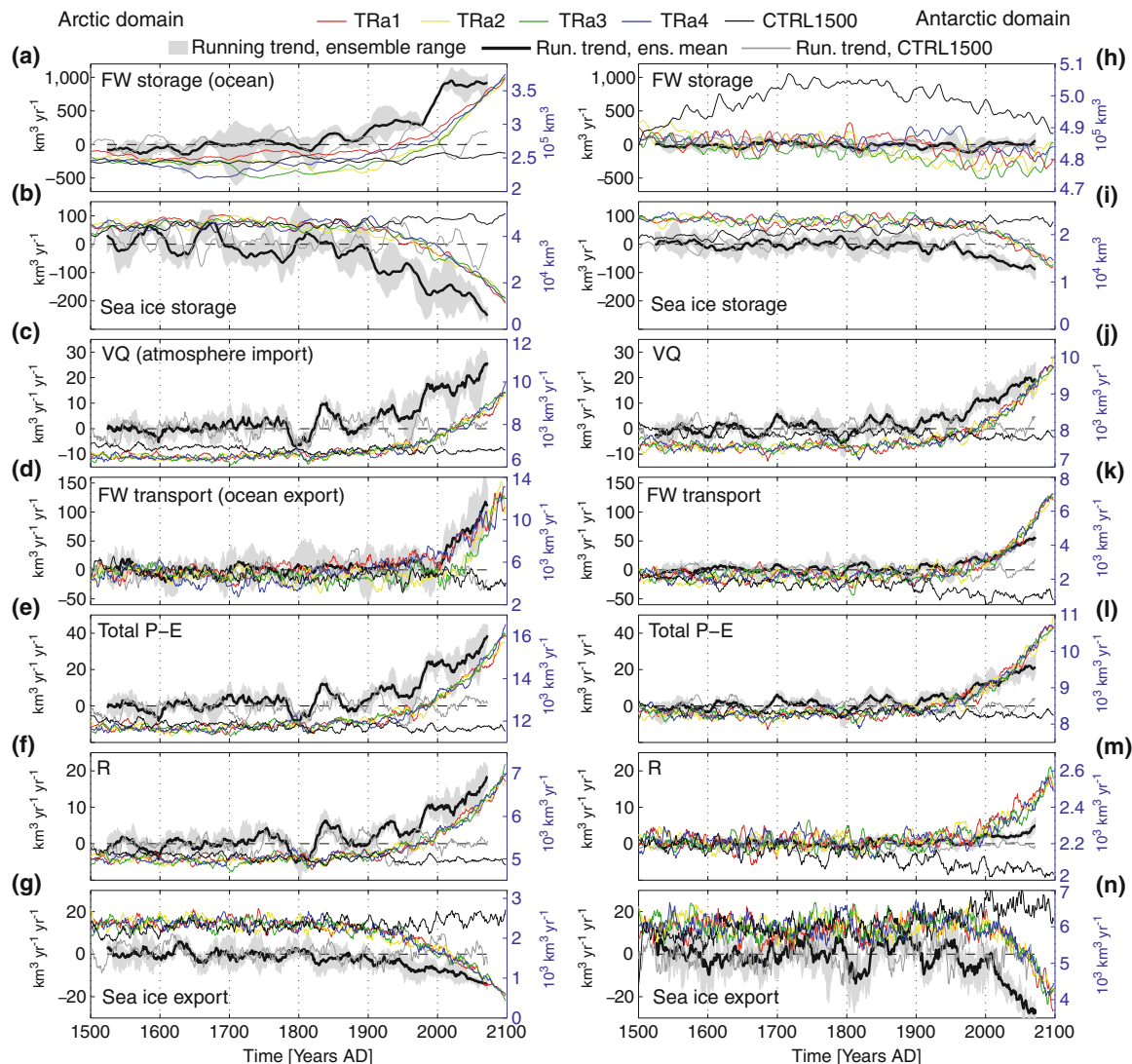
Fig. 8 Time series and trends of polar freshwater storage and transport terms. 50 Years running trends (ensemble range in *gray shading*, ensemble mean as thick *black line*, CTRL1500 as *gray line*; *left black* y-axis) and 5 years running means (transient simulations as *colored lines*, CTRL1500 as thin *black line*; *right blue* y-axis) of *FW* storage, sea ice storage, *VQ, FW* transport, total *P−E*, *R*, and sea ice

export for the Arctic (**a–g**) and Antarctic domain (**h–n**). Values are plotted at the middle-year of the 50 and 5 years window, respectively. A *narrow shading* of the running trend indicates a consistent behavior of the ensemble members, i.e., potentially externally forced variations. Opposed to that, a large spread of the *shading* indicates a period dominated by internal variability

ocean of roughly 26% (manifested in the positive anomalies close to the river's discharge areas in Fig. 7a, bottom panel). Further, the annual mean melt-freeze ratio of sea ice rises from 1.05 during Present-Day to 1.15 during the Future Projections, representing an enhanced release of sea ice-stored freshwater to the ocean (due to the large sea ice volume at present-day no sea ice-free summer conditions are reached in these simulations). This leads to a spatial shift in the freshwater flux to the ocean surface, causing

strong local anomalies in the GIN Seas (Fig. 7a, bottom panel). Together with *R*, sea ice is the main driver of changes in the ocean freshwater budget.

Overall, the freshwater flux from $P_{ocn}−E_{ocn}$ and *R* to the Arctic domain's ocean increases by 39% from Present-Day to the Future Projections. Consequently, the export of freshwater from the Arctic Ocean is strongly increased as well during the twenty-first century. Sea ice export, on the other hand, is decreased in all sectors and disappears

completely in the eastern Bering Sea and in the Labrador sector (Fig. 7). The latter causes the *FW* storage in the GIN Seas to decrease as less sea ice is transported there. This mechanism has been identified to counteract temperature-driven stratification and thereby maintaining deep-water formation in the GIN Seas (Holland et al. 2006b). The vast rest of the Arctic domain's ocean is freshening during the twenty-first century. The largest changes occur in the Beaufort Gyre, which strengthens and increases its fresh-water storage in the future (Fig. 4). Correlation and trend analysis suggest that, due to its proximity to the Beaufort Gyre, the *FW* transport through the CAA is coupled directly to the growing *FW* storage in the Gyre (not shown). Together with increased surface freshwater forcing in the CAA (Fig. 7a, bottom panel) and a growing sea surface height gradient across the CAA (as described by Jahn et al. (2010) for interannual transport variability) this results in an increase of the *FW* transport in the Labrador sector over the twenty-first century. This increase is about three times stronger than the increase of *FW* transport in the Irminger Sea sector (Fig. 7). The freshwater import through the Bering Strait decreases in line with the weak-ening of the meridional pressure gradient across the Bering Strait due to the freshening Arctic Ocean (Arzel et al. 2008).

The findings for the mean changes from Present-Day to the Future Projections are generally in agreement with numerous model studies focusing on the Arctic Ocean only (Holland et al. 2006a, b; Koenigk et al. 2007; Arzel et al. 2008). In some respect, however, different models still perform differently. Koenigk et al. (2007) project the Arctic Ocean total freshwater export to stay fairly constant until the twenty-second century, i.e., the decrease in sea ice export is matched by the increase in the liquid export. We find, when considering either the Arctic Ocean only or the complete Arctic domain north of 60°N, that the ocean increases its total export of freshwater significantly already during the twenty-first century. Arzel et al. (2008) dis-covered a threshold behavior of the Fram Strait through-flow as a consequence of ocean-atmosphere heat exchange in an A1B simulation which was not reproduced in our simulations. Here, the Fram Strait volume flux stays con-stant. The increase in *FW* transport, which we find in the Fram Strait, is mainly due to fresher waters transported and not due to changes in the volume flux (not shown). The proposed mechanism of Arzel et al. (2008) requires a strong reduction of sea ice in the Barents Sea at the beginning of the twenty-first century and a freshening of the GIN Seas in the late twenty-first century. While the first of these features occurs to a lesser extent (not shown), the second is not simulated at all in the CCSM3 (see Fig. 7).

Regarding the transient behavior of the freshwater budget remarkable changes in the trends of *FW* storage and sea ice storage are found in the second half of the twentieth century when these two terms accelerate their growth and decay rate by a factor of about two, respectively (Fig. 8). At the same time, the transport terms *VQ*, total *P−E*, and *R* show a strong increase to more positive trends as well. This indicates that a large part of the change in the Arctic freshwater cycle is evident well before the maximum warming in the simulations. This is in agreement with Arctic Ocean-only results from one high-resolution CCSM3 simulation using the A2 scenario (Holland et al. 2006b). There, solid and liquid freshwater transport as well as runoff show their largest changes in the period of 1975–2025 AD, in line with an ensemble using the A1B scenario (Holland et al. 2006b). The A1B scenario projects a GHGs concentration peak around 2050 AD. In our case, using the A2 scenario and the domain of 60−90°N, the same terms (*FW* transport, sea ice export, and *R*) have their largest trends at the end of the twenty-first instead of the twentieth century. A possible cause for this disagreement is the overestimation of end-twentieth century sea ice volume in our simulations. This delays polar amplification (Hol-land and Bitz 2003) and the peak in sea ice export and sea ice melt flux, which both occur later in the low-resolution CCSM3 ensemble. While we overestimate the absolute amount of sea ice in the Arctic Ocean, the evolution and amount of sea ice lost in the twenty-first century are similar to the high-resolution CCSM3 (Fig. 9b). A direct com-parison of flux terms for the domain 60−90°N from low- and high-resolution CCSM3 simulations shows that the trends of *P−E* over the ocean, *R*, sea ice melt flux, and *FW* transport are similar (Fig. 9c). However, the low-resolution CCSM3 simulation has a weaker *FW* transport resulting in a faster accumulation of *FW* during the twenty-first cen-tury. This strong *FW* storage increase is at the higher end in comparison to other models, but still falls within the standard deviation (Fig. 9a).

4 Freshwater balance of the Antarctic domain

4.1 Present-day climate

The Antarctic domain is characterized by a completely different geographic setting compared to the Arctic. 63% of the domain's area as well as the domain's lateral bound-aries at 60°S are covered by ocean, which—together with a larger atmospheric mass transport (not shown)—results in more water vapor advected (*VQ*) to the Antarctic domain than to the Arctic domain (Fig. 6). Due to the dominant circumpolar circulation this import of water vapor is uni-formly distributed along 60°S with a maximum in the sector north to the Ross Sea (Fig. 7). This corresponds well to observations (Tietäväinen and Vihma 2008). Total *Q* is
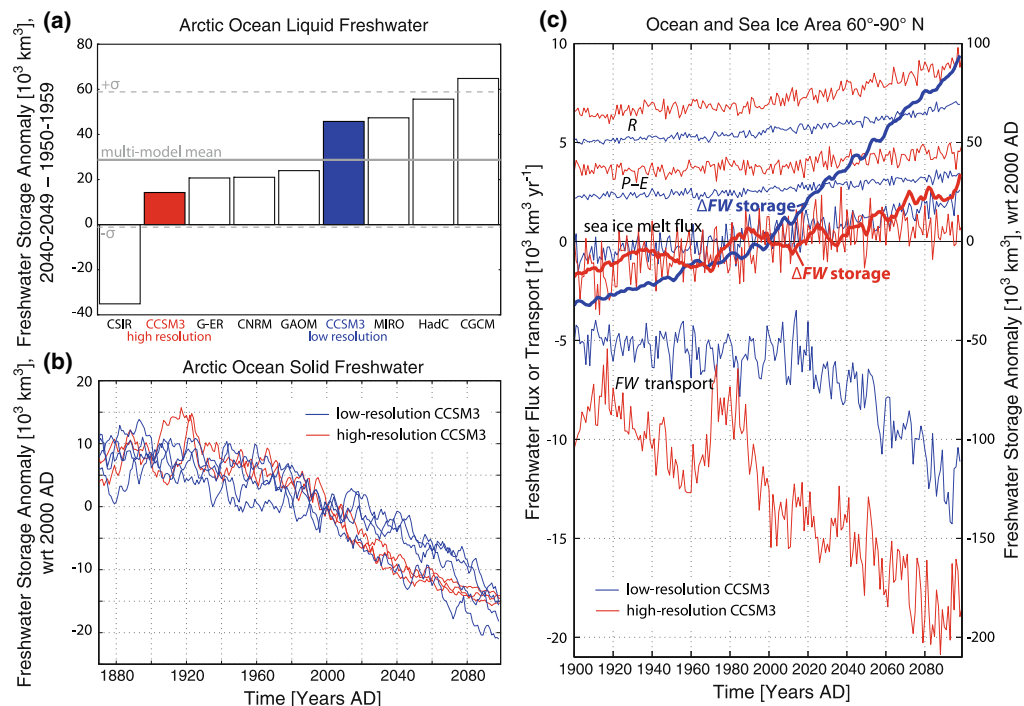
Fig. 9 **a** Change in Arctic Ocean freshwater storage of 2040–2049 AD relative to 1950–1959 AD from different models using a reference salinity of 34.8 g kg^{-1}. CCSM3 low-resolution corresponds to our ensemble mean. All other numbers are as in Fig. 11 from Holland et al. (2007) (M. Holland, pers. communication) and are based on the A1B scenario. Further details on these simulations in Holland et al. (2007). Note that our ensemble uses the A2 scenario, however, the forcing is very similar to the A1B scenario for the time period 1950–2049 AD (IPCC 2007). **b** Arctic Ocean sea ice storage as anomaly to the year 2000 AD from simulations with the high-resolution CCSM3, applying the A2 scenario, and our ensemble. **c** Freshwater fluxes and transports to the ocean at 60−90°N (*left axis*) and the anomalous ocean freshwater storage (reference salinity 34.88 g kg^{-1}) from one high-resolution CCSM3 simulation and our ensemble mean (*right axis*)

smaller than over the Arctic domain owing to the lower temperatures, especially south of 70°S, i.e., over the Antarctic ice sheet (not shown).

For the larger part, P falls on the sea ice and ocean surface while the Antarctic ice sheet receives only about 19% of total P during the reference period Present-Day. Due to the lower temperatures the portion of P that is evaporated to the atmosphere is smaller than in the Arctic domain. P over the ice sheet falls mainly as snow (not shown), which means that R is made up solely by the melt flux from the terrestrial snow layers.

During Present-Day the sea ice freshwater balance is positive as illustrated by the sea ice melt-freeze ratio of 0.96 (800 km^3 year^{-1}). However, as sea ice is exported at a rate of about 6,100 km^3 year^{-1} (more than a factor three of the Arctic domain's export rate during Present-Day) the sea ice volume shrinks nonetheless during Present-Day. In agreement with Schmitt et al. (2004), the vast majority of the sea ice export takes place north of the Weddell Sea (Fig. 7). As the FW transport in the Antarctic domain has

to be calculated from the residuals of the FW storage changes and the ocean surface fluxes, we cannot split it up into sectors. However, investigating a few years of sub-daily output the model has proven to be capable of simulating the Drake Passage effect (e.g., Talley 2008), i.e., the major freshwater export due to Ekman transport in the Drake Passage and the smaller return flow in the Atlantic sector.

4.2 Preindustrial changes

Looking at the preindustrial time periods Initial Conditions and the Maunder Minimum, the mean differences compared to Present-Day are generally less robust than in the Arctic domain. This could already be anticipated from the smaller preindustrial temperature anomalies in the Antarctic domain (Fig. 2). Nevertheless, we find significant reductions in VQ and Q during Initial Conditions and the Maunder Minimum (Fig. 6). Thereby the changes in VQ are uniformly distributed across the sectors, i.e., no large

changes in certain sectors dominate the total change in *VQ* (Fig. 7). This reduced *VQ* results in less total *P* and *P–E*, in turn influencing the *FW* transport, which is significantly smaller during the Maunder Minimum in three of the ensemble members. *R* and the export of sea ice remain unchanged. The melt and freeze rates of sea ice are significantly different compared to Present-Day, but not the ratio of the two. Therefore, sea ice production during Initial Conditions and the Maunder Minimum is only about $100 \text{ km}^3 \text{ year}^{-1}$ larger than during Present-Day. As a consequence the difference in sea ice volume between the preindustrial time periods and Present-Day is small, but significant in three ensemble members nevertheless (Fig. 6). When comparing with the first half of the twentieth century instead of Present-Day the difference quickly becomes insignificant. This confirms results by Sedláček and Mysak (2009), who found no significant long-term trend in simulated Southern Hemisphere sea ice volume between 1500 and about 1950 AD (see also our Fig. 8i). This means that the ocean and sea ice freshwater budget during Initial Conditions, the Maunder Minimum, and Present-Day are primarily controlled by the atmospheric input and stay approximately in balance. Note, however, that the unstable behavior of the *FW* storage in the CTRL1500 (Fig. 8h) points to a potential inaccuracy of the *FW* transport calculated from monthly means.

As in the Arctic domain, most variations within the preindustrial era in the Antarctic freshwater balance are not robust. In fact, only the reduction of the *FW* storage from Initial Conditions to the Maunder Minimum is significant in all four ensemble members (Table 2). At the same time, two members show a significant increase in sea ice storage. As no notable change in the total amount of freshwater in the domain is detectable, i.e., the fluxes at the boundary stay constant, this corresponds to a shift of freshwater from the ocean to the sea ice. However, the signal-to-noise ratio does not allow for an attribution to the external forcing. The same holds true for the comparison of Preindustrial with Initial Conditions, the Maunder Minimum, and the Dalton Minimum: no robust signal can be detected for any quantity of the budget as either significance is not reached or the ensemble members show significant, though opposed trends. This is not surprising as the Antarctic SAT during preindustrial times does not resemble the forcing variations such as the Maunder Minimum or the Dalton Minimum.

Similar to the high northern latitudes, the volcanic eruptions during the Dalton Minimum do not leave a significant imprint in the *P–E* and *VQ* fields south of 60°S. This result is confirmed by the mean response of *P–E* and *VQ* to the 21 largest eruptions from 1500–2000 AD in our simulations, as well as a case study of the atmospheric circulation response to Pinatubo (Robock

et al. 2007). The response is even weaker than in the high northern latitudes as the larger ocean area of the SH dampens the radiative perturbation from the erupted aerosols (Robock 2000) and as the stronger polar vortex of the SH is thought to be more resistant to perturbations (Stenchikov et al. 2002).

4.3 Future projections

For the Future Projections the changes are, similar to the Arctic domain, very robust as nearly all budget and flux terms in all ensemble members experience a significant shift in mean. The domain is fed by 20% more water vapor compared to Present-Day which mainly arises from increased moisture content (Liu and Curry 2010). The largest increase in *VQ* occurs in the Bellinghausen Sea (Fig. 7) where the frequency of occurrence of cyclones decreases, but on average cyclones carry more moisture into the domain (not shown, see also Lambert and Fyfe 2006; Lynch et al. 2006). As in the Arctic, the majority of this additional freshwater is precipitated onto the open ocean surface, which is enlarged due to the reduction of the sea ice area (−11%, not shown). The sea ice storage is reduced by 32%, indicating that sea ice is substantially thinned. This increases the freshwater flux to the ocean surface in large regions of the Southern Ocean south of 55°S (Fig. 7b, bottom panel). While sea ice export weakens in nearly all longitudinal sectors (Fig. 7), the export by *FW* transport strengthens. The latter dominates these changes as export substantially exceeds the import during the twenty-first century.

5 Summary and conclusion

We use an ensemble of four transient simulations with the low-resolution version of the CCSM3, spanning the time period from 1500 to 2100 AD, to investigate past and future changes of the polar freshwater balance. The simulations produce a realistic general NH temperature evolution over the past five centuries with an overestimated warming in the twentieth century due to missing aerosols (Hofer et al. 2011). Temperatures on the poles, however, are rather underestimated. The simulated present-day freshwater cycle of the Arctic Ocean agrees reasonably well with observations (Serreze et al. 2006), except that freshwater stored in sea ice and ocean is overestimated significantly.

We show that many of the transport and storage components in the present-day polar freshwater cycle are significantly different from preindustrial states and in particular from the projected future state. While this conclusion is valid for both polar domains the relative

magnitude of the differences is larger in the Arctic where temperature anomalies in the past and future are larger as well.

Regarding the Arctic, the simulated freshwater cycle appears to be closely coupled to temperature on decadal time scales. We showed this for the twentieth and twenty-first century in consistency with other model studies (Goosse and Holland 2005; Holland et al. 2007) as well as observational records (White et al. 2007). This relationship was found to hold beyond the temporal scope of the studies mentioned before as during the cold phase of the Little Ice Age simulated freshwater transports are smaller than during present-day and the domain contains less freshwater in total. As temperature rises during the twentieth and twenty-first century more water passes through the hydrological cycle and the reservoir of FW grows at the expense of the reservoir of sea ice and due to increased $P-E$ and R. Synchronously, the FW transport increases and represents a strengthening freshwater forcing to the North Atlantic. These features are consistent among most coupled GCMs (Holland et al. 2007), however, the magnitude of change depends on the model and its resolution. This is particularly evident for the reservoirs of sea ice and FW. Compared to the high-resolution CCSM3 the low-resolution has a weaker ocean heat transport into the Arctic and a weaker FW transport out of the Arctic. Resulting from that, sea ice is overestimated in this study, leading in turn to a lagged peak of freshwater release in the future. At the same time, the weak FW transport yields a reservoir of FW that grows faster than in the high-resolution CCSM3. Based on this, the magnitude of preindustrial changes might be model-dependent as well, which needs to be considered when interpreting these results.

Within the preindustrial era of 1500–1870 AD the Arctic domain's total amount of freshwater is largely controlled by VQ while for the present and future the changes in FW transport and sea ice export contribute crucially as well.

Sedláček and Mysak (2009) showed that during preindustrial times wind-stress plays an equally important role as direct radiative effects regarding changes in sea ice volume and ocean properties in the Arctic. At the same time, the sea ice volume was found to be basically insensitive to changes in radiative forcing as they occurred during the Maunder Minimum and the Dalton Minimum. We are unable to depict this hypothesis as precisely as the sensitivity study of Sedláček and Mysak (2009). At least we see a weak but significant response of sea ice storage and FW storage to changes in the external forcing occurring from 1500 AD to the Maunder Minimum. The Dalton Minimum, on the other hand, leaves no imprint on the sea ice and ocean freshwater storage, as its duration is too short to significantly affect these slow-reacting reservoirs. The atmospheric quantities of total $P-E$, VQ, and Q, on the

other hand, display a clear dip during the Dalton Minimum, forced primarily by the sun.

As our domain $60-90°N$ includes Greenland, in contrast to many other studies focusing on the Arctic Ocean only, we need to account for potential melt fluxes from the Greenland ice sheet when assessing the present-day and future state of this domain's freshwater balance. The processes of a melting or disintegrating ice sheet are not simulated by the land component of the CCSM3 due to the absence of a dynamic ice sheet model. However, recent estimates of both present-day (267 ± 38 km^3 year^{-1}; Rignot et al. 2008) and future (year 2100 AD, 220 km^3 year^{-1}, Ren et al. 2011; >400 km^3 year^{-1}, Graversen et al. 2011) Greenland mass balance are a magnitude smaller than the changes projected for other freshwater fluxes such as P, R, or the melting of sea ice. The projected acceleration of the Greenland mass loss by about $100-200$ km^3 year^{-1} over the twenty-first century even lies within the ensemble uncertainty for, e.g., changes in R or sea ice melting. Therefore, the absence of an ice sheet model does not render the Arctic freshwater balance of the CCSM3 unrealistic. Similar conclusions can be drawn for the Antarctic domain, where recent literature suggests the twenty-first century contribution of freshwater from the ice sheet (<500 km^3 year^{-1}, Pfeffer et al. 2008; Katsman et al. 2011) to be substantially smaller than changes in other components of the ocean's surface freshwater balance, e.g., $P-E$ (+1,400 km^3 year^{-1}). However, the estimates and projections from current literature for the Antarctic mass balance are far less robust than the ones for Greenland. Taking into account all possible scenarios in Pfeffer et al. (2008) and Katsman et al. (2011) it remains uncertain, whether the Antarctic ice sheet will retain a close-to-zero mass balance or become a significant source of freshwater within the twenty-first century.

The Antarctic domain's response to changes in external forcing is expected to be dampened compared to the Arctic. This is due to the more zonal circumpolar current in both atmosphere and ocean, hampering the heat exchange with lower latitudes, as well as the larger ocean area, acting to reduce amplitudes in surface warming due to changes in the radiative balance (IPCC 2007). Additionally, the ice and snow albedo feedback is smaller in the Antarctic domain (Masson-Delmotte et al. 2006). This was confirmed in our study as anomalies in the freshwater cycle are smaller than in the Arctic.

During the preindustrial period no significant and robust changes in the individual terms of the Antarctic freshwater balance could be detected from our ensemble, suggesting that minima in external forcing (Maunder Minimum, Dalton Minimum) do not leave an imprint on the SH high latitudes' water cycle. As FW transport and sea ice export

362   F. Lehner et al.: Freshwater balance of polar regions

do not change much during the first 450 years, the atmo-spheric import VQ is the controlling mechanism regarding the domain's total freshwater content. The future projec-tions then show a substantial acceleration of the hydro-logical cycle, affecting all fluxes, with a linear dependence on the SAT projections. Thereby, the strongly increasing FW transport strengthens the Antarctic domain as a fresh-water source to the lower latitude oceans. Liu and Curry (2010) stress the potentially too weak response of the twentieth century Southern Ocean climate to anthropogenic forcing in models due to an overestimated sea surface temperature internal variability. Taking into account this and a possible lack of decadal SAT variability in the southern high latitudes of the model, the simulated amplitudes in the budget and transport terms of the Ant-arctic domain have to be interpreted with caution as they might have been larger during preindustrial times than simulated in this study. Therefore, other millennial simu-lations with new and higher resolved models are in need, which – together with proxies – will add to the picture of past variations of the polar freshwater reservoirs.

References

ACIA (2005) Impacts of a warming Arctic. Arctic climate impact assessment. Cambridge University Press, Cambridge

Allen MR, Ingram WJ (2002) Constraints on future changes in climate and the hydrological cycle. Nature 419:224–232

Arzel O, Fichefet T, Goosse H, Dufresne JL (2008) Causes and impacts of changes in the Arctic freshwater budget during the twentieth and twenty-first centuries in an AOGCM. Clim Dyn 30:37–58

Bekryaev RV, Polyakov IV, Alexeev VA (2010) Role of polar amplification in long-term surface air temperature variations and modern Arctic warming. J Clim 23:3888–3906

Bryan FO, Danabasoglu G, Nakashiki N, Yoshida Y, Kim DH, Tsutsui J, Doney SC (2006) Response of the North Atlantic thermohaline circulation and ventilation to increasing carbon dioxide in CCSM3. J Clim 19:2382–2397

Collins WD et al (2006) The community climate system model: CCSM3. J Clim 19:2122–2143

Compo G et al (2010) The twentieth century reanalysis project. Q J R Meteorol Soc 137:1–28

Goosse H, Holland MM (2005) Mechanisms of decadal Arctic climate variability in the community climate system model, version 2 (CCSM2). J Clim 18:3552–3570

Graversen RG, Drijfhout S, Hazeleger W, van de Wal R, Bintanja R, Helsen M (2011) Greenlands contribution to global sea-level rise by the end of the 21st century. Clim Dyn. doi:10.1007/s00382-010-0918-8

Hack J, Caron J, Yeager SG, Oleson KW, Holland MM, Truesdale JE, Rasch PJ (2005) Simulation of the global hydrological cycle in the CCSM community atmosphere model version 3 (CAM3): mean features. J Clim 19:2199–2221

Hansen J, Ruedy R, Sato M, Lo K (2010) Global surface temperature change. Rev Geophys 48:RG4004. doi:10.1029/2010RG000345

Held IM, Soden BJ (2006) Robust responses of the hydrological cycle to global warming. J Clim 19:5686–5699

Hofer D, Raible CC, Stocker TF (2011) Variations of the Atlantic meridional overturning circulation in control and transient simulations of the last millennium. Clim Past 7:133–150

Holland MM, Bitz CM (2003) Polar amplification of climate change in coupled models. Clim Dyn 21:221–232

Holland MM, Bitz CM, Hunke EC, Lipscomb WH, Schramm JL (2006) Influence of the sea ice thickness distribution on polar climate in CCSM3. J Clim 19:2398–2414

Holland MM, Finnis J, Barrett AP, Serreze MC (2007) Projected changes in Arctic Ocean freshwater budgets. J Geophys Res 112:G04S55

Holland MM, Finnis J, Serreze MC (2006) Simulated Arctic Ocean freshwater budgets in the twentieth and twenty-first centuries. J Clim 19:6221–6242

Huntington TG (2005) Evidence for intensification of the global water cycle: review and synthesis. J Hydrol 319:83–95

IPCC (2001) Climate change 2001, the scientific basis. Intergovern-mental panel on climate change. Cambridge University Press, Cambridge

IPCC (2007) Climate change 2007, the science of climate change. Intergovernmental panel on climate change. Cambridge Univer-sity Press, Cambridge

IPCC SRES (2000) Special report on emissions scenarios. Intergov-ernmental panel on climate change, Cambridge University Press, Cambridge

Jahn A, Tremblay B, Mysak LA, Newton R (2010) Effect of the large-scale atmospheric circulation on the variability of the Arctic Ocean freshwater export. Clim Dyn 34:201–222

Katsman CA et al (2011) Exploring high-end scenarios for local sea level rise to develop flood protection strategies for a low-lying delta—the Netherlands as an example. Clim Change. doi:10.1007/s10584-011-0037-5, published online

Khon VC, Park W, Latif M, Mokhov II, Schneider B (2010) Response of the hydrological cycle to orbital and greenhouse gas forcing. Geophys Res Let 37:L19 705

Kiehl JT, Shields CA, Hack JJ, Collins WD (2006) The climate sensitivity of the community climate system model version 3 (CCSM3). J Clim 19:2584–2596

Koenigk T, Mikolajewicz U, Haak H, Jungclaus J (2007) Arctic freshwater export in the 20th and 21st centuries. J Geophys Res 112:G04S41

Lambert SJ, Fyfe JC (2006) Changes in winter cyclone frequencies and strengths simulated in enhanced greenhouse warming experiments: results from the models participating in the IPCC diagnostic exercise. Clim Dyn 26:713–728

Liu J, Curry R (2010) Accelerated warming of the Southern Ocean and its impacts on the hydrological cycle and sea ice. Proc Natl Acad Sci USA 107:14987–14992

Lynch A, Uotila P, Cassano JJ (2006) Changes in synoptic weather patterns in the polar regions in the twentieth and twenty-first centuries, part 2: Antarctic. Int J Climatol 26:1181–1199

Mann EM et al (2009) Global signatures and dynamical origins of the little ice age and medieval climate anomaly. Science 326: 1256–1260

Masson-Delmotte V et al (2006) Past and future polar amplification of climate change: climate model intercomparisons and ice-core constraints. Clim Dyn 26(5):513–529. doi:10.1007/s00382-005-0081-9

Pardaens AK, Banks HT, Gregory JM, Rowntree PR (2003) Freshwater transports in HadCM3. Clim Dyn 21:177–195

Peterson BJ, Holmes RM, McClelland JW, Vörösmarty CJ, Lammers RB, Shiklomanov AI, Shiklomanov IA, Rahmstorf S (2002) Increasing river discharge to the Arctic Ocean. Science 298: 2171–2173

Peterson BJ, McClelland JW, Curry R, Holmes RM, Walsh JE, Aagaard K (2006) Trajectory shifts in the Arctic and Subarctic freshwater cycle. Science 313:1061–1066

Pfeffer WT, Harper JT, O'Neel S (2008) Kinematic constraints on glacier contributions to 21st-century sea-level rise. Science 321:1340–1343.

Raible CC, Baruch Z, Saaroni H, Wild M (2010) Winter synoptic-scale variability over the Mediterranean Basin under future climate conditions as simulated by the ECHAM5. Clim Dyn 35:473–488

Raible CC, Yoshimori M, Stocker TF, Renold M, Casty C (2007) Extreme midlatitude cyclones and their implications for precipitation and wind speed extremes in simulations of the Maunder Minimum versus present day conditions. Clim Dyn 28:409–423

Rawlins MA et al (2010) Analysis of the Arctic system for freshwater cycle intensification: observations and expectations. J Clim 23:5715–5737

Rayner N, Parker D, Horton E, Folland C, Alexander L, Rowell D, Kent E, Kaplan A (2003) Global analyses of sea surface temperature, sea ice, and night marine air temperature since the late nineteenth century. J Geophys Res 108:ACL2–1–29

Ren D, Fu R, Leslie LM, Chen J, Wilson CR, Karoly DJ (2011) The Greenland ice sheet response to transient climate change. J Clim 24:3469–3483

Rignot E, Box JE, Burgess E, Hanna E (2008) Mass balance of the Greenland ice sheet from 1958 to 2007. Geophys Res Let 35:L20 502

Robock A (2000) Volcanic eruption and climate. Rev Geophys 38:191–219

Robock A, Adams T, Moore M, Oman L, Stenchikov G (2007) Southern Hemisphere atmospheric circulation effects of the 1991 Mount Pinatubo eruption. Geophys Res Let 34. doi:10.1029/2007GL031403

Schmitt C, Kottmeier C, Wassermann S, Drinkwater M (2004) Atlas of Antarctic Sea Ice Drift. Institute for Meteorology and Climate Research, University of Karlsruhe, Karlsruhe

Schneider DP, Ammann CM, Otto-Bliesner BL, Kaufman DS (2009) Climate response to large, high-latitude and low-latitude

volcanic eruptions in the community climate system model. J Geophys Res 114. doi:0.1029/2008JD011222

Seager R, Naik N, Vecchi GA (2010) Thermodynamic and dynamic mechanisms for large-scale changes in the hydrological cycle in response to global warming. J Clim 23:4651–4668

Sedláček J, Mysak LA (2009) Sensitivity of sea ice to wind-stress and radiative forcing since 1500: a model study of the little ice age and beyond. Clim Dyn 32:817–831

Serreze MC et al (2006) The large-scale freshwater cycle of the Arctic. J Geophys Res 111, 2005JC003 424

Sorteberg A, Walsh JE (2008) Seasonal cyclone variability at 70°N and its impact on moisture transport into the Arctic. Tellus 60:570–586

Steele M, Morley R, Ermold W (2001) A global ocean hydrography with a high-quality Arctic Ocean. J Clim 14:2079–2087

Stenchikov GI, Hamilton K, Stouffer RJ, Robock A, Ramaswamy V, Santer B, Graf HF, (2006) Arctic Oscillation response to volcanic eruptions in the IPCC AR4 climate models. J Geophys Res 111. doi:10.1029/2005JD006286

Stenchikov GL, Robock A, Ramaswamy V, Schwarzkopf M, Hamilton K, Ramachandran S, Oman L, (2002) Southern Hemisphere annular mode response to the 1991 Mount Pinatubo volcanic eruption. Eos Trans AGU 83, 13837–13858. Fall Meet. Suppl., Abstract A22D-09

Stocker TF, Raible CC (2005) Water cycle shifts gear. Nature 434:830–832

Syed TH, Famiglietti JS, Chambers DP, Willis JK, Hilburn K (2010) Satellite-based global-ocean mass balance estimates of interannual variability and emerging trends in continental freshwater discharge. Proc US Natl Acad Sci 107:17 916–17 921. doi:10.1073/pnas.1003292107

Talley L (2008) Freshwater transport estimates and the global overturning circulation: Shallow, deep and throughflow components. Prog Oceanogr 78:257–303

Thompson DWJ, Solomon S (2002) Interpretation of recent Southern Hemisphere climate change. Science 296:895–899

Tietäväinen H, Vihma T (2008) Atmospheric moisture budgets over Antarctica and the Southern Ocean based on the ERA-40 reanalysis. Int J Climatol 28:1977–1995

Walsh JE (2009) A comparison of Arctic and Antarctic climate change, present and future. Antarct Sci 21:179–188

White D et al (2007) The Arctic freshwater system: changes and impacts. J Geophys Res 112:G04S54

Williams PD, Guilyardi E, Sutton R, Gregory J, Madec G (2007) A new feedback on climate change from the hydrological cycle. Geophys Res Let 34. doi:10.1029/2007GL029275

Wu P, Wood R, Stott P (2005) Human influence on increasing Arctic river discharge. Geophys Res Let 32:2004GL021 570

Yeager SG, Shields CA, Large WG, Hack JJ (2006) The low-resolution CCSM3. J Clim 19:2545–2566

Yoshimori M, Raible CC, Stocker TF, Renold M (2010) Simulated decadal oscillations of the Atlantic meridional overturning circulation in a cold climate state. Clim Dyn 34:101–121. doi:10.1007/s00382-009-0540-9

Chapter 3

Testing the robustness of a precipitation proxy-based North Atlantic Oscillation reconstruction

Flavio Lehner, Christoph C. Raible, and Thomas F. Stocker

Testing the robustness of a precipitation proxy-based North Atlantic Oscillation reconstruction

Flavio Lehner [a,b,*], Christoph C. Raible [a,b], Thomas F. Stocker [a,b]

[a] Climate and Environmental Physics, Physics Institute, University of Bern, Switzerland
[b] Oeschger Centre for Climate Change Research, University of Bern, Switzerland

ARTICLE INFO

ABSTRACT

The reconstruction of past atmospheric circulation is crucial for the understanding of natural climate change and its driving factors. A recent reconstruction suggests that, during Medieval times, the European region was dominated by a persistent positive phase of the North Atlantic Oscillation (NAO), followed by a shift to a more oscillatory behavior. We test this hypothesis and the concept underlying the reconstruction in a pseudo-proxy approach using instrumental records, reanalysis data sets and millennial simulations with four different climate models. While a shift from a more positive to a more negative phase of the NAO seems to be likely, the amplitude and persistence of the reconstructed positive phase cannot be reproduced by models. The analysis further reveals that proxy locations that were used in the reconstruction are not always sufficient to describe the NAO. This is reflected in a failure of the reconstruction to verify against instrumental records of the NAO in the 19th century. By adding complementary proxies, the robustness of an NAO reconstruction can be improved to the degree that it would withstand the tests presented here.

1. Introduction

The North Atlantic Oscillation (NAO) is the dominant mode of atmospheric winter circulation over the North Atlantic and European region and is characterized by a meridional gradient in the distribution of atmospheric mass over the North Atlantic (Hurrell, 1995; Wanner et al., 2001). The NAO modulates the extra-tropical zonal flow and its positive and negative phases exhibit a strong control on northern and southern European seasonal temperature and precipitation. Therefore, the NAO has been of interest to human society and science for more than a century. Usually, the NAO is described by an index of the difference in normalized sea level pressure (SLP) over Iceland and the Azores (Rogers, 1984) whereby a high index corresponds to a deepened Icelandic Low and a strengthened Azores High. There are a number of robust alternatives to this classical definition of the NAO index. To mention the most commonly used ones: the principal component (PC) of the leading Empirical Orthogonal Function of the winter SLP in the North Atlantic-European sector (hereafter PC-based; e.g., Kutzbach, 1970), the normalized SLP difference between Iceland and Lisbon (e.g., Hurrell, 1995), or between Iceland and Gibraltar (e.g., Jones

et al., 1997). The latter index represents the longest instrumental time series of the NAO, going back to 1821 AD (Vinther et al., 2003).

However, in order to learn about the low-frequency variability and stability of the atmospheric patterns associated with the NAO, longer time series of the index are needed (Wanner et al., 2001, and references therein). Such an extension beyond the instrumental period can be achieved by using proxy data to reconstruct the NAO index over the past centuries (e.g., Appenzeller et al., 1998; Cook et al., 1998, 2002; Luterbacher et al., 1999, 2002; Cullen et al., 2001; Glueck and Stockton, 2001; Rodrigo et al., 2001; Mann, 2002; Casty et al., 2007; Trouet et al., 2009; Kuettel et al., 2010).

In the last years, several reconstruction attempts resulted in a diverse picture of the evolution of the NAO over past centuries (for an overview see, e.g., Pinto and Raible, 2012). The longest reconstruction (Trouet et al., 2009) reported an intriguingly persistent positive NAO index during the Medieval Climate Anomaly (MCA), which shifts into a more oscillatory behavior during the subsequent Little Ice Age (LIA). The MCA refers to the period ∼1000–1250 AD, during which relatively high solar irradiance prevailed together with a pause in large eruptions of tropical volcanoes (Fig. 1), causing widespread warming on the Northern Hemisphere. The LIA (∼1450–1700 AD) then featured decreased solar activity and an elevated volcanic activity, leading to a cooling. For a recent discussion on the timing and spatial characteristics of the MCA and LIA the reader is referred to Mann et al. (2009).

* Corresponding author. Tel.: +41 316318601.
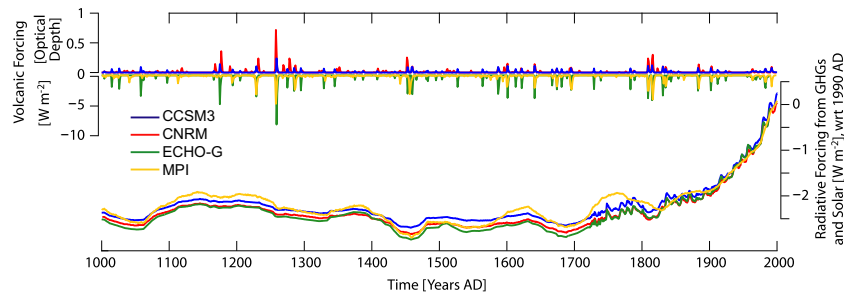 *E-mail address:* lehner@climate.unibe.ch (F. Lehner).

Fig. 1. Forcing used in the different model simulations, given as cumulative radiative forcing from greenhouse gases (GHGs: CO_2, N_2O, CH_4, calculated as in IPCC (2001)) and solar irradiance (right y-axis), with reference to (wrt) 1990 AD. For MPI, an Earth System Model that interactively calculates the CO_2, the mean CO_2 of the three ensemble members is used. Forcing from volcanic eruptions is given as optical depth (CCSM3, CNRM) and W m^{-2} (ECHO-G, MPI) (left y-axis).

The shift of the NAO suggested by Trouet et al. (2009) implies a fundamental change in dynamics and, if true, should be understood from a mechanistic point of view. Arising from tropical sea surface temperature anomalies, this NAO shift was proposed as a dynamical explanation for the European temperature evolution during that time. However, contradictory evidence from other proxy data suggests changes in winter-spring storminess to have been the distinct feature of the MCA-LIA climate transition in the North Atlantic-European area around 1400 AD (Meeker and Mayewski, 2002). Increased storminess, however, is usually expected to go along with more positive NAO values. A recent reconciliation of proxies and models provides a first explanation on how the two seemingly contradictory signals could be merged into a coherent story (Trouet et al., 2012). Robust reconstructions of past circulation changes are in any case a prerequisite to further improve our understanding of naturally forced climate change such as the MCA-LIA transition.

In the reconstruction of the NAO index, Trouet et al. (2009) used a precipitation proxy from Scotland (width of luminescent bands in a stalagmite from a sub-moorland site) and a drought proxy from Morocco (combination of 326 time series of ring width from cedars in the Atlas mountains) to describe the two hydrological centers of action that typically arise from an anomalous NAO: a rain band across the northern North Atlantic with increased precipitation in Scotland and western Scandinavia together with drier conditions in the western Mediterranean region in the case of a positive NAO index; and vice versa for the negative case (e.g., Hurrell, 1995; Wanner et al., 2001). The NAO reconstruction by Trouet et al. (2009) can be validated against the instrumental time series of the NAO in the time of overlap. When going beyond that, however, one has to assume a stable relationship between the proxy signal and the NAO index without being able to validate this assumption. By default, proxies are stationary in space and time, while atmospheric patterns are not (Raible et al., 2006). This challenges the stationarity assumption inherent in proxy-based reconstructions and calls for additional validation procedures applicable to these reconstructions.

The aim of this paper is to use reanalysis data and results from simulations with comprehensive climate models to test the longest proxy-based reconstruction of the NAO with respect to (1) the potential occurrence of persistent positive or negative phases of the NAO, (2) the robustness of certain proxy locations in describing centers of action of the NAO, and (3) the possibility of improving the reconstruction by additional proxies. Regarding the third point, our goal is to achieve an improvement of the reconstruction in a minimalistic approach, i.e., by providing only one additional proxy in the proximity of each NAO-related hydrological center of action.

In Section 2 we give a brief overview of the models and reanalysis data sets used as well as the methodology applied. The results

are presented in Section 3, subdivided in results from instrumental data, reanalyses and models. A discussion and conclusions follow in Sections 4 and 5.

2. Data and methods

For our analysis we use output from four coupled general circulation models of comparable complexity as well as two state-of-the-art reanalysis data sets (Table 1). The models CNRM-CM3.3 (Salas-Mélia et al., 2005; Swingedouw et al., 2011, hereafter CNRM), ECHO-G (González-Rouco et al., 2006), MPI-ESM (Jungclaus et al., 2010, hereafter MPI), and CCSM3 (low-resolution version, Hofer et al., 2011) were all run for the past millennium, an ensemble of four simulations with CCSM3 was run from 1500 to 2000 AD (used in, e.g., Lehner et al., in press). In addition, an ensemble of six simulations over the time period 1149–1499 AD was carried out with the medium-resolution CCSM3. This last time period corresponds to the transition phase from the MCA to the LIA.

The forcings from greenhouse gases (GHGs), total solar irradiance (TSI) and volcanic eruptions that were applied in the different simulations are shown in Fig. 1. While there exists some consensus on past variations of GHGs, the amplitude of the TSI is still a topic of debate (e.g., Steinhilber et al., 2009; Gray et al., 2010; Shapiro et al., 2011). The TSI reconstructions used here are all in the same range of having a relatively large amplitude (approximately −3.5 W m^{-2} during the Maunder Minimum compared to 1950–2000 AD). All models exhibit a realistic Northern Hemisphere temperature evolution over the past millennium representing a warm MCA and a cold LIA (for further details see references in Table 1). This temperature decrease from the MCA to the LIA is also recorded in proxies of the Central European

Table 1
Model simulations and reanalysis data used in this study. Note that Mitchell and Jones (2005) refers to CRU TS 2.1, while we use the newer version CRU TS 3.0 for which a publication is in preparation.

Model or data set	Resolution (atm/atm levels/ocn)	Time period used (number of runs)	Reference
CCSM3	T31/26/~3° × 3°	1000–2000 AD (1)	Hofer et al. (2011)
CCSM3	T31/26/~3° × 3°	1500–2000 AD (4)	Lehner et al. (in press)
CCSM3	T42/26/~1° × 1°	1149–1499 AD (6)	This study
CNRM	T63/31/~2° × 0.5–2°	1000–1999 AD (1)	Swingedouw et al. (2011)
ECHO-G	T30/19/~2.8° × 2.8°	1000–1990 AD (2)	González-Rouco et al. (2006)
MPI	T31/19/~3° × 3°	1000–2000 AD (3)	Jungclaus et al. (2010)
CRU Reanalysis	1° × 1°	1901–2009 AD (1)	Mitchell and Jones (2005)
20CR	2° × 2°	1871–2008 AD (56)	Compo et al. (2011)

region (e.g., Mangini et al., 2005). Mangini et al. (2005) is an Alpine winter temperature proxy used by Trouet et al. (2009) to illustrate the potential influence of the NAO on European winter temperature. The models simulate a cooling at this location as well (not shown), despite not simulating an MCA-LIA NAO decrease of the magnitude suggested by Trouet et al. (2009).

Regarding atmospheric modes, the models are able to reproduce the temporal and spatial patterns of the NAO with intermediate skill (CNRM, ECHO-G, MPI) and with good skill (CCSM3) (Stoner et al., 2009). As a reference Stoner et al. (2009) used the ERA-40 and NCEP reanalysis data sets which cover only the second half of the 20th century. Bearing in mind the 30-years resolution of the proxy NAO reconstruction, the ERA-40 and NCEP data sets are not of adequate length to be used in this study. We therefore refer to two slightly longer reanalyses (which, nevertheless, are relatively short): the station data-constrained precipitation and temperature reanalysis from the Climate Research Unit (CRU; Mitchell and Jones, 2005) and the hindcast ensemble simulation from the Twentieth Century Reanalysis Project (20CR; Compo et al., 2011). Additionally, we use several instrumental NAO indices going further back in time to test our results. It has been shown by Schmutz et al. (2000) and Cook et al. (2002, after Schmutz et al. (2000)) that the length of the validation/calibration period is crucial for the outcome of a reconstruction and that therefore the longest available instrumental time series should be used.

The model output and the reanalysis data sets are used in a perfect pseudo-proxy approach (e.g., Zorita et al., 2003) to mimic the two proxies used by Trouet et al. (2009) for a reconstruction of the NAO index over the past millennium. The qualifier "perfect" refers to the fact that we do not add artificial noise to the pseudo-proxy but assume the model simulation to represent reality. To mimic the first proxy, the Scotland stalagmite from Proctor et al. (2000), December–March precipitation from northern Scotland is extracted from models and reanalysis (hereafter P_s). For the second proxy, the tree ring-based drought reconstruction by Esper et al. (2007), the Standardized Precipitation Index (SPI; e.g., Guttman, 1999) is calculated from precipitation over Morocco and then averaged from February–June (P_m). These two pseudo-proxies are then treated as in Trouet et al. (2009) to calculate an NAO index: smoothed with a 30-year cubic spline, normalized over a common period, and subtracted from each other. As in Trouet et al. (2009), this index is hereafter called NAO$_{ms}$. To investigate the sensitivity of the NAO$_{ms}$ to the geographical location of the precipitation signal in models and reanalyses, we vary the averaging box for both proxy sites (four boxes each for Scotland and Morocco; see Fig. 2a). Additionally, we use December–March sea level pressure values from model simulations and 20CR to calculate PC-based (over domain 25–80°N/ 70°W-40°E), Iceland-Azores, Iceland-Lisbon, and Iceland-Gibraltar NAO indices, which are the commonly accepted, or classical, NAO indices (boxes, over which sea level pressure is averaged are marked in Fig. 2a). The corresponding station data-based indices are provided by the Climate Analysis Section of the National Center for Atmospheric Research in Boulder (Hurrell (1995); www.cgd.ucar.edu/cas/jhurrell/indices.html [November 2011]).

3. Results

In a first step, the agreement of NAO$_{ms}$ with classical NAO indices is tested in a surrogate of the real world – station data and reanalysis data sets. Thereby, we extend the set of tests that can be conducted compared to Trouet et al. (2009) both temporally and in terms of available data sets. In a second step, NAO$_{ms}$ is calculated from output of 17 transient simulations with four different models, totaling roughly 11,000 model years. In this approach we are interested more in the concept behind NAO$_{ms}$ and its robustness over time.

3.1. Instrumental data

In Fig. 2 the classical NAO indices (from station data) are plotted together with different realizations of the NAO$_{ms}$ to test their agreement. Fig. 2b shows the actual proxies used by Trouet et al. (2009) and the NAO$_{ms}$ together with the longest instrumental NAO index (1821–present, though the first two winter contain data gaps; Vinther et al., 2003), all as 30-yr smoothed time series. Surprisingly, the correlation over the full common period 1823–1993 AD of the sole Scotland precipitation proxy (P_s proxy) with the instrumental NAO index (1823–1993 AD: $r_{P_s\ proxy|NAO_{Vinther}} = 0.90, p < 0.01$) is slightly higher than the correlation of NAO$_{ms}$ with the instrumental NAO index (1823–1993 AD: $r_{NAO_{ms}|NAO_{Vinther}} = 0.81, p < 0.05$). Restricting the correlation to different segments of the full period reveals that the Morocco proxy supports the NAO$_{ms}$ only during the period of 1914–1993 AD when $r_{NAO_{ms}|NAO_{Vinther}}$ is larger than $r_{P_s\ proxy|NAO_{Vinther}}$ ($p < 0.3$), i.e., when the inclusion of the Morocco proxy improves the correlation. Using a longer time period, the NAO$_{ms}$ is less, or at best equally well correlated with the instrumental NAO index than is the sole Scotland precipitation proxy. Thus, the Morocco proxy seems to add little to the stability and accuracy of the NAO$_{ms}$. During the 19th century (1823–1899 AD), the correlation of both proxies, and consequently the NAO$_{ms}$, with the instrumental NAO index strongly decreases, suggesting that during that time neither the sole proxies nor the combined index can correctly describe the instrumental NAO index (visible also in Fig. 2b). This raises the question whether the validation period adopted in Trouet et al. (2009) is long enough and whether the proxies are capable of always adequately capturing the signal of the NAO's northern and southern centers of action. Note, that the correlations on the 30-year smoothed 19th century records are not significant due to the reduced number of degrees of freedom. Further, there remains some doubt about the reliability of the early instrumental pressure records due to missing metadata and data inhomogeneities (Vinther et al., 2003).

3.2. Reanalyses

For both reanalysis data sets the classical NAO indices agree well among each other (Fig. 2c,d). The correlation between PC-based, Iceland-Azores, Iceland-Lisbon, and Iceland-Gibraltar on basis of December–March means is 0.69–0.92 ($p < 0.001$; 20CR: 1871–2008 AD; CRU: 1901–2009 AD; Fig. 3a). These different indices are distributed across the estimated range of spatial variability of the NAO centers of action (Fig. 2a, see also Wanner et al., 2001). Therefore, they are potentially able to also capture the non-stationary spatial behavior of the NAO (at least for the winter NAO; Portis et al., 2001) and are regarded as a robust measure of the atmospheric circulation associated with the NAO.

In Fig. 2c the CRU data set is used as a source for the pseudo-proxies, i.e., to calculate NAO$_{ms}$. The gray shadings each represent 16 realizations (4 × 4 different boxes) of NAO$_{ms}$. Along with that, station data-based NAO indices are plotted. While reproducing the most recent decadal-scale negative-to-positive anomaly of the NAO, the NAO$_{ms}$ starts to diverge from the classical indices around the middle of the 20th century and further back. Fig. 2c also features the seasonal (December–March), unsmoothed NAO$_{ms}$ calculated from CRU (lightest gray shading). The comparison with the normal NAO$_{ms}$ suggests that through the normalization after the smoothing an apparently persistent strong ($>1.5\sigma$) positive or negative phase of the NAO can be obtained whereas actually there is just an increased frequency of more positive or negative seasons (not necessarily with an average of $\geq 1.5\sigma$). This is important to keep in mind when interpreting either the persistent +2 phase of the Medieval NAO$_{ms}$ by Trouet et al. (2009) or any smoothed index presented in the study
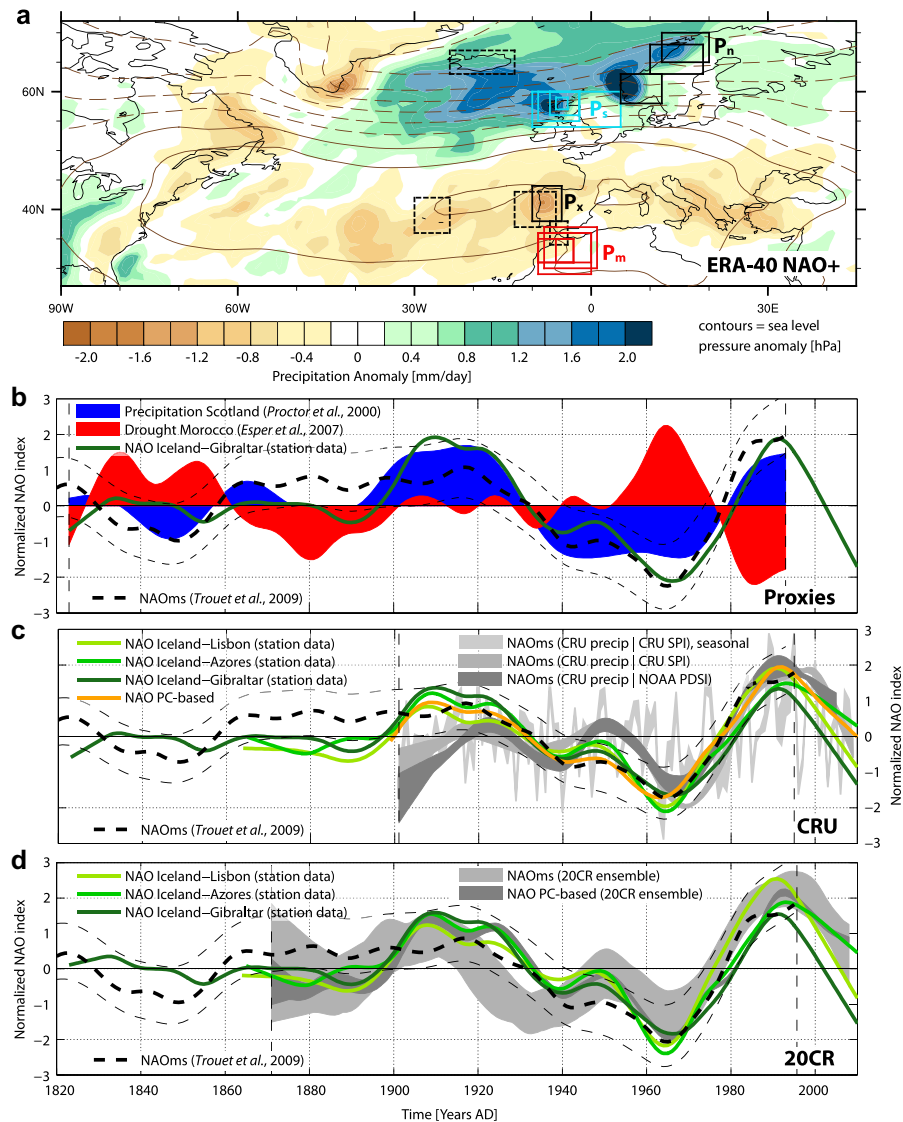
Fig. 2. (a) Precipitation and sea level pressure anomaly composite of the positive NAO phases (December–March PC-based > 1.5 – long-term mean) in the 1° × 1° ERA-40 reanalysis (1958–2001 AD; Uppala et al., 2005). Boxes indicate pseudo-proxies regions used in this study: dashed black = sea level pressure, blue = Scotland (P_s), red = Morocco (P_m), solid black = supporting precipitation pseudo-proxies over Scandinavia (P_n) and the Iberian Peninsula (P_x). (b) NAO$_{ms}$ from Trouet et al. (2009) and the proxies on which it is based. (c) NAO$_{ms}$ calculated with CRU (Scotland precipitation vs. Morocco SPI or PDSI). (d) NAO$_{ms}$ and PC-based NAO index calculated from 20CR. (c, d) Along with that up to four instrumental NAO indices are given. The common normalization period is indicated by the vertical dashed lines. (For interpretation of the references to color in this figure legend, the reader is referred to the web version of this article.)

here, as we apply the same method as Trouet et al. (2009) for reasons of optical comparability. Trouet et al. (2009), Fig. 1, is in that respect misleading, as both the individual proxy time series as well as the combined NAO$_{ms}$ are tagged "z-scored", when in fact only the two proxy time series have been normalized. The alternative use of the Palmer Drought Severity Index (PDSI; Dai et al., 2004) in the construction of the NAO$_{ms}$ further illustrates that the choice of the drought index for the Morocco pseudo-proxy has a small effect on the decadal-scale behavior of the NAO$_{ms}$ (Fig. 2c).

When the NAO$_{ms}$ is calculated from 20CR, the results are similar (Fig. 2d). The shift from a negative NAO phase during the 1960s–1970s

to a more positive NAO phase during the 1980s–1990s is recorded by the NAO$_{ms}$. However, when going further back in time the classical indices and the NAO$_{ms}$ start to diverge, despite the considerable range of the 20CR ensemble (4 × 4 different boxes × 56 ensemble members = 896 realizations of NAO$_{ms}$). At the same time the range of the PC-based (56 realizations) is narrower and follows the station data-based classical NAO indices more closely. This underlines the consistency of the classical NAO indices, which appears to be independent of the data source used (reanalysis or station data). Prior to about 1890 AD, the uncertainty of 20CR precipitation seems to be too large to constrain a clear NAO$_{ms}$ (Fig. 2d).

3.3. Models

3.3.1. Persistence of anomalous NAO phases

Due to the chaotic nature of the atmospheric circulation the coupled models are not expected to reproduce the decadal variability of the actual NAO. On longer time scales (or in case of a strong volcanic eruption), however, external forcing might impact climate variables that are crucial for the NAO. This then provides the opportunity to compare proxy and model NAO indices with regard to their low-frequency trends, i.e., a persistent positive NAO during the MCA and the suggested shift to a more negative NAO from the MCA to the LIA. However, none of the model simulations examined here shows century-scale persistent phases of positive or negative NAO, regardless of the index in question. In the smoothed and normalized time series the models show a few anomalous phases of up to 40−60 years length (Fig. 4). In Fig. 4a the Medieval part of the NAO_{ms} by Trouet et al. (2009) is plotted for comparison. It becomes apparent that the amplitude of the Medieval NAO_{ms} by Trouet et al. (2009) is extraordinary.

As a consequence of not simulating a century-scale persistent positive NAO, the models also do not reproduce the clear shift of the NAO index from positive to more negative values when going from the MCA into the LIA. None of the millennial simulations produces a significant shift (5% level using seasonal values) of the classical NAO indices from the MCA (1000−1250 AD) to the LIA (1450−1700 AD). Still, it is noteworthy that they simulate a reduction of the indices (the largest is −0.18 with unsmoothed and −0.75 with smoothed values). Our ensemble of the medium-resolution CCSM3, that covers the transition phase from the MCA to the LIA (1149−1499 AD), also does not produce significant reductions of the NAO index. Two of the six ensemble members even show an insignificant increase.

3.3.2. Robustness of NAO_{ms}

Regarding the correlation of NAO indices among each other (over the respective length of a simulation), the results are fairly similar to the reanalysis data sets: the correlation among the classical indices is significantly higher than that of the classical indices with the pseudo-proxy NAO_{ms} (Fig. 3a and b). Note, that the correlations in Fig. 3 are done on unsmoothed December−March means. Further, in the remaining part of the paper we show comparisons with PC-based and Iceland-Azores only, as Iceland-Lisbon and Iceland-Gibraltar are very similar to Iceland-Azores ($r = 0.88−0.93$ in 20CR and $r = 0.93−0.98$ in models, both $p < 0.001$). To test whether a correlation between two indices is stable over time, we calculate a 50-year moving window correlation of the two indices over the full length of a millennial simulation. A probability density function (PDF) is then calculated on the resulting time series, providing a measure on of how stable the relationship between two indices is. The PDF of the correlation among the classical indices is narrower than the PDF of the correlation of NAO_{ms} with classical indices (Fig. 3e). This model-independent finding underlines the robustness of the classical indices compared to the NAO_{ms}. The strength of the link between the NAO_{ms} and the classical indices, on the other hand, strongly varies from model to model. CNRM, for example, shows no, or only weak, correlations (−0.01 to +0.36) of NAO_{ms} with the classical NAO indices, while the three ensemble members of MPI all show correlations between 0.38 and 0.61. Also, the sensitivity of the NAO_{ms} to the location of the pseudo-proxy box seems to be model-dependent, as can be seen by the size of the spreads for the different models (Fig. 3e).

In Fig. 4, we select six periods in which disagreement between the NAO_{ms} and the classical indices occurs. In order to better understand the underlying circulation and precipitation pattern, we present a composite analysis over these selected periods on the basis of December−March means (Fig. 5). SLP and precipitation anomalies serve as a reference for the actual climate field simulated during these periods. Regressing the NAO_{ms} onto SLP resembles the circulation pattern indirectly proposed by the pseudo-proxy index. For the latter, the regression coefficients are multiplied by the mean of the unsmoothed NAO_{ms} during the selected period. In the following we classify these six periods into three types by looking at the classical NAO indices in Fig. 4: (i) when they are positive (periods 1 (1251−1265 AD) and 4 (1016−1037 AD); marked in Fig. 4), (ii) neutral, i.e., average within ±0.2, (periods 5 (1212−1237 AD) and 6 (1780−1797 AD)), or (iii) negative (periods 2 (1966−1983 AD) and 3 (1775−1803 AD)).

The cases of positive NAO both feature a clear NAO-positive SLP pattern, however, the locations of the centers of action vary. Especially the southern high pressure center can shift from the Azores (period 1) to the Iberian Peninsula (period 4). The northern center is located in the Iceland-Greenland region. While these situations resemble a positive NAO in the classical sense, they do not necessarily result in the precipitation pattern expected from reanalysis (e.g., Fig. 2a). During period 1 the slight eastward displacement of the high pressure center leads to a dry anomaly over Scotland and wetter conditions over large parts of the Mediterranean, in turn resulting in a negative NAO_{ms}. During period 4 the high pressure center spans from the Azores to Central Europe, resulting to a large extent in the precipitation signal known from reanalysis. However, Scotland lies just in between the wet and dry anomaly, and so the pseudo-proxies produce a neutral NAO_{ms}.

The cases of a neutral NAO both show a ridge of low pressure across the Atlantic which is bordered by elevated pressure in the North and South. In both cases, Scotland and Morocco receive opposite precipitation signals, however, in one case it is Scotland dry-Morocco wet (period 5) while in the other it is vice versa (period 6). Consequently, the NAO_{ms} falsely indicates negative and positive states of the NAO, respectively.

Finally, the cases of negative NAO both feature a negative SLP anomaly in the south with a northern counterpart of elevated pressure. In period 2, the southern low pressure center is weak and the negative NAO arises mainly from the widespread high pressure in the North. Both Scotland and Morocco do not experience a clear precipitation anomaly, which is why the NAO_{ms} is close to zero instead of negative. A similar situation occurs during period 3 when the low pressure center leads to a clear precipitation signal over large parts of the Iberian Peninsula, i.e., just North of Morocco. Morocco itself does not experience this anomaly. As Scotland experiences a weak wet phase, NAO_{ms} wrongly attributes this situation to an NAO-positive phase.

3.3.3. Stabilization of NAO_{ms}

In the previous section situations of disagreement between NAO_{ms} and the classical indices were examined. Reconciling those situations, it becomes apparent how additional pseudo-proxies could help making the NAO_{ms} more robust. For example, from reanalysis we expect Scotland and the Norwegian coast, as well as Morocco and the Iberian Peninsula, to have similar precipitation signals during positive or negative NAO phases (Fig. 2a). However, in several of the previously discussed situations this is not the case: the precipitation anomaly due to a certain NAO phase is displaced slightly to the North, leaving the Morocco or Scotland location without the expected signal. In these situations, the Iberian Peninsula and the Norwegian coast are perfectly situated to captured this signal and valuable information could be gained from proxies in these regions. The chance that a precipitation signal is missed by both Morocco and the Iberian Peninsula (Scotland and the Norwegian coast, respectively) is comparably small.

To test this concept, we define three artificial precipitation proxies along the Norwegian coast (P_n) and one over Portugal/Spain (P_x), marked in Fig. 2a. We average December−March precipitation over a certain geographical box and normalize the time series. The
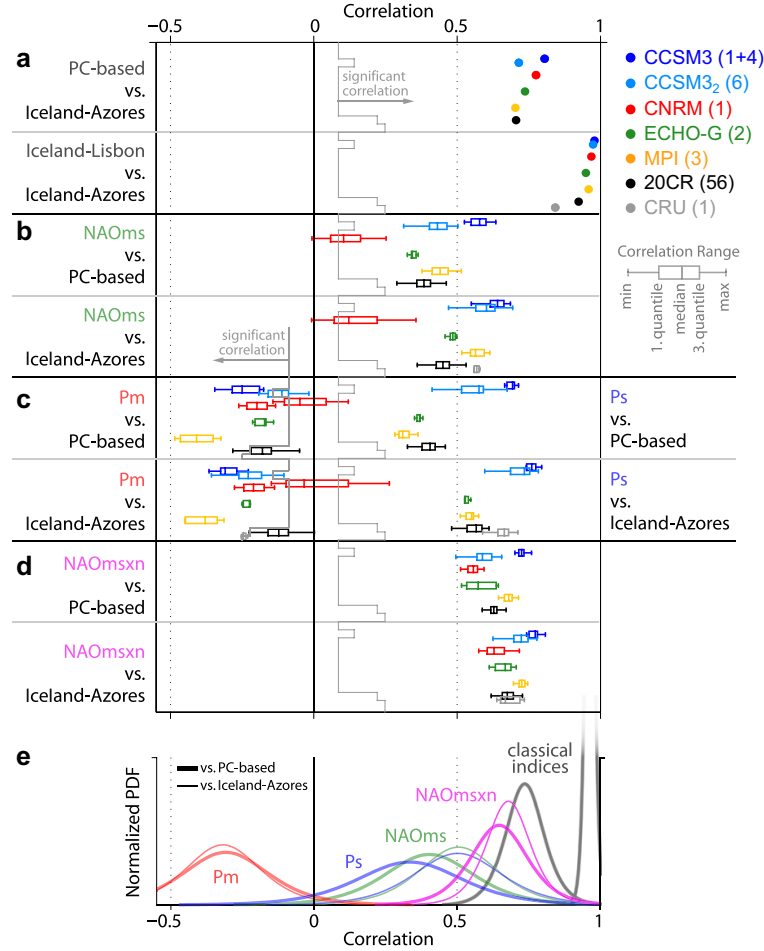
Fig. 3. Correlation of different NAO indices (December–March means, unsmoothed) from models and reanalyses: (a) between Iceland-Azores and two classical NAO indices (PC-based, Iceland-Lisbon), (b) between the perfect pseudo-proxy NAO$_{ms}$ and two classical NAO indices, (c) between Scotland and Morocco precipitation (P_s, P_m) and two classical NAO indices, (d) between the improved NAO$_{msxn}$ and two classical NAO indices. The range of each correlation in (b), (c), and (d) arises from varying the geographical boxes used for the calculation of NAO$_{ms}$, P_s, P_m, or NAO$_{msxn}$, as well as from the ensemble (in (a) only the ensemble mean is given). CCSM3$_2$ refers to the ensemble simulations over the MCA-LIA transition phase (1149–1499 AD). The number of ensemble members of a specific model is given in brackets in the upper right corner. The coefficient beyond which a correlation is significant (1% level) is indicated by the vertical gray line. (e) The probability density functions (PDF) are calculated from 50-year moving window correlations between different NAO indices for all the millennial model simulations (CCSM3$_2$ and reanalysis are excluded). Thereby they show the variability of the correlations through the course of a millennium simulation (details see text).

three P_n are then combined with the four P_s to form twelve versions of a new northern regional pseudo-proxy. For the southern center we combine P_x with all four P_m to form four versions of a southern regional pseudo-proxy. In order to determine the weights for such a combination we do a linear regression on the PC-based NAO index from the ensemble mean 20CR data with every combination of P_s and P_n (also taken from 20CR):

$$NAO_{20CR} = \beta_{sij} \cdot P_{si} + \beta_{nij} \cdot P_{nj} + \varepsilon_{ij}, \qquad (1)$$

where i and j indicate the different geographical boxes used, β_{sij} and β_{nij} are the regression coefficients associated with a certain combination of P_{si} and P_{nj}, and ε_{ij} is the residual to be minimized. Solving the model for all combinations of geographical boxes results in twelve pairs of the regression coefficients (the same is done for P_{mi} and P_x, resulting in four pairs of coefficients).

All coefficients of a specific P are averaged, leaving one coefficient for each P ($\overline{\beta_{sij}}, \overline{\beta_{nij}}, \overline{\beta_{mi}}, \overline{\beta_{xi}}$). This way we neglect differences within one region (e.g., among the three Scandinavia pseudo-proxies) and imply that it does not matter which pseudo-proxy from that region is used. Thereby, we also introduce some uncertainty compared to the prefect approach of calculating coefficients individually for each box and each model. Each pair of coefficients ($\overline{\beta_{sij}}/\overline{\beta_{nij}}$, $\overline{\beta_{mi}}/\overline{\beta_{xi}}$) is then scaled so that the sum of the two is one, representing the weights of P_s relative to P_n (P_m relative to P_x, respectively). According to this procedure, the weights are calculated and applied as follows to create a new NAO index

$$NAO_{msxn} = (0.52 \cdot P_s + 0.48 \cdot P_n) - (0.19 \cdot P_m + 0.81 \cdot P_x). \qquad (2)$$

NAO$_{msxn}$ is calculated for all models and reanalysis data sets with the weights from Eq. (2) and tested in the same manner as
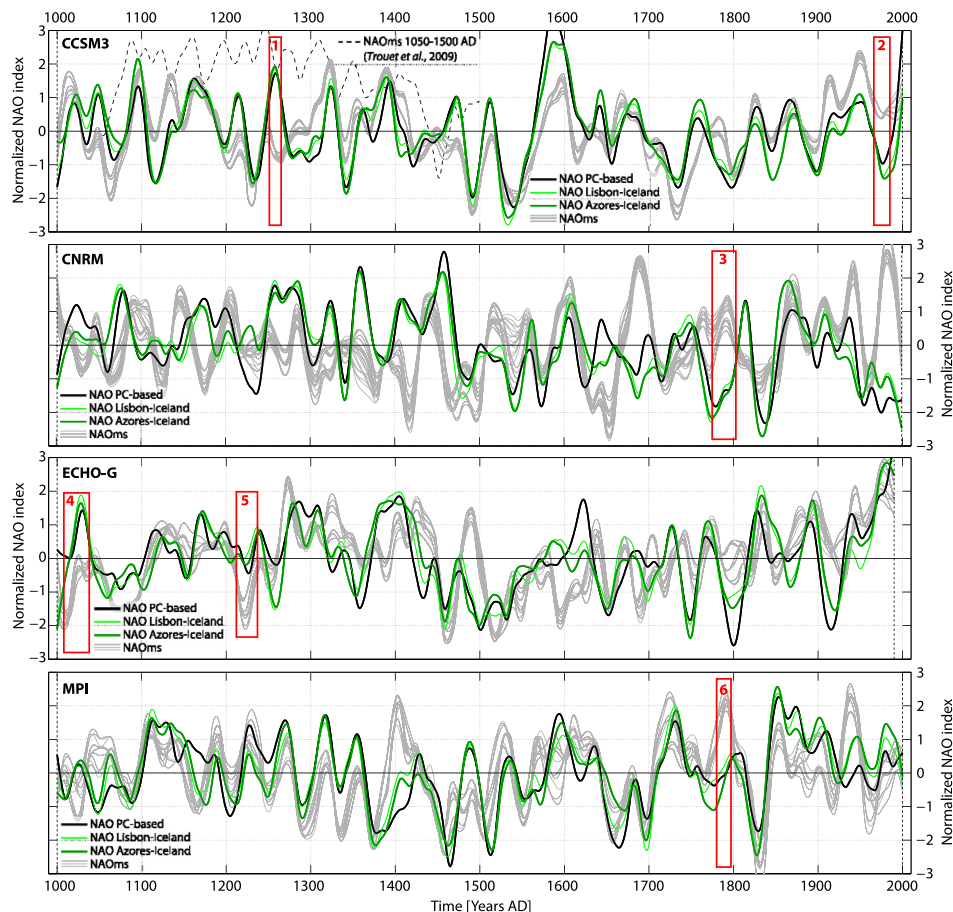
Fig. 4. NAO indices from four different models (denoted in the upper left corner of each subplot). Shown are the classical NAO indices PC-based, Lisbon-Iceland, and Azores-Iceland together with the NAO$_{ms}$, all calculated from model output. The time series are normalized over the common period indicated by the vertical dashed lines. A part of the NAO$_{ms}$ from Trouet et al. (2009) is given in (a) for comparative reasons. For the models with an ensemble, one representative simulation was chosen. Exemplary periods of disagreement between the classical NAO indices and the NAO$_{ms}$ are framed red and referred to in Fig. 5.

NAO$_{ms}$. The new NAO$_{msxn}$ on average correlates better with classical indices than does the NAO$_{ms}$: the correlation over the full length of the reanalyses or the model simulations is always larger than 0.49 (Fig. 3d). Thus this convergence of the different models in terms of full-length correlation illustrates that NAO$_{msxn}$ is a robust index, independent of the models' individual representation of precipitation. For example, while NAO$_{ms}$ appeared not to work in CNRM (correlations close to zero), NAO$_{msxn}$ shows comparable skill for all models. This increased robustness of the new index is also reflected in the PDFs of the moving window correlation. They are narrower, indicating that there are fewer 50-year periods of disagreement in the millennial simulations (Fig. 3e). Also, the number of winters in which the NAO$_{msxn}$ still disagrees with the classical indices (i.e., indices differing by more than 1) is reduced by about 50% compared to NAO$_{ms}$ across all models (not shown). All analyses presented in this section are also applied to the multi-century control simulations of the transient simulations, excluding the CNRM for which no control simulation was available (not shown). In all cases, the results were found to be the same, i.e., the correlations do not significantly differ from the transient simulations and no century-long persistent anomalous NAO phases

were found. It therefore appears that the results are not dependent on the transient external forcing.

4. Discussion

From reanalyses and instrumental records it becomes apparent that the NAO$_{ms}$ fails to verify against classical NAO indices during the early 20th and 19th century, as both proxies used in NAO$_{ms}$ are reversed in their relation to the NAO during that time. While the individual proxies used in Trouet et al. (2009) represent well verified reconstructions (see Proctor et al., 2000; Esper et al., 2007), their relation to the NAO is more difficult to proof. The challenges inherent in the use of other climate variables than sea level pressure to describe the NAO are illustrated also by the comparison of NAO$_{ms}$ with other existing NAO reconstructions (Table S1, supporting online material for Trouet et al., 2009): there exist correlations among these reconstructions, however, they temporally vary and they are not always significant. It seems therefore more likely that the proxies in NAO$_{ms}$ are not fully representative of the NAO during the 19th century.

When calculated from model output, the concept of NAO$_{ms}$ reveals similar weaknesses. The correlation with classical indices is
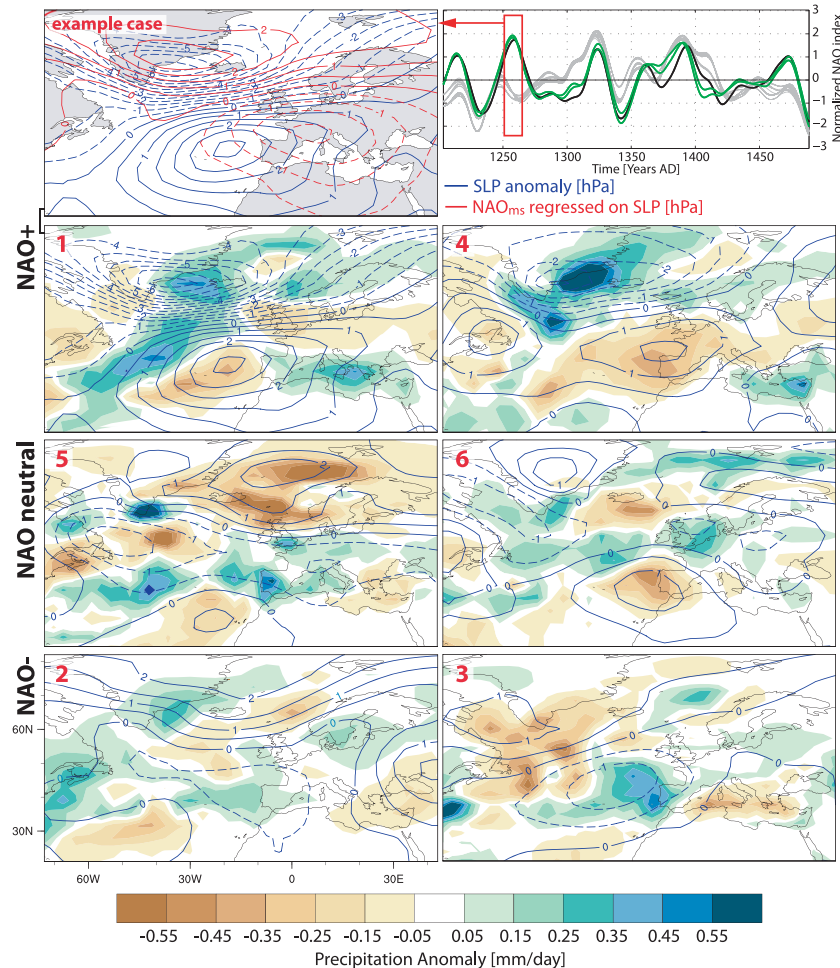
Fig. 5. Periods of disagreement between the classical NAO indices and the NAO$_{ms}$ in the models. The first row illustrates example case #1, the legend for the right panel is the same as in Fig. 4. In the example case #1 the red contours are the regression of the mean NAO$_{ms}$ onto the December–March SLP during the specific period. The second, third, and fourth row show examples for positive, neutral, and negative phases of NAO, respectively. The red numbers correspond to the frames in Fig. 4. Shown are the December–March precipitation (shading) and sea level pressure (SLP; blue contours) anomalies from the long-term mean. (For interpretation of the references to color in this figure legend, the reader is referred to the web version of this article.)

significantly lower than when classical indices are correlated among themselves. To a certain degree this comes as no surprise, as the classical indices are based directly on sea level pressure while the NAO$_{ms}$ uses precipitation, for which the NAO provides a smaller amount of explained variance (e.g., Dai et al., 1997). However, in the model simulations, the correlation between NAO$_{ms}$ and classical indices is also not stable over time, i.e., over the last millennium. This again points to the possibility that the NAO$_{ms}$ at times does not necessarily represent the NAO in the classical sense. Further, this finding is coherent with other model studies that found the relationship between NAO and precipitation not to be stable (Vicente-Serrano and Lopez-Moreno, 2008). In other words, the locations of the proxies in NAO$_{ms}$ are likely not optimal or sufficient to capture the signal from the large-scale circulation pattern. In particular, the Morocco proxy does not add significantly to the robustness of the NAO$_{ms}$ as it often lies just beyond the border of the southern hydrological center of action during anomalous NAO phases. To some extent this is true also for the Scotland proxy where the

precipitation band associated with the NAO can be located just north of the site. Additionally, bearing in mind the documented (Jung and Hilmer, 2001) and modeled (Ulbrich and Christoph, 1999; Raible et al., 2006) possibility of shifting NAO centers of action, the use of few and not particularly well located proxies casts doubt on the credibility of a reconstruction based on them.

Therefore, by complementing the Scotland proxy with a precipitation proxy from along the Norwegian coast, the description of the northern center of action of the NAO becomes substantially more robust. The same holds true for the southern center of action when we support Morocco by a precipitation proxy from the Iberian Peninsula. The so created new NAO index has a significant correlation with classical NAO indices of at least 0.49 for all models, reanalyses, and combinations of geographical boxes. Also, the temporal stability of the so created index is higher than of the NAO$_{ms}$, as the situations of disagreement with classical indices are greatly reduced in number. This qualifies the new index to be a robust description of the actual NAO behavior. Note, however, that in reality proxies to

complement the NAO$_{ms}$ by Trouet et al. (2009) at these locations have yet to be discovered. Additionally, in our minimalistic approach we do not consider potential other proxies (e.g., temperature) at other locations that might further improve the reconstruction (as done in, e.g., Luterbacher et al. (2002); Cook et al. (2002)).

Regarding the occurrence of persistent anomalous phases of the NAO, models do not simulate such phases with only the realistic natural and anthropogenic forcing applied (see also Yiou et al., 2012). This finding is valid for all the NAO indices, also the NAO$_{ms}$. At the same time the models produce a realistic temperature evolution over the study area, indicating that an NAO phase change of the amplitude suggested by Trouet et al. (2009) is not a prereq-uisite for the explanation of the MCA-LIA climate transition. Here, new experimental setups with artificially imposed persistent NAO phases are needed (similar to, e.g., Palastanga et al., 2011). Thereby, insights might also be gained concerning the question whether models generally lack the capability of simulating persistent phases of the NAO or if the loss of variance in the Medieval part of the NAO$_{ms}$ (which largely originates from the Scotland proxy) is an artifact of processes not related to the atmospheric circulation. By using several models with different resolutions we provide a large sample of physically consistent analogs to reality. Thereby, we can reduce, but not exclude, the chance that a severe model bias undermines the credibility of the results. In our study, eleven out of thirteen model simulations on average produce a reduction of the classical NAO indices from the MCA to the LIA. Even though none of these are significant, a small shift from a more positive to a more negative NAO phase cannot be excluded.

The pseudo-proxy exercise further shows that a smoothed and normalized NAO time series at times can have a larger mean than the annual values it is based on. This complicates the interpretation of the +2 amplitude of the NAO$_{ms}$ during the MCA and calls for a new assessment on what the actual multi-decadal variability of atmospheric circulation in the North Atlantic-European region has been in the first half of the past millennium.

Note, that the pseudo-proxy exercise is in many respects an idealized and simplified experiment as in reality a precipitation proxy inherits noise and measurement errors that are absent in our study. Even two NAO reconstructions using multiple and well distributed proxies do not necessarily agree, as can be shown at the example of Cook et al. (2002) vs. Luterbacher et al. (2002), and for longer time scales in Raible et al. (2005). We can nevertheless conclude that precipitation proxies in adequate locations are suited to reconstruct past circulation regimes, as suggested by Zorita and González-Rouco (2002). However, a reconstructed index' proposed physical meaning has to withstand thorough tests based on model simulations and reanalyses such as presented here.

5. Conclusions

The robustness of the proxy-based NAO reconstruction (NAO$_{ms}$) by Trouet et al. (2009) is tested in a perfect pseudo-proxy approach using comprehensive climate models, reanalysis data sets, and instrumental records. The failure of NAO$_{ms}$ to verify against classical NAO indices during the early 20th and 19th century urges future reconstructions to extend the calibration/validation period beyond the 20th century using reanalyses and instrumental data — a conclusion that was already reached a decade ago.

Model simulations reveal that the proxy locations used in the reconstruction by Trouet et al. (2009) are not always able to capture the NAO precipitation signal, resulting in decade-long periods of disagreement of NAO$_{ms}$ with the classical NAO indices. By using additional pseudo-proxies in the vicinity of the existing proxies we are able to catch the non-stationary NAO centers of action and improve the stability of the reconstruction concept. Thereby, we also

provide a physical explanation for the weaknesses of the NAO$_{ms}$ concept and lay out a framework of tests for future reconstructions.

Further, results from transient model simulations neither support a persistent positive NAO during the MCA, nor a strong phase shift of the NAO when passing into the LIA. The here presented evidence should motivate both the proxy and model community to work toward a revised assessment of the role of the NAO during the first half of the last millennium.

References

Appenzeller, C., Stocker, T., Anklin, M., 1998. North Atlantic Oscillation dynamics recorded in Greenland ice cores. Science 282, 446–449.
Casty, C., Raible, C.C., Stocker, T.F., Wanner, H., Luterbacher, J., 2007. A European pattern climatology 1766–2000. Climate Dynamics 29, 791–805.
Compo, G.P., Whitaker, J.S., Sardeshmukh, P.D., Matsui, N., Allan, R.J., Yin, X., Gleason Jr., B.E., Vose, R.S., Rutledge, G., Bessemoulin, P., Broennimann, S., Brunet, M., Crouthamel, R.I., Grant, A.N., Groisman, P.Y., Jones, P.D., Kruk, M.C., Kruger, A.C., Marshall, G.J., Maugeri, M., Mok, H.Y., Nordli, O., Ross, T.F., Trigo, R.M., Wang, X.L., Woodruff, S.D., Worley, S.J., 2011. The twentieth century reanalysis project. Quarterly Journal of the Royal Meteorological Society 137, 1–28.
Cook, E., D'Arrigo, R., Briffa, K., 1998. A reconstruction of the North Atlantic Oscil-lation using tree-ring chronologies from North America and Europe. The Holocene 8, 9–17.
Cook, E.R., D'Arrigo, R.D., Mann, M.E., 2002. A well-verified, multiproxy recon-struction of the winter North Atlantic Oscillation index since A.D. 1400. Journal of Climate 15, 1754–1764.
Cullen, H., D'Arrigo, R., Cook, E., Mann, M., 2001. Multiproxy reconstructions of the North Atlantic Oscillation. Paleoceanography 16, 27–39.
Dai, A., Fung, I., DelGenio, A., 1997. Surface observed global land precipitation variations during 1900–88. Journal of Climate 10, 2943–2962.
Dai, A., Trenberth, K., Qian, T., 2004. A global dataset of Palmer Drought Severity Index for 1870–2002: relationship with soil moisture and effects of surface warming. Journal of Hydrometeorology 5, 1117–1130.
Esper, J., Frank, D., Buentgen, U., Verstege, A., Luterbacher, J., 2007. Long-term drought severity variations in Morocco. Geophysical Research Letters 34.
Glueck, M.F., Stockton, C.W., 2001. Reconstruction of the North Atlantic Oscillation, 14291983. International Journal of Climatology 21, 1453–1465.
González-Rouco, J., Beltrami, H., Zorita, E., von Storch, H., 2006. Simulation and inversion of borehole temperature profiles in surrogate climates: spatial distribution and surface coupling. Geophysical Research Letters 33.
Gray, L.J., Beer, J., Geller, M., Haigh, J.D., Lockwood, M., Matthes, K., Cubasch, U., Fleitmann, D., Harrison, G., Hood, L., Luterbacher, J., Meehl, G.A., Shindell, D., van Geel, B., White, W., 2010. Solar influences on climate. Reviews of Geophysics 48.
Guttman, N., 1999. Accepting the standardized precipitation index: a calculation algorithm. Journal of the American Water Resources Association 35, 311–322.
Hofer, D., Raible, C.C., Stocker, T.F., 2011. Variations of the Atlantic meridional overturning circulation in control and transient simulations of the last millennium. Climate of the Past 7, 133–150.
Hurrell, J.W., 1995. Decadal trends in the North Atlantic Oscillation: regional temperatures and precipitation. Science 269, 676–679.
IPCC, 2001. Climate Change 2001, the Scientific Basis. Intergovernmental Panel on Climate Change. Cambridge University Press.
Jones, P.D., Jonsson, T., Wheeler, D., 1997. Extension to the North Atlantic Oscillation using early instrumental pressure observations from Gibraltar and south-west Iceland. International Journal of Climatology 17, 1433–1450.
Jung, T., Hilmer, M., 2001. The link between the North Atlantic Oscillation and Arctic Sea ice export through Fram Strait. Journal of Climate 14, 3932–3943.

Jungclaus, J.H., Lorenz, S.J., Timmreck, C., Reick, C.H., Brovkin, V., Six, K., Segschneider, J., Giorgetta, M.A., Crowley, T.J., Pongratz, J., Krivova, N.A., Vieira, L.E., Solanki, S.K., Klocke, D., Botzet, M., Esch, M., Gayler, V., Haak, H., Raddatz, T.J., Roeckner, E., Schnur, R., Widmann, H., Claussen, M., Stevens, B., Marotzke, J., 2010. Climate and carbon-cycle variability over the last millennium. Climate of the Past 6, 723–737.

Kuettel, M., Xoplaki, E., Gallego, D., Luterbacher, J., Garcia-Herrera, R., Allan, R., Barriendos, M., Jones, P.D., Wheeler, D., Wanner, H., 2010. The importance of ship log data: reconstructing North Atlantic, European and Mediterranean sea level pressure fields back to 1750. Climate Dynamics 34, 1115–1128.

Kutzbach, J., 1970. Large-scale features of monthly mean Northern Hemisphere anomaly maps of sea-level pressure. Monthly Weather Review 98, 708–716.

Lehner, F., Raible, C.C., Stocker, T.F., Hofer, D., in press. The freshwater balance of polar regions in transient simulations from 1500 to 2100 AD using a comprehensive coupled climate model. Climate Dynamics.

Luterbacher, J., Schmutz, C., Gyalistras, D., Xoplaki, E., Wanner, H., 1999. Reconstruction of monthly NAO and EU indices back to AD 1675. Geophysical Research Letters 26, 2745–2748.

Luterbacher, J., Xoplaki, E., Dietrich, D., Jones, P.D., Davies, T.D., Portis, D., Gonzalez-Rouco, J.F., von Storch, H., Gyalistras, D., Casty, C., Wanner, H., 2002. Extending North Atlantic Oscillation reconstructions back to 1500. Atmospheric Science Letters 2, 114–124.

Mangini, A., Spotl, C., Verdes, P., 2005. Reconstruction of temperature in the Central Alps during the past 2000 yr from a delta(18)O stalagmite record. Earth and Planetary Science Letters 235, 741–751.

Mann, E.M., Zhang, Z., Rutherford, S., Bradley, R.S., Hughes, M.K., Shindell, D., Ammann, C., Faluvegi, G., Ni, F., 2009. Global signatures and dynamical origins of the Little Ice Age and Medieval Climate Anomaly. Science 326, 1256–1260.

Mann, M., 2002. Large-scale climate variability and connections with the Middle East in past centuries. Climatic Change 55, 287–314.

Meeker, L., Mayewski, P., 2002. A 1400-year high-resolution record of atmospheric circulation over the North Atlantic and Asia. The Holocene 12, 257–266.

Mitchell, T.D., Jones, P.D., 2005. An improved method of constructing a database of monthly climate observations and associated high-resolution grids. International Journal of Climatology 25, 693.

Palastanga, V., van der Schrier, G., Weber, S.L., Kleinen, T., Briffa, K.R., Osborn, T.J., 2011. Atmosphere and ocean dynamics: contributors to the European Little Ice Age? Climate Dynamics 36, 973–987.

Pinto, J.G., Raible, C.C., 2012. Past and recent changes in the North Atlantic Oscillation. Wiley Interdisciplinary Reviews: Climate Change 3, 79–90.

Portis, D., Walsh, J., El Hamly, M., Lamb, P., 2001. Seasonality of the North Atlantic Oscillation. Journal of Climate 14, 2069–2078.

Proctor, C., Baker, A., Barnes, W., Gilmour, R., 2000. A thousand year speleothem proxy record of North Atlantic climate from Scotland. Climate Dynamics 16, 815–820.

Raible, C.C., Casty, C., Luterbacher, J., Pauling, A., Esper, J., Frank, D.C., Buentgen, U., Roesch, A.C., Tschuck, P., Wild, M., Vidale, P.-L., Schaer, C., Wanner, H., 2006. Climate variability-observations, reconstructions, and model simulations for the Atlantic-European and Alpine region from 1500–2100 AD. Climatic Change 79, 9–29.

Raible, C.C., Stocker, T.F., Yoshimori, M., Renold, M., Beyerle, U., Casty, C., Luterbacher, J., 2005. Northern hemispheric trends of pressure indices and atmospheric circulation patterns in observations, reconstructions, and coupled GCM simulations. Journal of Climate 18, 3968–3982.

Rodrigo, F., Pozo-Vazquez, D., Esteban-Parra, M., Castro-Diez, Y., 2001. A reconstruction of the winter North Atlantic Oscillation index back to AD 1501 using, documentary data in southern Spain. Journal of Geophysical Research 106, 14805–14818.

Rogers, J., 1984. The association between the North-Atlantic Oscillation and the Southern Oscillation in the Northern Hemisphere. Monthly Weather Review 112, 1999–2015.

Salas-Mélia, D., Chauvin, F., Déqué, M., Douville, H., Guérémy, J.F., Marquet, P., Planton, S., Royer, J.F., Tyteca, S., 2005. Description and Validation of the CNRM-CM3 Global Coupled Model. Tech. rep. CNRM/GMGEC.

Schmutz, C., Luterbacher, J., Gyalistras, D., Xoplaki, E., Wanner, H., 2000. Can we trust proxy-based NAO index reconstructions? Geophysical Research Letters 27, 1135–1138.

Shapiro, A.I., Schmutz, W., Rozanov, E., Schoell, M., Haberreiter, M., Shapiro, A.V., Nyeki, S., 2011. A new approach to the long-term reconstruction of the solar irradiance leads to large historical solar forcing. Astronomy and Astrophysics 529.

Steinhilber, F., Beer, J., Froehlich, C., 2009. Total solar irradiance during the Holocene. Geophysical Research Letters 36.

Stoner, A.M.K., Hayhoe, K., Wuebbles, D.J., 2009. Assessing General Circulation Model simulations of atmospheric teleconnection patterns. Journal of Climate 22, 4348–4372.

Swingedouw, D., Terray, L., Cassou, C., Voldoire, A., Salas-Mélia, D., Servonnat, J., 2011. Natural forcing of climate during the last millennium: fingerprint of solar variability. Climate Dynamics 36, 1349–1364.

Trouet, V., Esper, J., Graham, N.E., Baker, A., Scourse, J.D., Frank, D.C., 2009. Persistent positive North Atlantic Oscillation mode dominated the Medieval Climate Anomaly. Science 324, 78–80.

Trouet, V., Scourse, J.D., Raible, C.C., 2012. North Atlantic storminess and Atlantic Meridional Overturning Circulation during the last Millennium: reconciling contradictory proxy records of NAO variability. Global and Planetary Change 84–85, 48–55.

Ulbrich, U., Christoph, M., 1999. A shift of the NAO and increasing storm track activity over Europe due to anthropogenic greenhouse gas forcing. Climate Dynamics 15, 551–559.

Uppala, S., Kallberg, P., Simmons, A., Andrae, U., Bechtold, V., Fiorino, M., Gibson, J., Haseler, J., Hernandez, A., Kelly, G., Li, X., Onogi, K., Saarinen, S., Sokka, N., Allan, R., Andersson, E., Arpe, K., Balmaseda, M., Beljaars, A., Van De Berg, L., Bidlot, J., Bormann, N., Caires, S., Chevallier, F., Dethof, A., Dragosavac, M., Fisher, M., Fuentes, M., Hagemann, S., Holm, E., Hoskins, B., Isaksen, L., Janssen, P., Jenne, R., McNally, A., Mahfouf, J., Morcrette, J., Rayner, N., Saunders, R., Simon, P., Sterl, A., Trenberth, K., Untch, A., Vasiljevic, D., Viterbo, P., Woollen, J., 2005. The ERA-40 re-analysis. Quarterly Journal of the Royal Meteorological Society 131, 2961–3012.

Vicente-Serrano, S.M., Lopez-Moreno, J.I., 2008. Nonstationary influence of the North Atlantic Oscillation on European precipitation. Journal of Geophysical Research 113.

Vinther, B., Andersen, K., Hansen, A., Schmith, T., Jones, P., 2003. Improving the Gibraltar/Reykjavik NAO index. Geophysical Research Letters 30.

Wanner, H., Brönnimann, S., Casty, C., Gyalistras, D., Luterbacher, J., Schmutz, C., Stephenson, D.B., Xoplaki, E., 2001. North Atlantic Oscillation – concepts and studies. Surveys in Geophysics 22, 321–382.

Yiou, P., Servonnat, J., Yoshimori, M., Swingedouw, D., Khodri, M., Abe-Ouchi, A., 2012. Stability of weather regimes during the last millennium from climate simulations. Geophysical Research Letters.

Zorita, E., González-Rouco, F., 2002. Are temperature-sensitive proxies adequate for North Atlantic Oscillation reconstructions? Geophysical Research Letters 29.

Zorita, E., Gonzalez-Rouco, F., Legutke, S., 2003. Testing the Mann et al. (1998) approach to paleoclimate reconstructions in the context of a 1000-yr control simulation with the ECHO-G coupled climate model. Journal of Climate 16, 1378–1390.

Chapter 4

Amplified inception of European Little Ice Age by sea ice-ocean-atmosphere feedbacks

Flavio Lehner, Andreas Born, Christoph C. Raible, and Thomas F. Stocker

Abstract

The inception of the Little Ice Age ($\sim$1400-1700 AD) is believed to have been driven by an interplay of external forcing and climate system-internal variability. While the hemispheric signal seems to have been dominated by solar irradiance and volcanic eruptions, the understanding of mechanisms shaping the climate on continental scale is less robust. In an ensemble of transient model simulations and a new type of sensitivity experiments with artificial sea ice growth we identify a sea ice-ocean-atmosphere feedback mechanism that amplifies the Little Ice Age cooling in the North Atlantic-European region and produces the temperature pattern suggested by paleoclimatic reconstructions. Initiated by increasing negative forcing, the Arctic sea ice substantially expands at the beginning of the Little Ice Age. The excess of sea ice is exported to the subpolar North Atlantic, where it melts, thereby weakening convection of the ocean. Consequently, northward ocean heat transport is reduced, reinforcing the expansion of the sea ice and the cooling of the Northern Hemisphere. In the Nordic Seas, sea surface height anomalies cause the oceanic recirculation to strengthen at the expense of the warm Barents Sea inflow, thereby further reinforcing sea ice growth. The absent ocean-atmosphere heat flux in the Barents Sea results in an amplified cooling over Northern Europe. The positive nature of this feedback mechanism enables sea ice to remain in an expanded state for decades up to a century, favoring sustained cold periods over Europe such as the Little Ice Age. Support for the feedback mechanism comes from recent proxy reconstructions around the Nordic Seas.

4.1   Introduction

The past 1,000 years are a prime target for studies of internal variability of the climate system because of the relatively weak orbital and solar forcing and the abundance of climate proxy reconstructions. The most prominent departures from the mean climate trend during that time were the Medieval Climate Anomaly (MCA, ∼950-1250 AD), a relatively warm period with stronger solar irradiance and the subsequent Little Ice Age (LIA, ∼1400-1700 AD), a cooling period of reduced solar irradiance and increased volcanic activity (Mann et al., 2009). Cooling from early anthropogenic land cover changes is negligible before 1500 AD (e.g., Bauer et al., 2003). While the global signal of the MCA-LIA transition is attributed to the changes in external forcing of solar irradiance and volcanic eruptions, climate variations on continental scales are less understood (Wanner et al., 2008, and references therein). Temperature reconstructions suggest that the cooling of the LIA was neither spatially nor temporally uniform (e.g., Matthews and Briffa, 2005; Wanner et al., 2011). Thus, feedback mechanisms within the climate system are necessary to explain this heterogeneity. In Europe, for example, the reconstructed cooling during the LIA was strongest in the North, while it was weaker towards the South (Mann et al., 2009). This has been interpreted as a fingerprint of a shift from a persistent positive to a negative North Atlantic Oscillation (NAO; Trouet et al., 2009), but the robustness of this NAO reconstruction remains questionable (Lehner et al., 2012a; Pinto and Raible, 2012).

The apparent difficulties of relating the MCA-LIA transition to fundamental changes in the leading mode of atmospheric winter variability opens the opportunity for alternative mechanisms which employ also other components of the climate system, namely the ocean or the sea ice. Zhong et al. (2011) forced a climate model with a series of decadally-paced volcanic eruptions, while leaving solar irradiance constantly at 1000 AD levels. They found a sea ice-ocean feedback loop that allows Arctic sea ice cover to remain in an extended state and cool the Northern Hemisphere for decades after the last volcanic eruptions. Based on these findings, Miller et al. (2012) proposed a volcanic trigger for the onset of the LIA in the North Atlantic-European region.

Abrupt climate shifts in the absence of strong forcing changes (such as the occurrence of the LIA) have been identified in observations and climate models before. Using a long and unforced climate model simulation, Goosse et al. (2002) describe events of spontaneous weakening of convection in the Nordic Seas that cause century-long hemispheric and Arctic cooling. Similar cooling events in a climate model forced with slightly varying solar irradiance were attributed to a shut-down of the Barents Sea inflow (Semenov et al., 2009), a crucial transport branch of warm and salty Atlantic waters into the Arctic (Ingvaldsen et al., 2004). In the context of Twentieth century warming events in the Arctic, many studies suggest that the Barents Sea inflow, if strengthened, can explain part of the warming and the corresponding sea ice retreat (e.g., Bengtsson et al., 2004; Årthun et al., 2012). While the Barents Sea inflow is driven partly by regional winds (Ingvaldsen et al., 2004), its strengths and composition is also remotely forced by advection of North Atlantic thermohaline properties (Holliday et al., 2008). The advection of these properties, in turn, depends largely on the strength of the broader scale North Atlantic circulation, described by the Atlantic Meridional Overturning Circulation (AMOC). New proxy evidence from the North Atlantic and adjacent basins points towards the AMOC and associated ocean currents having played an amplifying role in the MCA-LIA transition (Spielhagen et al., 2011; Hald et al., 2011; Wanamaker Jr et al., 2012; Kuhnert and Mulitza, 2011).

The aim of this study is to investigate the role of the Barents Sea inflow and the associated sea ice-ocean-atmosphere coupling at the inception of the LIA in the North Atlantic-European

region. To that end, we use transient model simulations, covering the transitional period from 1150 to 1500 AD. While the coolest period of the European LIA was around 1650-1700 AD, roughly 70% of the European cooling since the MCA occurred before 1500 AD, as reconstructions by Mann et al. (2009) illustrate. Additionally, we conduct sensitivity experiments in which sea ice is artificially grown in the Barents and the Labrador Sea to investigate feedbacks potentially associated with the MCA-LIA transition. The latter experiments are, to our knowledge, a novelty in coupled modeling and provide useful new insights on the dynamics of sea ice-ocean interaction. They are also a new tool in the context of paleoclimatology, as the few existing experiments that introduced sea ice perturbations in a coupled model mainly focus on future climate change: by sudden removal of the Arctic sea ice (Schröder and Connolley, 2007; Tietsche et al., 2011) or by tuning the ice albedo (Bitz et al., 2006; Holland et al., 2006) the resilience of sea ice to projected warming has been investigated.

This paper is structured as follows: a description of the model and experimental setup is presented in Section 2. In Section 3 and 4 the transient and the sensitivity experiments, are examined with a focus on feedbacks within the climate system. A discussion and conclusions follow in Section 5.

4.2   Data and methods

4.2.1   Model description

We use the Community Climate System Model 3 (CCSM3) provided by the National Center for Atmospheric Research (NCAR) (Collins et al., 2006). It is a coupled model with the components atmosphere, ocean, sea ice, and land surface all communicating through a coupler without flux correction. The CCSM3 has been used in various studies addressing questions of paleo climate (e.g., Liu et al., 2009; Yoshimori et al., 2010; Hofer et al., 2011, 2012a,b; Lehner et al., 2012a,b; Wilmes et al., 2012), present-day and future climate (e.g., Meehl et al., 2006), as well as in sensitivity experiments applying freshwater hosing (e.g., Stocker et al., 2007) or idealized CO_2 increase (e.g., Bryan et al., 2006). We use the intermediate resolution version of CCSM3 (Otto-Bliesner et al., 2006). The atmosphere and land surface components are truncated at T42, resulting in a horizontal resolution of approximately $2.8° \times 2.8°$; the atmosphere has 26 levels reaching up to 8.3 hPa. The ocean and sea ice components both operate on a nominal 1° resolution grid, however, the displacement of the North Pole into Greenland allows for a higher resolution in the Arctic and an open passage through the Canadian Arctic Archipelago. The ocean component has a maximum of 40 levels at depth. The sea ice component is the Community Sea Ice Model (CSIM), applying elastic-viscous-plastic dynamics and thermodynamics.

4.2.2   Control simulation

An overview of the simulations conducted for this study is given in Table 4.1. The control simulation (CTRL) is an equilibrium simulation using constant values of 1150 AD for total solar irradiance (TSI; 1,366.4 W m^{-2}), CO_2 (283.9 ppm), CH_4 (704.9 ppb), and N_2O (265.0 ppb). CTRL is a branch from the preindustrial simulation (perpertual 1870 AD conditions) described by Otto-Bliesner et al. (2006).

Despite representing the relatively warm climate of the MCA (as compared to the almost-linear orbital cooling trend over the last millennium), Northern Hemisphere winter (November-April) temperature in the CTRL is on average 2.6 °lower than in a 1990 control simulation with the same model, owing primarily to substantially lower greenhouse gas concentrations. This results in sea ice concentrations being larger than today in most locations of the Northern

Table 4.1: List of all simulations.

Name	Description	Length (number of runs)
CTRL	1150 AD equilibrium simulation	494 years (1)
TR1-TR6	Transient simulation (1150-1500 AD)	351 years (6)
TR_novolc	Transient simulation (1150-1500 AD), but without volcanoes	351 years (1)
BSf25	Sea ice growth enhanced in Barents Sea by a factor f'=25 for 100 years, then switched off artificial growth	200 years (1)
LSf25	Sea ice growth enhanced in Labrador Sea by a factor f'=25 for 100 years, then switched off artificial growth	200 years (1)

Hemisphere. During winter (November-April) large parts of the Barents and Labrador Sea are covered by sea ice >15% (Fig. 4.1a). Both the seasonal and interannual variability is largest in the Barents Sea. There, most of the newly formed winter sea ice is exported northward to the Arctic Ocean. At the same time, the sea ice cover is sensitive to interannual variations in the inflow of warm Atlantic waters, characterizing the Barents Sea as a key region in the Arctic-North Atlantic freshwater cycle. The atmospheric winter circulation in the North Atlantic-European area is dominated by the well-known North Atlantic Oscillation (NAO) pattern, featuring a low pressure system just south of Iceland and a high pressure system over the Azores (Fig. 4.1b). The cyclonic circulation of the northern center of action transports heat northward on its eastern side, thereby contributing to the comparably mild climate of Northern Europe. The largest interannual variability in SLP occurs to the North-West of this low pressure system resembling the non-stationary northern center of action of the NAO (Fig. 4.1b).

4.2.3   Transient simulations

The transient simulations (TR1-TR6) were branched from different initial conditions of CTRL applying the same time-varying external forcing of TSI, greenhouse gases, and volcanic eruptions for the period 1150-1500 AD (the forcings used are as described in Yoshimori et al., 2010). Compared to the bulk of recent TSI reconstructions (for an overview see Schmidt et al., 2012), our TSI has a relatively large amplitude of approximately 2.3 W m^{-2} from the MCA (in this study defined as 1150-1200 AD) to the LIA (1450-1500 AD)[1]. The forcings and their radiative effect are shown in Fig. 4.2a and b. In these forcing datasets the time around 1150 AD marks the beginning of a decrease in TSI, i.e., the inception of the Little Ice Age (LIA). This is reflected in a decreased Northern Hemisphere temperature and an increased Arctic sea ice extent (Fig. 4.2c and d), two features well reproduced by the model when compared with proxies (IPCC, 2007; Kinnard et al., 2011). However, the minimum and maximum of both temperature and sea ice fall just within the uncertainty of the reconstructions, although the applied solar forcing is relatively strong. In the following, the term 'negative forcing' is used when the decrease in TSI from MCA to LIA and the radiative cooling from volcanoes are adressed in an integral manner. The initial conditions for the different transient simulations were selected to cover a range of states of the Atlantic Meridional Overturning Circulation (AMOC), as the North Atlantic, European, and Arctic climate is substantially influenced by the strength of the AMOC (e.g., Hofer et al., 2011). In the following sections,

---

[1]For comparison with other studies: the TSI amplitude from the Maunder Minimum to the period 1950-2000 AD is 3.3 W m^{-2}.
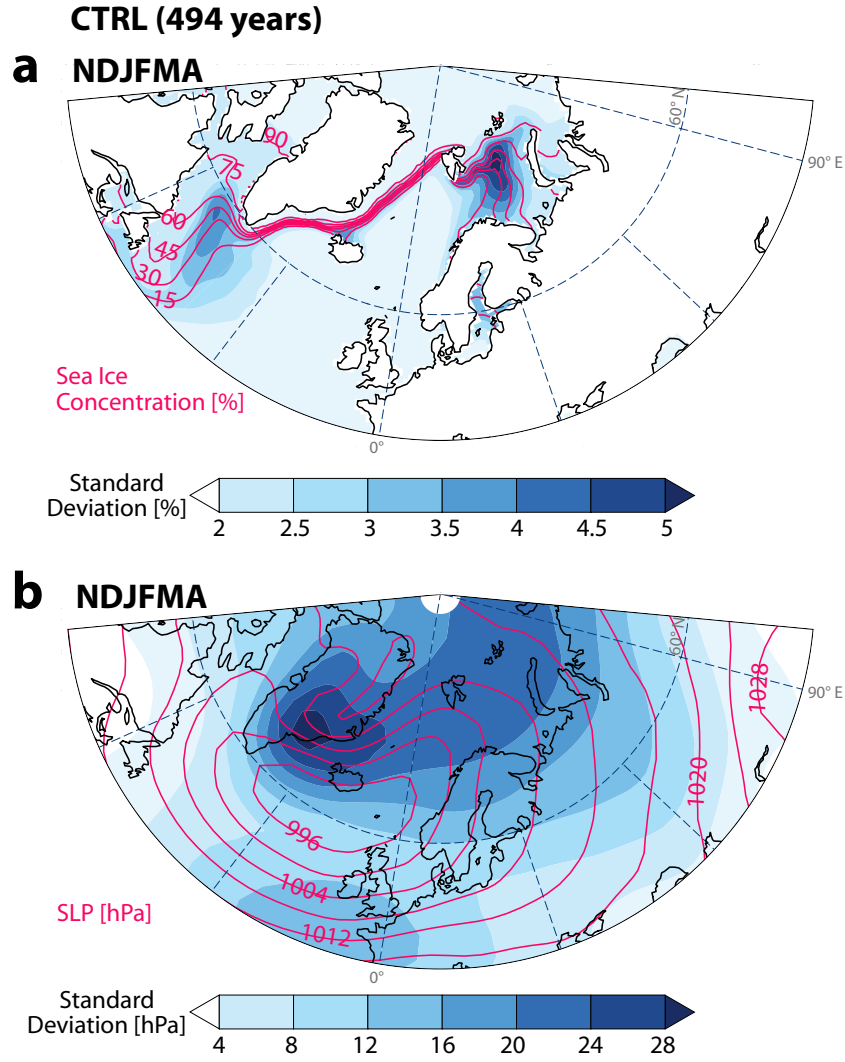
Figure 4.1: Long-term winter (November-April) mean and standard deviation from CTRL for (a) sea ice concentration and (b) sea level pressure (SLP).

we refer to the ensemble mean of TR1-TR6 as the transient simulations. Further, one of the transient simulations was rerun without volcanic eruptions (TR_novolc) to determine the impact of variations in TSI and greenhouse gases only.

When comparing with proxy reconstructions at coarse temporal resolution a low-pass Fourier filter is applied to the model time series. After transformation of the time series to the frequency domain, frequencies above the frequency $\nu_0 > \frac{1}{T}$ are set to zero, where T is the cut-off period (30, 40, 80 years, respectively). In order to reduce Gibbs phenomenon artifacts from a sharp cut-off, we use a smooth transition phase (roll-off) between $\nu = \nu_0 \pm \frac{\nu_0}{2}$.

4.2.4 Artificial sea ice growth simulations

In addition to the transient ensemble, two 200-year long sensitivity experiments were branched from CTRL in which perpetual 1150 AD conditions apply, but sea ice growth in the Barents Sea (experiment called BSf25) and Labrador Sea (LSf25) was artificially enhanced by a factor of 25 for the first 100 years (Fig. 4.3a and Table 4.1). The regions of artificially enhanced sea ice growth were chosen for their distinct roles in the freshwater cycle of the Arctic-North Atlantic area: the Labrador Sea imports sea ice that melts locally, while the Barents Sea rather acts as a source of sea ice, especially in colder climates such as the LIA. By enhancing
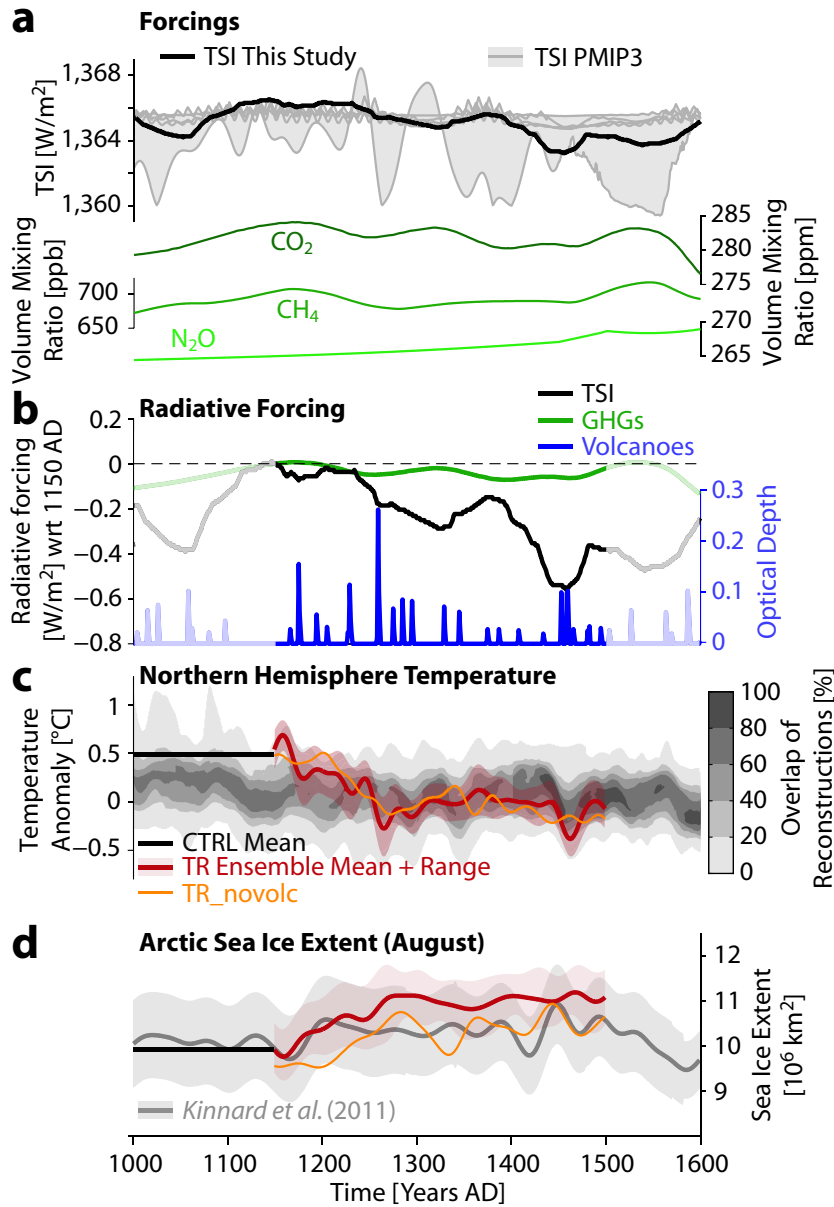
Figure 4.2: (a) Forcing used in the model simulations which cover the time period 1150-1500 AD: total solar irradiance (TSI) used in this study and from the protocol of the third Paleoclimate Modelling Intercomparison Project (Schmidt et al., 2012); changes in greenhouse gases (GHGs: CO_2, CH_4, N_2O). (b) Cumulative radiative forcing from GHGs (calculated as in IPCC, 2001) and TSI (assuming a global average albedo of 0.31), with reference to (wrt) 1150 AD; changes in the annual mean visible band optical depth due to volcanic eruptions. (c) Northern Hemisphere annual mean temperature anomaly from reconstructions (gray shading; Fig. 6.13d IPCC (2007)) and the model simulations (30-year fourier-filtered). The reconstructions are wrt 1500-1899 AD. As the simulations do not cover that time period they are adjusted to have the same mean as the reconstructions time series during the overlapping time period, i.e., from 1150-1500 AD. (d) August Arctic sea ice extent (sea ice concentration >15%) from the reconstruction of Kinnard et al. (2011) and the model simulations (80-year fourier-filtered).

sea ice growth in the Labrador Sea (LSf25) we transform this region into a sea ice source. Thereby we directly increase the amount of sea ice in a region crucial for deep water formation (Bryan et al., 2006), aiming for a relatively rapid response of the AMOC. This makes LSf25 comparable to classical freshwater hosing experiments, which are often set in a similar location. In the Barents Sea experiment (BSf25), on the other hand, we only enhance the natural role this basin plays in the freshwater cycle.

Frazil ice is the first stage of ice growth, resulting from strong heat loss over areas of open water:

$$V_{frazil} = -\frac{Q}{H} \cdot f' \cdot \Delta t \cdot \frac{1}{\rho_{ice}} \cdot A, \tag{4.1}$$

where V_{frazil} is the volume of new ice added to the first ice category (i.e., frazil ice), Q is the heat flux to open water for this new ice, H is enthalpy for new ice, f' is the perturbation factor introduced (25 in this study), Δt is the model time step, ρ_{ice} the density of ice, and A the area of sea ice growth. By enhancing growth only for frazil ice, the direct disturbance is minimal as the model dynamics remain unchanged. The model retains the freedom to melt and redistribute the additional frazil ice, change its mechanical characteristics by mixing with other ice categories, and to form congelation ice on the newly formed ice cover in the subsequent growth seasons. Note that by multiplying the model-derived heat flux the seasonality of ice growth as well as the distribution of newly formed ice remains consistent in the coupled system. In contrast to other studies, the additional sea ice is not added at once or prescribed as lower boundary condition (e.g., Petoukhov and Semenov, 2010; Li et al., 2010).
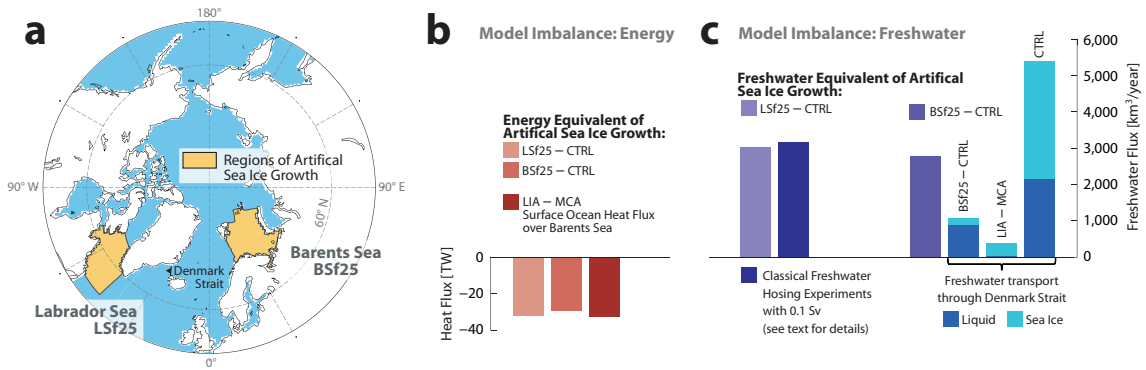

Figure 4.3: (a) Map of the Arctic with the regions of artificial sea ice growth. (b) Estimates of the model imbalance in energy; shown are average anomalies of the first 100 years of BSf25 and LSf25 from the CTRL and the LIA−MCA difference in ocean-atmosphere heat flux over the Barents Sea. (c) Estimates of the model imbalance in freshwater; shown are average anomalies of the first 100 years of BSf25 and LSf25 from the CTRL mean. For comparison with the LSf25 experiment the amount of freshwater put into the subpolar North Atlantic in classical freshwater hosing experiments is given. For comparison with the BSf25 experiment the annual freshwater transport through the Denmark Strait (see map in (a) for location) is given for BSf25 (first 100 years)−CTRL mean, LIA−MCA, and CTRL mean. Liquid freshwater transports are calculated to a reference salinity of 34.7 (see text for further details).

Due to the modification of the sea ice code, freshwater and heat are not conserved in these experiments (Fig. 4.3b, c). The brine rejection by frazil ice growth is calculated in the ocean component and does not take into account the perturbation factor f', which is only applied in the ice component. Therefore, brine rejection is underestimated, making the model fresher wherever the additional sea ice melts. Along the same lines, when the additional sea ice melts (anywhere in the ocean) it will consume heat from the ocean that has not been introduced into the ocean before, because the air-sea heat flux Q is not changed. This eventually makes the model colder on a global scale. However, by design of the sea ice perturbation, no imbalances are introduced locally in the forcing regions. Heat and freshwater flux anomalies there are the result of reactions of the coupled climate system to the anomalous forcing, as intended for the present study. This makes it impossible to determine the exact location of occurring imbalances, which is also why we refrain from any flux adjustments to compensate.

To put these imbalances into context we compare them to other processes. Fig. 4.3b shows the energy equivalent of the anomalous annual frazil ice growth. This is estimated from the difference in 100 year cumulative frazil ice growth between the two sensitivity experiments and CTRL (for CTRL the average over four 100 years segments is used) multiplied by the specific heat capacity of ice. The two sensitivity experiments extract a similar amount of energy from the system (around 30 TW), which is comparable to the reduction in ocean-atmosphere heat flux over the Barents Sea in the transient simulations. If we reintroduced this energy in situ, most of it would instantly radiate to the atmosphere as during winter sea surface temperatures usually exceed air temperatures in the Barents Sea (not shown). This would disturb the lower atmosphere, similar to artificial sea ice growth via changes in albedo, which is another reason to refrain from flux adjustment.

Fig. 4.3c shows the imbalance in freshwater for the two sensitivity experiments, derived from the average anomalous annual frazil ice growth, which is 3,035 km^3 yr^{-1} in LSf25 and 2,783 km^3 yr^{-1} in BSf25 (Fig. 4.3c). Over the 100 years of the artificial sea ice growth, this translates into additional frazil ice volume of about 300·10^3 km^3 and 280·10^3 km^3, respectively. The amount of additional freshwater delivered to the system in LSf25 is reminiscent of freshwater amounts deployed into the subpolar North Atlantic in classical hosing experiments (e.g., Stouffer et al., 2006; Stocker et al., 2007). There, hosing with 0.1 Sv (3,154 km^3 yr^{-1}) triggers an AMOC reduction in the order of 4 Sv, which is comparable to the 2-3 Sv reduction that occurs in our transient simulations (see section 4.3). In LSf25 most of the artificially grown sea ice melts in situ or in the subpolar North Atlantic, characterizing LSf25 in many ways as a classical hosing experiment, where a deep water formation region is forced with an anomalous freshwater flux.

BSf25, on the other hand, aims at amplifying already occurring transports of sea ice and freshwater, such as the transport through Denmark Strait. In the CTRL, roughly 5,200 km^3 yr^{-1} of freshwater flow southward through the Denmark Strait in solid and liquid form (applying a reference salinity of 34.7; for calculation of freshwater transport see, e.g., Lehner et al., 2012b). In the transient simulations this transport increases from MCA to LIA by about 400 km^3 yr^{-1}, primarily driven by larger sea ice transport. In BSf25 approximately 2,800 km^3 yr^{-1} of freshwater is added as artificially grown sea ice in the Barents Sea. However, the Denmark Strait transport increases only by about 1,000 km^3 yr^{-1}. Thus, about two-thirds of this additional freshwater stays north of Denmark Strait, for example as on average about 1.5 m thicker sea ice in the Arctic. A large portion of this 1,000 km^3 yr^{-1} is made up by liquid freshwater. This indicates that part of the additional sea ice from the Barents Sea melts on its way to the Denmark Strait. The sea ice portion of this increased Denmark Strait transport (about 100 km^3 yr^{-1}) is nonetheless crucial for the experiment's purpose of mimicking the MCA-LIA changes as sea ice is more potent in disturbing convection sites than advection of liquid freshwater (Born et al., 2010).

Clearly, these imbalances are not optimal, however, the comparison reveals them to be of moderate magnitude. More importantly, it is shown that the sensitivity experiments simulate the processes as intended, i.e., a direct disturbance of the convective site in the Labrador Sea (in LSf25) and an increased transport of sea ice and freshwater through Denmark Strait (in BSf25). Additional comparisons with the transient simulations further strengthens the confidence in the design of the sensitivity experiments (see section 4.4).

4.3 Transition from the Medieval Climate Anomaly to the Little Ice Age

The simulations with transient forcings aim at realistically simulating the transition from the MCA to the LIA. By using a six-member ensemble of these transient simulations we are able to obtain robust results that stand out against the natural variability inherent in the sixfold simulation of this specific time period (6×351 years). In the following, we first present the significant changes during the transition phase, which occur due to the negative forcing. Additionally, we identify a positive sea ice-ocean feedback mechanism in these simulations which substantially amplifies these changes and is potentially able to sustain the cold conditions of the LIA even in the absence of negative forcing. Based on the results of our transient ensemble simulations we summarize this feedback hypothesis, containing two feedback loops (in what follows we use the term 'feedback mechanism' to describe collectively both feedback loops). In the subsequent section we then go ahead to test the hypothesis in the framework of artificial sea ice growth experiments.

4.3.1 Main climate response

Shortly after initialization of the transient simulations the Northern Hemisphere temperature starts to decrease in response to the decreasing TSI and the large volcanic eruptions occurring between 1150 AD and 1300 AD (Fig. 4.2c). In particular, the large eruption at 1258 AD and the three smaller ones following shortly after cause a significant hemispheric cooling. After about a century of stable TSI and few volcanic eruptions between 1300 and 1400 AD, the Spörer Minimum with its pronounced TSI minimum and two large eruptions in the 1450s cause another temperature drop, coinciding with the beginning of the coolest period of the last millennium in reconstructions (∼1400-1700 AD, e.g., Mann et al., 2009).

As another consequence of the negative forcing at the beginning of the transition period, sea ice extent and volume increase in the entire Arctic region. In the transient simulations, the largest expansion of sea ice occurs in the Atlantic sector, namely the Barents and Labrador Sea (Fig. 4.4). In the Barents Sea, the enhanced sea ice cover reduces the strong ocean-atmosphere heat flux from the warm Atlantic waters that usually enter the Barents Sea. As this local heat source weakens, a significant elevation of SLP over the Barents Sea develops (Hoskins and Karoly, 1981) and becomes the dominant feature of winter atmospheric circulation change during that time (Fig. 4.4a). This SLP anomaly does not translate into a strong high pressure system as in, e.g., Petoukhov and Semenov (2010), but into a horizontal contraction of the northern center of action of the NAO. The direct thermal effect of the capped ocean-atmosphere heat flux together with increased advection of cold Arctic air due to the SLP anomaly cause enhanced cooling over the Barents Sea and Northern Europe, both in winter and – to a lesser degree – in summer (Fig. 4.4a and b).

4.3.2 Feedback mechanism

Arctic-North Atlantic feedback loop

The first feedback loop starts with an increase of sea ice in the Barents Sea, a region known to be a strong source of sea ice, where a large part of the sea ice produced locally is exported to the Arctic Ocean. The Arctic Ocean itself exports sea ice mainly through Fram Strait (∼97% in CTRL), where indeed the annual sea ice transport is slightly increased (from 3,280 to 3,450 km^3 yr^{-1}). A portion of the Barents Sea sea ice is also exported to the Nordic Seas
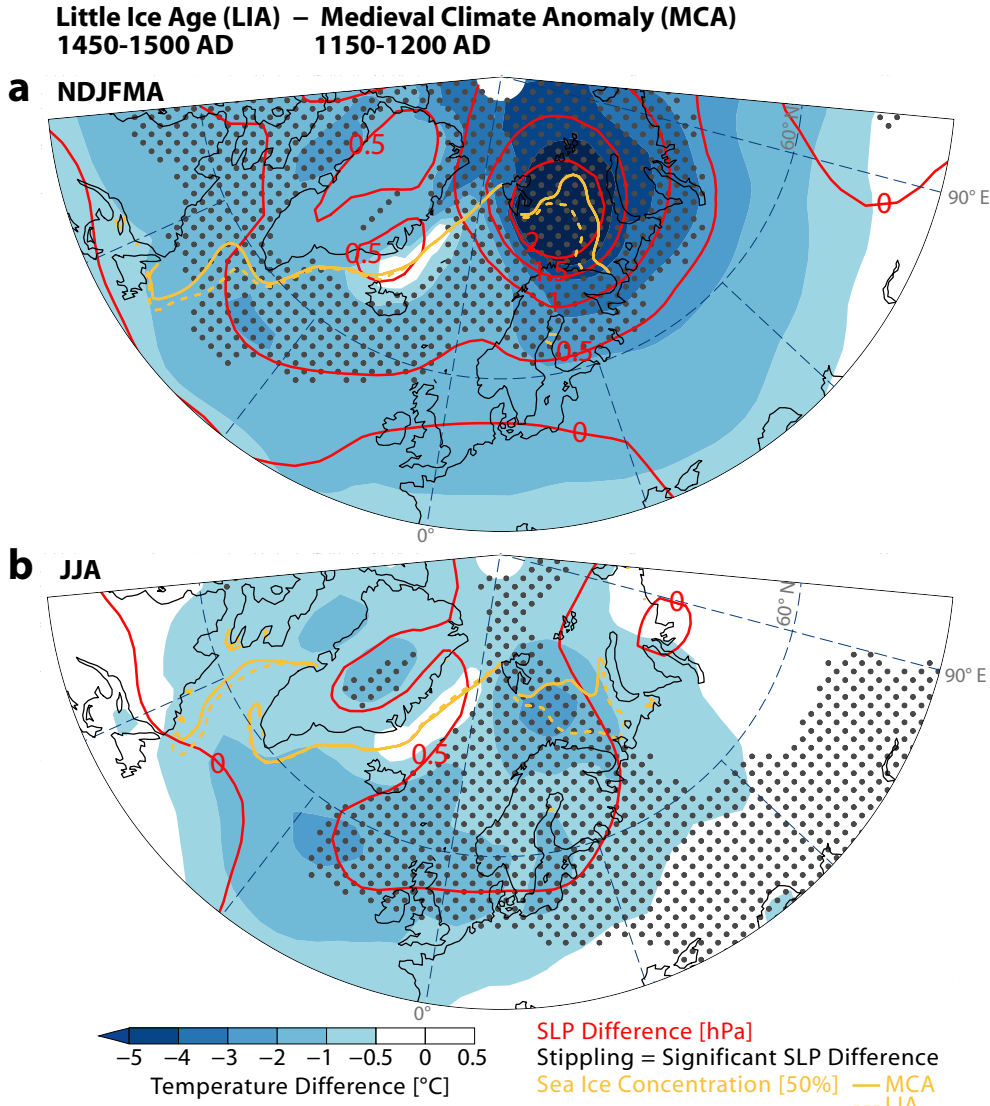
Figure 4.4: Little Ice Age (LIA) − Medieval Climate Anomaly (MCA) difference in sea level pressure (SLP), surface air temperature (only significant differences are shaded), and sea ice concentration for (a) November-April means and (b) for June-August means. Significance at the 5% level is tested with a two-sided t-test.

by the exiting branch of the East Spitsbergen Current, which strongly increases its transport of sea ice (from 100 to 310 km^3 yr^{-1}) from the MCA to the LIA. While part of the anomalous sea ice being exported from the Barents Sea and the Arctic Ocean melts in the Nordic Seas, another part is transported further South by the East Greenland Current, eventually being carried around the southern tip of Greenland to reach the Labrador Sea (Fig. 4.5a). Finally, the sea ice melts either in the Labrador Sea or in the adjacent subpolar North Atlantic. With the decreasing radiative forcing at the inception of the LIA the portion that melts in the Labrador Sea gets smaller while the portion exported to the North Atlantic grows (not shown). Changes in sea ice volume transport through Denmark Strait are dominated by changes in sea ice volume rather than circulation. Therefore, transport anomalies pointing northward indicate reduced ice thickness rather than reversed transport direction (Fig. 4.5a).

In the North Atlantic the melting sea ice then causes a temperature and salinity drop at the sea surface, which leads to increased stratification and weakened convection, illustrated by a shoaling of the mixed layer depth at the Labrador Sea exit (Fig. 4.5a). Thereby the
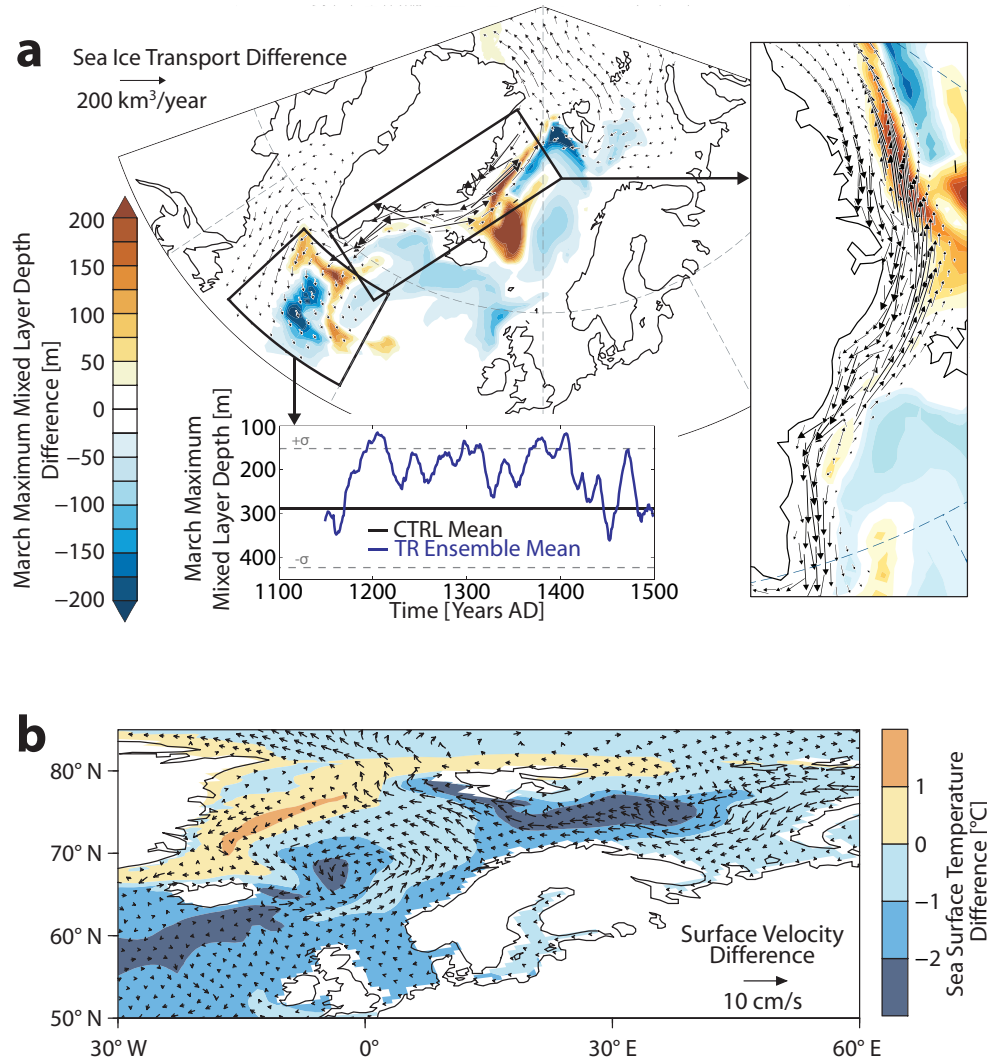
Figure 4.5: (a) Little Ice Age (LIA) − Medieval Climate Anomaly (MCA) difference in sea ice transport
(November-April means, only differences >15 km³/yr are shown) and LIA − MCA March maximum mixed
layer depth (time series is ensemble mean 5-year running mean averaged over indicated region). The inset
zooms in on the anomalous southward transport of sea ice along the coast of Greenland. (b) LIA − MCA
difference in annual mean ocean surface currents (top 15 m) and sea surface temperature.

surface waters become lighter and decrease the sea surface height (SSH) gradient that drives
the Subpolar Gyre (SPG). The SPG (average of barotropic stream function 48-65° N and
60-10° W) weakens by 5% from the MCA to the LIA, closely followed by a 7% weakening
of the AMOC (maximum of the meridional overturning circulation in the Atlantic north of
28° N). A two-year lag correlation between the two indices of 0.75 (p<0.001, based on annual
means) illustrates the near-synchronous basin-wide circulation slowdown. Consequently, the
heat and salt transport into the Nordic Seas, the Barents Sea, and the Arctic Ocean decreases
as well (not shown). This causes the mixed layer depth to shoal in the northern Nordic Seas
as well (Fig. 4.5a), which in turn weakens the overturning cell in the Nordic Seas (not shown).
As the sea ice in the central Arctic Ocean thickens, initial sea ice growth and the accompanied
brine rejection are decreased, which leads to a weakening of the convection also in the Arctic
Ocean (similar to Zhong et al., 2011). This ultimately results in a reduced northward heat
transport, that in turn reinforces sea ice growth in the Barents Sea and thereby closes the
positive feedback loop.

Barents Sea feedback loop

Our simulations indicate that in addition to the overall reduced heat transport into the Nordic Seas there is a more regional feedback loop, which involves the reorganization of ocean currents in the Nordic Seas. The Norwegian Atlantic Current usually carries warm and salty Atlantic waters up to the Barents Sea opening where it is partitioned into Barents Sea inflow, West Spitsbergen Current and waters recirculating in the Nordic Seas. During the MCA-LIA transition, the recirculating current strengthens and redirects the warm Atlantic waters towards Greenland, resulting in elevated sea surface and air temperatures East of Greenland (Figs. 4.4 and 4.5b). At the same time the other currents transport less water. The Barents Sea inflow (calculated as the difference of the barotropic stream function between Spitsbergen and the North Cape), for example, is reduced by 35%, corresponding to 1.27 Sv (Fig. 4.6a). As a consequence of the reduced inflow of warm waters, the sea ice edge in the Barents Sea advances further South (Fig. 4.6c) leading in turn to increased SLP (Fig. 4.6d) and a strong drop in regional temperature (Fig. 4.6e).

To further investigate the mechanisms causing the decreased Barents Sea inflow, we select a transect across the Barents Sea opening (Fig. 4.7). The LIA−MCA difference in ocean density indicate that the Barents Sea shelf becomes lighter as we move towards the LIA (Fig. 4.7c). This can be attributed to the increased sea ice cover as well as to the reduced inflow of salty Atlantic waters, both contributing to surface freshening which reduces density. Indeed, the density differences in the Barents Sea are largest at the surface, thereby strengthening the halocline. The strong halocline in turn forces the warm and salty Atlantic waters that enter the Barents Sea to subside below the lighter surface waters, causing a warming below approximately 100 m (Fig. 4.7c) and reinforcing the freshening of the upper 100 m. The Nordic Seas, on the other hand, become denser due to the recirculating Atlantic waters (Fig. 4.7c). These opposing density trends result in a stronger SSH gradient across the Barents sea transect (Fig. 4.7b), which will drive an anoumalous circulation (see below).

The LIA−MCA differences in the sea ice concentration (Fig. 4.7b), SLP (expressed as geopotential height), and air temperature (Fig. 4.7a) in the Barents Sea transect indicate a strong ocean-atmosphere coupling: the largest atmospheric cooling occurs exactly over the advanced sea ice edge, caused by the covered ocean surface heat flux. The near-surface cooling, in turn, causes air to descend and geopotential height and SLP to increase over the Barents Sea. This local baroclinic response is consistent with atmosphere-only sensitivity experiments by Petoukhov and Semenov (2010), in which sea ice concentration in the Barents-Kara Sea region was prescribed to change from 80% to 100% (similar to the MCA-LIA changes from 88.5% to 96.7% over the same region in our transient simulations). However, for sea ice concentration changes from 80% to 40% Petoukhov and Semenov (2010) found a barotropic response, indicating possible non-linearities in the sea ice-atmosphere coupling. The increased SLP over the Barents Sea implies changes in wind stress and Ekman transport. Such changes have been discussed as potential causes for changes in ocean circulation, such as a strengthened recirculation in the Nordic Seas or a reduction of the Barents Sea inflow (Semenov et al., 2009). In our study, the annual mean Ekman transport integrated over the Barents Sea opening (0.33 ± 0.38 Sv in CTRL) is an order of magnitude smaller than the actual total Barents Sea inflow (3.58 ± 0.79 Sv in CTRL), in good agreement with observational estimates of this relation (Ingvaldsen et al., 2004). Further, the Ekman transport integrated over the Barents Sea opening does not change significantly from the MCA to the LIA (+0.06 Sv), while the total Barents Sea inflow decreases by 1.27 Sv, thereby out-ruling Ekman transport as the direct driver of the reduced Barents Sea inflow during the LIA.

Instead, the reduction of the Barents Sea inflow from the MCA to the LIA can be explained
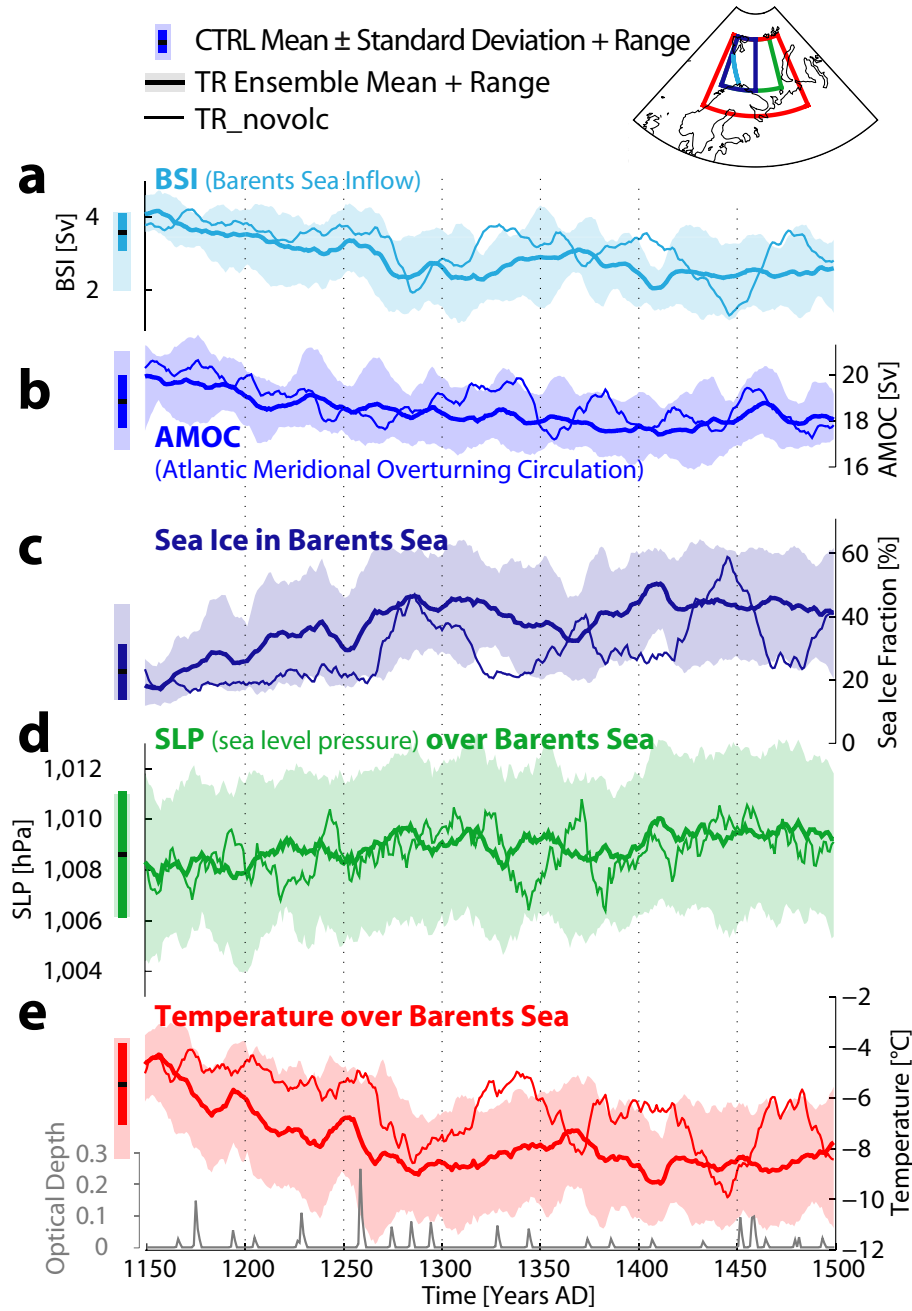
Figure 4.6: (a) Barents Sea inflow as difference of barotropic stream function between Spitsbergen and Norway (see map) and Atlantic Meridional Overturning Circulation as maximum of the meridional overturning circulation north of 28° N. (b) Sea ice concentration in the western Barents Sea (see map). (c) Sea level pressure and (d) temperature over the Barents Sea (see map) and annual mean optical depth changes due to volcanic eruptions. All time series, except optical depth, are 5-year running means from annual means. Long-term annual mean, ±1 standard deviation of annual means, and range of 5-year running means from CTRL are indicated as bars on the left side.

by the SSH gradient change of 0.146 m across the Barents Sea opening (see Fig. 4.7 for the location of the two points used to calculate the SSH gradient). The change in the Nordic Seas recirculation is estimated by applying the geostrophic equation together with the distance across δx ($940 \cdot 10^3$ m) and depth z (183 m) of the Barents Sea opening:

$$\Delta F_g = -\frac{g}{f} \frac{\Delta \delta \eta}{\delta x} \cdot \delta x \cdot z, \qquad (4.2)$$
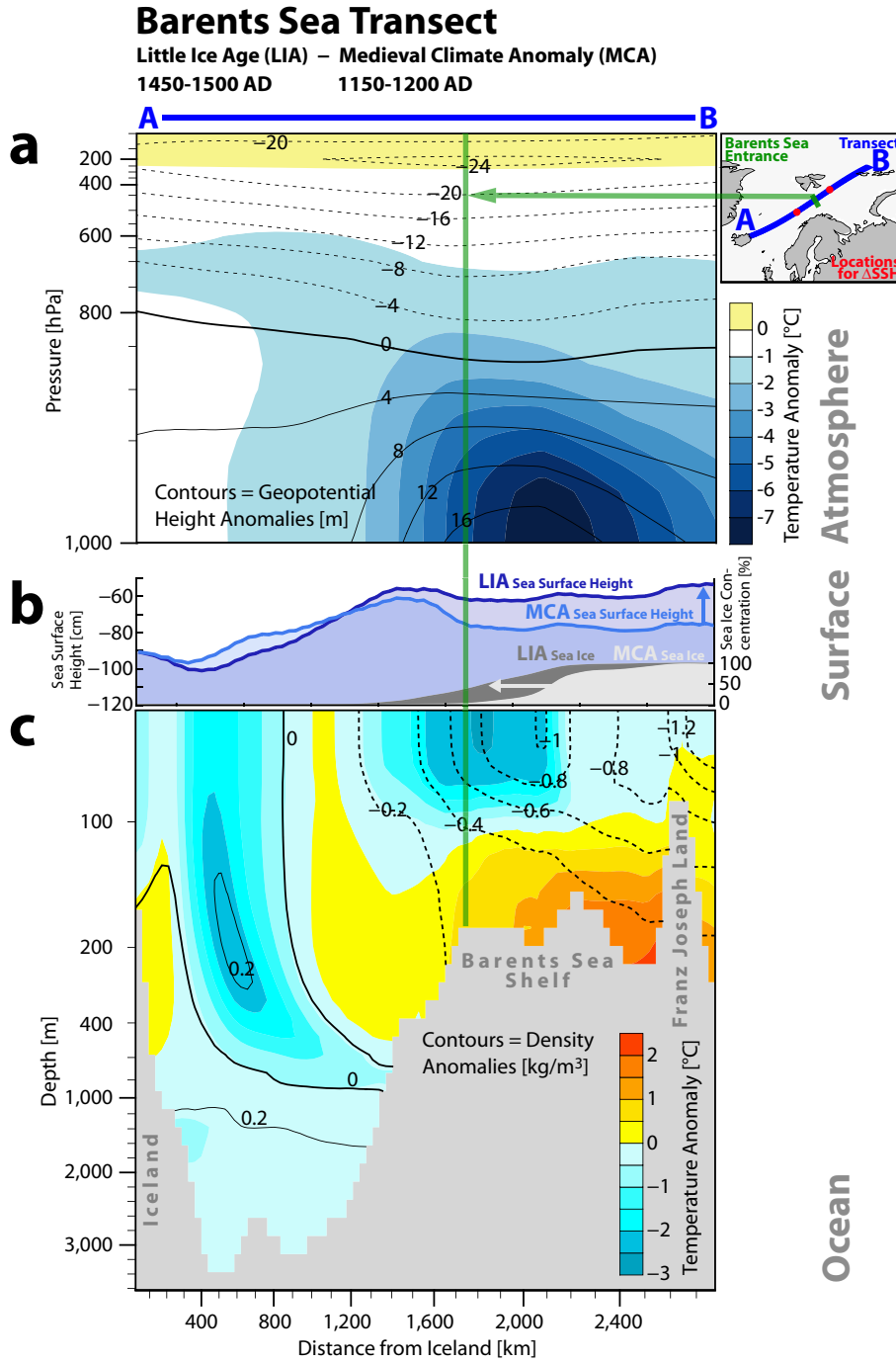
Figure 4.7: Transect across the Barents Sea from Iceland (A, see map) to Franz Josef Land (B). Little Ice Age (LIA) − Medieval Climate Anomaly (MCA) winter (November-April) difference in (a) air temperature and geopotential height, (b) sea surface height (SSH, as anomaly to global mean, which is zero) and sea ice concentration, (c) ocean density (contours) and temperature (shading). The red dots on the map indicate the locations used to derive SSH-driven transport anomalies across the Barents Sea opening (see text for details).

where ΔF_g is the change in geostrophic volume transport, g the gravitational acceleration, f the coriolis parameter at 75° N, $\Delta\delta\eta$ the change of the SSH gradient. Using the LIA−MCA change in $\delta\eta$ of 0.146 m, ΔF_g amounts to −1.86 Sv, indicating a substantial strengthening of the recirculation. The SSH-driven changes of the Norwegian Coastal Current, on the other hand, are an order of magnitude smaller (not shown). Considering continuity in the partitioning of the water masses in the Nordic Seas, this implies that the reduction of the

Barents Sea inflow of -1.27 Sv is largely a consequence of the strengthened recirculation in the Nordic Seas. The SSH anomalies in the Barents Sea are primarily density-driven, however, changes in Ekman transport within the Barents Sea contribute as well: density anomalies at the location used to calculate the SSH gradient (see map in Fig. 4.7) explains 64% of the SSH gradient change, leaving the remaining 36% to wind-induced rearrangement of the water masses within the Barents Sea. It therefore appears that, in summary, the initial sea ice growth in the Barents Sea reinforces itself via the sustained weakening of the Barents Sea inflow, which in turn is caused by sea ice-induced changes in both density and winds over the Barents Sea.

4.3.3 Excluding volcanic eruptions

One additional transient simulation was conducted from 1150-1500 AD, in which volcanic eruptions were excluded (TR_novolc). Fig. 4.2c shows that in TR_novolc the Northern Hemisphere cools with a comparable magnitude as in the transient simulations including volcanic eruptions, which might raise the question whether volcanic eruptions are at all needed to explain the inception of the LIA. However, the applied solar forcing has a relatively large amplitude and therefore likely dominates the cooling trend in both the transient ensemble simulations and in TR_novolc. Given the still open discussion on past TSI amplitudes this prevents us from concluding that volcanic forcing is a non-crucial factor for triggering the LIA. Further, Zhong et al. (2011) have shown that when starting from slightly colder conditions (their control simulation applies a 1.4 W m^{-2} weaker TSI than this study's CTRL) volcanic forcing alone can lead to significant hemispheric cooling and consequent sea ice expansion. Addditional evidence for the importance of volcanic forcing comes from Fig. 4.2d, where the lack of volcanic eruptions causes a larger discrepancy between the transient ensemble and TR_novolc than in case of the Northern Hemisphere temperature (Fig. 4.2c). Also, Fig. 4.6c and e show that in the Barents Sea the absence of volcanic eruptions results in only intermittent periods of increased sea ice fraction and decreased temperatures. In particular, this is evident during the period 1150-1250 AD, when TSI is roughly unchanged compared to CTRL and the largest forcing impact would come from volcanic eruptions. However, over the full length of the simulation all quantities stay within the range of the transient ensemble, qualitatively reproducing the MCA-LIA transition (Fig. 4.6). Thus, sequenced volcanic eruptions appear to be crucial for maintaining an expanded sea ice margin, but not for triggering the overall climate response.

4.4 Artificial sea ice growth experiments

The sensitivity experiments BSf25 and LSf25 aim at simulating specific aspects of the sea ice changes occurring during the MCA-LIA transition and thereby try to determine the role of the Barents and Labrador Sea in this transition. In both sensitivity experiments artificial sea ice growth occurs during the first 100 years. During the second 100 years this forcing is switched off to observe how fast the system returns to its initial state. We first discuss the results of the experiments in context of the MCA-LIA climate transition. In a second part, additional technical details about the experiments are presented.

4.4.1 Main climate response

The anomalies in SLP, temperature and sea ice from years 50-99 of LSf25 and BSf25 against the CTRL (Fig. 4.8a and b) bear strong resemblance with the LIA$-$MCA anomalies from the transient simulations (Fig. 4.4a): an advanced sea ice edge in the Barents Sea geographically coincides with increased SLP and decreased temperatures. At the same time the western Nordic Seas experience a warming due to a strengthened recirculation (Fig. 4.8c and d).

Thus, the sensitivity experiments show that a climate response which is qualitatively similar to the transient simulations can be induced by the artificial sea ice growth in either of the two regions Barents or Labrador Sea.
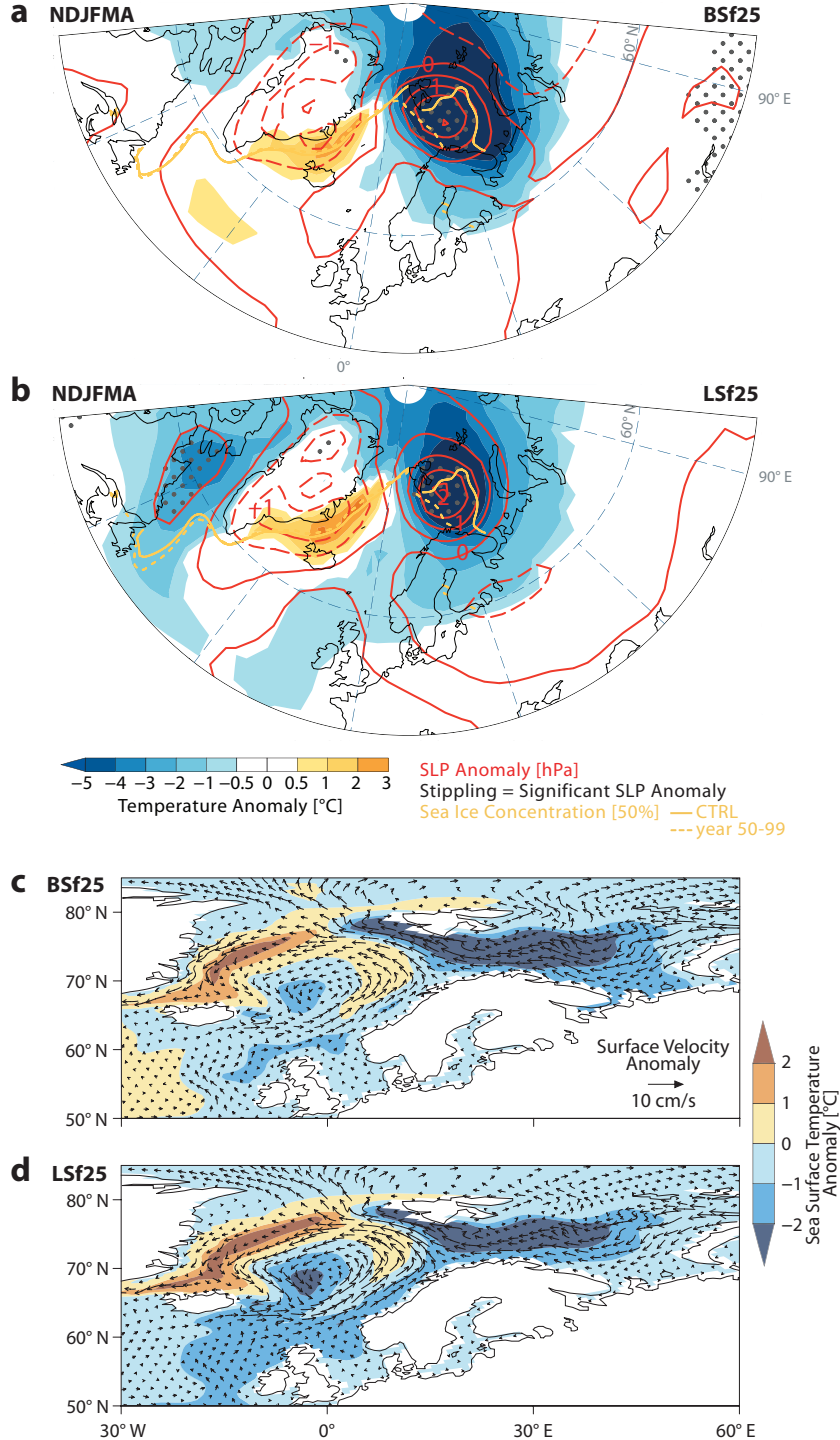

Figure 4.8: (a-b) Anomalies in sea level pressure (SLP), surface air temperature (only significant anomalies are shaded), and sea ice concentration for November-April means from the years 50-99 of (a) BSf25 (artificial sea ice growth in Barents Sea) and (b) LSf25 (artificial sea ice growth in Labrador Sea) − mean of CTRL. Significance of SLP changes is tested at the 5% level with a two-sided t-test. (c-d) Anomalies in ocean surface currents (top 15 m) and sea surface temperature from the years 50-99 of (c) BSf25 − mean of CTRL and (d) LSf25 − mean of CTRL.

4.4.2 Feedback mechanism

We investigate the same indices as in the transient simulations to identify the Arctic-North Atlantic feedback loop as well as the more regional Barents Sea feedback loop in the sensitivity experiments (Fig. 4.9).
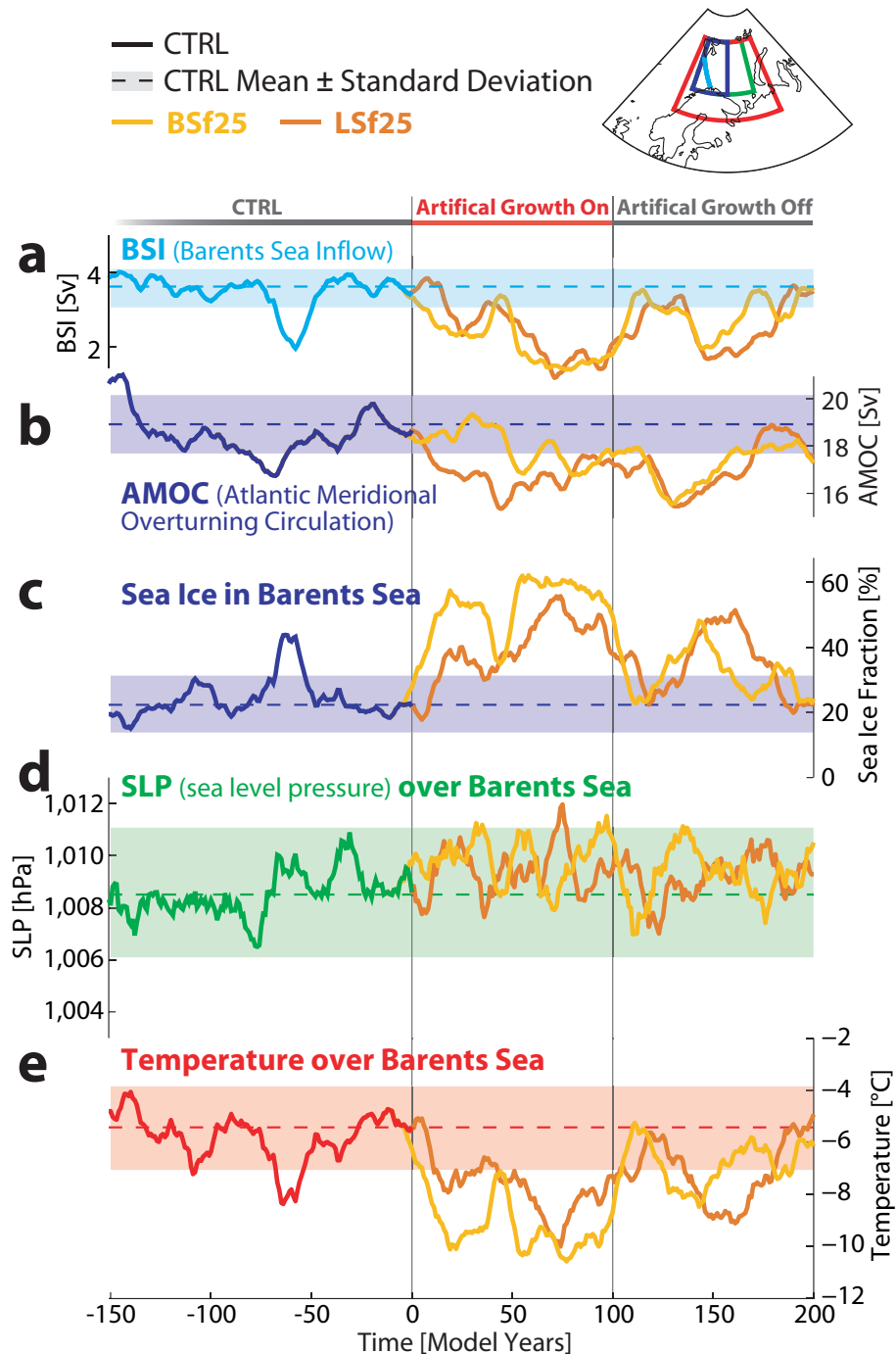

Figure 4.9: As Fig. 4.6 but for CTRL (only 150 years are shown), BSf25, and LSf25. All time series are 5-year running means, however, the standard deviation is based on annual values of the entire CTRL of 494 years.

In the BSf25 experiment, the sea ice concentration in the Barents Sea increases rapidly as the artificial sea ice growth starts (Fig. 4.9b). At the same time, the Barents Sea inflow is weakened by about 50%, overlaid by natural variability such as a short-lived resumption after

about 40 years (Fig. 4.9a). Not surprisingly, this short-lived resumption – with a small lag – can be identified in the sea ice index, illustrating the sensitivity of the Barents Sea sea ice cover to the inflow of warm Atlantic waters. The AMOC, on the other hand, remains in the range of natural variability until around model year 45, when it drops below the 1-σ range of CTRL (Fig. 4.9b). This time lag resembles the chain of events from excess sea ice production in the Barents Sea, the transport of this sea ice through Fram Strait and along the East side of Greenland, its engagement in the convective feedback in the Labrador Sea and ultimately the substantial weakening of the AMOC. In accordance with the advancing sea ice edge in the Barents Sea, regional SLP and temperature rise and fall, respectively (Fig. 4.9d and e). This shows that in the BSf25 experiment the interplay between Barents Sea sea ice cover, Barents Sea inflow, SLP, and temperature is at work decades before the AMOC responds and itself influences the Nordic Seas. Therewith the independence and full closure of the Barents Sea feedback loop is illustrated.

In LSf25 the artificial sea ice growth transforms the Labrador Sea into a strong sea ice source. The additional sea ice is melted in-situ or exported to the adjacent subpolar North-Atlantic (not shown). In any case, the strong freshwater forcing from the additional sea ice reduces convection in the North Atlantic and leads to a constant reduction of the AMOC until about model year 50, when it stabilizes (Fig. 4.9b). With a lag of about 10 years the Barents Sea inflow starts to weaken as well, a relation which matches our observations from CTRL, where the AMOC leads the Barents Sea inflow on average by 13 years (r = 0.66, p < 0.01 on 5-year running means). Further, this lag of about one decade is reminiscent of the time scale associated with advection of salinity anomalies in the SPG, as they have been observed (e.g., Dickson et al., 1988; Belkin, 2004) and modeled (e.g., Häkkinen, 1999) in context of the Great Salinity Anomalies of the twentieth Century. As soon as the inflow of Atlantic water weakens, the sea ice in the Barents Sea starts to increase, thereby, again, mirroring variability of the inflow. As a consequence of the increased sea ice cover in the Barents Sea, SLP rises and temperature falls (Fig. 4.9d and e). From this point on, the two sensitivity experiments qualitatively agree, illustrating the connection of the two regions Barents and Labrador Sea via a complex feedback mechanism.

There is evidence from CTRL that this feedback mechanism is active already in the control climate, however, in the absence of negative external forcing is unable to destabilize the system in a sustainable manner. Fig. 4.9 shows that in the 150 years of CTRL leading up to the start of the sensitivity experiments there occurs a short excursion of all quantities that very much resembles the feedback mechanism: the AMOC falls below the 1-σ range of the CTRL at about −60 years, upon which the Barents Sea inflow drops markedly, sea ice and SLP increase, and temperature falls (Fig. 4.9a-e). However, all quantities return to CTRL mean values within 10-15 years as the circulation changes are not large enough as to qualitatively change the discussed feedback mechanism.

4.4.3 Self-sustained feedback mechanism

The existence of apparently destabilizing positive feedback loops raises the question of self-sustainability of such feedback loops. Zhong et al. (2011) found the Arctic-North Atlantic feedback loop to be self-sustaining in two out four cases, whereby they revealed necessary preconditions for the North Atlantic. To test whether this self-sustainability exists in our experiments as well, we stop the artificial sea ice growth after 100 years. In both sensitivity experiments the Barents Sea sea ice edge retracts to CTRL levels within a decade (Fig. 4.9c). This is primarily a result of sea ice top melt, which is large due to the perpetual high solar irradiance of 1150 AD. In the absence of the artificial sea ice growth, this process acts to quickly push back the sea ice edge. As the sea ice retreats, the SSH gradient across the
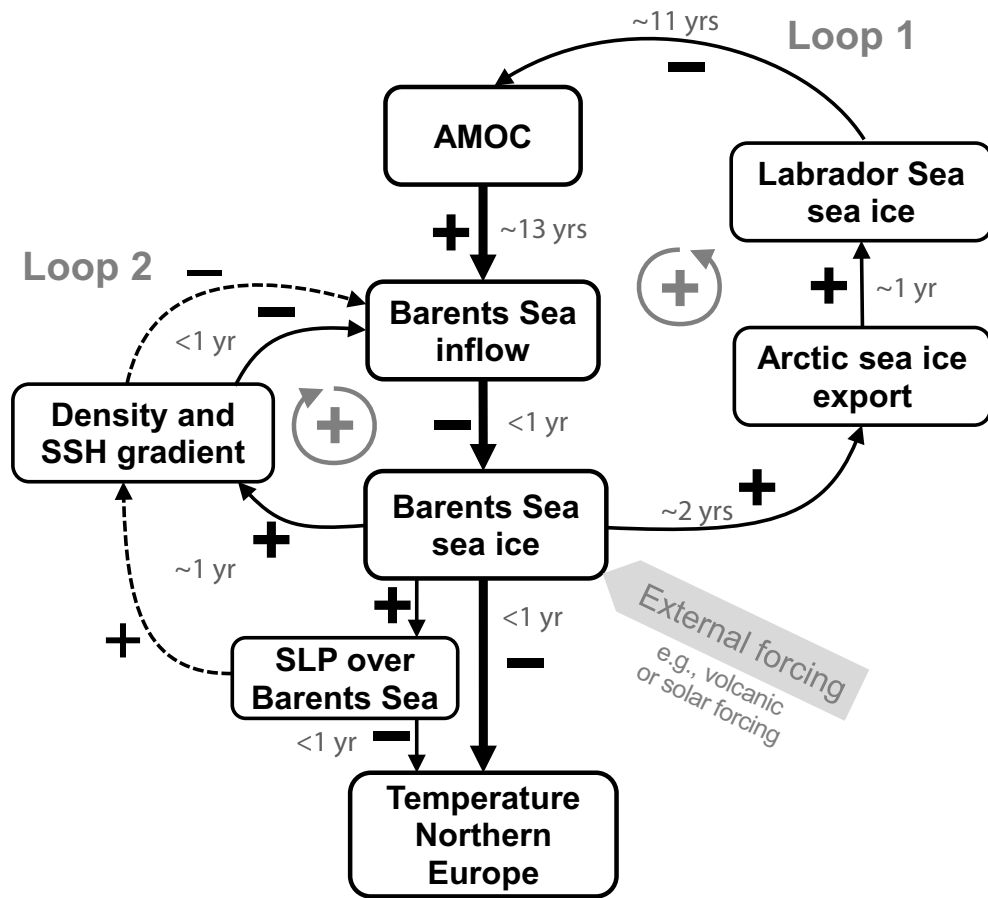
Figure 4.10: Schematic overview of the feedback loops associated with the Medieval Climate Anomaly-Little Ice Age transition, including estimates of time lags. Positive correlation between two processes is indicated with +, negative correlation with −. Negative external forcing leads to increased sea ice in the Arctic, especially in the Barents Sea. Loop 1: this causes an increased Arctic sea ice export and subsequently an increased import of sea ice into the Labrador Sea. As this sea ice melts, it weakens the Atlantic Meridional Overturning Circulation (AMOC), which in turn reduces the Barents Sea inflow of warm waters, causing further sea ice growth. Loop 2: increased sea ice causes the Barents Sea to become fresher and less dense. Additional, but slightly less important, wind changes due to elevated sea level pressure (SLP) increase the sea surface height (SSH) in the Barents Sea (dashed). As a result of these two processes, the SSH gradient across the Barents Sea opening increases, further reducing the Barents Sea inflow and thereby supporting sea ice growth. Finally, the increased sea ice cover has a direct thermal effect, decreasing surface air temperatures over Northern Europe and an indirect effect by inducing elevated sea level pressure (SLP) that allows for the advection of cold Arctic air towards Europe.

Barents Sea opening weakens and the Barents Sea inflow recovers (Fig. 4.9a). It therefore seems that the smaller-scale Barents Sea feedback loop is not self-sustaining. The AMOC, however, remains on a reduced level for decades, eventually triggering another passage of the Arctic-North Atlantic feedback loop, thereby also triggering the Barents Sea feedback loop again: about 40 years after switching off the artificial sea ice growth the Barents Sea inflow weakens (Fig. 4.9a), leading to increased sea ice (Fig. 4.9c), elevated SLP (Fig. 4.9d), and cooler temperatures (Fig. 4.9e). The two experiments conducted here provide evidence that the European climate is vulnerable to destabilizing positive feedbacks, given the appropriate external trigger in the form of negative radiative forcing. The sustained weakening of the AMOC is able to move the North Atlantic-European climate to a cooler state and keep it there for decades. Fig. 4.10 summarizes the feedback mechanism and depicts the two feedback loops at work.
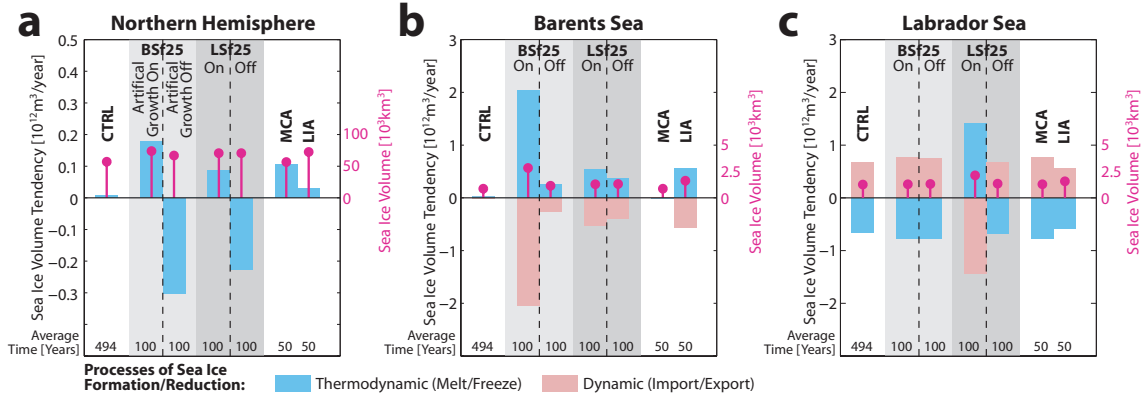
Figure 4.11: Annual mean sea ice volume tendency (split up in thermodynamic and dynamic terms; blue and red bars, left y-axis) and sea ice volume (thin magenta bars with dots, right y-axis) integrated over (a) the Northern Hemisphere from CTRL, from the artificial sea ice growth experiments (BSf25 and LSf25, grouped in two 100 year intervals during which artificial sea ice growth was switched on and off, respectively), and from the transient simulations (MCA = Medieval Climate Anomaly, 1150-1200 AD; LIA = Little Ice Age, 1450-1500 AD). (b-c) The same for the Barents and Labrador Sea, respectively.

Fig. 4.11 depicts the changes occurring in sea ice volume and sea ice volume tendency as a response to the artificial sea ice growth. On a hemispheric scale the sea ice volume increase over the first 100 years in BSf25 and LSf25 ($+13.3 \cdot 10^3$ km^3 and $+13.4 \cdot 10^3$ km^3, respectively) is of a similar magnitude as the one found in the transient simulations from MCA to LIA ($+15.7 \cdot 10^3$ km^3; Fig. 4.11a). This also implies that the sea ice growth rate (given as thermodynamic volume tendency) in BSf25 and LSf25 is significantly larger than in the transient simulations, as there the sea ice volume increase takes place over a longer time period (351 instead of only 100 years). After stopping the artificial sea ice growth in both experiments BSf25 and LSf25 the hemispheric sea ice volume remains elevated compared to CTRL, confirming the self-sustainability of the feedback mechanism discussed before.

The Barents Sea during CTRL is in near-balance regarding annual mean sea ice production and export (Fig. 4.11b). Until the LIA, however, the Barents Sea has become a net source of sea ice in the transient simulations. Nonetheless, the Barents Sea's own sea ice volume has also increased. This behavior is successfully mimicked in the BSf25 experiment, as sea ice growth and export, as well as sea ice volume strongly increase during the first 100 years. During the second 100 years the sea ice volume is reduced again, but the Barents Sea retains its role as a sea ice source. Interestingly, the same behavior is observed when we artificially grow sea ice in the Labrador Sea (LSf25), which illustrates the inherent linkage of the Labrador and Barents Sea that constitutes our feedback mechanism, i.e., the linkage of the two feedback loops.

In contrast to the Barents Sea, the Labrador Sea is a sea ice sink (in CTRL, but also during the MCA-LIA transition; Fig. 4.11c). At the inception of the LIA, both import and melting of sea ice increase, which is in line with the shoaling of the mixed layer depth in the region of the Labrador Sea (Fig. 4.5a). During the LSf25 experiment, however, sea ice grows in the Labrador Sea and is then exported to the subpolar North Atlantic, leading to a reduction in the AMOC similar to the transient simulations. Once the artificial sea ice growth is stopped, the Labrador Sea switches back into the role of a sea ice sink and the sea ice volume decreases rapidly. During the BSf25 experiment, the Labrador Sea imports more sea ice and melting is increased as well compared to CTRL. Thereby, the behavior of the Labrador Sea during the MCA-LIA transition is mimicked and the linkage of the Labrador and Barents Sea is illustrated again, this time in the opposite direction.

4.5   Discussion and conclusions

This study investigates the role of sea ice-ocean-atmosphere coupling in shaping regional climate during the inception of the LIA. Using an ensemble of transient simulations with CCSM3 we find the transitional phase from MCA to LIA to be dominated by a cooling and strong advances in sea ice cover on the Northern Hemisphere. In the Barents Sea, the advancing sea ice cover reduces the ocean-atmosphere heat flux and thereby cools the larger area. Additionally, increasing SLP over the Barents Sea allows for southward advection of cold Arctic air, resulting in an enhanced cooling over Northern Europe that qualitatively fits well with proxy-based temperature reconstructions (Mann et al., 2009). This chain of events offers an explanation for the regional temperature evolution during the MCA-LIA transition that does not rely on significant changes in the NAO, which are ambiguous (Trouet et al., 2012) and are not found to occur in several simulations using state-of-the-art coupled atmosphere-ocean climate models (Lehner et al., 2012a; Yiou et al., 2012). There remain, however, questions on the role of the stratosphere-troposphere coupling in the context of low-frequency variability of the atmosphere and the ability of climate models to simulate this coupling (e.g., Spangehl et al., 2010; Manzini et al., 2012). The majority of the climate models (including CCSM3) of the third Coupled Model Intercomparison Project (CMIP3) apply only relatively crude stratospheric dynamics, owing to low vertical resolution of the stratosphere (e.g., Cordero and Forster, 2006). This has been suggested as cause for them not reproducing the low-frequency atmospheric variability proposed by the reconstruction (e.g., Mann et al., 2009).

Confirming and expanding findings by Zhong et al. (2011), we identify a sea ice-ocean feedback loop that lays the foundation for the changes in surface climate described above. Following negative radiative forcing from volcanic eruptions and decreasing TSI at the inception of the LIA (1150-1300 AD), Arctic sea ice volume and extent grow significantly. As this anomalous sea ice is increasingly exported to the Labrador Sea and subpolar North Atlantic, it cools and freshens the surface waters and reduces convection. Consequently, the Subpolar Gyre and the AMOC are weakened, which leads to reduced transport of heat into the Nordic Seas, the Barents Sea and the Arctic Ocean. Weakening of convective deep water formation in the Nordic Seas and the Arctic Ocean further reduces the import of heat, thereby reinforcing the initial sea ice expansion.

In addition, another feedback loop between the Barents Sea and the Nordic Seas further amplifies the sea ice growth and the regional cooling at the beginning of the LIA. Upper ocean density changes, together with wind-driven reorganization of water masses, increase the Barents Sea SSH, ultimately reducing the inflow of warm Atlantic waters into the Barents Sea and strengthening the recirculation in the Nordic Seas. Contrary to Semenov et al. (2009) changes in Ekman transport at the Barents Sea opening are found to be negligible. Using sensitivity experiments with artificial sea ice growth in the Barents and Labrador Sea, we are able to prove the existence and closure of both feedback loops detected in the transient simulations. After switching off the artificial sea ice growth for the second 100 years of the experiments, Arctic sea ice remains in an expanded state for decades, confirming the potential self-sustainability of the Arctic sea ice cover due to these feedback loops (Zhong et al., 2011).

Support for this modeling result comes from new foraminifera-based proxies in the Fram Strait (Spielhagen et al., 2011) and off the coast of a Norwegian fjord (Hald et al., 2011). Water temperatures in both proxies are controlled largely by the amount of Atlantic waters in the mean flow as the proxies are located on distinct pathways for Atlantic waters into the Arctic. At these locations a near-synchronous drop in upper-ocean water temperature occurred at the onset of the LIA, indicating a reduced amount of Atlantic waters arriving (Fig. 4.12a and b). This shift is remarkably well reproduced by the model, which captures both the timing
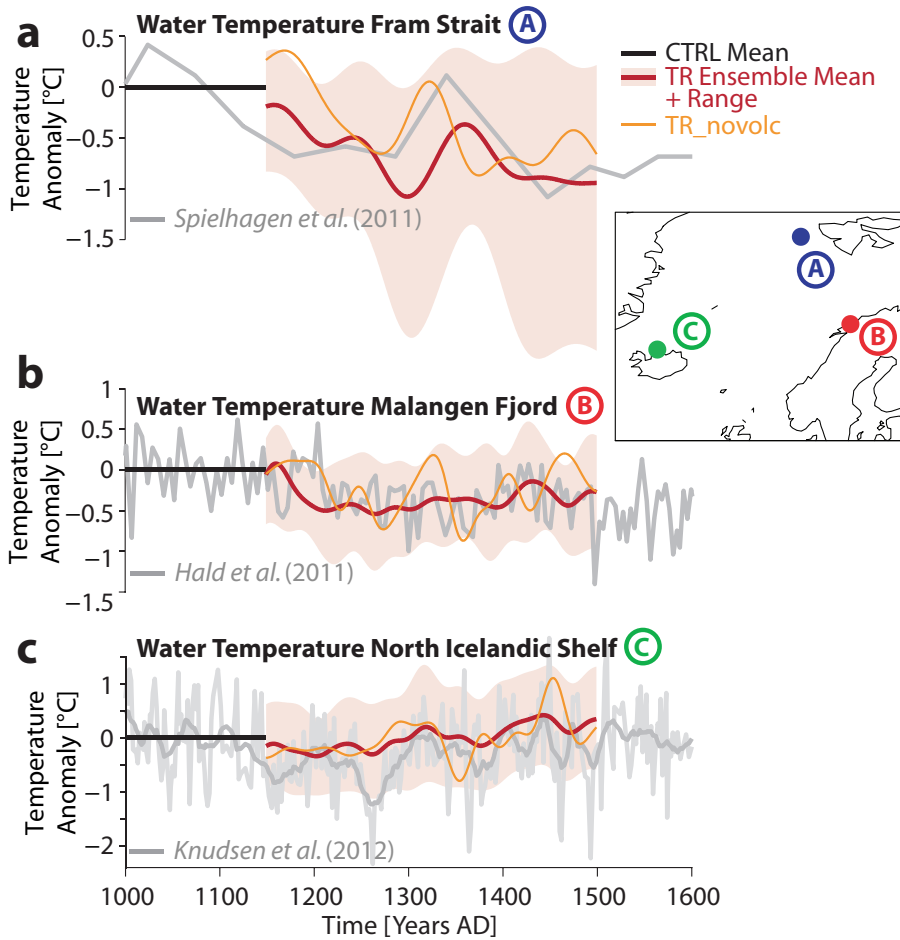
Figure 4.12: (a) Water temperature anomaly in the eastern Fram Strait from Spielhagen et al. (2011) (with reference to (wrt) 823-1074 AD) and in the model simulations (wrt long-term mean of CTRL; ~78° N/8.5-11.5° E; average over 200-300 m depth). (b) Water temperature anomaly in the Malangen Fjord from Hald et al. (2011) (wrt 1000-1149 AD) and in the model simulations (40-year fourier-filtered; wrt long-term mean of CTRL; ~70° N/16.5-18.1° E; at 47 m depth). (c) Water temperature anomaly (annual and 5-year running mean; wrt 1001-1150 AD) on the North Icelandic Shelf from Knudsen et al. (2012) and in the model simulations (40-year fourier-filtered; wrt long-term mean of CTRL; ~66.0-67.0° N/19.0-21.3° E; at surface).

and magnitude of the shift. Further, new results from the North Icelandic Shelf indicate a small temperature increase during the MCA-LIA transition (Fig. 4.12c; Knudsen et al., 2012) that corresponds to a northward shift of the oceanic polar front, allowing Atlantic species to enter the Nordic Seas. This signal is reproduced as well by the model, corroborating the coherent picture of oceanic changes in the Nordic Seas during the MCA-LIA transition: while the overall heat transport into the Nordic Seas is reduced, changes in the distribution of the Atlantic water leave a distinct pattern of localized warming and cooling around the Nordic Seas.

Excluding volcanic eruptions in one of the transient simulations yields a similar hemispheric temperature and sea ice response as in the simulations with volcanoes, however, the sea ice cover does not consequently remain in its expanded state as compared to the all-forcing simulations (both Arctic-wide and in the Barents Sea). Nevertheless, it appears that the origin of the negative forcing (TSI or volcanoes) is not crucial as long as it is persistent enough to trigger the destabilizing feedback mechanism described in this study. As the amplitude of the past TSI variations, and therewith its importance in triggering the MCA-LIA transition, remains debated (e.g., Gray et al., 2010; Shapiro et al., 2011; Miller et al., 2012), it is

difficult to attribute quantitative importance to either of the two forcings. While this is a pressing question in the context of paleoclimate sensitivity, it is beyond the scope of this study.

Further, many recent studies describe large events of internal variability in the climate system that are able to derail temperature and sea ice from the path anticipated solely from the external forcing: Kinnard et al. (2011) suggest that Arctic summer sea ice decreased post-1500 AD (i.e., during a period of negative forcing), a suggestion for which Crespin et al. (2009) provide support from modeling with data assimilation. However, both studies acknowledge that the absence of changes in heat transport into the Arctic Ocean during that time (Spielhagen et al., 2011) complicates the explanation for such anomalous behavior in Arctic temperature and sea ice.

Along the same lines, non-linear dynamics such as the feedbacks described in this study can depend crucially on the background climate, as shown also at the example of climate impacts of volcanic eruptions (e.g., Otterå et al., 2010; Zhong et al., 2011; Zanchettin et al., 2012) or ocean-atmosphere coupling (e.g., Yoshimori et al., 2010). To that end, transient ensemble simulations as well as sensitivity experiments, together with new proxies will help to constrain the uncertainties associated with the MCA-LIA transition and improve our understanding of mechanisms governing climate on the regional scale.

Acknowledgements

Bibliography

Årthun, M., T. Eldevik, L. H. Smedsrud, O. Skagseth, and R. B. Ingvaldsen, 2012: Quantifying the influence of Atlantic heat on Barents Sea ice variability and retreat. *J. Clim.* (25), 4736–4743, doi:10.1175/JCLI-D-11-00466.1.

Bauer, E., M. Claussen, and V. Brovkin, 2003: Assessing climate forcings of the Earth system for the past millennium. *Geophys. Res. Let.* (30), doi:10.1029/2002GL016639.

Belkin, I., 2004: Propagation of the "Great Salinity Anomaly" of the 1990s around the northern North Atlantic. *Geophys. Res. Let.* (31), doi:10.1029/2003GL019334.

Bengtsson, L., V. Semenov, and O. Johannessen, 2004: The early twentieth-century warming in the Arctic - A possible mechanism. *J. Clim.* (17), 4045–4057, doi:10.1175/1520-0442(2004)017<4045:TETWIT>2.0.CO;2.

Bitz, C., P. Gent, R. Woodgate, M. Holland, and R. Lindsay, 2006: The influence of sea ice on ocean heat uptake in response to increasing $CO2$. *J. Clim.* (19), 2437–2450, doi:10.1175/JCLI3756.1.

Born, A., K. H. Nisancioglu, and P. Braconnot, 2010: Sea ice induced changes in ocean circulation during the Eemian. *Clim. Dyn.* (35), 1361–1371, doi:10.1007/s00382-009-0709-2.

Bryan, F. O., G. Danabasoglu, N. Nakashiki, Y. Yoshida, D.-H. Kim, J. Tsutsui, and S. C. Doney, 2006: Response of the North Atlantic thermohaline circulation and ventilation to increasing carbon dioxide in CCSM3. *J. Clim.* (19), 2382–2397.

Collins, W. D., et al., 2006: The Community Climate System Model version 3 (CCSM3). *J. Clim.* (19), 2122–2143, doi:10.1175/JCLI3761.1.

Cordero, E. C. and P. M. d. F. Forster, 2006: Stratospheric variability and trends in models used for the IPCC AR4. *Atmos. Chem. Phys.* (6), 5369–5380.

Crespin, E., H. Goosse, T. Fichefet, and M. E. Mann, 2009: The 15th century Arctic warming in coupled model simulations with data assimilation. *Clim. Past* (5), 389–401.

Dickson, R. R., J. Meinke, S. A. Malmberg, and A. J. Lee, 1988: The "Great Salinity Anomaly" in the northern North Atlantic 1968-1982. *Prog. Oceanogr.* (20), 103–151, doi:10.1016/0079-6611(88)90049-3.

Goosse, H., H. Renssen, F. Selten, R. Haarsma, and J. Opsteegh, 2002: Potential causes of abrupt climate events: A numerical study with a three-dimensional climate model. *Geophys. Res. Let.* (29), doi:10.1029/2002GL014993.

Gray, L. J., et al., 2010: Solar influences on climate. *Rev. Geophys.* (48), doi:10.1029/2009RG000282.

Häkkinen, S., 1999: A simulation of thermohaline effects of a great salinity anomaly. *J. Clim.* (12), 1781–1795, doi:10.1175/1520-0442(1999)012<1781:ASOTEO>2.0.CO;2.

Hald, M., G. Salomonsen, K. Husum, and L. Wilson, 2011: A 2000 year record of Atlantic Water temperature variability from the Malangen Fjord, northeastern North Atlantic. *The Holocene* (21), 1049–1059.

Hofer, D., C. C. Raible, A. Dehnert, and J. Kuhlemann, 2012a: The impact of different glacial boundary conditions on atmospheric dynamics and precipitation in the North Atlantic region. *Clim. Past* (8), 935–949, doi:10.5194/cp-8-935-2012.

Hofer, D., C. C. Raible, N. Merz, A. Dehnert, and J. Kuhlemann, 2012b: Simulated winter circulation types in the North Atlantic and European region for preindustrial and glacial conditions. *Geophys. Res. Let.* (39), doi:10.1029/2012GL052296.

Hofer, D., C. C. Raible, and T. F. Stocker, 2011: Variations of the Atlantic meridional overturning circulation in control and transient simulations of the last millennium. *Clim. Past* (7), 133–150, doi:10.5194/cp-7-133-2011.

Holland, M. M., C. M. Bitz, E. C. Hunke, W. H. Lipscomb, and J. L. Schramm, 2006: Influence of the sea ice thickness distribution on polar climate in CCSM3. *J. Clim.* (19), 2398–2414.

Holliday, N. P., et al., 2008: Reversal of the 1960s to 1990s freshening trend in the northeast North Atlantic and Nordic Seas. *Geophys. Res. Let.* (35), doi:10.1029/2007GL032675.

Hoskins, B. J. and D. J. Karoly, 1981: The steady linear response of a spherical atmosphere to thermal and oro-graphic forcing. *J. Atm. Sci.* (38), 1179–1196, doi:10.1175/1520-0469(1981)038<1179:TSLROA>2.0.CO;2.

Ingvaldsen, R., L. Asplin, and H. Loeng, 2004: The seasonal cycle in the Atlantic transport to the Barents Sea during the years 1997-2001. *Continental Shelf Research* (24), 1015–1032, doi:10.1016/j.csr.2004.02.011.

IPCC, 2001: *Climate Change 2001: The Scientific Basis. Contribution of Working Group I to the Third Assess-ment Report of the Intergovernmental Panel on Climate Change*, Cambridge University Press, Cambridge, United Kingdom and New York, NY, USA, 881 pp.

IPCC, 2007: *Climate Change 2007: The Physical Science Basis. Contribution of Working Group I to the Fourth Assessment Report of the Intergovernmental Panel on Climate Change*, Cambridge University Press, Cambridge, United Kingdom and New York, NY, USA, 996 pp.

Kinnard, C., C. M. Zdanowicz, D. A. Fisher, E. Isaksson, A. de Vernal, and L. G. Thompson, 2011: Reconstructed changes in Arctic sea ice over the past 1,450 years. *Nature* (479), 509–U231, doi: 10.1038/nature10581.

Knudsen, K. J., J. Eiríksson, and H. B. Bartels-Jónsdóttir, 2012: Oceanographic changes through the last millennium off North Iceland: Temperature and salinity reconstructions based on foraminifera and stable isotopes. *Marine Micropaleontology* (84-85), 54–73, doi:10.1016/j.marmicro.2011.11.002.

Kuhnert, H. and S. Mulitza, 2011: Multidecadal variability and late medieval cooling of near-coastal sea surface temperatures in the eastern tropical North Atlantic. *Paleoceanogr.* (26), PA4224, doi: 10.1029/2011PA002130.

Lehner, F., C. C. Raible, and T. F. Stocker, 2012a: Testing the robustness of a precipitation proxy-based North Atlantic Oscillation reconstruction. *Quat. Sci. Rev.* (45), 85–94, doi:10.1016/j.quascirev.2012.04.025.

Lehner, F., C. C. Raible, T. F. Stocker, and D. Hofer, 2012b: The freshwater balance of polar regions in transient simulations from 1500 to 2100 AD using a comprehensive coupled climate model. *Clim. Dyn.* (39), 347–363, doi:10.1007/s00382-011-1199-6.

Li, C., D. S. Battisti, and C. M. Bitz, 2010: Can North Atlantic Sea Ice Anomalies Account for Dansgaard-Oeschger Climate Signals? *J. Clim.* (23), 5457–5475, doi:10.1175/2010JCLI3409.1.

Liu, Z., et al., 2009: Transient simulation of last deglaciation with a new mechanism for Bolling-Allerod warming. *Science* (325), 310–314, doi:10.1126/science.1171041.

Mann, E. M., et al., 2009: Global signatures and dynamical origins of the Little Ice Age and Medieval Climate Anomaly. *Science* (326), 1256–1260, doi:10.1126/science.1177303.

Manzini, E., C. Cagnazzo, P. G. Fogli, A. Bellucci, and W. A. Mueller, 2012: Stratosphere-troposphere coupling at inter-decadal time scales: Implications for the North Atlantic Ocean. *Geophys. Res. Let.* (39), doi:10.1029/2011GL050771.

Matthews, J. and K. Briffa, 2005: The 'Little Ice Age': Re-evaluation of an evolving concept. *Geografiska Annaler Series A - Physical Geography* (87A), 17–36, doi:10.1111/j.0435-3676.2005.00242.x.

Meehl, G., et al., 2006: Climate change projections for the twenty-first century and climate change commitment in the CCSM3. *J. Clim.* (19), 2597–2616, doi:10.1175/JCLI3746.1.

Miller, G. H., et al., 2012: Abrupt onset of the Little Ice Age triggered by volcanism and sustained by sea-ice/ocean feedbacks. *Geophys. Res. Let.* (39), doi:10.1029/2011GL050168.

Otterå, O. H., M. Bentsen, H. Drange, and L. Suo, 2010: External forcing as a metronome for Atlantic multidecadal variability. *Nature Geoscience* (3), 688–694, doi:10.1038/NGEO955.

Otto-Bliesner, B., R. Tomas, E. Brady, C. Ammann, Z. Kothavala, and G. Clauzet, 2006: Climate sensitivity of moderate- and low-resolution versions of CCSM3 to preindustrial forcings. *J. Clim.* (19), 2567–2583, doi:10.1175/JCLI3754.1.

Petoukhov, V. and V. A. Semenov, 2010: A link between reduced Barents-Kara sea ice and cold winter extremes over northern continents. *J. Geophys. Res.* (115), doi:10.1029/2009JD013568.

Pinto, J. G. and C. C. Raible, 2012: Past and recent changes in the North Atlantic Oscillation. *Wiley Inter-disciplinary Reviews: Climate Change* (3), 79–90, doi:10.1002/wcc.150.

Schmidt, G. A., et al., 2012: Climate forcing reconstructions for use in PMIP simulations of the Last Millennium (v1.1). *Geoscientific Model Development* (5), 185–191, doi:10.5194/gmd-5-185-2012.

Schröder, D. and W. M. Connolley, 2007: Impact of instantaneous sea ice removal in a coupled general circulation model. *Geophys. Res. Let.* (34), doi:10.1029/2007GL030253.

Semenov, V. A., W. Park, and M. Latif, 2009: Barents Sea inflow shutdown: A new mechanism for rapid climate changes. *Geophys. Res. Let.* (36), doi:10.1029/2009GL038911.

Shapiro, A. I., W. Schmutz, E. Rozanov, M. Schoell, M. Haberreiter, A. V. Shapiro, and S. Nyeki, 2011: A new approach to the long-term reconstruction of the solar irradiance leads to large historical solar forcing. *Astronomy & Astrophysics* (529), doi:10.1051/0004-6361/201016173.

Spangehl, T., U. Cubasch, C. C. Raible, S. Schimanke, J. Koerper, and D. Hofer, 2010: Transient climate simulations from the Maunder Minimum to present day: Role of the stratosphere. *J. Geophys. Res.* (115), doi:10.1029/2009JD012358.

Spielhagen, R. F., et al., 2011: Enhanced modern heat transfer to the Arctic by warm Atlantic water. *Science* (331), 450–453, doi:10.1126/science.1197397.

Stocker, T. F., A. Timmermann, M. Renold, and O. Timm, 2007: Effects of salt compensation on the climate model response in simulations of large changes of the Atlantic meridional overturning circulation. *J. Clim.* (20), 5912–5928, doi:10.1175/2007JCLI1662.1.

Stouffer, R. J., et al., 2006: Investigating the causes of the response of the thermohaline circulation to past and future climate changes. *J. Clim.* (19), 1365–1387.

Tietsche, S., D. Notz, J. H. Jungclaus, and J. Marotzke, 2011: Recovery mechanisms of Arctic summer sea ice. *Geophys. Res. Let.* (38), doi:10.1029/2010GL045698.

Trouet, V., J. Esper, N. E. Graham, A. Baker, J. D. Scourse, and D. C. Frank, 2009: Persistent positive North Atlantic Oscillation mode dominated the Medieval Climate Anomaly. *Science* (324), 78–80, doi:10.1126/science.1166349.

Trouet, V., J. D. Scourse, and C. C. Raible, 2012: North Atlantic storminess and Atlantic Meridional Overturning Circulation during the last Millennium: Reconciling contradictory proxy records of NAO variability. *Global and Plan. Change* (84-85), 48–55, doi:10.1016/j.gloplacha.2011.10.003.

Wanamaker Jr, A. D., P. G. Butler, J. D. Scourse, J. Heinemeier, J. Eiríksson, K. L. Knudsen, and C. A. Richardson, 2012: Surface changes in the North Atlantic meridional overturning circulation during the last millennium. *Nature Communications* (3), 1–7, doi:10.1038/ncomms1901.

Wanner, H., O. Solomina, M. Grosjean, S. P. Ritz, and M. Jetel, 2011: Structure and origin of Holocene cold events. *Quat. Sci. Rev.* (30), 3109–3123, doi:10.1016/j.quascirev.2011.07.010.

Wanner, H., et al., 2008: Mid- to Late Holocene climate change: An overview. *Quat. Sci. Rev.* (27), 1791–1828, doi:10.1016/j.quascirev.2008.06.013.

Wilmes, S. B., C. C. Raible, and T. F. Stocker, 2012: Climate variability of the mid- and high-latitudes of the Southern Hemisphere in ensemble simulations from 1500 to 2000 AD. *Clim. Past* (8), 373–390, doi:10.5194/cp-8-373-2012.

Yiou, P., J. Servonnat, M. Yoshimori, D. Swingedouw, M. Khodri, and A. Abe-Ouchi, 2012: Stability of weather regimes during the last millennium from climate simulations. *Geophys. Res. Let.* (39), doi:10.1029/2012GL051310.

Yoshimori, M., C. C. Raible, T. F. Stocker, and M. Renold, 2010: Simulated decadal oscillations of the Atlantic meridional overturning circulation in a cold climate state. *Clim. Dyn.* (34), 101–121, doi:10.1007/s00382-009-0540-9.

Zanchettin, D., C. Timmreck, H.-F. Graf, A. Rubino, S. Lorenz, K. Lohmann, K. Krueger, and J. H. Jungclaus, 2012: Bi-decadal variability excited in the coupled ocean-atmosphere system by strong tropical volcanic eruptions. *Clim. Dyn.* (39), 419–444, doi:10.1007/s00382-011-1167-1.

Zhong, Y., G. H. Miller, B. L. Otto-Bliesner, M. M. Holland, D. A. Bailey, D. P. Schneider, and A. Geirsdottir, 2011: Centennial-scale climate change from decadally-paced explosive volcanism: A coupled sea ice-ocean mechanism. *Clim. Dyn.* (37), 2373–2387, doi:10.1007/s00382-010-0967-z.

Chapter 5

Outlook

The aim of this thesis was to investigate aspects of the hydrological cycle under different forcing conditions as they occurred in the past 1,000 years and will likely occur in the future. The use of coupled models enabled the detailed investigation of processes in response to forcing changes. Thereby, models complement proxy reconstructions, which are often challanged to provide a dynamical explanation of the reconstructed signal. Currently, it is still common to publish a paleoclimatic reconstruction without proper support from models. Models, while being validated against observations with increasing rigor, can always only provide an incomplete rendition of reality and are prone to biases. In that sense, the importance of and need for combining and integrating proxy and model results became apparent throughout this thesis when either models were found to disagree with reconstructions or when reconstructions neglected dynamical information from models.

This thesis is therefore a step towards more inter-disciplinary climate sciences if we still consider climate modelling and paleoclimate reconstruction as distinct disciplines. It provides a number of examples on how the parallel use of proxy and model information can deepen our understanding of the climate system's response to different forcings. Nevertheless, more work is needed to tighten the collaboration between proxy and model community. A selection of ideas with reference to this thesis' results is given below.

Polar freshwater cycle

The study by Lehner et al. (2012b) provides the first assessment of the polar freshwater cycle in multi-century transient simulations with a comprehensive coupled model. Despite applying an ensemble of simulations to increase the robustness of our results, the use of only a single model represents a clear caveat of this study. Further, the model resolution was shown to play a non-negligible role as well for the outcome of the assessment. An update of the results is now possible with the new PMIP3/CMIP5 simulations at higher spatial resolution. In light of recent observational evidence regarding the Arctic freshwater reservoirs (Kinnard et al., 2011; Morison et al., 2012; Long and Perrie, 2012; Stroeve et al., 2012; Stammer et al., 2011), such a re-assessment could be carried out with consideration of changing atmospheric circulation patterns, oceanic pathways, or new projections of future sea ice changes and Greenland ice sheet melt.

NAO reconstruction

Lehner et al. (2012a) showed that the concept of the millennial NAO reconstruction by Trouet et al. (2009) was not robust on decadal time scales and made suggestions for improvements derived from a simple pseudo-proxy approach using models and reanalyses. Since 2009, a small number of proxies have been published which might be used in a revised version of the millennial NAO reconstruction. To that end, the framework presented in Lehner et al.

(2012a) can readily be applied to a new or extended set of proxies to validate the skill of such a new proxy set in describing the NAO pattern. In collaboration with French colleagues such an attempt is in preparation.

Lehner et al. (2012a) also showed that the hydrological signature of the NAO varies considerably over time and that the stationarity assumption inherent in proxy-reconstructions becomes harder to justify, a conclusion that is not new (see, e.g., Raible et al., 2006). While calibration errors, dating uncertainty, or chronology errors of the proxies are commonly included in a reconstruction's error bars, the susceptibility of a reconstruction concept to the stationarity assumption is hardly explored in a systematic manner. The increasing number of last millennium simulations with GCMs would allow to scan the range of probable hydrological signatures for a given reconstructed NAO phase state and time. In contrast to the classical proxy-surrogate ranking (PSR; Graham et al., 2007), which reorders model output to maximize coherence with the reconstruction, such an approach would embrace the full uncertainty of the coupled system in that it also considers cases in which a certain proxy set might misinterpret the large-scale atmospheric circulation pattern.

Sea ice experiments

The sensitivity experiments with artificial sea ice growth introduced by Lehner et al. (in press) are a new tool for paleoclimatic research that could be applied to other questions as well. Dansgaard-Oeschger (D-O) events are a prominent example for climate variations that are thought to be associated at least partly with changes in sea ice. A study by Li et al. (2010) tackled this issue by prescribing different sea ice distributions to an atmosphere-only model. The precipitation and temperature responses to these sea ice changes were found to be coherent with proxy signals during D-O events. Li et al. (2010) also assigned differing importance to different spatial patterns of sea ice changes. Our approach offers to revisit these conclusions in a fully-coupled system, which would allow to study the interaction of sea ice, ocean, and atmosphere during the abrupt warming events. Therefore, the sea ice could be artificially melted instead of grown, and the geographical location of this artificial sea ice melt could be varied in different experiments. Further, such an exercise also provides the opportunity to develop and improve our approach. Sea ice growth could be controlled from the ocean component alone, allowing salt conservation in the model.

Bibliography

Graham, N. E., et al., 2007: Tropical Pacific – mid-latitude teleconnections in medieval times. *Clim. Change* (83), 241–285.

Kinnard, C., C. M. Zdanowicz, D. A. Fisher, E. Isaksson, A. de Vernal, and L. G. Thompson, 2011: Reconstructed changes in Arctic sea ice over the past 1,450 years. *Nature* (479), 509–U231, doi: 10.1038/nature10581.

Lehner, F., A. Born, C. C. Raible, and T. F. Stocker, in press: Amplified inception of European Little Ice Age by sea ice-ocean-atmosphere feedbacks. *J. Clim.*

Lehner, F., C. C. Raible, and T. F. Stocker, 2012a: Testing the robustness of a precipitation proxy-based North Atlantic Oscillation reconstruction. *Quat. Sci. Rev.* (45), 85–94, doi:10.1016/j.quascirev.2012.04.025.

Lehner, F., C. C. Raible, T. F. Stocker, and D. Hofer, 2012b: The freshwater balance of polar regions in transient simulations from 1500 to 2100 AD using a comprehensive coupled climate model. *Clim. Dyn.* (39), 347–363, doi:10.1007/s00382-011-1199-6.

Li, C., D. S. Battisti, and C. M. Bitz, 2010: Can North Atlantic Sea Ice Anomalies Account for Dansgaard-Oeschger Climate Signals? *J. Clim.* (23), 5457–5475, doi:10.1175/2010JCLI3409.1.

Long, Z. and W. Perrie, 2012: Air-sea interactions during an Arctic storm. *J. Geophys. Res.* (117), doi: 10.1029/2011JD016985.

Morison, J., R. Kwok, C. Peralta-Ferriz, M. Alkire, I. Rigor, R. Andersen, and M. Steele, 2012: Changing Arctic Ocean freshwater pathways. *Nature* (481), 66–70, doi:10.1038/nature10705.

Raible, C. C., et al., 2006: Climate variability-observations, reconstructions, and model simulations for the Atlantic-European and Alpine region from 1500-2100 AD. *Clim. Change* (79), 9–29, doi:10.1007/s10584-006-9061-2.

Stammer, D., N. Agarwal, P. Herrmann, A. Koehl, and C. R. Mechoso, 2011: Response of a Coupled Ocean-Atmosphere Model to Greenland Ice Melting. *Surv. Geophys.* (32), 621–642, doi:10.1007/s10712-011-9142-2.

Stroeve, J. C., V. Kattsov, A. Barrett, M. Serreze, T. Pavlova, M. Holland, and W. N. Meier, 2012: Trends in Arctic sea ice extent from CMIP5, CMIP3 and observations. *Geophys. Res. Let.* (39), doi: 10.1029/2012GL052676.

Trouet, V., J. Esper, N. E. Graham, A. Baker, J. D. Scourse, and D. C. Frank, 2009: Persistent positive North Atlantic Oscillation mode dominated the Medieval Climate Anomaly. *Science* (324), 78–80, doi: 10.1126/science.1166349.

Appendix A

Last millennium simulation with the CESM

This appendix provides an overview on the status of a simulation of the last millennium with the fully-coupled Community Earth System Model (CESM) that runs at the Swiss National Supercomputing Center (CSCS) in Lugano, Switzerland. In the following, the simulation is motivated in a short introduction, including a paragraph on the Paleoclimate Model Intercomparison Project, from which many guidelines for the experimental setup of this simulation are derived. Then, the model and experimental setup are described. Further, a short review of the model performance at CSCS is given. Finally, preliminary results are discussed.

A.1 Motivation

The last millennium represents a key period for the study of climate variability as the external forcing of orbital and solar parameters was comparably weak, while at the same time the abundance of proxy reconstruction provides robust evidence of climate variability on decadal to centennial time scales. Climate models are a good tool to investigate the mechanisms behind this natural climate variability and to provide a dynamically consistent framework for the spatially fixed proxy reconstructions. Thereby, we establish and fortify an understanding of the climate system's sensitivity – a crucial prerequisite to be able to project future changes of the climate system.

Since the initial use of computers to numerically describe the climate system, the computational capacity has increased exponentially. The scientific community harvests this progress by constantly increasing the climate models' complexity and spatial resolution (see Fig. 1.2, IPCC, 2007). Knutti and Sedláček (2012) estimate that between the last two generations of climate models the computational capacity has increased by a factor of about 60. At least 50% of this capacity increase went into model complexity and the development of new model versions, while the other half was partitioned between increased model resolution and the need to simulate more model years.

The division of Climate and Environmental Physics (KUP) at the University of Bern has a long history of model development and use. For large parts of the 1970s and 1980s simple box models were used to complement studies of the carbon cycle and oceanic tracers. At the beginning of the 1990s, a first successfully coupling of a zonally averaged ocean and atmosphere model (Stocker et al., 1992) laid the foundation for a Bern climate model that, in the following decades, developed into a full-featured Earth System Model of Intermediate Complexity with a variety of applications in paleo- as well as future climate research (e.g., Müller et al., 2006; Steinacher et al., 2010; Ritz et al., 2011; Stocker et al., 2011). However, it was not until the beginning of the National Centre for Competence in Research (NCCR) Climate in 2001 that

a comprehensive General Circulation Model (GCM) was used at KUP. The choice fell on the model family of the National Center for Atmospheric Research (NCAR) in Colorado, USA, that includes GCMs with and without carbon cycle, the code of which is publicly available and well documented. After successful installation on the Swiss Supercomputer in Ticino, the Community Climate System Model version 2 (CCSM2) was subsequently used for a wide range of studies (Yoshimori et al., 2005, 2006; Raible et al., 2005, 2006, 2007). Collaboration with the NCAR and CSCS allowed for a good maintenance of the model and a step-wise upgrading from version 2 to version 3 (studies: Stocker et al., 2007; Casty et al., 2007; Yoshimori et al., 2010; Renold et al., 2010; Spangehl et al., 2010; Hofer et al., 2011; Büntgen et al., 2011; Wilmes et al., 2012; Lehner et al., 2012a,b, in press), and to version 4 (studies: Hofer et al., 2012a,b) in the following years. In 2010, the NCAR released its newest model version, the Community Earth System Model (CESM), a model that combines both high complexity, variable spatial resolution, and a state-of-the-art carbon cycle, thereby making full use of the grown computational capacity.

In a joint effort of the division groups for carbon cycle (Prof. Fortunat Joos) and coupled modeling (Prof. Thomas Stocker, PD Christoph Raible) a poposal was submitted at the CSCS, applying for over $4.5 \cdot 10^6$ CPU-hours to perform a simulation of the last millennium with the new CESM. The rationale behind this joint project is to output variables from the carbon cycle and the physical climate system on a high spatial and temporal resolution to enable both division groups to utilize the simulation. The unique dimensions of the project manifest themselves in large storage requirements and time-intensive post-processing. This project also complements a last millennium simulation with CCSM4 by the NCAR, which does not include the prognostic carbon cycle in the ocean (Landrum et al., 2013).

Scientifically, the project is primarily motivated by a lack of consensus on the amplitude of the external forcing of the climate system during the last millennium. The common approach to tackle this problem is to run different models with different forcing datasets and compare the results to observations and reconstructions, thereby looking for plausible combinations of model sensitivity and forcing amplitude. The fifth Coupled Model Intercomparison Project (CMIP5) represents the current coordinated effort by modeling groups around the world to provide a set of comparable simulations with different models to be investigated in the lead-up to the IPCC's Fifth Assessment Report (Taylor et al., 2012). Besides various simulations of the twentieth century and the future, CMIP5 covers three paleo-climate simulations for the Last Glacial Maximum, the mid-Holocene and the last millennium. In collaboration with the Paleoclimate Model Intercomparison Project's third phase (PMIP3; Otto-Bliesner, 2009) a protocol was set up that includes recommendations to the modeling groups regarding forcing files, variable selection, and post-processing (Schmidt et al., 2011).

From a practical point of view, the project is motivated by the wish to be able to design the specific model experiments, and to have the full model output available "in-house", i.e., without having to download model output from another modeling group's server, as this usually is a time-consuming procedure without guaranteed completeness of data.

A.2   Model

The Community Earth System Model (CESM) is a fully-coupled state-of-the-art Earth System Model developed by the National Center for Atmospheric Research (NCAR) and was released in 2010. The model code is freely available from the CESM website which also features detailed documentation, input datasets, diagnostics scripts, as well as some model output. As mentioned in section A.1 the CESM is the latest in a series of models developed at the NCAR over the last two decades. In the following the model components are introduced; here

the focus is set on improvements over CCSM3 rather than on a comprehensive description of each component.

A.2.1   Model components

In terms of physics CESM relies on the fourth version of the Community Climate System Model (CCSM4; a comprehensive description can be found in Gent et al., 2011). However, a carbon cycle is included in CESM's components of atmosphere, land, and ocean, distinguishing it from CCSM4 and qualifying the model as a full-featured Earth System Model. The CESM version used here is release 1.0.1. and includes representations of the atmosphere, land, ocean, and sea ice, all coupled trough a flux coupler. The advantage of CESM over its precursors CCSM3, CCSM2, and CSM1 is its user-friendly handling (in part due to a new coupling infrastructure) that allows for a variety of model resolutions or component combinations.

The atmospheric component of CESM 1.0.1 is the Community Atmosphere Model version 4 (CAM4; Neale et al., 2010a), successor to CAM3 that has been used as part of CCSM3 in the previous chapters of this thesis. The core changed from a spectral core used in CAM3 to a Lin-Rood finite volume core (Lin, 2004), resulting in less numerical noise. The horizontal resolution is $1.25° \times 0.9°$ with 26 vertical levels in the so-called $1°$ version used here. Changes to the convection scheme as compared to CAM3 cover the inclusion of deep convection in the momentum equation (Richter and Rasch, 2008) and the use of a dilute, rather than an undilute, approximation in the plume calculation, i.e., allowing an ascending air parcel to mix entropy properties with the free troposphere (Neale et al., 2008). This yields a more realistic frequency and intensity of deep convection. A major deficiency of CAM3 was the overestimation of low clouds in the Arctic, leading to a radiation bias. This has been addressed by a new parameterization of cloud fraction prediction that acts to reduce excessive wintertime polar cloudiness (Vavrus and Waliser, 2008). Further improvements in Arctic climate have been achieved within CAM5, however, this version was not yet available at the commencing time of our simulation.

The land component is the Community Land Model version 4 (CLM4; Lawrence et al., 2011), successor to CLM3 and the interim version CLM3.5, and operates on the same horizontal resolution as CAM4. Improvements and novelties, as compared to CLM3, include hydrological properties (such as surface runoff, including a separation of liquid and frozen river runoff, groundwater and permafrost schemes, a new snow model, canopy interception), plant functional type dependency on the soil moisture stress function, and a prognostic carbon-nitrogen cycle. The latter prognostically calculates vegetation, litter, soil carbon and nitrogen states, and vegetation phenology. Further, it is now possible to simulate transient land cover and land-use changes.

The ocean component is the Parallel Ocean Program version 2 (POP2; Smith et al., 2010; Danabasoglu et al., 2012), successor to POP in CCSM3. The horizontal resolution is identical to the $1°$ version of POP used in CCSM3 with a pole displaced to Greenland. The vertical resolution is increased to 60 levels with the upper 20 levels having a thickness of 10 meters. Changes to the parameterization for the transition of meso-scale eddies from the deeper ocean to the surface and the introduction of time and space-dependent thickness and isopycnal diffusivity coefficients lead to a more realistic representation of ocean eddy energy (Danabasoglu et al., 2008; Danabasoglu and Marshall, 2007). Adjustments to the vertical mixing terms and the introduction of a new parameterization for sub-meso-scale eddies yield more realistic mixing and stratification properties. Finally, a new parameterization improves the penetration depth of deep ocean overflows (Danabasoglu et al., 2010). Embedded in POP2 is the Biogeochemical Elemental Cycle model (BEC Moore et al., 2004) that builds on a nutrient-phytoplankton-zooplankton-detritus food web model and distinguishes three phytoplankton

functional types (Long et al., 2013). Carbon export and remineralization are parameterized according to Armstrong et al. (2002). pH, pCO_2, bicarbonate and carbonate ion concentrations are diagnosed from prognostic dissolved inorganic carbon, alkalinity, and temperature- and salinity-dependent equilibrium coefficients. Material reaching the ocean bottom is remineralized in one timestep, i.e., no sediment storage module is included. River discharge from CLM4 does not carry dissolved tracers but nitrogen deposition at the ocean surface can be prescribed.

The sea ice component is the Community Ice Code version 4 (CICE4) from the Los Alamos National Laboratories (Hunke and Lipscomb, 2010), which succeeds CSIM from CCSM3, and operates on the same horizontal resolution as POP2. Among the most important improvements is a new radiative transfer scheme that allows the incorporation of melt ponds or black carbon (Briegleb and Light, 2007; Holland et al., 2012). Given the improved cloud parameterization in CAM4, the sea ice albedo – a classical tuning parameter – can now be set at more realistic values.

A.2.2   Improvements and biases

Regarding the physical climate of the model and comparing to twentieth century observations, major improvements over CCSM3 can be found in the frequency of ENSO variability and the sea surface temperature correlations within the Pacific Ocean (Gent et al., 2011). This is in part due to higher vertical resolution in the upper ocean, leading to a bias reduction in the mean and the annual cycle of sea surface temperature along the equator in the eastern Pacific. The new overflow parameterizations improve the representation of the Atlantic Meridional Overturning Circulation, which is important for a correct energy and salt balance in the ocean basins. Another relevant improvement of CCSM4 is the annual cycle of water storage on land, resulting in more realistic river runoff and latent heat flux. The latter is especially important in the context of simulations of future climate change, as it yields a better representation of extreme events, such as heat waves and heavy rainfall (Gent et al., 2011). Improved sea ice distribution in the Labrador Sea arises from reduced along-coast viscosity in the ocean component, in turn yielding a more realistic location of the deep water formation site in that region (Jochum et al., 2008). Even though CCSM4 uses CAM4, and not the improved CAM5, the amount of low clouds in the Arctic is significantly improved over CAM3 in CCSM3. This results in realistic shortwave radiation at the surface in summer and allows to implement sea ice albedo values that are within the range of observations, while in CCSM3 they were tuned unrealistically to compensate for the cloud bias.

Major physical biases that remain in CCSM4 are a double Inter-Tropical Convergence Zone, biases in the latitudinal distribution of the shortwave and longwave cloud forcing, regional surface temperature biases, and the missing indirect effect of aerosols in CAM4. Note that many of these issues are addressed in the fifth version of CAM (Neale et al., 2010b; Meehl et al., 2013).

The carbon cycle of CESM has not yet been analyzed in as much detail as the physical part. Compared to the scarce observations during the twentieth century, CESM captures the spatial structure and seasonality of surface carbon fields over most parts of the ocean (Long et al., 2013). A major bias occurs in the Southern Ocean, where uptake of anthropogenic carbon is underestimated due to underestimated water mass formation. The land carbon cycle is in reasonable agreement with observational estimates but also underestimates uptake of anthropogenic carbon during the twentieth century (Keith Lindsay, personal communication and Lawrence et al., 2012).

A.3   Experimental setup and performance

A.3.1   Simulations

We conducted a 258-yr control simulation with 850 AD forcing that was branched from year 351 of a 1850 AD fully-coupled control simulation by the NCAR (b40.coup_carb.004). The surface climate is in reasonable equilibrium, while the global average ocean temperature exhibits a small cooling trend of approximately $-0.03\,\mathrm{K}\,100\,\mathrm{yr}^{-1}$ (for more diagnostics of b40.coup_carb.004 the reader is referred to CESM website[1]). However, restart files for the land are taken from a 850 AD control simulation, kindly provided by Sam Levis (NCAR, Boulder). This has the advantage that the soil and ecosystem carbon stocks are closer to 850 AD conditions than in the 1850 AD control simulation. The computational resources did not allow us to run the model into equilibrium before the start of the transient simulation. Most quantities of the surface climate (e.g., surface temperature, sea ice, upper ocean temperature) can, however, be considered reasonably equilibrated at the end of the control simulation. Trends are still detectable in slow-reacting quantities such as deep ocean temperature or soil carbon storage and should be addressed in future use of the simulation.

A.3.2   Forcing

The general uncertainties in determining the external forcing of the climate system over the last millennium have been discussed in the introduction to this thesis. In the following only the forcing files used in our simulation are presented. These are mostly consistent with the setup applied by the NCAR for their last millennium simulation with CCSM4 (Landrum et al., 2013), which follows PMIP3 protocol for the period 850-1850 AD and CMIP5 protocol for 1850 AD onwards.

Total solar irradiance

The PMIP3 protocol provides a series of different reconstructions of total solar irradiance (TSI) to be used in model simulations, which represented, at the time of initialization of PMIP3, the state-of-the-art knowledge on the topic (Schmidt et al., 2011). However, with more recent attempts to reconstruct TSI over the last millennium (Shapiro et al., 2011) it became clear that a consensus on the amplitude of past variability in TSI could not yet be reached. In light of these results we chose to conduct a simulation in which we use a different solar forcing than prescribed by PMIP3 protocols in order to take into account the newly widened envelope of uncertainty surrounding reconstructions of solar activity (Schmidt et al., 2012).

The TSI used for our simulation, S, is derived from the TSI used by the NCAR, S_{NCAR}, for their last millennium simulation (Landrum et al., 2013), which bases on Vieira and Solanki (2010) from 850-1834 AD when it merges with Lean et al. (2005). The reconstruction by Vieira and Solanki (2010) originates from a physical model of the solar surface magnetic flux and its relationship with cosmogenic isotopes measured on Earth. A synthetic 11-year solar cycle is added to the TSI reconstruction (Schmidt et al., 2011). Further, TSI is shifted down by $4.785\,\mathrm{W}\,\mathrm{m}^{-2}$ as compared to the PMIP3 present-day reference (TSI at year 2007 AD = $1365.7240\,\mathrm{W}\,\mathrm{m}^{-2}$; Wang et al., 2005) to account for the climate sensitivity of CESM. However, we chose to scale the TSI from NCAR, S_{NCAR}, to have a somewhat larger amplitude from present-day to the Maunder Minimum (0.2% as compared to 0.1% in S_{NCAR}):

$$S = 2.2635 \cdot (S_{NCAR} - \overline{S_{NCAR}}) + \overline{S_{NCAR}}. \tag{A.1}$$

---

[1] www.cesm.ucar.edu/experiments/cesm1.0 ; search for 'b40.coup_carb.004'

Considering the Earth as a sphere with an average albedo of 0.3, this translates into a radiative forcing difference as compared to S_{NCAR} of about 0.26 $W\,m^{-2}$ during the Maunder Minimum. Fig. A.1a shows the different TSI reconstructions proposed by the PMIP3 protocol as anomalies to 1850 AD together with the TSI used by the NCAR (S_{NCAR}) and in our simulation. It becomes evident that our TSI lies in between the large-amplitude reconstruction by Shapiro et al. (2011) and the bulk of small-amplitude reconstructions of the original PMIP3 protocol (Schmidt et al., 2011). This allows for potentially interesting comparisons of our simulation with the last millennium simulation by the NCAR as well as other modeling groups' simulation. Changes in ozone due to TSI variability are not included in our simulation.
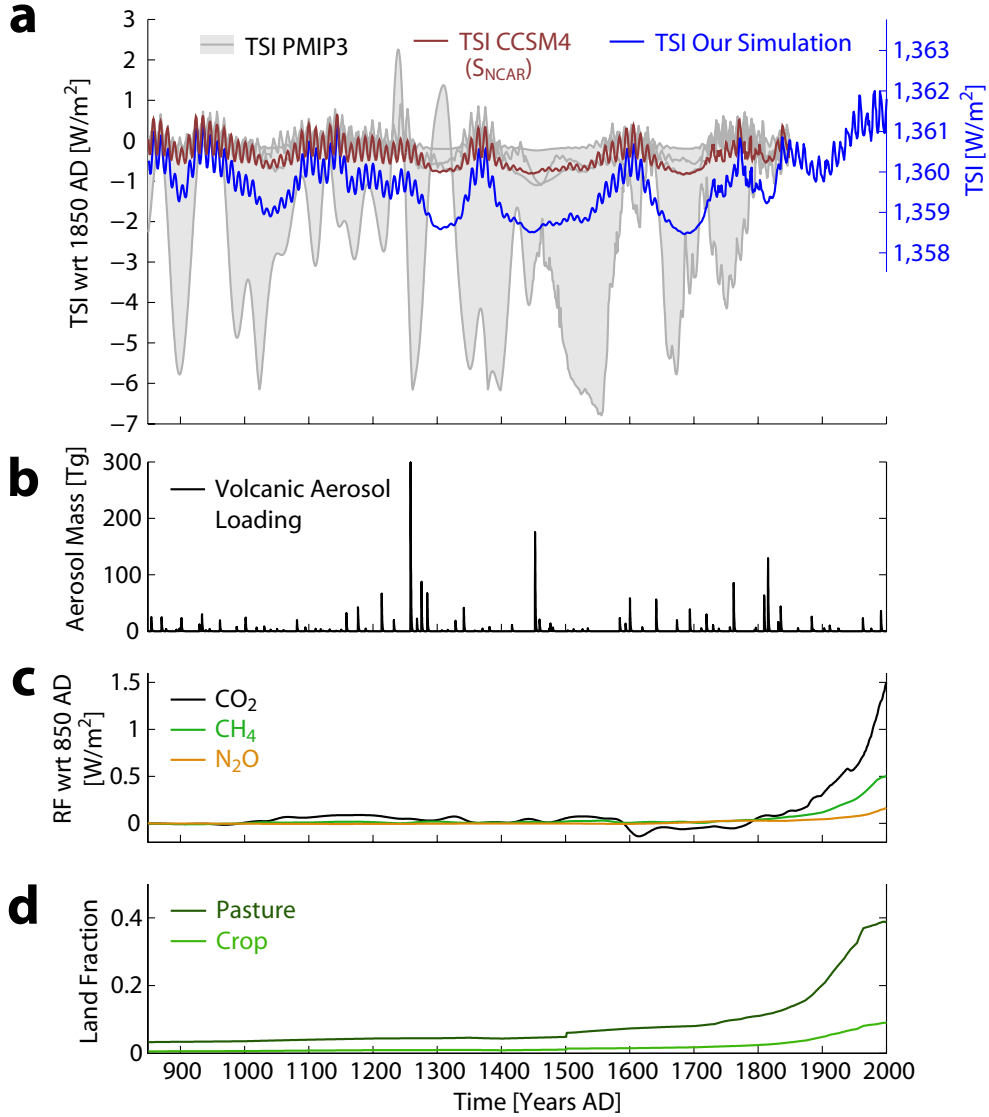

Figure A.1: Forcings used in the last millennium simulation with CESM. (a) Our TSI in comparison with the different TSI reconstructions proposed by PMIP3. (b) Volcanic forcing as total volcanic aerosol mass. (c) Radiative forcing (RF, calculated according to IPCC, 2001) from the greenhouse gases CO_2, CH_4, and N_2O. (d) Major changes in land cover.

The insolation due to Earth's orbital configuration is calculated online according to Berger (1978). When applying time-variant orbital parameters, this translates into a Northern Hemisphere boreal summer insolation decrease of approximately 0.5% from 850 to 2005 AD (Landrum et al., 2013). However, due to technical limitations in the model version 1.0.1, the

orbital parameters are set constant to 1990 AD values in this simulation. When compared
to the CCSM4 simulation with time-varying orbital parameters (Fig. A.2a), the discrepancy
between the two simulations remains undetectable in the trend of Arctic summer temperature
(Fig. A.2b), a measure that recently has been proposed to be significantly affected by orbital
parameters already on timescales of centuries to millennia (Kaufman et al., 2009). In fact,
the Arctic medium- to low-frequency summer temperature anomalies in CESM span a very
similar range as in CCSM4, despite CESM not accounting for time-varying orbital parameters
(Fig. A.2c). In other words, we fail to attribute these amplitudes in Arctic summer tempera-
ture to changes in orbital parameters alone, as detected by Kaufman et al. (2009). Note, that
we apply a TSI with larger amplitudes than CCSM4, that – together with sea ice feedbacks
– may well mask or compensate the missing forcing from time-varying orbital parameters in
CESM. While the time-invariant orbital forcing represents a caveat that likely has a small
impact on absolute Arctic summer temperatures, it does not render the simulation unrealistic
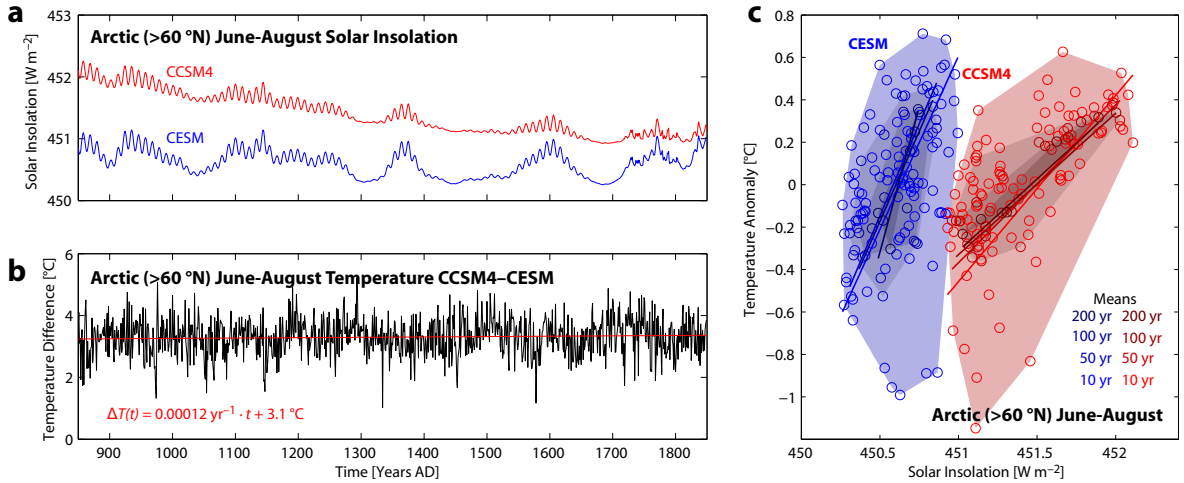as will be illustrated in other examples in the following.

Figure A.2: (a) Mean June-August (JJA) Arctic (>60° N) solar insolation in CCSM4 applying time-varying
orbital parameters and CESM applying fixed orbital parameters. (b) Arctic JJA temperature difference
between CCSM4 and CESM. The least-squares linear trend of this temperature difference is given in red. The
general offset in absolute temperatures between the two simulations may arise from the average difference
in TSI, sea ice-albedo feedbacks, or the difference in JJA insolation. (c) Arctic JJA temperature anomalies
(from their 850-1850 AD mean) versus solar insolation as 10-yr, 50-yr, 100-yr, and 200-yr means (100, 20, 10,
and 5 circles, respectively; from light to dark) from CCSM4 and CESM (red and blue, respectively). The
least-squares linear trend for each cloud of 10-yr, 50-yr, 100-yr, and 200-yr means is given in the respective
color. The shading envelops the range of temperature versus solar insolation for each cloud of means. The
temperature ranges of CCSM4 and CESM are comparable despite the differences in JJA insolation.

Volcanic eruptions

The volcanic forcing follows Gao et al. (2008) from 850-2001 AD, a reconstruction which bases
on volcanic deposition signals in 54 ice core records from both the Arctic and Antarctica
(Fig. A.1b). Note, that differences exist to the other PMIP3-proposed reconstruction by
Crowley et al. (2008) with respect to the exact timing and the magnitude of some of the
large eruptions (Schmidt et al., 2011). These arise from different transfer functions used
to convert sulphate concentrations in ice cores to aerosol optical depth and from different
criteria in screening for globally important eruptions. The reconstruction provides estimates
of the stratospheric sulfate aerosol loadings from volcanic eruptions as a function of latitude,
altitude, and month and is implemented in CESM as a fixed single-size distribution in the
three layers in the lower stratosphere (Neale et al., 2010a).

Greenhouse gases and aerosols

The temporal evolution of long-lived greenhouse gases (GHGs: CO_2, CH_4, and N_2O) is pre-scribed based on estimates from high-resolution Antarctic ice cores (Fig. A.1c). While the carbon cycle module interactively calculates the CO_2 concentration forced only by land use changes (see section A.3.2) and fossil fuel emissions (post-1750 AD, following Andres et al., 2012), it is radiatively inactive. Instead, the ice core data are used to prescribe CO_2 in the radiative code to keep the physical model as close to reality as possible. For CO_2 and CH_4 the Law Dome ice core is used, while for N_2O multiple ice cores are combined to increase robustness. At mid-twentieth century the ice core records are joined with measurements (for details see Schmidt et al., 2011, and references therein). Variations in the GHG concentrations pre-1800 AD are primarily due to natural variability and feedbacks in the carbon and nitrogen cycle, while from the nineteenth century onward anthropogenic fossil fuel burning and land-use change result in a strong increase in GHG concentrations. Aerosols such as sulfate, black and organic carbon, dust, and sea salt are implemented as non-time-varying, perpetually in-ducing the spatial distributions of the 1850 AD control simulation by the NCAR (Landrum et al., 2013). Post-1850 AD, the time-varying aerosol datasets provided by Lamarque et al. (2010) are used.

Land use and land cover changes

Land use and land cover (LULC) changes from 850-1500 are based on Pongratz et al. (2008), who applied a population-based approach on country level to estimate past agricultural activity. At the year 1500 AD this dataset is joined with Hurtt et al. (2011), a synthesis dataset that – based on Integrated Assessment Models – extends into the future. Up until about 1850 AD global anthropogenic LULC changes are small; however, they can have regional impacts (e.g., in parts of Asia). Towards the industrial era LULC changes accelerate, dominated by the expansion of crop land and pasture. Due to the lack of consensus on past LULC changes, the two datasets do not join smoothly but exhibit a step-wise change in the distribution of crop land and pasture at the year 1500 AD (Fig. A.1d). Note, that other modeling groups linearly interpolate every grid cell between the Pongratz et al. (2008) 1500 AD value and the Hurtt et al. (2011) 1700 AD value (Marco Steinacher, personal communication; Eby et al., in press).

Ocean forcings

Nitrogen (NH_x and NO_y) input to the ocean is held constant until it starts to be time-varying from 1850 AD onwards, following Lamarque et al. (2010). Iron fluxes from sediments are held fixed.

A.3.3   Model output

The four model components atmosphere, ocean, land, and sea ice all output monthly means of their variables in so-called history files. In the atmosphere a selected number of variables (precipitation, specific humidity, temperature, sea level pressure, winds, and geopotential height) are output as half-daily means in order to be able to analyze synoptic-scale phenomena such as storm tracks, blockings, or extreme events. In the ocean some biogeochemical variables are output as daily vertical integrals and some three-dimensional tracers are output as annual means.

A.3.4   Model performance

The model was installed on a Cray XT5 at the CSCS (at that time located in Manno) in the summer of 2010. The machine was upgraded to a Cray XE6 during the fall of 2011 (see

Table A.1). In collaboration with staff at CSCS and NCAR the configuration of the cores was optimized to obtain the most efficient performance given a throughput of >10 model year/day (see Table A.2). This way, a simulation of the last millennium would be possible within one year, i.e., the usual allocation period for computing time at CSCS. Due to the large number of three-dimensional tracers involved in the oceanic carbon cycle, the ocean component of the model is the computationally most expensive one. Therefore, we run the ocean parallel to all the other components. Through linearly increasing the number of cores used for the ocean we determine the scalability of the ocean component. Once the optimal configuration is found for the ocean, the other components are configured to run just as long as the ocean to maximize the efficiency of the whole configuration (so-called load balancing).

Table A.1: Overview of the machines used at CSCS.

	Cray XT5	Cray XE6
Processors	six-core AMD Opteron	2 × 16-core AMD Opteron
	Istanbul @ 2.4 GHz	Interlagos @ 2.1 Ghz
Nodes	12 cores per node	32 cores per node
Memory	16 GB per node	32 GB per node
Operating System	Cray Linux Environment	Cray Linux Environment

Table A.2: Benchmarks of CESM 1.0.1 for the Cray XT5 and XE6 at CSCS. The best configuration for each machine is given in the upper part of the table, while the lower part shows the corresponding performance. Cost indicates the total computing time of all central processing units (CPUs) for one model year, which is a measure of efficiency. Throughput indicates the number of model years which can be computed in 24 hours and is a measure of speed.

| | Cray XT5 | | | | Cray XE6 | | | |
	CPU	Root	Tasks	× Threads	CPU	Root	Tasks	× Threads
Coupler	896	0	224	× 4	256	256	256	× 1
Land ice (inactive)	1	0	1	× 1	1	0	1	× 1
Land	256	0	64	× 4	96	0	96	× 1
Sea ice	640	64	160	× 4	160	96	160	× 1
Atmosphere	896	0	224	× 4	512	0	512	× 1
Ocean	480	224	120	× 4	256	512	256	× 1
# of CPU	1,376				768			
Cost	2,613 CPU h/sim y				2,138 CPU h/sim y			
Throughput	12.64 sim y/day				8.62 sim y/day			

When the machine was upgraded to a Cray XE6 this configuration had to be changed. The new nodes combine 32 instead of 12 cores, and since only complete nodes can be booked for computation, the distribution of the nodes on the different model components had to be adapted to be – if possible – a multiple of 32. The upgrade resulted in more cores being available at CSCS, however, in the case of CESM increased communication between the cores actually resulted in a throughput decrease of over 30% (see Table A.2).

A.4   Preliminary results

Beginning of May 2013, the simulation is at the year 1850 AD. The plan is to continue it until 2100 AD, using the RCP 8.5 scenario from 2006 AD onwards. Here, a few climate parameters are investigated that shed light on the trends and amplitudes of the already simulated climate (850-1850 AD) and how they compare with reconstructions.

A.4.1   Surface climate

Surface air temperature

The simulated annual mean Northern Hemisphere (NH) surface air temperature (SAT) follows the general evolution expected from proxy reconstructions: a warm Medieval Climate Anomaly (MCA, ~950-1250 AD) and a transition into the colder Little Ice Age (LIA, ~1200-1700 AD; Fig. A.3). The NH MCA-to-LIA cooling amounts to about 0.26 °C (taking the time periods defined before, as in Mann et al., 2009). In the simulation the inception of the LIA occurs in concert with the decreasing TSI and the sequence of strong volcanic eruptions during the thirteenth century. Reconstructions differ substantially in this matter and start to cool as early as 1100 AD or as late as 1400 AD. Note, that new regional multi-proxy reconstructions of temperature are becoming available within the PAGES 2K network (PAGES 2k network, 2013) that allow an in-depth comparison of past regional temperature evolution. They provide no support for a globally synchronous MCA or LIA but show a clear tendency towards colder temperatures over most continents in the second half of the millennium.

Fig. A.3 additionally displays the NH temperature evolution of simulations by other PMIP3-contributing modeling groups currently available on the PMIP3 archive (number of ensemble members in brackets): BCC-CSM1-1 (1), CCSM4 (1), CSIRO-Mk3L-1-2 (1), FGOALS-gl (1), GISS-E2-R (4), HadCM3 (1), IPSL-CM5A-LR (1), MPI-ESM-P (1). Other modeling groups will contribute their simulations to PMIP3, however, at the moment these are the once which provide monthly SAT. The simulation with MIROC-ESM exhibits a strong drift over the last millennium and is therefore not shown here. Generally, the models are within the range of the reconstructions (Fig. A.3). Notable disagreement among the models exists (i) on the amplitude of the MCA, where most models show colder conditions than CESM and CCSM4, and (ii) on the response to volcanic eruptions, where CESM and CCSM4 are among the more sensitive models (FGOALS-gl, on the other hand, shows basically no response to the large 1258 AD-eruption). The absolute NH annual mean temperature (850-1850 AD) in PMIP3 models ranges from 12.00 °C to 14.66 °C .

The CCSM4 simulation by the NCAR (Landrum et al., 2013), which differs from our simulation in initial conditions and TSI amplitude, shows a largely coherent behavior in terms of amplitude and decadal variability as compared to our simulation (correlation of annual means $r = 0.82$, p<0.001). This indicates that TSI (in combination with volcanic forcing) paces decadal to centennial SAT variability. It also indicates that the common underlying physical components of the two models (especially CAM4, POP2, CICE) are relatively insensitive to differences in the TSI amplitude of the magnitude seen here (see section A.3.2). Indeed, the Maunder Minimum (1675-1704 AD), the period of largest TSI difference between CCSM4 and CESM (1.5 W m^{-2}), is only 0.14 °C cooler in CESM.

The impact of volcanic eruptions in CESM is generally stronger than anticipated by most reconstructions (an oversensitivity of CCSM4 to volcanoes based on twentieth century simulations has been reported by Meehl et al., 2012). Considerable disagreement between models and reconstructions in general exists on the magnitude of the eruptions at 1258 AD and around 1350 AD. The 1258 AD eruption is the largest during the last millennium in recent reconstructions and its climatic impact was likely enhanced through the cumulative effect
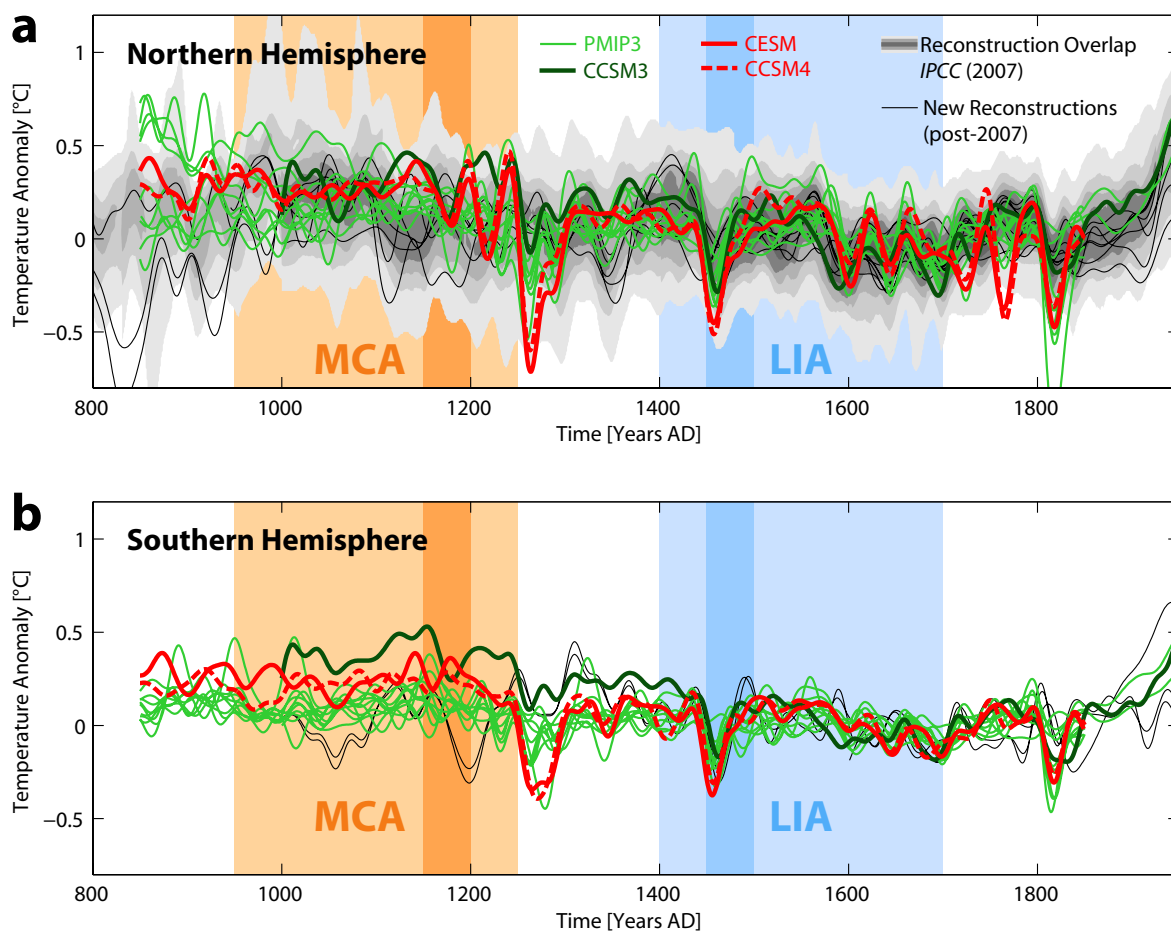
Figure A.3: (a) Northern Hemisphere and (b) Southern Hemisphere temperature anomalies with reference to 1500-1899 AD in model simulations and reconstructions. The shading indicates the reconstruction overlap from the last IPCC report (IPCC, 2007), black lines are newer reconstructions (NH: Ammann and Wahl (2007); Hegerl et al. (2007); Mann et al. (2008); Leclercq and Oerlemans (2012); SH: Mann et al. (2008); Leclercq and Oerlemans (2012). If a reconstruction is not available over the full reference period, it is scaled to have the same mean as the time series of maximum overlap from the shading during the time when the two time series overlap. Last millennium simulations contributing to the third Paleoclimate Model Intercomparison Project (PMIP3) are given in green (some extend to the year 2005 or beyond). The last millennium simulation with CCSM3 by Hofer et al. (2011) is given in dark green. All time series have been smoothed by a fourier filter with a 30-year cut-off period. The Medieval Climate Anomaly (MCA) and the Little Ice Age (LIA) are indicated as defined in Mann et al. (2009, light shading) and Lehner et al. (in press, darker shading).

of three smaller eruptions following shortly after (Gao et al., 2008; Crowley et al., 2008). However, the pronounced cooling that is simulated by the models for this eruption cluster is largely absent in temperature reconstructions. Controversial, around 1350 AD temperature reconstructions show a decadal-scale cooling due to volcanoes that is absent in the models, as the volcanic forcing that is used in the models shows only two relatively small eruptions around that time. Part of this incoherent picture may arise from the unknown aerosol size distribution for past eruptions (Timmreck et al., 2010) and the unknown geographic location of past volcanic eruptions (Schneider et al., 2009). As many proxy reconstructions of temperature rely heavily on tree ring data it is worth noting that the dendrochronology community currently debates whether the trees' response to volcanic eruptions resembles the true magnitude of the eruption (Mann et al., 2012; Anchukaitis et al., 2012).

The Southern Hemisphere (SH) generally shows a similar SAT evolution as the NH with the signature of the MCA and LIA superimposed on a millennial cooling trend. However, due to

the dampening effect of the higher ocean-to-land ratio on the SH the SAT variations resulting from TSI fluctuations and volcanic eruptions are smaller than on the NH. Over the second half of the last millennium the simulation is in reasonable agreement with the small number of reconstructions that exist for the SH. Between 1000 and about 1300 AD the reconstructions show variations that are not reproduced by the model. Again, the cluster of volcanic eruptions starting at 1258 AD does not leave a marked response in the reconstructions, but does so in the models. However, this cluster of volcanic eruptions has a far greater impact in CESM and CCSM4 than in the other models. The eruptions in the 1450s then trigger a more coherent behavior of the models. The absolute SH annual mean temperature (850-1850 AD) in PMIP3 models ranges from $11.37\,°C$ to $14.09\,°C$.

Sea ice

Due to the sparseness of observational data or proxies during preindustrial times it is difficult to validate sea ice in simulations of the last millennium. A recent multi-proxy approach yielded a millennial reconstruction of pan-Arctic August sea ice extent that models can be compared to (Kinnard et al., 2011). Our simulation is in reasonable agreement with the reconstruction and captures both absolute values and amplitudes (Fig. A.4). However, the considerable reduction of sea ice extent reconstructed for the time around 1600 AD is not fully reproduced by the simulation, which is a the upper end of the uncertainty band of the reconstruction at that time. Kinnard et al. (2011) hypothesize that only a strengthened inflow of warm Atlantic waters through Fram Strait could have produced such a reduction in Arctic sea ice cover during a time of wide-spread atmospheric cooling (LIA). The corresponding proxy from the Fram Strait (water temperature at depth of Atlantic water inflow), however, does not show a marked increase in Atlantic inflow at that time (Spielhagen et al., 2011). In our simulation no direct relation between the annual mean ocean heat transport (OHT; relative to a reference temperature of $-0.1\,°C$) through Fram Strait and Arctic summer sea ice extent is detectable as there exists no significant (lag-)correlation. The OHT through Fram Strait (88 ± 19 TW) shows strong interannual and decadal variability. The fairly short observational records (e.g., Schauer et al., 2004, reported 28-46 TW during three years) make it hard to validate the model, and the comparison to the proxy reconstruction by Spielhagen et al. (2011) reveals no clear coherence between reconstruction and model. Of the other models only CCSM4 reproduces the reconstructed sea ice extent with comparable accuracy as CESM. The other models either do not show the distinct increase in sea ice extent after 1200 AD or are substantially off in terms of absolute values.

Inception of the Little Ice Age

Chapter 4 of this thesis features a study on the role of the Arctic sea ice during the transition from the MCA to the LIA (1150-1500 AD) using an ensemble of simulations with CCSM3. Increasing sea ice in the Barents Sea, accompanied by increased SLP and ambient cooling, was found to amplify the cooling in Northern Europe at the inception of the LIA. The new simulation with CESM and other models offers the possibility for a comparison with the CCSM3 results. While the proposed mechanism appears robust within the CCSM3 ensemble, the comparison with new PMIP3 simulations from other models shows a more heterogeneous picture regarding the pattern of sea ice, temperature, and sea level pressure during the MCA-LIA transition (Fig. A.5).

When considering the same time period as in chapter 4, 1450-1500 AD (LIA) and 1150-1200 AD (MCA), the models agree on an amplified cooling over Northern Europe and Northern Russia (multi-model mean in Fig. A.5). However, the change in sea ice distribution (indicated here by the shift of the line of 50% sea ice concentration) and the SLP anomaly
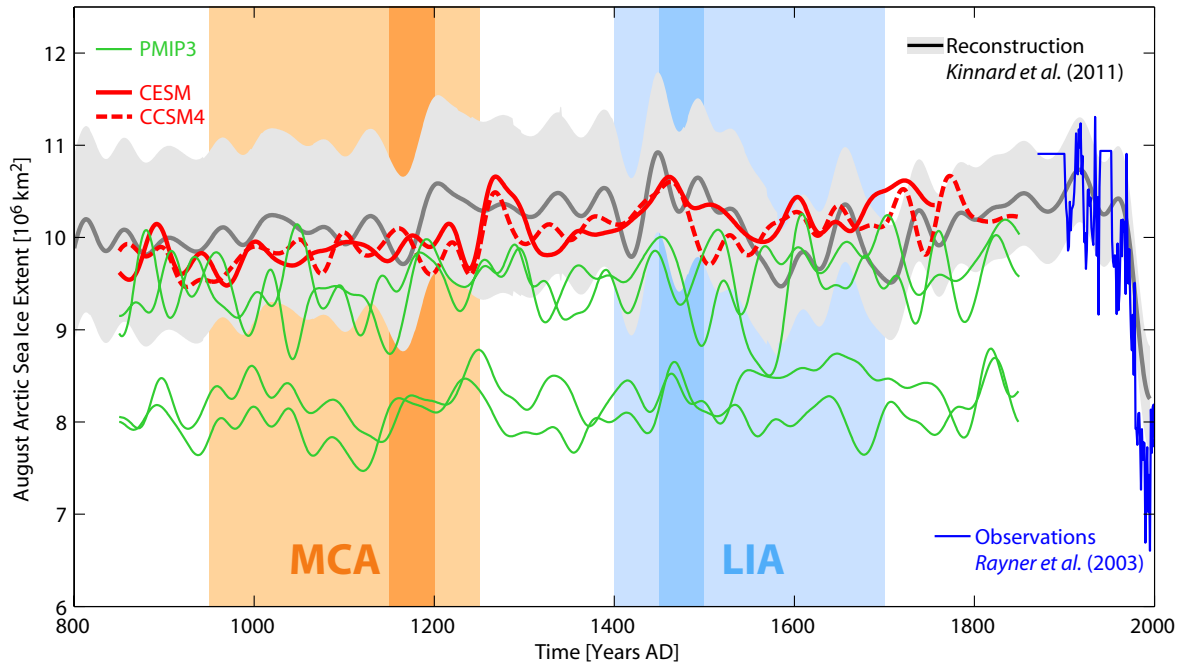
Figure A.4: August Arctic sea ice extent in model simulations and a reconstruction by Kinnard et al. (2011). Sea ice extent is calculated as the area with 15% and more sea ice cover. Observations are from Rayner et al. (2003). Model time series have been smoothed by a Fourier filter with a 40-year cut-off period. The Medieval Climate Anomaly (MCA) and the Little Ice Age (LIA) are indicated as defined in Mann et al. (2009, light shading) and Lehner et al. (in press, darker shading).

differ considerably between the models. The analysis in chapter 4 revealed that the mechanism – advancing sea ice, increasing SLP, decreasing temperature in the Barents Sea – is quite sensitive to the location of the sea ice edge, which is why a different sea ice distribution will likely yield a different climate response as compared to CCSM3.

CSIRO-Mk3L-1-2 shows a similar pattern as CCSM3 in all quantities. The other models have either different sea ice distributions or do not show a clear, i.e. significant, link between changes in sea ice and SLP. A remarkable discrepancy occurs in the response of CESM and CCSM4. As mentioned before, the physical components of these two models differ only in terms of the applied solar forcing, yet their SLP anomalies are markedly different. In CESM SLP increases in the area of the increased sea ice cover, in line with CCSM3. Controversial, CCSM4, while also simulating a slight increase in sea ice, shows a widespread decrease in SLP in the Arctic region. The picture becomes slightly more coherent when looking at annual means (Fig. A.6).

When considering the time periods used in Mann et al. (2009), 1400-1700 AD (LIA) and 950-1250 AD (MCA), the picture is similarly heterogeneous (Fig. A.7). CESM and CCSM4 display a comparable cooling pattern over Northern Europe and Russia and a similar sea ice distribution, while showing somewhat different SLP anomalies. Two models (IPSL-CM5A-LR and BCC-CSM1-1) even simulate substantial warming over the North Atlantic, leading to a small retreat of sea ice in the Labrador Sea during the LIA. The amplified cooling over Northern Europe and Russia seen in the reconstruction is not coherent across all models. Nevertheless, due to the large anomalies in CESM and CCSM4 it emerges as the dominant signature in the multi-model mean.

Finding the reasons for the discrepancy between CESM and CCSM4, or between the different models in general, is not straightforward. Due to the large internal variability, of e.g., SLP, and the relatively weak external forcing applied to last millennium simulations (as compared

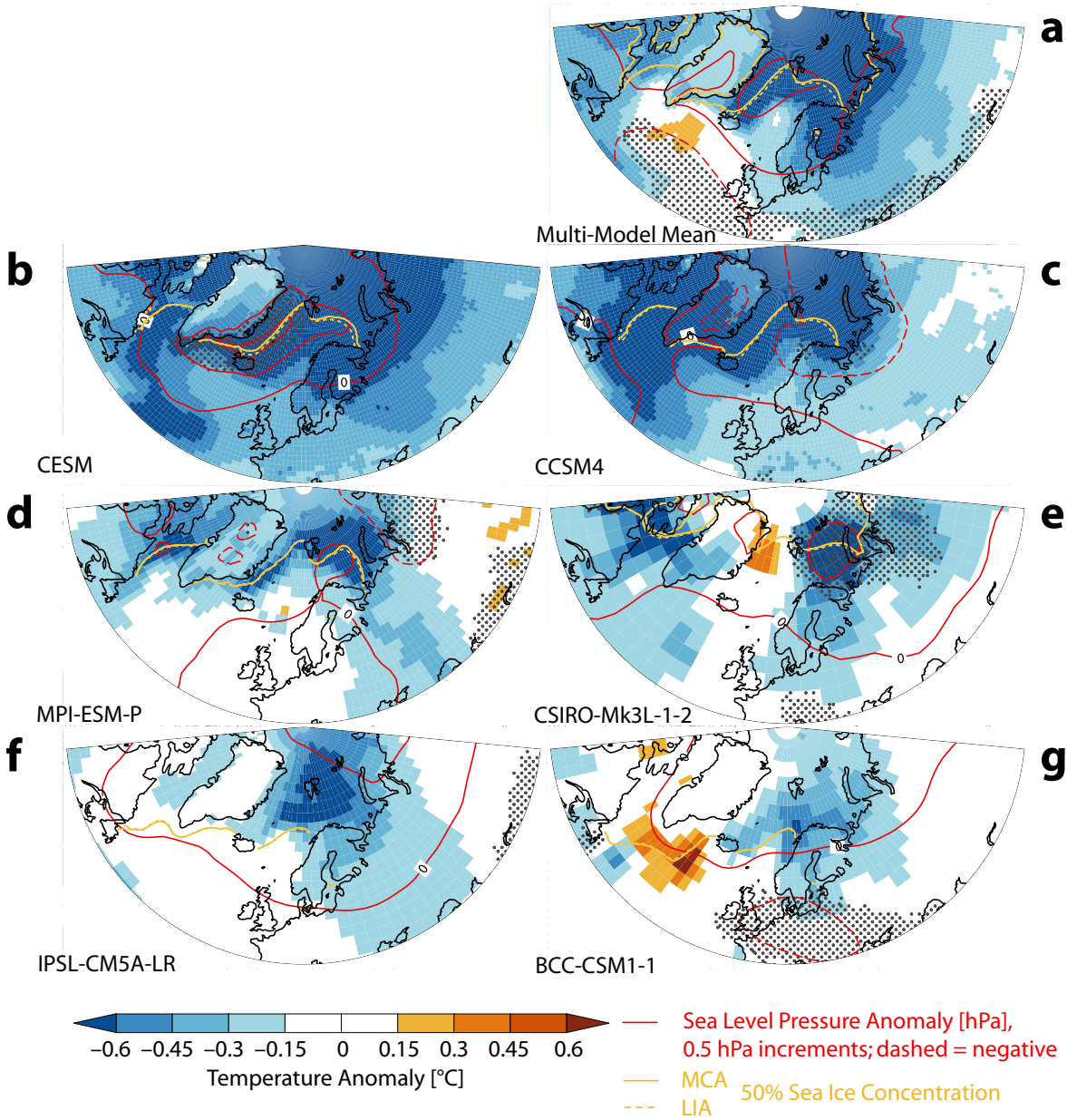**LIA (1450-1500) – MCA (1150-1200), NDJFMA, Multi-Model**

Figure A.5: November-April mean Little Ice Age (LIA, 1450-1500 AD) − Medieval Climate Anomaly (MCA, 1150-1200 AD) difference in sea level pressure (SLP, stippling indicates significance at the 5% level in a two-sided t-test), surface air temperature, and sea ice concentration. Time periods are as in Lehner et al. (in press). (a) Multi-model mean of PMIP3 models plus CESM. (b-g) Individual models.

to glacial-interglacial forcing) the signal-to-noise ratio is small for many of the simulated quantities. Differences in explicit physics or parameterizations of models add another possibility for discrepancies. Most importantly, however, for all these models only a single last millennium simulation exists to date, making it virtually impossible to conduct proper detection and attribution (see section 1.1.3).

Ideally, these issues are tackled using ensemble simulations with different models. As alluded to in the introduction of this thesis, this is quite costly and not yet common practice in paleoclimatic research with coupled models. Rather, (i) ensembles over shorter time periods are used or (ii) the individual model simulations are averaged into one multi-model mean.
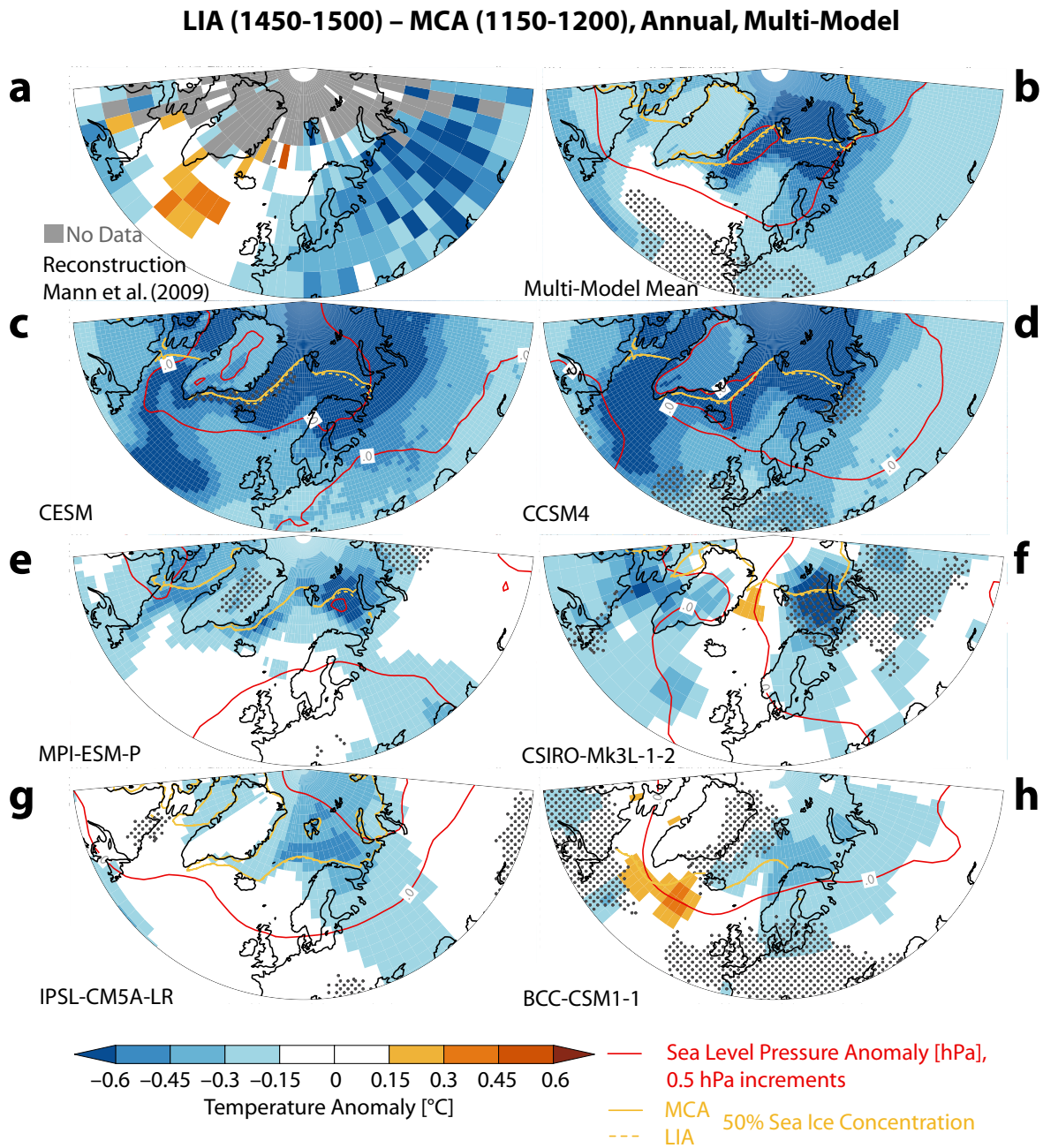
Figure A.6: Same as Fig. A.5 but for annual means. (a) Reconstructed temperature anomaly. (b) Multi-model mean of PMIP3 models plus CESM. (c-h) Individual models.

The first approach was applied in chapter 4 (Lehner et al., in press): six ensemble members with CCSM3, differing only by their initial conditions, show a heterogeneous response to the external forcing (Fig. A.8). Although not as heterogeneous as among different models (Figs. A.5, A.6 and A.7), the anomaly patterns in sea ice and SLP still differ considerably between the ensemble members. However, while not significant in every individual member, the sea ice increase, the cooling, and the positive SLP anomaly over the Barents Sea clearly stand out as significant features of the ensemble mean.

The second approach, a multi-model mean, has the advantage of sampling different physically self-consistent models, thereby reducing the risk that an important process is missed – a risk inherent in the first approach. On the other hand, a common problem of unweighted multi-
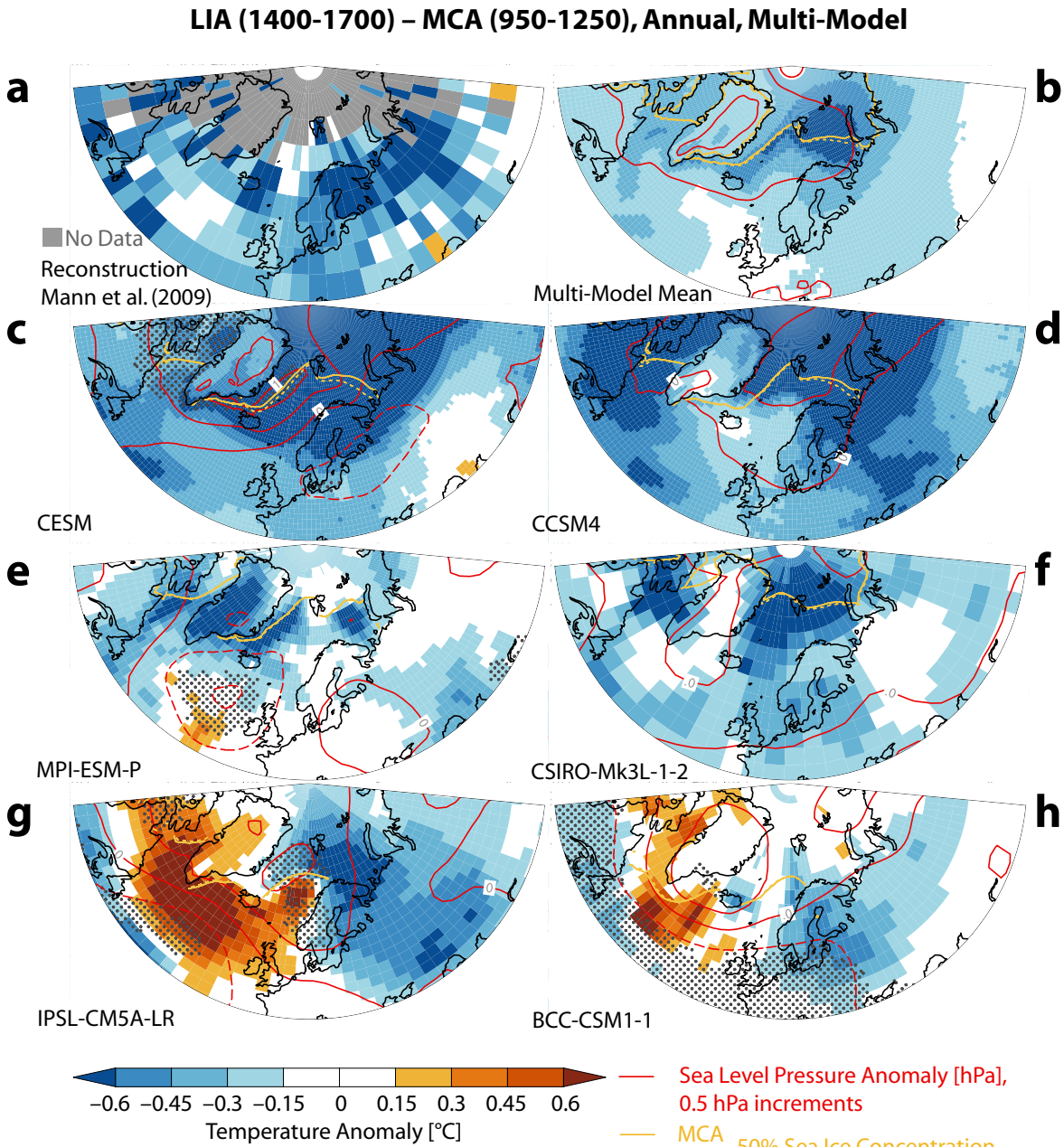
Figure A.7: Same as Fig. A.6 but for the time periods as in Mann et al. (2009): Little Ice Age (LIA, 1400-1700 AD) − Medieval Climate Anomaly (MCA, 950-1250 AD).

model means is its susceptibility to outliers or models with strong anomalies (e.g., Tebaldi and Knutti, 2007), such as CESM and CCSM4, which have relatively large anomalies over the Barents and Nordic Seas, potentially dominating the multi-model mean (Figs. A.6 and A.7).

Overall, however, the combination of the CCSM3 ensemble simulations together with the PMIP3 multi-model mean draws a relatively consistent picture of an amplified LIA-cooling over the Barents Sea and Northern Europe that seems to be closely linked with changes in sea ice cover.
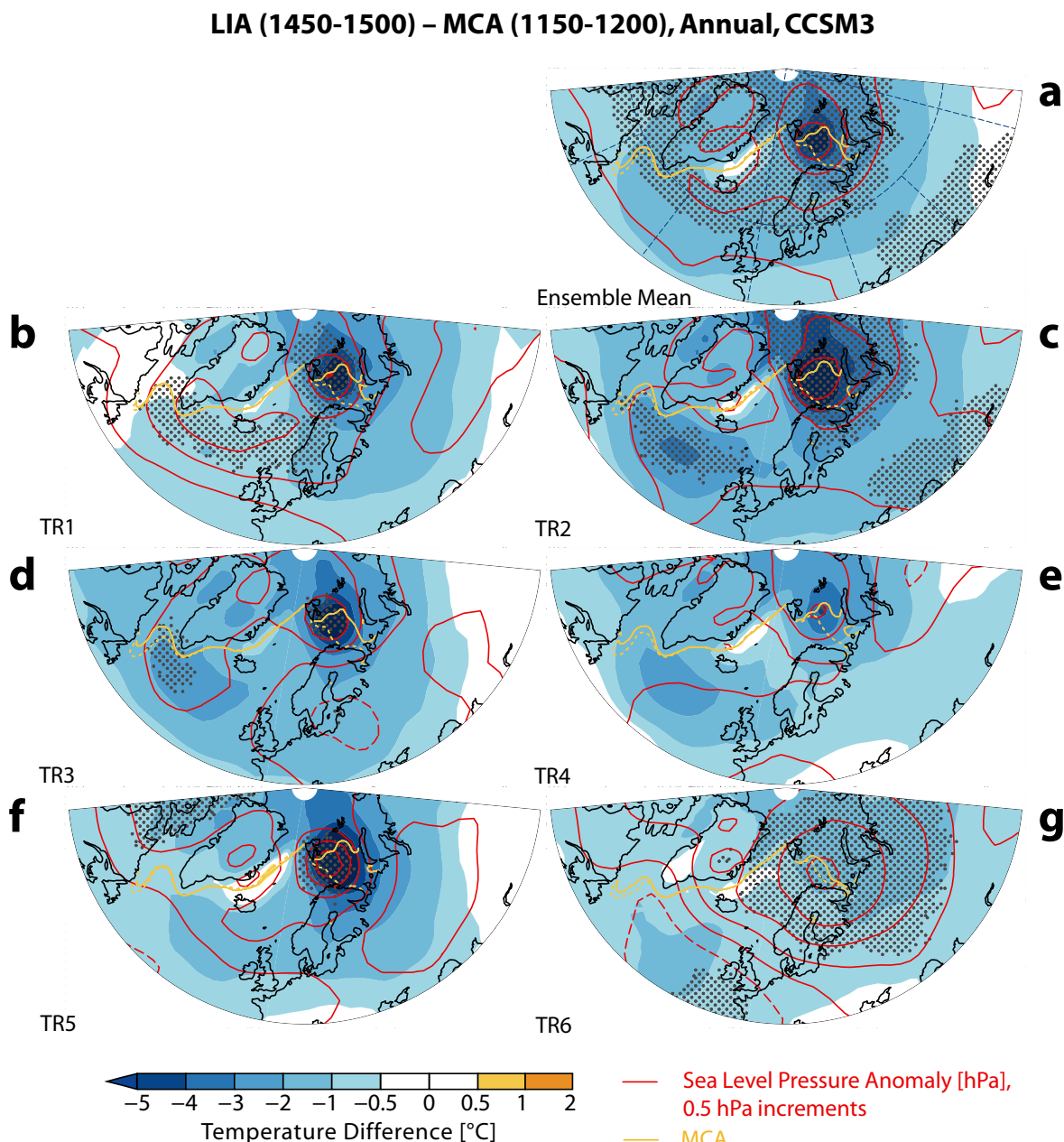
LIA (1450-1500) – MCA (1150-1200), Annual, CCSM3

Figure A.8: Same as Fig. A.6 but with CCSM3 from Lehner et al. (in press): (a) ensemble mean and (b-g) the individual ensemble members.

A.4.2 Modes of variability

With the last millennium simulations from CESM and the PMIP3 models at hand, an update of the study in chapter 3 can be provided by briefly revisiting the questions whether, (i), the simulated North Atlantic Oscillation (NAO) shows persistent positive or negative phases or, (ii), if coherent low-frequency behavior exists among the models.

Fig. A.9 displays the NAO indices from CESM, the PMIP3 models, the reconstruction by Trouet et al. (2009), and an instrumental record (Vinther et al., 2003). While there exists some coherence between reconstruction and models from 1600-1850 AD, the multi-model evolution of the NAO does not support the reconstructed persistent positive NAO during the MCA. However, Landrum et al. (2013) indicate a tendency towards positive values in CCSM4 during
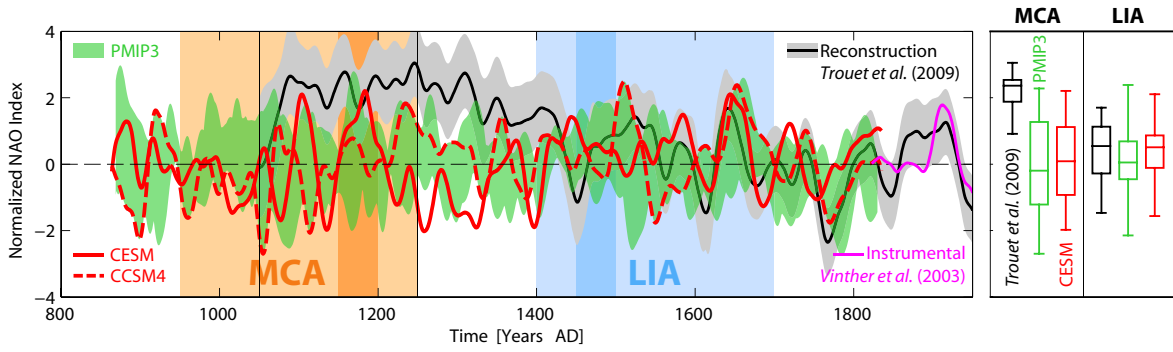
Figure A.9: The North Atlantic Oscillation (NAO) in simulations of the last millennium, defined as the first Empirical Orthogonal Function of November-March mean sea level pressure (SLP). Time series have been smoothed with a 30-year cubic spline and then normalized to make them comparable with the reconstruction by Trouet et al. (2009). The index by Vinther et al. (2003) is the longest instrumental record of the NAO, using SLP data from Gibraltar and Reykjavik. The Medieval Climate Anomaly (MCA) and the Little Ice Age (LIA) are indicated as defined in Mann et al. (2009, light shading) and Lehner et al. (in press, darker shading). The panel on the right shows boxplots of the NAO during the MCA (1010-1250 AD, indicated by black vertical lines) and the LIA in the reconstruction and the models.

1130-1330 AD. Clearly, it is difficult to draw robust conclusions on this as there exists only a single realization of CCSM4. The fact that neither CESM nor the median of PMIP3 model reproduces the CCSM4 tendency towards positive values during MCA suggests that external alone forcing cannot account for this signal. In that sense, the results from the new generation of models are compatible with older models, however, further investigation is needed as to the forced versus unforced oscillations in the NAO in model simulations of the last millennium. In any case, as discussed in Lehner et al. (2012a), additional proxies are required to improve the reconstructions and to clarify the role of the NAO during the last millennium.

A.4.3   Carbon cycle

The CESM includes an interactive carbon cycle module that allows to study the response of the carbon cycle to transient external forcing. To date, no transient last millennium simulation with the full carbon cycle version of CESM has been conducted. Lawrence et al. (2012) investigated the sensitivity of the land carbon cycle only to prescribed land cover changes from 1850-2100 AD. Keith Lindsay and co-authors have submitted a paper looking at the full carbon cycle, including the biogeochemical cycle in the ocean and prognostic exchanges with the atmosphere, in historical simulations from 1850-2005 AD. Considering other models, there exists a number of simulations (1850-2100 AD) from groups participating in the Coupled Climate-Carbon Cycle Model Intercomparison Project (C^4MIP; Friedlingstein et al., 2006) and, more recently, an intercomparison of last millennium simulations from EMICs (Eby et al., in press). Jungclaus et al. (2010) were the first to use a comprehensive coupled Earth system model with interactive carbon cycle, the MPI-ESM, to run an ensemble of last millennium simulations.

Fig. A.10 provides an overview of the carbon cycle during the last millennium as simulated by CESM. The land biosphere is a carbon sink during most of the first half of the last millennium, but becomes a source as anthropogenic land cover changes start to have a larger-scale impact on the carbon cycle (Fig. A.10b and c). This shift is somewhat abrupt around 1500 AD due to the unsmoothed merging of two forcing datasets (see section A.3.2). The ocean acts the other way around, being a carbon source at the beginning and becoming a sink in the second half of the last millennium. Towards the end of the simulation, anthropogenic emissions of carbon from fossil fuel combustion start to become significant. The residual of the

fluxes from and to the biosphere and ocean represents changes in the atmospheric reservoir of carbon, illustrated in Fig. A.10d by the simulated CO_2 concentration. The amplitude of the simulated concentration does not compare favorably with the one reconstructed from ice cores, raising the question whether the sensitivity of the carbon cycle to external forcing is too weak in CESM. Ensemble simulations with the MPI-ESM, another state-of-the-art Earth System Model, also do not fully reproduce the reconstructed amplitudes (Jungclaus et al., 2010). Further, Earth system models of intermediate complexity or vegetation models driven by GCMs do also not reproduce the uptake of carbon by either ocean or land needed to explain the reconstructed amplitudes (Renato Spahni, personal communication; Stocker et al., 2011). Additionally, the seasonal cycle is underestimated, at least when compared to twentieth century observations.

Given the shortness of our control simulation (258 years) and the long adjustment time of the carbon cycle (approximately 500 years; Keith Lindsay, personal communication, who conducted a >1,000 years 1850 AD control simulation), the carbon reservoirs in the land and ocean can probably not be considered in equilibrium. Due to computational constraints the control simulation could not be extended beyond the point of branching for the transient simulation. Therefore, a proper estimation of the long-term trend from a long control simulation is not possible (as done for example in chapter 2). During the control simulation the land ecosystem (excluding soils) accumulates carbon at about $8.4 \, \mathrm{Pg} \, \mathrm{C} \, 100 \, \mathrm{yr}^{-1}$, the soils at about $4.1 \, \mathrm{Pg} \, \mathrm{C} \, 100 \, \mathrm{yr}^{-1}$ (Fig. A.10e). These trends seem to persist at the beginning of the transient simulation, when the total land ecosystem and soil accumulate carbon at the rate of $7.9 \, \mathrm{Pg} \, \mathrm{C} \, 100 \, \mathrm{yr}^{-1}$ and $3.1 \, \mathrm{Pg} \, \mathrm{C} \, 100 \, \mathrm{yr}^{-1}$, respectively, during the first 200 years. These rates decrease and become zero and $0.6 \, \mathrm{Pg} \, \mathrm{C} \, 100 \, \mathrm{yr}^{-1}$, respectively after about 550 years.

A.4.4 Outlook

With the preindustrial part of the last millennium simulation completed (850-1850 AD), a variety of paleoclimatic research questions can be addressed. First steps have been made by briefly revisiting research questions of other chapters, dealing with the role of the NAO and the Arctic sea ice during the MCA-LIA transition. Within the same time period, the half-daily model output allows us to study the number and intensity of North Atlantic storms, potentially contributing to the long-standing debate on the driving mechanisms of the MCA-LIA transition (e.g., Trouet et al., 2009, 2012; Lehner et al., 2012a, in press). Also, the comparison with CCSM4 provides the opportunity to estimate the impact of different TSI amplitudes on the climate in the same physical model. Together with the PMIP3 simulations by other models and a growing number of proxies there exists an extended basis for tackling these paleoclimatic issues.

Regarding the carbon cycle, the simulation enables the high-resolution study of natural climate-carbon cycle interactions. Of particular interest will be the continuation of the simulation from 1850 AD into the twentieth century and the subsequent comparison with other CESM simulations that started in 1850 AD (conducted by the NCAR and Kathrin Keller at KUP). These simulations are typically started from equilibrated initial conditions for 1850 AD, which are expected to differ from our transient model state at the year 1850 AD. Thereby, the importance of inertia in the coupled climate-carbon cycle system can be investigated.
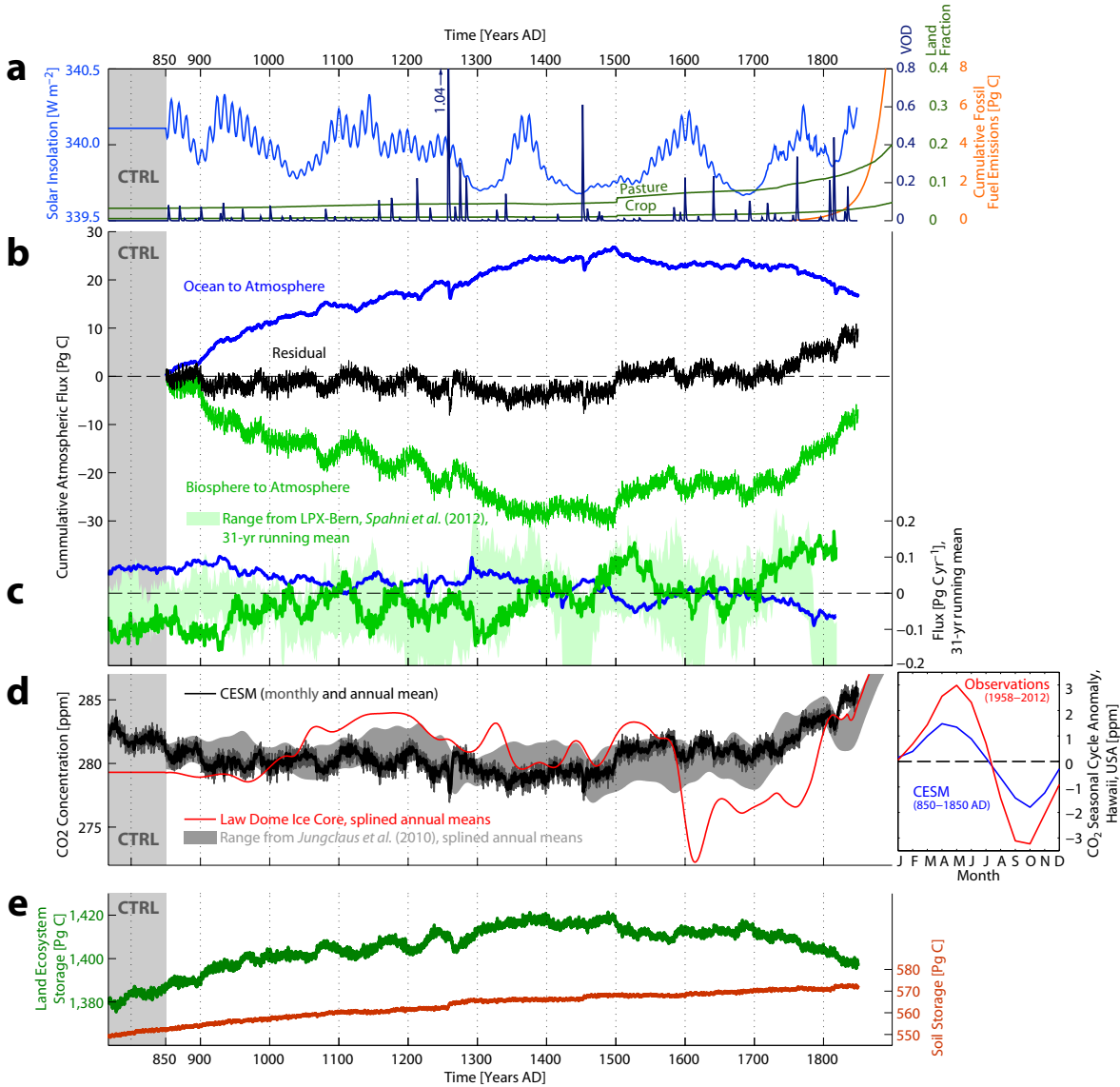
Figure A.10: The carbon cycle in CESM. (a) Forcings applied to the simulation: solar insolation, optical depth from volcanic aerosols (VOD), land cover changes, and prescribed carbon (C) emissions from fossil fuel combustion. (b) Cumulative C fluxes from the ocean to the atmosphere, from the biosphere to the atmosphere, and the sum of the two. (c) 31-yr running mean C fluxes from the biosphere and ocean to the atmosphere; negative values indicate a sink, positive values a source. The range of the LPX-Bern vegetation model forced by GCM climate data is given in light-green shading (Spahni et al., 2012). (d) Global mean atmospheric CO_2 concentration as calculated interactively by CESM and MPI-ESM (Jungclaus et al., 2010), and as prescribed in the radiative code based on splined ice core data. The inset on the right side shows the seasonal cycle of detrended atmospheric CO_2 over Hawaii from twentieth century observations (NOAA/ESRL and Scripps Institution of Oceanography) and from CESM. (e) Total land ecosystem and soil C storage. 83 years of the control simulation (CTRL) leading up to the start of the transient simulation are indicated by light gray shading.

Bibliography

Ammann, C. M. and E. R. Wahl, 2007: The importance of the geophysical context in statistical evaluations of climate reconstruction procedures. *Clim. Change* (85), 71–88, doi:10.1007/s10584-007-9276-x.

Anchukaitis, K. J., et al., 2012: Tree rings and volcanic cooling. *Nature Geoscience* (5), 836–837, doi: 10.1038/ngeo1645.

Andres, R. J., et al., 2012: A synthesis of carbon dioxide emissions from fossil-fuel combustion. *Biogeosciences* (9), 1845–1871, doi:10.5194/bg-9-1845-2012.

Armstrong, R., C. Lee, J. Hedges, S. Honjo, and S. Wakeham, 2002: A new, mechanistic model for organic carbon fluxes in the ocean based on the quantitative association of POC with ballast minerals. *Deep Sea Res. Part II* (49), 219–236.

Berger, A. L., 1978: Long-term variations of caloric insolation resulting from the earth's orbital elements. *J. Atm. Sci.* (35), 2362–2367, doi:10.1016/0033-5894(78)90064-9.

Briegleb, B. P. and B. Light, 2007: Tech. Rep. A delta-Eddington multiple scattering parameterization for solar radiation in the sea ice component of the Community Climate System Model, National Center for Atmospheric Research (NCAR). 100 pp.

Büntgen, U., et al., 2011: Causes and consequences of past and projected Scandinavian summer temperatures, 500-2100 AD. *PLOS ONE* (6), doi:10.1371/journal.pone.0025133.

Casty, C., C. C. Raible, T. F. Stocker, H. Wanner, and J. Luterbacher, 2007: A European pattern climatology 1766-2000. *Clim. Dyn.* (29), 791–805, doi:10.1007/s00382-007-0257-6.

Crowley, T. J., G. Zielinski, B. Vinther, R. Udisti, K. Kreutzs, J. Cole-Dai, and E. Castellano, 2008: Volcanism and the Little Ice Age. *PAGES newsletter* (16), 22–23.

Danabasoglu, G., S. C. Bates, B. P. Briegleb, S. R. Jayne, M. Jochum, W. G. Large, S. Peacock, and S. G. Yeager, 2012: The CCSM4 ocean component. *J. Clim.* (25), 1361–1389, doi:10.1175/JCLI-D-11-00091.1.

Danabasoglu, G., R. Ferrari, and J. C. McWilliams, 2008: Sensitivity of an ocean general circulation model to a parameterization of near-surface eddy fluxes. *J. Clim.* (21), 1192–1208, doi:10.1175/2007JCLI1508.1.

Danabasoglu, G., W. G. Large, and B. P. Briegleb, 2010: Climate impacts of parameterized Nordic Sea overflows. *J. Geophys. Res.* (115), doi:10.1029/2010JC006243.

Danabasoglu, G. and J. Marshall, 2007: Effects of vertical variations of thickness diffusivity in an ocean general circulation model. *Ocean Modelling* (18), 122–141, doi:10.1016/j.ocemod.2007.03.006.

Eby, M., et al., in press: Historical and idealized climate model experiments: an EMIC intercomparison. *Clim. Past.*

Friedlingstein, P., et al., 2006: Climate-carbon cycle feedback analysis: Results from the C^4MIP model intercomparison. *J. Clim.* (19), 3337–3353, doi:10.1175/JCLI3800.1.

Gao, C., A. Robock, and C. Ammann, 2008: Volcanic forcing of climate over the past 1500 years: An improved ice core-based index for climate models. *J. Geophys. Res.* (113), doi:10.1029/2008JD010239.

Gent, P. R., et al., 2011: The Community Climate System Model Version 4. *J. Clim.* (24), 4973–4991, doi: 10.1175/2011JCLI4083.1.

Hegerl, G. C., T. J. Crowley, M. Allen, W. T. Hyde, H. N. Pollack, J. Smerdon, and E. Zorita, 2007: Detection of human influence on a new, validated 1500-year temperature reconstruction. *J. Clim.* (20), 650–666, doi:10.1175/JCLI4011.1.

Hofer, D., C. C. Raible, A. Dehnert, and J. Kuhlemann, 2012a: The impact of different glacial boundary conditions on atmospheric dynamics and precipitation in the North Atlantic region. *Clim. Past* (8), 935–949, doi:10.5194/cp-8-935-2012.

Hofer, D., C. C. Raible, N. Merz, A. Dehnert, and J. Kuhlemann, 2012b: Simulated winter circulation types in the North Atlantic and European region for preindustrial and glacial conditions. *Geophys. Res. Let.* (39), doi:10.1029/2012GL052296.

Hofer, D., C. C. Raible, and T. F. Stocker, 2011: Variations of the Atlantic meridional overturning circulation in control and transient simulations of the last millennium. *Clim. Past* (7), 133–150, doi:10.5194/cp-7-133-2011.

Holland, M. M., D. A. Bailey, B. P. Briegleb, B. Light, and E. Hunke, 2012: Improved sea ice shortwave radiation physics in CCSM4: the impact of melt ponds and aerosols on Arctic sea ice. *J. Clim.* (25), 1413–1430, doi:10.1175/JCLI-D-11-00078.1.

Hunke, E. C. and W. H. Lipscomb, 2010: Tech. Rep. CICE: the Los Alamos sea ice model documentation and software user's manual version 4.1, Los Alamos National Laboratory (LANL). 76 pp.

Hurtt, G. C., et al., 2011: Harmonization of land-use scenarios for the period 1500-2100: 600 years of global gridded annual land-use transitions, wood harvest, and resulting secondary lands. *Clim. Change* (109), 117–161, doi:10.1007/s10584-011-0153-2.

IPCC, 2001: *Climate Change 2001: The Scientific Basis. Contribution of Working Group I to the Third Assessment Report of the Intergovernmental Panel on Climate Change*, Cambridge University Press, Cambridge, United Kingdom and New York, NY, USA, 881 pp.

IPCC, 2007: *Climate Change 2007: The Physical Science Basis. Contribution of Working Group I to the Fourth Assessment Report of the Intergovernmental Panel on Climate Change*, Cambridge University Press, Cambridge, United Kingdom and New York, NY, USA, 996 pp.

Jochum, M., G. Danabasoglu, M. Holland, Y. O. Kwon, and W. G. Large, 2008: Ocean viscosity and climate. *J. Geophys. Res.* (113), doi:10.1029/2007JC004515.

Jungclaus, J. H., et al., 2010: Climate and carbon-cycle variability over the last millennium. *Clim. Past* (6), 723–737, doi:10.5194/cp-6-723-2010.

Kaufman, D. S., et al., 2009: Recent warming reverses long-term Arctic cooling. *Science* (325), 1236–1239, doi:10.1126/science.1173983.

Kinnard, C., C. M. Zdanowicz, D. A. Fisher, E. Isaksson, A. de Vernal, and L. G. Thompson, 2011: Reconstructed changes in Arctic sea ice over the past 1,450 years. *Nature* (479), 509–U231, doi:10.1038/nature10581.

Knutti, R. and J. Sedláček, 2012: Robustness and uncertainties in the new CMIP5 climate model projections. *Nature Climate Change*, doi:10.1038/NCLIMATE1716, published online.

Lamarque, J. F., et al., 2010: Historical (1850-2000) gridded anthropogenic and biomass burning emissions of reactive gases and aerosols: methodology and application. *Atmospheric Chemistry and Physics* (10), 7017–7039, doi:10.5194/acp-10-7017-2010.

Landrum, L., B. L. Otto-Bliesner, E. R. Wahl, A. Conley, P. J. Lawrence, N. Rosenbloom, and H. Teng, 2013: Last millennium climate and its variability in CCSM4. *J. Clim.* (26), 1085–1111, doi:10.1175/JCLI-D-11-00326.1.

Lawrence, D. M., et al., 2011: Parameterization improvements and functional and structural advances in version 4 of the Community Land Model. *J. of Adv. in Modeling Earth Systems* (3), doi:10.1029/2011MS000045.

Lawrence, P. J., et al., 2012: Simulating the biogeochemical and biogeophysical impacts of transient land cover change and wood harvest in the Community Climate System Model (CCSM4) from 1850 to 2100. *J. Clim.* (25), 3071–3095, doi:10.1175/JCLI-D-11-00256.1.

Lean, J., G. Rottman, J. Harder, and G. Kopp, 2005: SORCE contributions to new understanding of global change and solar variability. *Solar Physics* (230), 27–53, doi:10.1007/s11207-005-1527-2.

Leclercq, P. W. and J. Oerlemans, 2012: Global and hemispheric temperature reconstruction from glacier length fluctuations. *Clim. Dyn.* (38), 1065–1079, doi:10.1007/s00382-011-1145-7.

Lehner, F., A. Born, C. C. Raible, and T. F. Stocker, in press: Amplified inception of European Little Ice Age by sea ice-ocean-atmosphere feedbacks. *J. Clim.*

Lehner, F., C. C. Raible, and T. F. Stocker, 2012a: Testing the robustness of a precipitation proxy-based North Atlantic Oscillation reconstruction. *Quat. Sci. Rev.* (45), 85–94, doi:10.1016/j.quascirev.2012.04.025.

Lehner, F., C. C. Raible, T. F. Stocker, and D. Hofer, 2012b: The freshwater balance of polar regions in transient simulations from 1500 to 2100 AD using a comprehensive coupled climate model. *Clim. Dyn.* (39), 347–363, doi:10.1007/s00382-011-1199-6.

Lin, S., 2004: A "vertically Lagrangian" finite-volume dynamical core for global models. *Mon. Weather Rev.* (132), 2293–2307, doi:10.1175/1520-0493(2004)132<2293:AVLFDC>2.0.CO;2.

Long, M. C., K. Lindsay, S. Peacock, J. K. Moore, and S. C. Doney, 2013: 20th century oceanic carbon uptake an1 d storage in CESM1(BGC). *J. Clim.*, doi:10.1175/JCLI-D-12-00184.1, early online release.

Mann, E. M., et al., 2009: Global signatures and dynamical origins of the Little Ice Age and Medieval Climate Anomaly. *Science* (326), 1256–1260, doi:10.1126/science.1177303.

Mann, M. E., J. D. Fuentes, and S. Rutherford, 2012: Underestimation of volcanic cooling in tree-ring-based reconstructions of hemispheric temperatures. *Nature Geoscience* (5), 202–205, doi:10.1038/NGEO1394.

Mann, M. E., Z. Zhang, M. K. Hughes, R. S. Bradley, S. K. Miller, S. Rutherford, and F. Ni, 2008: Proxy-based reconstructions of hemispheric and global surface temperature variations over the past two millennia. *Proc. Natl. Acad. Sci.* (105), 13 252–13 257, doi:10.1073/pnas.0805721105.

Meehl, G. A., et al., 2012: Climate system response to external forcings and climate change projections in CCSM4. *J. Clim.* (25), 3661–3683, doi:10.1175/JCLI-D-11-00240.1.

Meehl, G. A., et al., 2013: Climate change projections in CESM1(CAM5) compared to CCSM4. *J. Clim.*, doi:10.1175/JCLI-D-12-00572.1, early online release.

Moore, J., S. Doney, and K. Lindsay, 2004: Upper ocean ecosystem dynamics and iron cycling in a global three-dimensional model. *Global Biogeochem. Cyc.* (18), doi:10.1029/2004GB002220.

Müller, S. A., F. Joos, N. R. Edwards, and T. F. Stocker, 2006: Water mass distribution and ventilation time scales in a cost-efficient, three-dimensional ocean model. *J. Clim.* (19), 5479–5499, doi:10.1175/JCLI3911.1.

Neale, R. B., J. H. Richter, and M. Jochum, 2008: The impact of convection on ENSO: from a delayed oscillator to a series of events. *J. Clim.* (21), 5904–5924, doi:10.1175/2008JCLI2244.1.

Neale, R. B., et al., 2010a: Tech. Rep. Description of the NCAR Community Atmosphere Model (CAM 4.0), National Center for Atmospheric Research (NCAR). 212 pp.

Neale, R. B., et al., 2010b: Tech. Rep. Description of the NCAR Community Atmosphere Model (CAM 5.0), National Center for Atmospheric Research (NCAR). 268 pp.

Otto-Bliesner, B., 2009: Modeling and sata syntheses of past climates. *EOS, Trans. Am. Geophys. Union* (90).

PAGES 2k network, 2013: Continental-scale temperature variability during the past two millennia. *Nature Geoscience* (6), 339–346.

Pongratz, J., C. Reick, T. Raddatz, and M. Claussen, 2008: A reconstruction of global agricultural areas and land cover for the last millennium. *Global Biogeochem. Cyc.* (22), doi:10.1029/2007GB003153.

Raible, C., T. Stocker, M. Yoshimori, M. Renold, U. Beyerle, C. Casty, and J. Luterbacher, 2005: Northern hemispheric trends of pressure indices and atmospheric circulation patterns in observations, reconstructions, and coupled GCM simulations. *J. Clim.* (18), 3968–3982, doi:10.1175/JCLI3511.1.

Raible, C. C., M. Yoshimori, T. F. Stocker, and C. Casty, 2007: Extreme midlatitude cyclones and their implications for precipitation and wind speed extremes in simulations of the Maunder Minimum versus present day conditions. *Clim. Dyn.* (28), 409–423, doi:10.1007/s00382-006-0188-7.

Raible, C. C., et al., 2006: Climate variability-observations, reconstructions, and model simulations for the Atlantic-European and Alpine region from 1500-2100 AD. *Clim. Change* (79), 9–29, doi:10.1007/s10584-006-9061-2.

Rayner, N., D. Parker, E. Horton, C. Folland, L. Alexander, D. Rowell, E. Kent, and A. Kaplan, 2003: Global analyses of sea surface temperature, sea ice, and night marine air temperature since the late nineteenth century. *Journal of Geophysical Research* (108), ACL2–1–29.

Renold, M., C. C. Raible, M. Yoshimori, and T. F. Stocker, 2010: Simulated resumption of the North Atlantic meridional overturning circulation - Slow basin-wide advection and abrupt local convection. *Quat. Sci. Rev.* (29), 101–112, doi:10.1016/j.quascirev.2009.11.005.

Richter, J. H. and P. J. Rasch, 2008: Effects of convective momentum transport on the atmospheric circulation in the Community atmosphere Model, version 3. *J. Clim.* (21), 1487–1499, doi:10.1175/2007JCLI1789.1.

Ritz, S. P., T. F. Stocker, and F. Joos, 2011: A coupled dynamical ocean-energy balance atmosphere model for paleoclimate studies. *J. Clim.* (24), 349–375, doi:10.1175/2010JCLI3351.1.

Schauer, U., E. Fahrbach, S. Osterhus, and G. Rohardt, 2004: Arctic warming through the Fram Strait: Oceanic heat transport from 3 years of measurements. *J. Geophys. Res.* (109), doi:10.1029/2003JC001823.

Schmidt, G. A., et al., 2011: Climate forcing reconstructions for use in PMIP simulations of the last millennium (v1.0). *Geoscientific Model Development* (4), 33–45, doi:10.5194/gmd-4-33-2011.

Schmidt, G. A., et al., 2012: Climate forcing reconstructions for use in PMIP simulations of the Last Millennium (v1.1). *Geoscientific Model Development* (5), 185–191, doi:10.5194/gmd-5-185-2012.

Schneider, D. P., C. M. Ammann, B. L. Otto-Bliesner, and D. S. Kaufman, 2009: Climate response to large, high-latitude and low-latitude volcanic eruptions in the Community Climate System Model. *J. Geophys. Res.* (114), doi:10.1029/2008JD011222.

Shapiro, A. I., W. Schmutz, E. Rozanov, M. Schoell, M. Haberreiter, A. V. Shapiro, and S. Nyeki, 2011: A new approach to the long-term reconstruction of the solar irradiance leads to large historical solar forcing. *Astronomy & Astrophysics* (529), doi:10.1051/0004-6361/201016173.

Smith, R., et al., 2010: Tech. Rep. The Parallel Ocean Program (POP) Reference Manual, Los Alamos National Laboratory (LANL). 140 pp.

Spahni, R., F. Joos, B. D. Stocker, M. Steinacher, and Z. C. Yu, 2012: Transient simulations of the carbon and nitrogen dynamics in northern peatlands: from the Last Glacial Maximum to the 21st century. *Clim. Past Discuss.* (8), 5633–5685, doi:10.5194/cpd-8-5633-2012.

Spangehl, T., U. Cubasch, C. C. Raible, S. Schimanke, J. Koerper, and D. Hofer, 2010: Transient climate simulations from the Maunder Minimum to present day: Role of the stratosphere. *J. Geophys. Res.* (115), doi:10.1029/2009JD012358.

Spielhagen, R. F., et al., 2011: Enhanced modern heat transfer to the Arctic by warm Atlantic water. *Science* (331), 450–453, doi:10.1126/science.1197397.

Steinacher, M., et al., 2010: Projected 21st century decrease in marine productivity: a multi-model analysis. *Biogeosciences* (7), 979–1005.

Stocker, B. D., K. Strassmann, and F. Joos, 2011: Sensitivity of Holocene atmospheric CO2 and the modern carbon budget to early human land use: analyses with a process-based model. *Biogeosciences* (8), 69–88, doi:10.5194/bg-8-69-2011.

Stocker, T. F., A. Timmermann, M. Renold, and O. Timm, 2007: Effects of salt compensation on the climate model response in simulations of large changes of the Atlantic meridional overturning circulation. *J. Clim.* (20), 5912–5928, doi:10.1175/2007JCLI1662.1.

Stocker, T. F., D. G. Wright, and L. A. Mysak, 1992: A zonally averaged, coupled ocean-atmosphere model for paleoclimate studies. *J. Clim.* (5), 773–797.

Taylor, K. E., R. J. Stouffer, and G. A. Meehl, 2012: An overview of CMIP5 and the experiment design. *Bull. Am. Meteorol. Soc.* (93), 485–498, doi:10.1175/BAMS-D-11-00094.1.

Tebaldi, C. and R. Knutti, 2007: The use of the multi-model ensemble in probabilistic climate projections. *Phil. Trans. Roy. Soc., London* (365), 2053–2075, doi:10.1098/rsta.2007.2076.

Timmreck, C., H.-F. Graf, S. J. Lorenz, U. Niemeier, D. Zanchettin, D. Matei, J. H. Jungclaus, and T. J. Crowley, 2010: Aerosol size confines climate response to volcanic super-eruptions. *Geophys. Res. Let.* (37), doi:10.1029/2010GL045464.

Trouet, V., J. Esper, N. E. Graham, A. Baker, J. D. Scourse, and D. C. Frank, 2009: Persistent positive North Atlantic Oscillation mode dominated the Medieval Climate Anomaly. *Science* (324), 78–80, doi:10.1126/science.1166349.

Trouet, V., J. D. Scourse, and C. C. Raible, 2012: North Atlantic storminess and Atlantic Meridional Overturning Circulation during the last Millennium: Reconciling contradictory proxy records of NAO variability. *Global and Plan. Change* (84-85), 48–55, doi:10.1016/j.gloplacha.2011.10.003.

Vavrus, S. and D. Waliser, 2008: An improved parametrization for simulating Arctic cloud amount in the CCSM3 climate model. *J. Clim.* (21), 5673–5687, doi:10.1175/2008JCLI2299.1.

Vieira, L. E. A. and S. K. Solanki, 2010: Evolution of the solar magnetic flux on time scales of years to millenia. *Astronomy & Astrophysics* (509), doi:10.1051/0004-6361/200913276.

Vinther, B., K. Andersen, A. Hansen, T. Schmith, and P. Jones, 2003: Improving the Gibraltar/Reykjavik NAO index. *Geophys. Res. Let.* (30), doi:10.1029/2003GL018220.

Wang, Y., J. Lean, and N. Sheeley, 2005: Modeling the sun's magnetic field and irradiance since 1713. *Astrophysical Journal* (625), 522–538, doi:10.1086/429689.

Wilmes, S. B., C. C. Raible, and T. F. Stocker, 2012: Climate variability of the mid- and high-latitudes of the Southern Hemisphere in ensemble simulations from 1500 to 2000 AD. *Clim. Past* (8), 373–390, doi:10.5194/cp-8-373-2012.

Yoshimori, M., C. C. Raible, T. F. Stocker, and M. Renold, 2006: On the interpretation of low-latitude hydrological proxy records based on Maunder Minimum AOGCM simulations. *Clim. Dyn.* (27), 493–513, doi:10.1007/s00382-006-0144-6.

Yoshimori, M., C. C. Raible, T. F. Stocker, and M. Renold, 2010: Simulated decadal oscillations of the Atlantic meridional overturning circulation in a cold climate state. *Clim. Dyn.* (34), 101–121, doi:10.1007/s00382-009-0540-9.

Yoshimori, M., T. Stocker, C. Raible, and M. Renold, 2005: Externally forced and internal variability in ensemble climate simulations of the Maunder Minimum. *J. Clim.* (18), 4253–4270, doi:10.1175/JCLI3537.1.

Acknowledgements

I would like to thank . . .

Publications

Lehner, F., Raible, C. C., & Stocker, T. F., 2012a. Testing the robustness of a precipitation proxy-based North Atlantic Oscillation reconstruction, *Quat. Sci. Rev.*, 45, 85–94.

Lehner, F., Raible, C. C., Stocker, T. F., & Hofer, D., 2012b. The freshwater balance of polar regions in transient simulations from 1500 to 2100 AD using a comprehensive coupled climate model, *Clim. Dyn.*, 39, 347–363.

Lehner, F., Born, A., Raible, C. C., & Stocker, T. F., in press. Amplified inception of European Little Ice Age by sea ice-ocean-atmosphere feedbacks, *J. Clim.*.

Erklärung

gemäss Art. 28 Abs. 2 RSL 05

Name/Vorname: Flavio Lehner

Matrikelnummer: 02–058–467

Studiengang: Climate Sciences

                              Bachelor ☐   Master ☐   Dissertation ☒

Titel der Arbeit: Estimating natural and anthropogenic responses of the water cycle in the Earth system using comprehensive coupled climate models

Leiter der Arbeit: Prof. Dr. Thomas F. Stocker

Ich erkläre hiermit, dass ich diese Arbeit selbständig verfasst und keine anderen als die angegebenen Quellen benutzt habe. Alle Stellen, die wörtlich oder sinngemäss aus Quellen entnommen wurden, habe ich als solche gekennzeichnet. Mir ist bekannt, dass andernfalls der Senat gemäss Artikel 36 Absatz 1 Buchstabe o des Gesetzes vom 5. September 1996 über die Universität zum Entzug des auf Grund dieser Arbeit verliehenen Titels berechtigt ist.

Bern, 28. Mai 2013

Curriculum vitæ

Personal Data

Name	Flavio Lehner
Date of birth	September 28, 1984
Place of origin	Basel BS

Education

1991–1995	PRIMARY SCHOOL, Basel, Switzerland
1995–1998	ORIENTATION SCHOOL, Basel, Switzerland
1998–2003	GYMNASIUM Leonhard, Basel, Switzerland
2004–2007	BACHELOR OF SCIENCE IN GEOSCIENCES at the University of Basel, Switzerland
2007–2009	MASTER OF SCIENCE IN CLIMATE SCIENCES at the University of Bern and the Oeschger Centre for Climate Change Research, Switzerland
2008–2009	MASTER THESIS at the division of Climate and Environmental Physics, Physics Institute, University of Bern, Switzerland (Thesis advisors: Prof. Dr. Thomas F. Stocker and PD Dr. Christoph Raible)
2009–2013	PH. D. THESIS at the division of Climate and Environmental Physics, Physics Institute, University of Bern, Switzerland (Thesis advisors: Prof. Dr. Thomas F. Stocker and PD Dr. Christoph Raible)

Conferences, workshops, and seminars

2009	EGU General Assembly 2009, Vienna, Austria (*talk*)
2009	Visit at Institute of Low-Temperature Science, Hokkaido University, Sapporo, Japan (*invited talk*)
2010	EGU General Assembly 2010, Vienna, Austria (*two talks*)
2010	NCCR Young Researchers Meeting 2010, Murten, Switzerland
2011	NCCR Summer School 2011, Grindelwald, Switzerland (*poster*)
2011	Workshop "Weather and Climate Extremes During the Past 100 years", Diessenhofen, Switzerland (*poster*)
2011	"Climate Change Scenario Workshop", Zurich, Switzerland
2011	INQUA 2011, Bern, Switzerland (*poster*)
2012	Oeschger Centre Plenary Meeting, Bern, Switzerland (*talk*)
2012	ESF Conference "Modes of Variability in the Climate System: Past-Present-Future", Obergurgl, Austria (*talk*)
2012	EGU General Assembly 2012, Vienna, Austria (*two talks*)
2012	NCCR Summer School 2012, Monte Verità, Switzerland (*poster*)
2012	Visit at Laboratoire des Sciences du Climat et de l'Environnement, Gif-sur-Yvette, France (*invited talk*)
2013	PAGES Young Scientists Meeting and Open Science Meeting, Goa, India (*poster and talk*)